PETROLOGY AND GEOCHEMISTRY OF FELSIC MAGMATIC ROCKS OF DIBANG VALLEY, ARUNACHAL PRADESH

THESIS SUBMITTED IN PARTIAL FULFILMENT OF THE REQUIREMENTS
FOR THE DEGREE OF DOCTOR OF PHILOSOPHY

By

DIEZENEINO MEYASE

Ph.D/GEL/00088 of 2017

DEPARTMENT OF GEOLOGY, SCHOOL OF SCIENCES
NAGALAND UNIVERSITY, KOHIMA CAMPUS
MERIEMA- 797004
NAGALAND, INDIA
AUGUST 2025

PETROLOGY AND GEOCHEMISTRY OF FELSIC MAGMATIC ROCKS OF DIBANG VALLEY, ARUNACHAL PRADESH

By

DIEZENEINO MEYASE

Ph.D/GEL/00088 of 2017

Prof. VIKOLENO RINO
Supervisor

In partial fulfilment of the requirements for the degree of Doctor of Philosophy in Geology of Nagaland University

2025

NAGALAND UNIVERSITY

Dr.VIKOLENO RINO
Professor
Department of Geology
Kohima Campus, Meriema
797 004

Mobile : 8787467916
E-mail : vikolenorino@nagalanduniversity.ac.in

CERTIFICATE

The thesis presented by Ms. Diezeneino Meyase, Ph.D, Research Scholar of the Department of Geology, Nagaland University, Kohima Campus, Meriema bearing Registration No. Ph.D/GEL/00088 of 30th August 2017 embodies the results of investigations carried out by her under my supervision and guidance.

I certify that this work has not been presented for any degree elsewhere and that the candidate has fulfilled all conditions laid down by the University.

Place: KOHIMA
Date:

(VIKOLENO RINO)
Supervisor

NAGALAND UNIVERSITY

August 2025

DECLARATION

I, Ms. Diezeneino Meyase, hereby declare that the subject matter of this thesis is the record of work done by me, that the contents of this Thesis did not form basis of the award of any previous degree to me or to the best of my knowledge to anybody else. It is also declared that the thesis has not been submitted by me for any research degree in any other University/Institute.

This thesis is submitted to the Nagaland University, in partial fulfilment for the degree of Doctor of Philosophy in Geology under the supervision of Prof. Vikoleno Rino of Nagaland University.

Date:

Place: Department of Geology
Nagaland University
Kohima Campus, Meriema

DIEZENEINO MEYASE
Ph.D. Scholar
Department of Geology
Regd. No. Ph.D/GEL/00088

Head
(Prof. Vikoleno Rino)

Supervisor
(Prof. Vikoleno Rino)

नागालैण्ड विश्वविद्यालय

NAGALAND UNIVERSITY

(A Central University established by the Act of Parliament No.35 of 1989)

Headquarters: Lumami, Dist: Zunheboto, (Nagaland), Pin Code-798627

PLAGIARISM UNDERTAKING

Name of Scholar	Diezeneino Meyase
Registration Number	Ph.D/GEL/00088 of 30th August, 2017
Title of PhD Thesis	Petrology and Geochemistry of Felsic Magmatic Rocks of Dibang Valley, Arunachal Pradesh
Name &Institutional Address of the Supervisor/Co-Supervisor	Prof. Vikoleno Rino, Department of Geology, Nagaland University, Kohima Campus, Meriema
Name of the Department and School	Department of Geology/ School of Sciences
Date of submission	
Date of plagiarism check	12/08/2025
Name of the software used	DrillBit

I hereby declare /certify that the Ph.D. thesis submitted by me is complete in all respects, as per the guidelines of the Nagaland University. I also certify that the thesis (soft copy) has been checked for plagiarism using DrillBit plagiarism detection software. It is also certified that the contents of the electronic version of the thesis are the same as the final hard copy of the thesis. A copy of the report generated by the DrillBit plagiarism detection software is also enclosed.

Date: (Name and Signature of the Scholar)
Place:

Name & Signature of the Supervisor with seal

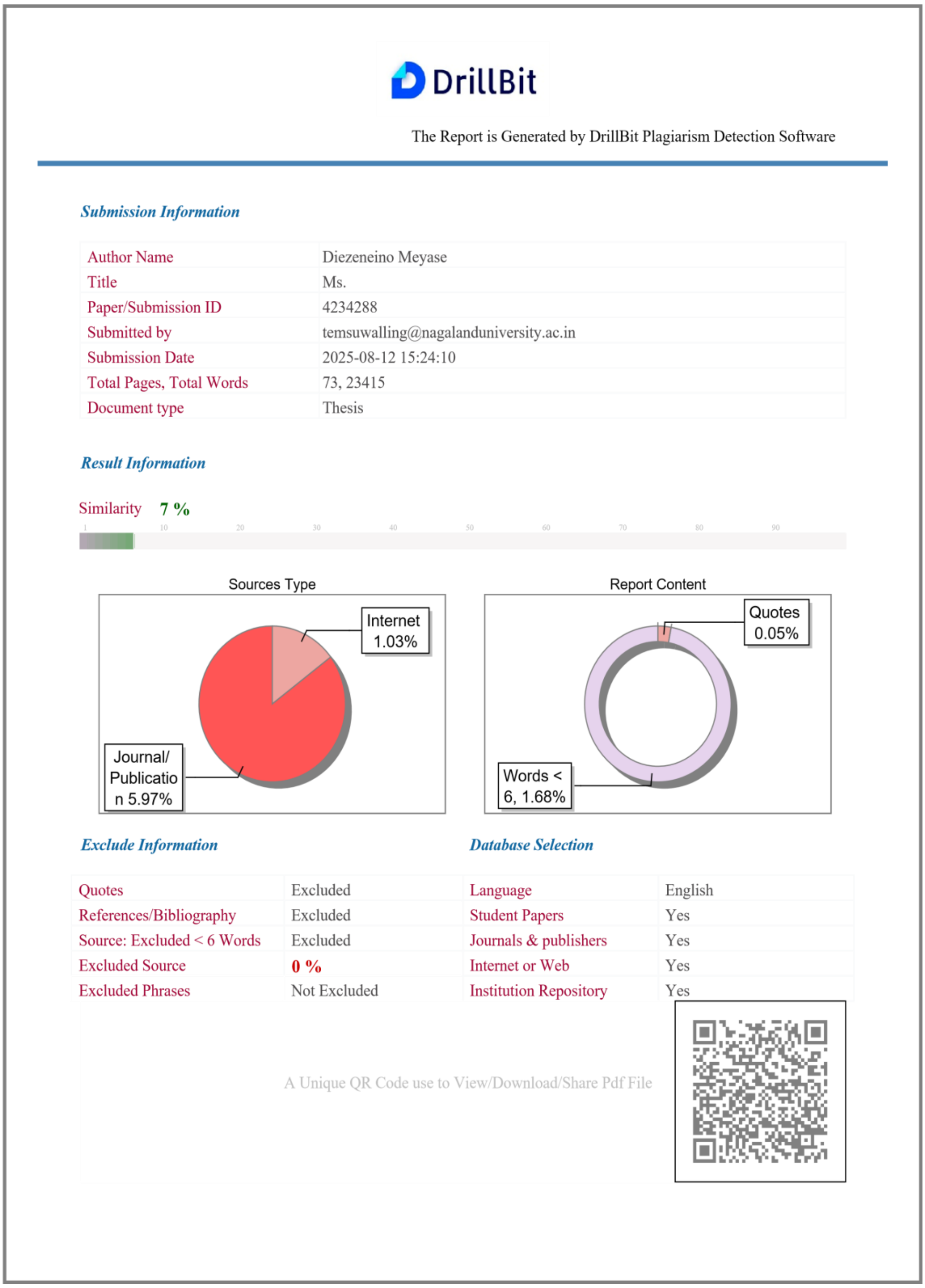

DrillBit

The Report is Generated by DrillBit Plagiarism Detection Software

Submission Information

Author Name	Diezeneino Meyase
Title	Ms.
Paper/Submission ID	4234288
Submitted by	temsuwalling@nagalanduniversity.ac.in
Submission Date	2025-08-12 15:24:10
Total Pages, Total Words	73, 23415
Document type	Thesis

Result Information

Similarity **7 %**

Sources Type

Report Content

Exclude Information

Quotes	Excluded
References/Bibliography	Excluded
Source: Excluded < 6 Words	Excluded
Excluded Source	**0 %**
Excluded Phrases	Not Excluded

Database Selection

Language	English
Student Papers	Yes
Journals & publishers	Yes
Internet or Web	Yes
Institution Repository	Yes

A Unique QR Code use to View/Download/Share Pdf File

ACKNOWLEDGEMENT

At the very outset, I thank the Almighty God for all His abundant blessings during the entire course of my research work, which has made this academic pursuit possible.

This thesis is the result of several years of research, and it would not have been possible without the guidance, support, and encouragement of many people to whom I am deeply grateful.

First and foremost, I express my profound gratitude to my supervisor, ***Prof. Vikoleno Rino****, for her invaluable guidance, continuous support, and patience throughout my Ph.D. journey. Her expertise, constructive feedback, and encouragement have been crucial in shaping this research and in fostering my academic growth. I am also grateful to* ***Shri Vizhoto Hibo****, Supervisor's spouse, who accompanied us during the extensive fieldwork and left no stone unturned in easing the fieldwork.*

I also extend my sincere thanks to the members of my Research Advisory Committee, ***Prof. Santosh Kumar Singh and Dr. Ch. Mangi Khuman****, for their insightful comments, valuable suggestions, and encouragement, which have greatly enriched this work.*

I also take this time to thank my batchmates, Dr. Akhrulu Vero, Dr. Vilavonuo Keditsu, Dr. Mademshila Jamir, Dr. Mehilo Apon, Dr. Keneisazo Nagi, and Mrs. Hievinu Olivia Richa for their selfless involvement, assistance, and encouragement till the completion of this thesis. I am forever indebted to them.

Special thanks to Dr. Mehilo Apon, Mr. Arite Khape, and Ms. Rokozono Nagi for their support and assistance in all technical matters, and Dr. Anettsungla for the constant support, insightful suggestions, and discussions. I am deeply thankful for the time, effort, and expertise they so willingly shared, which has been invaluable to the successful completion of this work

Special gratitude is extended to Dr. A. Moalong Kichu, Mr. Thecau Meru, and Mr. Avotso Meyase for their invaluable assistance during the fieldwork. My sincere thanks and deep appreciation are also extended to all the enthusiastic and seasoned *research scholars from the Department of Geology, Nagaland University, whose names could not be mentioned individually. I remain deeply grateful to them for their encouragement, generosity, support, and insightful discussions that have made this journey more enjoyable and meaningful.*

I am also deeply appreciative of the Head of Department, all the teaching faculty members, and technical staff of the Department of Geology, Nagaland University, for providing a stimulating academic environment and for their assistance in various aspects of this study.

Finally, but not least, I owe my deepest gratitude to my family. Their unconditional love, encouragement, prayers, sacrifices, and steadfast support have been my greatest source of strength. This achievement is as much theirs as it is mine.

(Diezeneino Meyase)

PARTICULARS OF THE CANDIDATE

NAME OF THE CANDIDATE : Diezeneino Meyase
DEGREE : Ph.D.
DEPARTMENT : Geology
TITLE OF THE THESIS : Petrology and Geochemistry of Felsic Magmatic Rocks of Dibang Valley, Arunachal Pradesh

DATE OF ADMISSION : 30th August 2017

APPROVAL OF RESEARCH PROPOSAL : 16th August 2018

REGISTRATION NUMBER AND DATE : Ph.D/GEL/00088 of 30/08/2017

Head of the Department

BIODATA OF THE CANDIDATE

I. PAPERS PUBLISHED

- **Diezeneino Meyase**, Vikoleno Rino, Santosh Kumar & Rokozono Nagi (2023). "Magnetic susceptibility, mineral chemistry, and geothermobarometry of granitoids from Lohit Plutonic Complex, Arunachal Trans-Himalaya, Northeast India: Implications on emplacement and crystallization conditions of oxidized calc alkaline magmatic arc system" Island Arc, 32(1), e12479. https://doi.org/10.1111/iar.12479

II. ABSTRACT PUBLISHED/ORAL PRESENTATION

1. "Magnetic susceptibility of felsic magmatic rocks from Dibang valley, Arunachal Pradesh" at Geoyouth: 10th All India Students' Symposium on Geology" organized by the Department of Geology, Mohanlal Sukhadia University, Udaipur, Rajasthan, held from 1st-2nd February 2020.
2. "Mineral chemistry and redox condition of Lohit Plutonic Complex, Arunachal Pradesh" at the 6th National Geo-Research Scholar's Meet held at University of Ladakh, Leh Campus, Ladakh, organized by WIHG, Dehradun from 07-10th June 2022.
3. "Mafic-Felsic magma interaction of granitoids and microgranular enclaves in Lohit Plutonic Complex, Arunachal Trans-Himalaya, Northeast India: constraint from field, petrography, mineralogy, geochemistry and U-Pb SHRIMP chronology" at 37th International Geological Congress in Busan, South Korea, organized by the IUGS, held from 25th to 31st August 2024.

III. AWARDS/ RECOGNITION

1. **"Best paper presentation"** award at the Geoyouth: 10th All India Students' Symposium on Geology" organized by the Department of Geology, Mohanlal Sukhadia University, Udaipur, Rajasthan, held from 1st-2nd February 2020.
2. Vice-Chancellor's Award for **"Best Scholar of the Year 2024"** in recognition and appreciation for recording the highest number of book transactions in the

Library on 6th September, 2024, by the Vice-Chancellor, Nagaland University at Kohima Campus, Meriema.

3. **UGC-NET JRF, 2017**

IV. WORKSHOPS AND SEMINARS/WEBINARS ATTENDED

1. Workshop on “Advanced Petrography” organised by Gauhati University from 26th June to 1st July, 2018.
2. National workshop on “Sequence Stratigraphy and Basin Analysis”, Department of Geology, Nagaland University, Kohima campus, Meriema, held from 26th-30th November, 2018, sponsored by Nagaland University and Oil India Ltd.
3. 4th National Geo-Research Scholars Meet on “Geo-Sciences for Society” organised by Wadia Institute of Himalayan Geology, Dehradun from 23rd-24th June, 2020.
4. National Workshop on “Recent Advances in Geosciences” organised by Department of Geosciences, Dr. B.R. Ambedkar University, Etcherla, Srikakulam on 31st July, 2020.
5. e-training on “Refresher Course on Igneous and Metamorphic Petrography” conducted by RTD, ER, GSITI, Kolkata from 17th-21st August, 2020.
6. e-training on “Fundamentals of Structural Geology” exclusively for SC and ST conducted by RTD, NER, GSITI, Shillong from 24th-26th August, 2020.
7. E-training on “Fundamentals of Mapping in Tertiary Terrain” organised by
8. e-training on “Basic course on GIS and its application” organised by GSITI, Hyderabad from 17th – 19th September 2020.
9. e-training on “Basic course on application of geochemical analytical data in earth sciences” organised by GSI RTD, Western Region, Jaipur from 21st – 25th September 2020.
10. Refresher course on “Igneous petrography, petrogenesis and geochemistry” organised by GSITI, Hyderabad from 8th – 14th October, 2020.
11. Advanced Training Programme on “Granite and related rocks” organised by Department of Geology, Centre of Advanced Studies, Kumaun University, Nainital, Uttarakhand from 5th – 11th September, 2022.

Preface

The present study has been undertaken to unravel the petrogenetic processes and evolutionary history of a part of the Lohit Plutonic Complex granitoids exposed in the Dibang Valley district of Arunachal Pradesh. The findings of this research are systematically compiled into eight chapters, each addressing a distinct aspect of the investigation.

The thesis begins with **Chapter 1**, which introduces the study area, along with the objectives and scope of the research. **Chapter 2** outlines the stratigraphic and tectonic framework of the region, including its regional stratigraphy, geological setting, and lithological distribution. Special emphasis is also placed on the Magnetic Susceptibility characteristics of the granitoids and their geological implications. **Chapter 3** details the methodologies adopted in the course of this research.

Chapter 4 presents petrographic and mineralogical descriptions of the various granitoids. Detailed observation of the textural features and modal analysis is discussed here. **Chapter 5** focuses on mineral chemistry, with emphasis on amphibole and biotite composition, to constrain the redox conditions of the felsic magmas. Interpretations regarding oxygen fugacity, nature of magma, and tectonic environment are discussed in detail. **Chapter 6** examines the whole-rock geochemical characteristics of the granitoids to trace the processes of magma evolution, tectonic setting, and magma source. **Chapter 7** presents detailed zircon morphological and textural observations. It includes concordia diagrams and weighted mean age calculated from the analyzed zircons. The thesis concludes with **Chapter 8**, which thoroughly discusses and summarizes the obtained results and interpretations.

This study integrates magnetic susceptibility, mineral chemistry, geochemistry, and geochronology of the Dibang Valley granitoids, Arunachal Pradesh. Through petrological, mineralogical (EPMA), and bulk geochemical analyses, it offers new insights into their petrogenesis and tectonic significance.

It is hoped that the results presented here will not only contribute to the existing geological knowledge of the Lohit Plutonic Complex but also serve as a valuable resource and foundation for future research in the region.

CONTENTS

LIST OF FIGURES

LIST OF TABLES

CHAPTER- 1

INTRODUCTION

Arunachal Pradesh, also known as the “Land of the Rising Sun,” is a hilly tract in northeastern India, situated at the foot of the Himalayas. Spanning 83,743 sq. km, it is the state with the maximum area in the northeast. It lies between 26˚28ˈN and 29˚30ˈN latitudes and 91˚30ˈE and 97˚25ˈE longitudes. It shares borders with Bhutan to the west, Tibet to the north, Myanmar and the Indian north-eastern state of Nagaland to the south and southeast, and the Indian north-eastern state of Assam to the southwest. It is divided into three regions- western, central, and eastern.

Eastern Arunachal Pradesh is also called Mishmi Himalaya or Lohit Himalaya. It comprises three major river valleys: the Siang Valley in the west, the Dibang river valley in the center, and the Lohit river valley in the east. The study area, Dibang Valley, forms a part of the Eastern Himalaya and falls under the Mishmi Massif (also known as Lohit Himalaya) of Arunachal Pradesh. Dibang Valley district, with its headquarters in Anini, ranks as the largest in Arunachal Pradesh and has the lowest population density in India. It is bordered by Lohit in the south-east, lower Dibang in the South, East Siang and Upper Siang in the West, and China in the North and Northeast. The entire territory forms a complex hilly system. It constitutes a critical geological section in eastern Arunachal Himalaya and is regarded as the eastward continuation of Tibet’s Gangdese batholith.

1.1 LOCATION AND ACCESSIBILITY

Dibang Valley district is located between 28˚22ˈN and 29˚27ˈN latitudes and 95˚15ˈE and 96˚35ˈE longitudes. Covering an area of 9129 sq. km, it is part of the Survey of India Toposheet Nos. 82P/13 and 82P/14. Dibang Valley is accessible through land routes, though the road system in the region is largely undeveloped. Most distances are travelled over simple tracks, though there are a few all-weather roads. National Highway (NH 313) connects Meka, near Roing, and Anini. The interior hilly parts of the district are sparsely connected by mud roads and foot-tracks. The nearest airport is in Dibrugarh, Assam, which is 148 Km away from Roing. The nearest railway station is the 'New Tinsukia Junction,' 138 km from Roing.

1.2 PHYSIOGRAPHY AND DRAINAGE

Physiographically, Arunachal Pradesh comprises towering snow-clad peaks, steep precipitous gorges, lush green valleys, and innumerable streams. The high peaks reach a total height of 7000 meters above m.s.l, and the plains have an altitude of fewer than 300 meters. The region is differentiated into four physiographic domains viz. i) the Himalayan range, which stretches from the Bhutan border to the Dibang and Lohit valleys terminating against the Tidding-Tuting suture; ii) Trans-Himalayan range lies to the north of the Indus-Tsangpo suture with a syntaxial bend near Tuting, iii) Naga-Patkai range marks the southern boundary of the upper Brahmaputra Plain and constitues a portion of the Arakan Yoma mountain chain, and iv) the alluvial plains in Arunachal Pradesh is the eastern limit of the Brahmaputra plain and is bounded by the Himalayan range in the east and north, and by the Naga-Patkai range in the south. Dibang Valley district is divided into the Upper and Lower Dibang Valley. Most of the valley comprises undulated, rugged mountains with lush green valleys, deep gorges, captivating waterfalls, and numerous meandering rivers and turbulent streams.

Dibang Valley is drained by the Dibang River, an upstream tributary of the Brahmaputra River of Assam. The river originates near Keya Pass along the Indo-Chinese border in the Upper Dibang Valley district. The overall drainage pattern is dendritic to sub-parallel. The river, measuring approximately 195 km from source to confluence, exhibits a braided channel morphology, undergoes frequent channel shifts giving rise to multiple terraces on either side of its banks. The Dibang River joins the Lohit River near Sadiya town in the state of Assam. Some important tributaries are the Sisar, Tangon, Emra, Mathun, Dri, and Ithun. Along its course, the Dibang is joined by several tributaries such as Ilu, Imu, Ahi, Epipani, Ashu and Deopani rivers. Several tributaries, such as the Airi, Ilu, Imu, Ahi, Ashu, Epipani, and Eze (Deopani) joins with the Dibang along its course. Most of these tributaries merge with it in the upper hilly reaches, thereby forming a wide, fan-shaped catchment basin.

1.3 CLIMATE AND RAINFALL

The climate of Dibang district is mainly affected by orography. The lower altitudes experience a sub-tropical climate with high rainfall and humidity. The temperature ranges between 15-30˚C in summer and 14-21˚C in winter. Whereas, the higher altitudes possess an alpine climate with cool temperatures of 0-20 ˚C and witness snowfall during winters. The monsoon usually begins in April and continues up to September. It experiences heavy rainfall, which varies from 3000mm to 3281.33mm. The period from January to March is said to be the pre-monsoon period, and October to December is considered the post-monsoon period.

1.4 FLORA, FAUNA, AND CULTIVATION

The district has a vibrant floral and faunal diversity due to high altitudinal variation. It is very rich in wildlife, and in 1991, the Dibang Wildlife Sanctuary with an area of 4,146 sq. km was set up. The faunal diversity comprises species of high mountain zones, and as many as 156 mammals and 137 bier species are reported. Faunal species in the region include the Serow Leopard, Red Panda, Tiger, Orange Bellied Himalayan Squirrel, barking deer, Musk Deer, wild boar, Himalayan black bear, snow leopard, and Sun Bear are found. Rare mammals such as Mishmi takin, red goral, and Gongshan muntjac find a habitat in the forest of Dibang Valley. The Pheasant species is common among the birds in the forest and has a viable population of Mishmi Monal, Red Breasted Hill Partridges, Blood Pheasants, Khalliji Pheasant, and Blyths's Tragopan. Sub-tropical evergreen forests of Oak, Rhododendron, Holock, Maple, Juniper, and Pine trees cover the hilly parts of the region. Medicinal plants such as Mishmi Teeta, Centella, Ginseng, etc., are popular in the area. The people cultivate rice on the terraced hillslopes, as well as corn (maize), millet, potatoes, cotton, and oranges in the more level patches bordering the rivers.

1.5 HUMAN HABITATION

Arunachal Pradesh has a population of about 14,84,000 (as of the 2011 census) and is inhabited by 26 major tribes and more than 100 subtribes. Some of the chief/major tribes are the Monpas from Tawang area bordering Bhutan, Aka (Hruso) in Tenga and

Bichom valleys, the Daflas between Kameng and Subansiri rivers, the Nyishi in central and western Arunachal, the Adis (formerly known as Abors) from Siang and lower Dibang valley, the Mishmis (Digaru, Idu, Miju) from Dibang and Lohit valleys, and the Tai-Khamptis primarily inhabiting the Namsai and Changlang districts.

The 2011 census data of the district of Dibang Valley reports a total population of 7,948 with a population density of 0.8 inhabitants per square kilometer. The Mishmi tribes- Digaru-Mishmi (Taraons), Miju-Mishmi, and Idu-Mishmi (Chulikatta) are the primary tribes in Dibang Valley. Additionally, other tribes such as Tai-Khampti, and Singpho inhabit the region. The people are of Mongoloid race and speak dialects of the Tibeto-Burman linguistic family. The people predominantly practice agriculture and horticulture, while a few are engaged in other government and small business sectors. The inhabitants also practice handicrafts such as cane working, cloth weaving, silver working, and blacksmithing. Anini is the chief settlement in the region. The Idu Mishmi priests perform a somber dance called Igu, which is intimately connected with the region.

1.6 PREVIOUS WORK

The earliest geological studies on the Arunachal Himalaya were initiated in 1825 by Wilcox, who made observations in the Lohit Frontier Division. Subsequently, Godwin-Austin (1875), La Touche (1885), Maclaren (1904), Coggin-Brown (1912), and others outlined the general geological characteristics of the Arunachal Himalaya. Later on, detailed geology, structure, geodynamics, and geochronology of various litho units constituting the Arunachal Himalayan segments have been conducted by many workers (Dikshitulu et al., 1995; Kumar, 1997; Verma, 1999; Acharyya, 2000; Nandy, 2001; Gururajan and Choudhuri, 2003, and references therein).

Extensive exposure of felsic magmatic rocks is observed in the Arunachal Himalaya of northeast India (Kumar, 1997), which are present in association with the Mishmi crystallines and the sheared litho-units of the Tidding suture zone of Dibang Valley. The tectonic evolution of the Eastern Arunachal Himalaya is highly debatable. According to Gururajan and Choudhuri (2003), the region comprises of three tectonic units: the Mishmi Crystallines forming an extension of the Eastern Himalaya; the

Eastern Belt of Lohit Plutonic Complex, representing a continuation of the central Myanmar Metamorphic Belt; and the Western Belt correlating with the Gangdese Batholith of Tibet. Eastern Arunachal Block (also known as Mishmi Block) is considered as either a continuation of the Western Arunachal Himalaya (Gansser, 1964; Thakur and Jain, 1975; Acharyya, 1980; Singh and Chowdhury, 1990; Burg et al., 1998; DiPietro and Pogue, 2004; Mishra, 2009) or part of the Eurasian Plate, equivalent to the Mogok Metamorphic Belt (Gururajan and Choudhuri, 2003; Sarma et al., 2009). Misra (2009) conducted a detailed geological mapping of the various lithounits exposed along the Dibang and Lohit and Valleys to understand the complex's lithological variations, structural characteristics, and petrological evolution. Comprehensive structural investigations and analyses of the Mishmi Massif across parts of Dibang district and collision-induced deformation of the Lohit batholith were executed by Goswami (2011) and Sarma et al. (2012), wherein they shed light on various complicated structural deformations and their imprints upon the lithology. Studies on tectonics and crustal shortening in the eastern Arunachal Himalaya conducted by Ningthoujam et al. (2015) suggested that shortening is maximum in this region and could be a result of the bending of Eastern Himalayan Syntaxis. Their findings also revealed that the Siwaliks had been completely eroded, indicating a very high rate of erosion.

Detailed petrography and geochemical studies of the Lohit Plutonic Complex are numerable, and research literature was lacking until recent years. Goswami, (2013a and 2013b) and Pebam and Kamalakannan (2019) worked on the petrogenetic and geochemical signatures of the Lohit Plutonic Complex. Their findings suggested a metaluminous (I-type) variant for the granitoids and opined toward subduction-related magmatism in a convergent plate scenario. Comprehensive work on magnetic susceptibility, mineral chemistry, and geothermobarometry of granitoids of Lohit Plutonic Complex with emphasis on the redox condition, nature, and tectono-magmatic environment has been given by Meyase et al. (2023) (present work).

Country rock xenoliths and dioritic (mafic magmatic) enclaves have been reported in some granitoids of Lohit Valley (Gururajan and Choudhuri, 2003). Research on enclaves hosted in Indian granitoids is very sparse, and limited studies have been undertaken using modern methods of igneous petrology and geochemistry (e.g., Kumar et al., 2005; Kumar and Rino, 2006; Kumar, 2008, 2010; Kumar and Pathak, 2010; Kumar and Pieru, 2010; Kumar et al., 2017).

Very scant geochronological data on the various lithologies of the Lohit Plutonic Complex exist. Based on zircon U-Pb dating, the Lohit Batholith was active from the Late Jurassic (ca. 148 Ma) to Early Cretaceous (ca. 110–96 Ma) and correlated with those of Gangdese Batholith along the Yarlu-Tsanpo suture and the Tidding suture (Lin et al., 2013). On the basis of the reports of U-Pb zircon dating of gabbro and diorite, two stages of magmatic activity (ca. 145 and ca. 100-90 Ma) have been suggested in the Lohit Plutonic Complex (Bikramaditya et al., 2017). Recently, U-Pb geochronological analyses of zircon revealed episodic magmatism with Zircon U-Pb age of ca. 153.4Ma for garnetiferous granite gneiss, ca. 117Ma and 49.5Ma for magmatic rocks of LPC, and ca. 35.6-30 Ma for the crustally derived leucogranites (Pebam et al.,2021).

1.7 Aim and scope of work

The present research object, i.e., the Dibang valley felsic magmatic rocks, is a part of the Lohit Plutonic Complex (LPC) of Eastern Arunachal Pradesh, which is believed to be a continuation of the Gangdese batholith of southern Tibet. Country rock xenoliths and microgranular enclaves (ME) have been reported in some granitoids of the Lohit and Dibang valleys (Gururajan and Choudhuri, 2003). The whole-rock geochemical database of the Dibang Valley granitoids is sporadic and sparse. Moreover, phase relationships, granite series assessment, and crystallization conditions of the Dibang Valley granitoids still remain unknown. Hence, to explore the genetic type and deep processes of the felsic magmatic rocks of a part of the LPC, Dibang Valley has been selected as the research object.

In light of the above review on the existing research and knowledge gap on magmatic rocks of the Dibang Valley, we aim to deduce the granite series, assess the redox condition, nature, origin and physicochemical conditions of the granitoids of Dibang valley, based on a new set of magnetic susceptibility data, the mineral chemistry of ferromagnesian minerals (amphibole and biotite), plagioclase and oxides, and from the whole-rock geochemical database of the granitoids from Dibang Valley.

The following are the aims and objectives that were framed to fulfil the research gap on the felsic magmatic rocks of Dibang Valley. These objectives are achieved by employing systematic field and laboratory investigations.

- To establish the field relationships between the granitoids and associated lithounits
- To document the geological, lithological, and textural variations in the granitoids of the study area
- To evaluate the granite series (magnetite vs. ilmenite series)

- To estimate physical and chemical conditions (P, T, fO_2, fH_2O) of granitoid plutons
- To assess the protoliths, magmatic processes, and tectonic settings of granitoid magmas

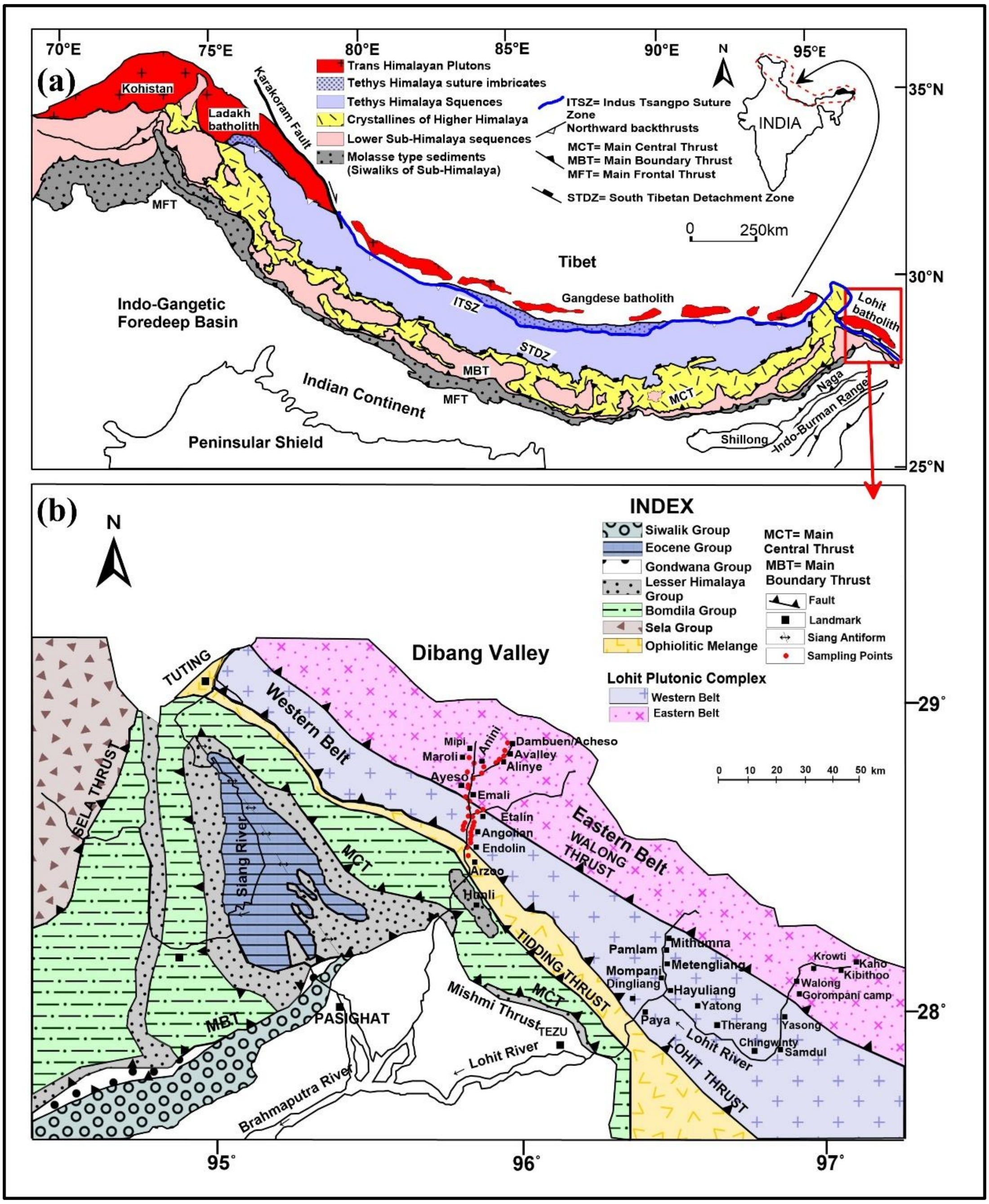

Figure 1: (a) Simplified tectonic map of the Himalaya (after Bikramaditya et al., 2020; Burg and Bouilhol, 2018; Gansser, 1974). (b) Geological map of the Lohit Plutonic Complex (LPC) (after Goswami, 2013b; Gururajan and Choudhuri, 2007; Misra, 2009).

CHAPTER-2

GEOLOGY, FIELD RELATIONSHIPS, AND MAGNETIC SUSCEPTIBILITY

2.1 INTRODUCTION

Arunachal Pradesh is a part of the Eastern Himalayan Mountain Belt. Several tectonic divisions with characteristic lithostratigraphic attributes have been identified in Arunachal Himalaya. While these divisions have features that are similar to other parts of the Eastern Himalaya, they also exhibit several distinct differences due to Arunachal's unique tectonic location at the Eastern Himalayan syntaxial bend. Based on the spatial distribution of these tectonic belts, Arunachal can broadly be divided into three domains, viz., western domain (Kameng and Subansiri districts), central domain (Siang districts), and eastern domain (Dibang, Lohit, and Anjaw). Each of these domains has characteristic and distinctive lithologic and tectonic attributes.

The Easternmost Arunachal Himalaya forms a complex triple junction marking the convergence of the Indian and Eurasian plates with the Northern end of the Myanmar plate (Ningthoujam et al., 2015). The Indus-Tsangpo suture zone, which is considered the zone where the Indian plate collided with the Tibetan plate, marks the boundary between the continental plates of India and Eurasia.

2.2 REGIONAL GEOLOGY AND TECTONICS OF EASTERN ARUNACHAL HIMALAYA

The Eastern Himalaya curves sharply in its easternmost part, known as Arunachal Himalaya, and has a regional strike from NE-SW to NW-SE across the Eastern Syntaxial Bend. The Lohit and Dibang valleys, also called as the Mishmi block (Thakur and Jain, 1974; Nandy, 1976; Singh and Malhotra, 1983; Kumar, 1997), is situated at the hinge zone of the syntaxial bend in Arunachal Himalaya (Figure 1). These units form a tectonic roof (Sarma et al., 2009) or tectonic linkage (Nandy, 1981) between the E-W trending Eastern Himalaya and the NNE-SSW trending Indo Myanmar Mobile Belt in the southeast. This region is divided into five thrust-bound tectonostratigraphic units by various workers (Misra, 2009; Sarma et al., 2012). Thakur and Jain (1975) delineated several thrust sheets. From the southwest to the northeast, these structural units are: (1) Sewak Group, (2) Lalpani Group, (3) Sela, Bomdila, and Mayodia Groups, (4) Tidding Formation (ophiolite mélange), and (5) Lohit Plutonic Complex (LPC). In this region, significant crustal shortening is evident. The Tethyan Himalayan Sequence (THS) is missing, probably due to the extreme crustal shortening and overthrusting that occurred in this syntaxial bend (Ningthoujam et al., 2015; Sarma et al., 2017; Haproff et al., 2019). Also, the Tertiary fluvial sediments of the Siwalik and the Gondwana Group are absent, likely due to being truncated by the Mishmi Thrust or eroded out completely (Gururajan and Choudhuri, 2003; Choudhuri et al., 2009).

The Proterozoic-Cambrian age rocks of the Lesser Himalaya are the Sewak and Lalpani Groups, and they comprise low-grade metasedimentary rocks (Misra and Singh, 2002; Gururajan and Choudhuri, 2003; Richards et al., 2005; Misra, 2009) that are directly thrust over the recent alluvium of the Siwaliks along the Mishmi Thrust. The Higher Himalaya rocks of Palaeoproterozoic to Ordovician age, comprising of medium to high-grade crystallines of the Bomdila and Mayodia Groups, are thrusted along the Main Central Thrust (MCT), and the lithounits lie above the Lesser Himalayan rocks. The Lohit Plutonic Complex, which represents the easternmost part of the Trans Himalaya range, and the adjacent Tidding Formation are restricted to the eastern limb of the Himalayan syntaxis (Thakur and Jain, 1975; Gururajan and Choudhuri, 2003). The meta-volcanics (Tuting meta-volcanics) and ultramafic/ophiolite mélange of the Tidding Formation overlie the Mayodia crystallines along the Tidding Thrust and are limited to the north by the Lohit Plutonic Complex (LPC). The LPC is of batholithic dimensions and represents the most prominent geological unit in Eastern Arunachal Pradesh. It is separated from the underlying Mishmi crystallines and Tidding Formation by the Lohit Thrust.

The tectonostratigraphic succession of the Eastern Himalaya is given in Table 1. The following section provides a summary of the various lithotectonic units.

Table 1: Tectonostratigraphic succession of Eastern Arunachal Himalaya (after Gururajan and Choudhuri, 2003; Misra, 2009; Goswami, 2013b; Ningthoujam, 2015).

Regional Unit	**Tectonic unit**	**Sub-unit**	**Lithounit**
Trans Himalaya	Lohit Plutonic Complex	Western Belt	Intrusive leucogranite, tourmaline-bearing pegmatites, aplite dyke, trondhjemite, mylonitic gneiss, meta-diorite, dacite, pegmatite, hornblendite
		---------------------Walong Thrust--------------------	
		Eastern Belt	Quartz diorite, meta-diorite, sillimanite gneiss with marble bands, garnetiferous gneiss, and schist, meta-granodiorite
-----------------------------------Lohit Thrust--			
Suture zone	Tiding Formation		Intrusive leucogranite, chlorite schist, metavolcanics, foliated quartzite, epidotes, serpentinized peridotite, and amphibolite schist
-----------------------------------Tidding Thrust---			
Greater Himalaya	Mayodia Group		Kyanite-sillimanite bearing garnet, biotite gneiss, foliated quartzite, gneiss, and amphibolite
--------------------------------MCT--			

Lesser Himalaya	Sewak Group		Mylonitic augen gneiss, quartzite, sericite, phyllonite, crystalline limestone, foliated sericitic chlorite
	-----------------------Lalpani Thrust------------------------------		
	Lalpani Group		Garnet-biotite schist, foliated quartzite, garnetiferous gneiss, marble, carbonaceous schist, amphibolite, mica schist
-----------------------------------Mishmi Thrust---			
Sub-Himalaya	Siwaliks		Eroded

I. Lesser Himalayan (LH) unit

The Lesser Himalayan rocks in Eastern Arunachal are represented by the Sewak and Lalpani Group of rocks. The entire sequence is bounded between two regional thrusts- the Mishmi Thrust in the south and the Main Central Thrust (MCT) north (Figure 2.1b).

Sewak Group comprises of thick succession of low-grade (greenschist facies) metamorphics which are well-exposed near Sewak Pass in Lohit district (Misra and Singh, 2002). It is exposed as a contiguous belt in the southern foothills, while towards the north of the Higher Himalaya region, it appears as a tectonic window (called the Hunli window) in the upstream segments of the Dibang River and overlies the Mayodia thrust sheet. It essentially consists of chlorite-grade metamorphics at the bottom, progressing to kyanite-grade upwards in the succession. The lithological assemblage includes phyllonitic sericite-chlorite, sericitized and foliated quartzite, quartz porphyry, mylonitic augen gneiss, and limestone (Gururajan and Choudhuri, 2003; Misra, 2009). Proximal to the Mishmi Thrust, a prominently developed and laterally persistent band of sericitized and chloritized phyllonite and mylonitized augen gneiss displays intense deformation features, characterized by pervasive crumpling, cataclastic textures, and ductile shearing (Misra, 2009).

Lalpani group comprises medium-grade (epidote-amphibolite facies) metamorphic rocks that tectonically overlie the lower-grade Sewak Group along the Lalpani Thrust. The lithology consists of amphibolite schist, garnet-biotite schist, chlorite schist, carbonaceous schist, garnetiferous gneiss, banded gneiss, foliated micaceous quartzite, and minor marble (Gururajan and Choudhuri, 2003; Misra, 2009).

The grade of metamorphism in the Lesser Himalaya demonstrates inverted metamorphism, as it exhibits a change from greenschist to amphibolite facies across the structural section (Gururajan and Choudhuri, 2003; Misra, 2009), with the Lalpani Thrust serving as the demarcating boundary between the two grades.

I. Higher Himalaya (HH)/ Central Crystalline Complex

This tectonic unit is bounded between the Main Central Thrust (MCT) in the south and Tidding Thrust (TT) in the north. They comprise of medium to high-grade metamorphic units classified into distinct but tectonically related groups, namely Bomdila, Sela, and Mayodia Groups.

Sela Group of rocks extensively outcrops around the Sela Pass and higher altitudes in western Arunachal Pradesh (Tawang-Dirang-West Kameng areas). Characterized by granulite facies rocks, it constitutes the highest-grade metamorphic assemblage in Arunachal Pradesh. It predominantly comprises migmatites, garnetiferous gneiss, sillimanite-kyanite-garnet gneiss, calc-gneiss/marble, and profuse intrusions of tourmaline granite.

Bomdila Group of rocks are low to medium grade metasediments with associated gneisses and younger granitoids, and mostly exposed in central and parts of western Arunachal Pradesh. A comparable sequence comprising of granite gneiss, mica schist, quartzite, amphibolite, and minor marble bands occurring in the Dibang and Lohit Valley is referred to as the Ithun Formation.

Mayodia Group is an extensive succession of high-grade crystallines with mineral assemblage (kyanite-silimanite-staurolite grade) indicative of amphibolite facies metamorphism. It is well exposed in the eastern section around Mayodia Pass along the Roing-Anini road in Dibang Valley (Misra and Singh, 2002). It comprises of a complex suite of garnet-biotite schists and gneisses with kyanite-sillimanite in its mineralogy, psammitic gneiss, quartzo-feldspathic gneiss, and amphibolite. It tectonically overlies the low-grade Lalpani metasediments along the MCT, and the lithology is highly sheared, mylonitized, and sericitized in the vicinity of the thrust (Misra, 2009). These are comparable with the Sela Group of western Arunachal Pradesh (Das et al., 1976)

II. Trans Himalaya

The NNW-SSE trending Trans Himalayan range formed due to the subduction and eventual closure of the Neo-Tethyan oceanic lithosphere, followed by the collision between the Indian and Asian continental plates around 55Ma (Rowley, 1996; Najman et al., 2010). It is juxtaposed against the Higher Himalayan rocks along the Tidding suture and encompasses two main lithopackages, viz, the ophiolitic mélange of the lower Tidding Formation and granitoids of Lohit Plutonic Complex, separated by the Lohit Thrust (Thakur and Jain, 1975).

Tidding Formation tectonically lies above the Central Crystallines along the Tidding Thrust. The ophiolitic mélange has been considered to be the southeast continuation of the ITSZ (Acharyya, 1987; Gururajan and Choudhuri, 2003; Mitchell, 1981; Singh and Choudhury, 1990; Thakur and Jain, 1975) that developed as a result of India-Asia collision and closure of the Neo-Tethyan Ocean during the Mesozoic and Early Tertiary. It is dominantly made up of meta-volcanics, often referred to as Tuting meta-volcanics, foliated quartzite, serpentinized peridotites, grey marble bands with epidote, and leucogranite intrusions. In the Dibang Valley, dykes and sills of ultramafics, gabbro, and hornblende-pegmatite intrude the lithounits. The ultramafics found around Mayodia region occur as a remnant of a thrust sheet (nappe) overlapping the gneisses of the Bomdila Group (Kumar et al., 2000). The Tuting metavolcanics (chlorite schist, actinolite-tremolite schist) are commonly interlayered with bands of marble, graphitic schist, minor chert, rhythmite, and conglomerate. Tectonized silvers of serpentinized peridotite lenses and talc schist occur within the sequence.

Lohit Plutonic Complex (LPC) overthrusts the Tidding rocks along a NE dipping thrust known as the Lohit Thrust (Nandy, 1976), which cuts across Endolin in Dibang Valley and east of Paya in Lohit Valley (Figure 1b). They are predominantly multiphase plutonic rocks correlated with the granitoids of Ladakh Batholith in the west, Gangdese Batholith of Tibet, and the Mogok Metamorphic Belt of Myanmar (Lin et al., 2013; Haproff et al., 2019; Bikramaditya et al., 2019). The plutonic complex comprises of diorite, tonalite-trondhjemite, granodiorite, biotite-granite, leucogranite, banded gneiss, biotite-rich garnetiferous gneiss, schists, aplite veins, and tourmaline-bearing pegmatites. The LPC is divided into the western and eastern belts (Figure 1b) by the Walong Thrust.

The present study area lies in the Dibang Valley of this plutonic complex, and the detailed geology and tectonics of the complex are discussed in the following section.

2.3 GEOLOGY AND TECTONICS OF LOHIT PLUTONIC COMPLEX

The batholithic scale of the Lohit Plutonic Complex (LPC) is a conspicuous feature in the eastern Arunachal Himalaya with a general trend of NW-SE (Figure 1b). The LPC is located to the east of the Eastern Syntaxis in the eastern Arunachal Himalaya and is considered as the southeastern continuation of the Gangdese arc system of southern Tibet (Figure 1b). The LPC represents an Andean-type calc-alkaline magmatic arc formed by subduction of the Neo-Tethys oceanic lithosphere beneath the Eurasian continental plate (Goswami, 2013b). The LPC is about 100km wide in the Lohit valley and extends over 250km in the NW-SE direction from the Noa Dihing valley to the Dibang Valley and further in the NW direction (Goswami, 2011).

The LPC consists of multiple igneous intrusions thrust over the ophiolite mélange of Tidding Formation along a NE-dipping thrust known as the Lohit thrust (Nandy, 1976). Extensive exposures of LPC granitoids occur in the Dibang and Lohit valleys. The LPC has been classified into western and eastern belts, divided by the Walong Thrust (Gururajan and Choudhuri, 2007). Western belt is bounded by the Lohit Thrust at the base and Walong Thrust at the top. Along the Walong thrust, garnet-sillimanite gneisses intercalated with marble bands representing country rocks of the southern margin of the Asian continent are exposed (Gururajan and Choudhuri, 2007). The Lohit and Walong thrust zones constitute the last phase of deformation in this region with the development of NE-plunging lineation (Gururajan and Choudhuri, 2003). The belt of the LPC is moderately to highly deformed and foliated and is traversed by a number of shear zones parallel to the regional trend.

The western belt of the LPC is dominated by diorites and quartz diorites with occasional mafic microgranular enclaves (ME), tonalite, granodiorite, hornblende granite, and pegmatites (Goswami, 2013a and b; Gururajan and Choudhuri, 2003; Misra, 2009), mylonitic gneiss, metadiorites, and metagranodiorites (Ningthoujam et al., 2015), thrusted over the Tiding ophiolite melange. Early phase gabbro bodies enclosed within the quartz diorite were observed in the western belt, but they are absent in the eastern belt. Eastern belt comprises foliated quartz diorite, granodiorite, migmatite, intruded by younger aplite, pegmatite, and leucogranite.

The LPC granitoids and associated magmatic rocks were generated by partial melting of the lithospheric mantle wedge triggered by the influx of hydrous fluids released from the subducting slab, and subsequently emplaced within the lower crust (Bikramaditya et al., 2020). Leucogranite and pegmatite represent the late phase magmatic event (Goswami, 2013b; Pebam and Kamalakannan, 2019). Multiple magmatic events have been recorded, which are responsible for the felsic-mafic magmatic rocks now exposed on the LPC. Lin et al. (2013) recorded felsic magmatism from 148 to 96 Ma Late Jurassic (ca 148 Ma) to Early Cretaceous (ca. 110-96 Ma) synchronous to the Gangdese Batholith along the Yarlung Tsangpo-Tidding suture. A similar age of Late Jurassic–Cretaceous age (ca 156-69 Ma) for the LPC granitoids, correlatable with the northern Gangdese Batholith, is also recorded (Haproff et al., 2020). Recently, Bikramaditya et al. (2020) reported two stages of mafic magmatic activities (ca 145 and 107-90 Ma) based on U-Pb zircon isotopes. Furthermore, Pebam and Kamalakannan, (2019) reported a slightly lower but broadly contemporaneous timing of felsic magmatism (117 and 49.5 Ma) as the earlier workers. The youngest intrusive phase represented by the leucogranites records Cenozoic age (35.6 to 30 Ma)

(Pebam and Kamalakannan, 2019) related to post-collisional tectonomagmatic history of the LPC. Recorded evidence of older Mesoproterozoic basement rocks (ca. 1286 Ma) in LPC is correlated with the oldest rocks recorded in the Bomi-Chayu Complex of Lhasa (Haproff et al., 2019). Thus, the available geochronological data from LPC corroborate the contemporaneous tectonothermal events recorded along the Trans-Himalayan magmatic arc leading to the emplacement of the large magmatic suites, e.g., Ladakh Batholith, Gangdese Bathloith, and the Lohit batholith (this study).

2.4 GEOLOGY AND FIELD RELATIONSHIP

Dibang Valley of Arunachal Pradesh, located at the hinge of the eastern Himalayan Syntaxis, has undergone a complex history of crustal shortening/deformation resulting in complicated structural features, recrystallisation, and magmatic activities owing to the collision and subduction of the Indian plate under the Eurasian plate. The various lithologies observed in the Dibang Valley along the transect Roing-Mayudia-Hunli-Anini are huge piles of metamorphic rocks represented by augen gneiss, quartzite, amphibolite, metapelitic and metabasic rocks, mafic and ultramafics, carbonate rocks, homblendite, serpentinite, crystalline limestone, and Lohit granitoids.

The Pleistocene River Terraces are observed in and around Roing along Deopani River and are thrust over by the Proterozoic gneisses and Mayodia ultramafics along the Main Central Thrust. The sediments of the Siwalik and Gondwana Groups are not observed in the Dibang Valley. The Proterozoic Roing Gneiss of Lower Dibang Valley, which is correlated with the Bomdila Group, essentially comprises of biotite gneiss, augen gneiss, minor amphibolite, and quartzite. The rocks are highly sheared and deformed, evident from the ribbon structures, rotated feldspar augens, boudins, etc, especially in the Ithun River section (Sarma et al., 2012). The Mayodia Group is represented by the rocks of amphibolite facies metamorphism, and are commonly sheared.

The metasediments and metavolcanics, referred to as Dibang Group by Sarma et al. (2012), lie above the high-grade metamorphics, separated by the Tidding Thrust and considered as the lateral equivalent of Tidding Formation (Nandy, 2005). They are designated as the metavolcanic Ithun Formation and metasedimentary Hunli

Formation (Burhauddin and Nandy, 2004). The Ithun Formation comprises of amphibolite schist, hornblende schist, and actinolite-chlorite schist intercalated with quartzite bands, while the Hunli Formation is made up of metapelites (schists and phyllites), metabasics, and pockets of limestone. Compact limestone bands are observed associated with actinolite schists in areas like Arzoo, Endolin, and Riyali. These lithounits are then thrust over by the huge multi-phase intrusives of diorite-tonalite-granodiorite-granite-leucogranite masses along the Lohit Thrust.

The granitoids in Dibang Valley are broadly classified into older quartz diorite, granodiorite, granite, and younger intrusive leucogranite. The gabbro represents the early (fractionated) magmatic phase. Small, lenticular, ovoid to subrounded, dark-colored, fine-grained, microgranular enclaves (ME) are found hosted within the quartz diorite and granodiorite. The ME often shows sharp, crenulated, or diffused boundaries with host granitoids. Several workers (Gururajan and Choudhuri, 2003; Choudhuri et al., 2009; Sarma et al., 2012; Haproff et al., 2018) have established the intense degree of deformation in four phases in the rocks of the entire complex, especially in the vicinity of the thrusts. Additionally, the inverted metamorphism in the crystallines is attributed to post-metamorphic shearing processes (Choudhuri et al., 2009).

2.4.1 GRANITOIDS OF DIBANG VALLEY

The granitoids of Dibang Valley are intrusive into the metasediments and early-stage diorite and gabbro. Based on field observation, megascopic characters, and mode of occurrence, the granitoids of Dibang Valley are classified as quartz diorite, granodiorite, and leucogranite. They are heterogeneous and vary from coarse-grained quartz diorite to medium-grained leucogranite and foliated biotite-rich granodiorite. The quartz diorite and granodiorites mostly appear to have a greyish hue with variable textures, and also host some mafic enclaves of varying shape and sizes. Overall, they are associated with diorite, gabbro, metasediments, migmatites, with numerous intrusions of quartz veins, leucogranite, and tourmaline-bearing pegmatites.

QUARTZ DIORITE

Quartz diorite is the dominant granitoid variant in the western belt and is well exposed along the Arzoo-Etalin transect of Dibang valley. Moderate occurrence is also observed along the Etalin-Anini-Dambuen transect in the eastern belt. They are dark grey in colour and have a medium to coarse-grained texture (Figure 2.1a). Local variation in mafic (biotite and amphibole) and felsic (quartz and feldspar) minerals is observed. Quartz diorites are highly deformed in the Lohit thrust zone, which is evident from the foliated texture exhibited by those quartz diorites (Figure 2.1b). Microgranular enclaves (ME) having sub-rounded, lenticular, and irregular shapes are commonly observed to be hosted within the quartz diorites (Figure 2.1c). The size of the MEs observed near Etalin and Angolian varies between 2x0.5″ to 8x4″ approximately, and mostly have diffused or sharp boundaries and also display consistent, identical mineral lineation during magmatic flowage. In Anini, the quartz-diorites host large enclaves (9x4 inches approx.) with sharp contact with the host. From Anini to Maroli village, the quartz diorites are commonly intruded by biotite-rich leucogranites and quartz veins (Figure 2.1d).

GRANODIORITE

The granodiorites are mostly gneissic and are the dominant variety in the eastern belt, though a good number of outcrops are exposed in the western belt as well. The gneissossity is defined by alternate bands of darker ferromagnesian minerals and the lighter feldspathic minerals. They are light grey in colour, medium-grained, equigranular, and phenocryst-free. The granodiorites in and around Embolin and Endolin are usually non-foliated, medium to coarse-grained, and have a greenish tint due to alteration of minerals to chlorite and epidote minerals (Figure 2.2a). Sub-rounded ME (~5 cm in diameter) and some irregular-shaped enclaves with diffused boundaries are observed near Angolian (Figure 2.2 a&b). The granodiorites exposed in the Etalin to Anini transect are highly foliated and gneissic, medium-grained, and often intruded by quartz veins (Figure 2.2c), containing abundant biotite, pegmatite, and leucogranite. In comparison to the quartz diorites, the granodiorites contain more mafic enclaves. Within the granodiorites of Alinye and Avalley, several small, irregular, and elongated MEs with diffused boundaries have been observed. Smaller (4x1.5 inches approx.) lens-shaped enclaves have also been observed hosted within gneissic granodiorites in Anini (Figure 2.2d).

GRANITE

The occurrence of granites has been observed only in the eastern belt along the Alinye-Dambuen transect. They are mostly light grey and have a speckled salt and pepper appearance as a result of the mineral association of quartz and feldspar with biotites (Figure 2.3a). The granites from Dambuen are greyish with a pinkish tint in some outcrops. They have a coarse-grain size with randomly oriented phenocrysts of plagioclase and K-feldspar (Figure 2.3b). No enclaves have been observed within the granites.

LEUCOGRANITE

The leucogranites are greyish-white leucocratic, with a medium-grain texture. The occurrence of leucogranites in the western belt is limited, with few occurrences in Etalin close to the Walong Thrust, while the huge leucogranite exposures are observed mostly in the eastern belt in and around Emali and Ayeso. No mafic enclaves have been observed to be enclosed within them. About 3 km away from Emali, leucogranites exhibiting gneissosity have been observed. In Ayeso, the leucogranite is foliated and in contact with metasediments (Figure 2.3 d&e). The leucogranites from these areas are two-mica leucogranites and comprise both biotite and muscovite, as well as garnet in their mineral assemblage.

2.4.2 SAMPLE AND LOCATION

Locations of representative granitoid samples collected along the Arzoo-Etalin-Anini-Dambuen transect are indicated in the traverse map of Dibang Valley in Figure 2.4.

2.5 MAGNETIC SUSCEPTIBILITY OF GRANITOIDS OF DIBANG VALLEY

Magnetic Susceptibility (MS) is a first-order petrophysical parameter to determine the magnetic state of a granitic outcrop. This property aids in classifying granitoids and provides an approximate indicator of granite origin (e.g., Ellwood and Wenner, 1981).

The MS of granitic rocks is heterogeneous and in most cases displays a roughly bimodal pattern. Measurement of magnetic and weakly magnetic minerals in terms of MS values (MS in 10^{-3}SI units) can be used as an index to differentiate granitic rocks into two series viz., the Magnetite Series (MS $>3.0 \times 10^{-3}$ SI units) characterized by the occurrence of magnetite and/or magnetite-ilmenite and the Ilmenite series (MS $\leq 3.0 \times 10^{-3}$ SI units) characterized by the occurrence of ilmenite (Ishihara, 1977) corresponding to oxidized I-type and reduced S-type granites respectively (Takagi, 2004).

These MS values reflect the oxygen fugacity of the granitic magma. The magnetite- and ilmenite-series nature of granites can be correlated with intensive variables (fO_2, f_{H2O}, a_{H2O}) indicated by chemistry of hydrous mafic silicates (Wones, 1981, Czamanske et al., 1981), which may together point to nature of felsic melt evolution, operative elemental substitution in silicate structure appropriate to host magma type (Abdel-Rahman, 1994).

In the present study, the MS measurements (in 10^{-3} SI units) were measured and recorded using the Kappameter KM-7 model. The measurements were taken from fresh granitoid outcrops on even surfaces. Measured MS values (in 10^{-3} SI units) are further calibrated according to recommended factors for degree of rock-surface unevenness: 1 mm – 1.07, 2 mm – 1.15, 3 mm – 1.23, 4 mm – 1.32 and 5 mm – 1.41.

The location, average, and range of MS values (in 10^{-3} SI units) of the Dibang granitoids are given in Table 2. Spatial variation in the MS values is displayed in the contour map (Figure 2.5). Magnetic Susceptibility measurements along the Arzoo-Etalin, Etalin-Anini, Anini-Dambuen, and Anini-Maroli transects are discussed below.

Arzoo to Etalin:

This transect lies in the western belt of LPC and is dominated by quartz diorites. The quartz diorite in Arzoo records high Magnetic Susceptibility values that range from 14.49 to 19.29 $\times 10^{-3}$ SI unit corresponding to magnetite series granite. However, the quartz diorites Angolian and Etalin records comparatively lower MS values ranging from 0.113-0.875 $\times 10^{-3}$ SI unit corresponding to ilmenite series granite. The granodiorites from Embolin, Andolin and Angolian, records yet lower MS values from 0.041 to 0.188 x10^{-3} SI unit.

Etalin to Anini:

This transect lies in the eastern belt and comprises the older quartz diorite and foliated granodiorite, and the younger leucogranites. The quartz diorite outcrop located approximately 10 km before Anini township records a low MS value of 0.069-0.358 x10^{-3} SI unit. Granodiorites from Etalin and Emali areas also record similar low values ranging from 0.035-2.065 x10^{-3} SI unit corresponding to ilmenite series granite. The leucogranites from Etalin and Emali have comparatively higher MS values ranging from 1.264-9.064 x10^{-3} SI unit corresponding to both ilmenite and magnetite series granite.

Anini to Maroli and Dambuen:

The quartz diorites from Anini and Alinye areas are exclusively ilmenite series granitoids with MS value ranging from 0.150-1.082 x10^{-3} SI unit. While those from Dambuen records slightly higher values of 2.763-4.463 x10^{-3} SI unit corresponding to magnetite series. In Maroli, the quartz diorites have a low MS of 0.108-0.183 x10^{-3} SI. The granodiorites from Alinye and Avalley have a large variation in the MS values, varying between 2.191-10.596 x10^{-3} SI unit and 1.638-4.849 x10^{-3} SI unit, respectively and are classified as both ilmenite and magnetite series granitoids. The leucogranites located about 12km from Emali record low MS values between 0.030-0.673 x10^{-3} SI unit classifying as ilmenite series. However, a large variation is recorded from the gneissic leucogranites in Ayeso with average MS values ranging from 3.018-17.495 x10^{-3} SI unit corresponding to magnetite series. The granites from Alinye has low value of 0.030-0.673 x10^{-3} SI unit. While, the coarse-grained granite from Acheso has a measured MS value of 2.430-5.397 x10^{-3} SI unit.

Overall, the MS values of the Dibang Valley granitoids indicate a bi-modal pattern corresponding to 64% ilmenite (reduced; S-type) series and 36% magnetite (oxidised; I-type) series granites. This variation in the MS values of the granitoids can be attributed to the alteration of ferromagnetic minerals, and later tectonic and deformational processes that acted upon them after their emplacement and crystallisation.

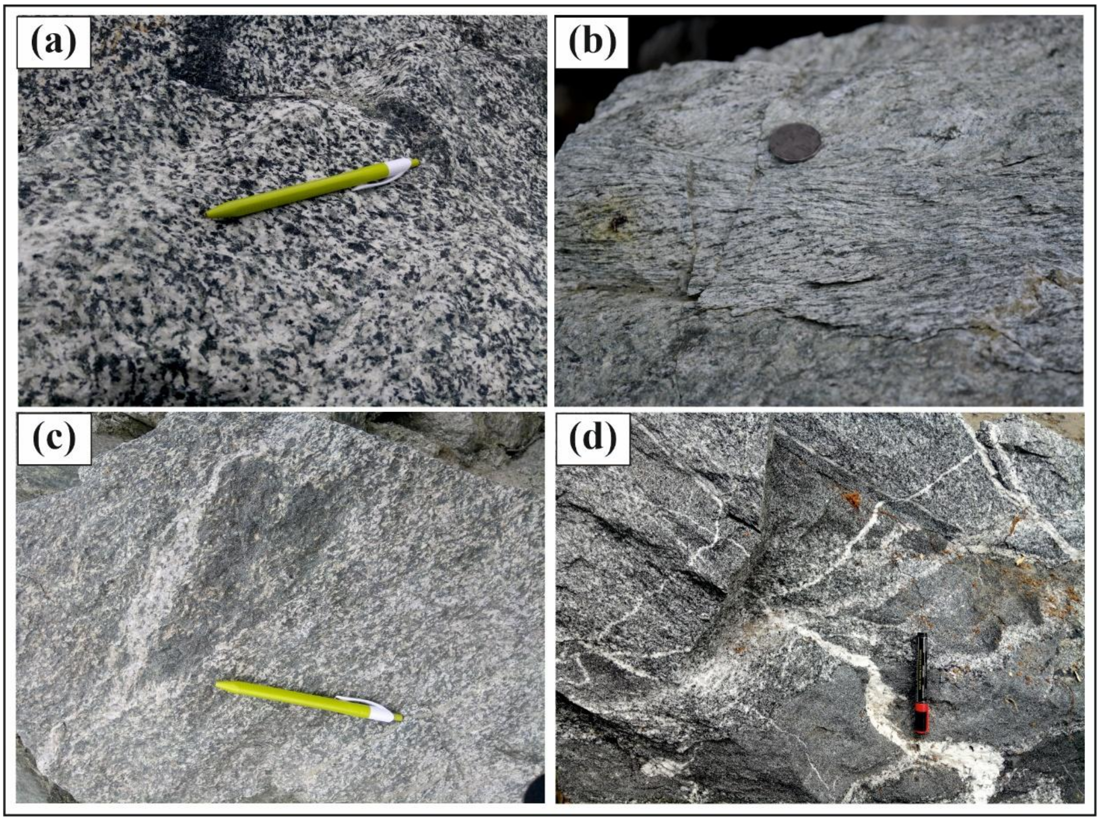

Figure 2.1: Field photographs of quartz diorites (a) dark grey, coarse grained quartz diorite outcrop; (b) deformed and foliated quartz diorite near the Lohit Thrust; (c) irregular shaped microgranular enclave (ME) with diffused boundary; (d) quartz diorite of Maroli with quartz vein intrusions. (Length of pen: 5.5 inch; diameter of coin: 1 inch)

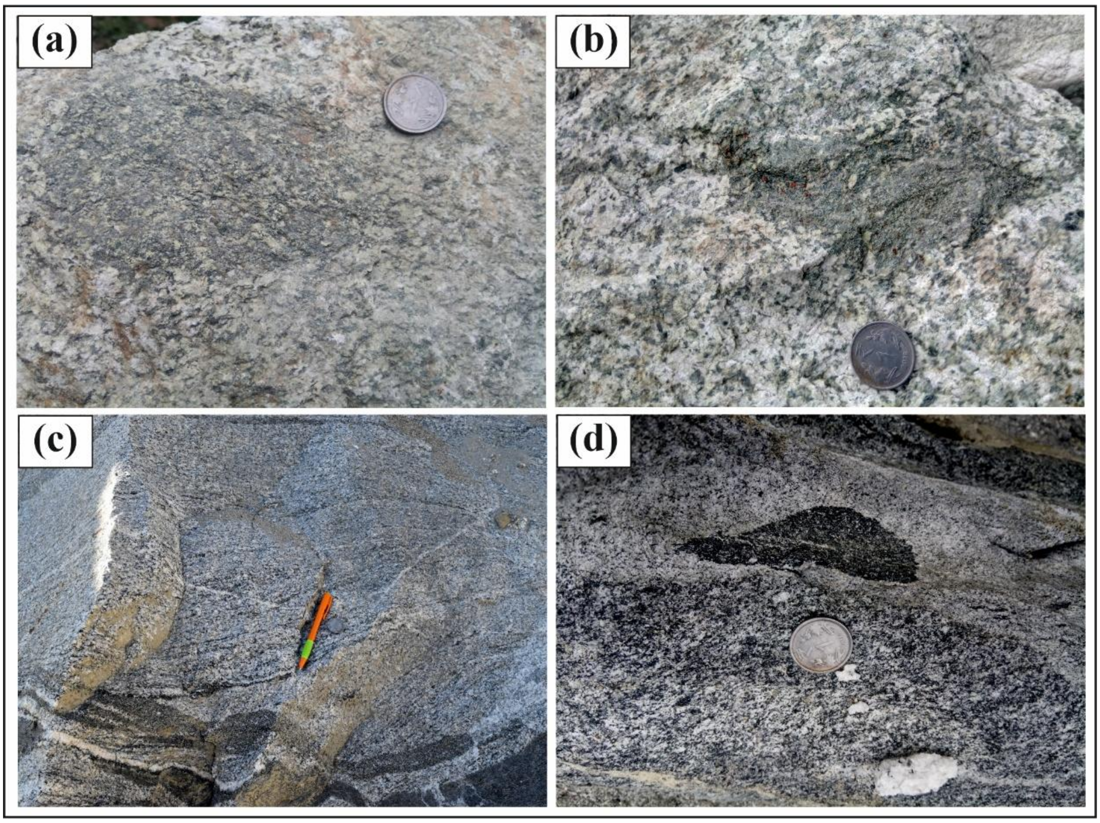

Figure 2.2: Field photographs of granodiorite showing (a) a granodiorite having a greenish tint due to alteration and hosting a sub-rounded microgranular enclave (ME); (b) an irregular shaped ME with diffused boundary; (c) medium grained, gneissic granodiorite with quartz vein intrusions exposed between Etalin and Anini; (d) lens-shaped ME with sharp boundary with the host granodiorite in Anini

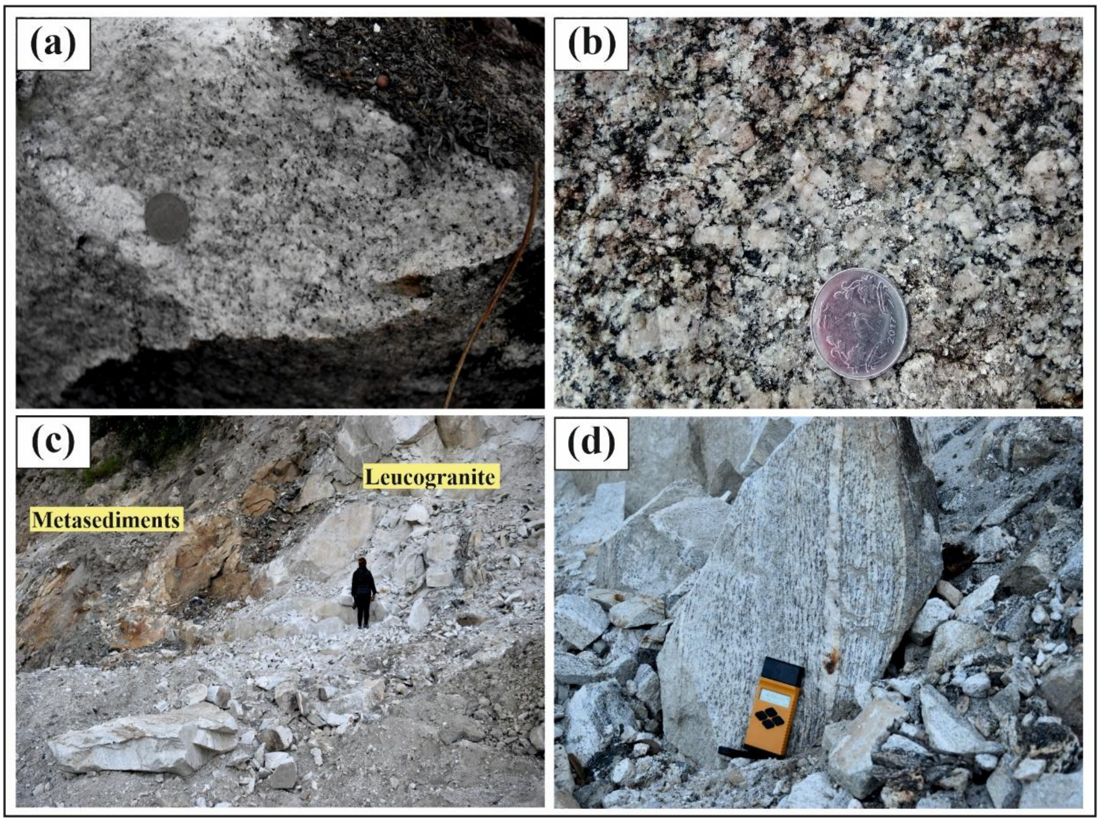

Figure 2.3: Field photographs of granite and leucogranite. (a) light grey granite from Alinye; (b) randomly oriented phenocrysts of feldspars in the granite of Dambuen; (c) leucogranite outcrop in contact with metasediments in Ayeso; (d) foliated leucogranite where gneissosity is defined by alternate alignment of mafic and felsic minerals.

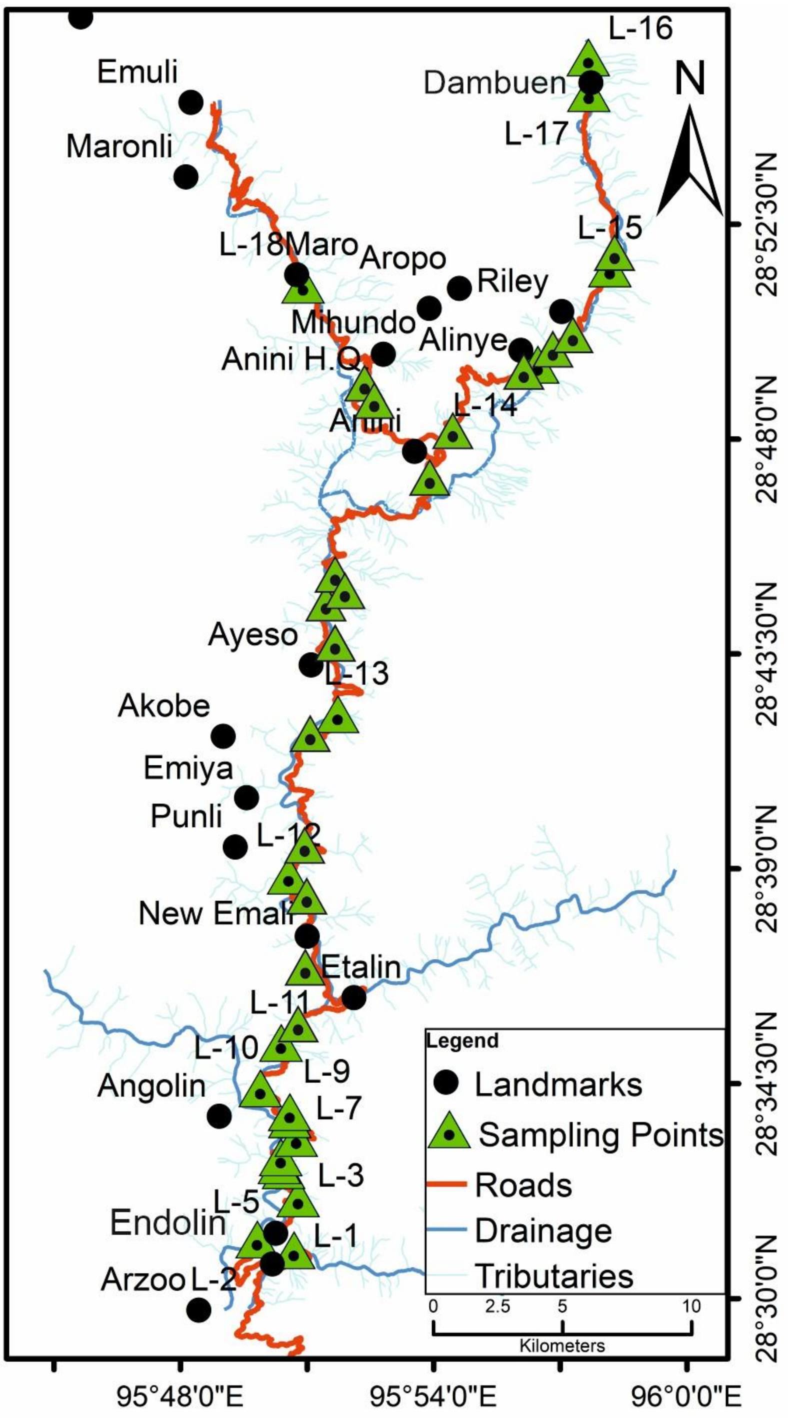

Figure 2.4: Transect map of Dibang Valley, Arunachal Pradesh showing the sampling locations of present study.

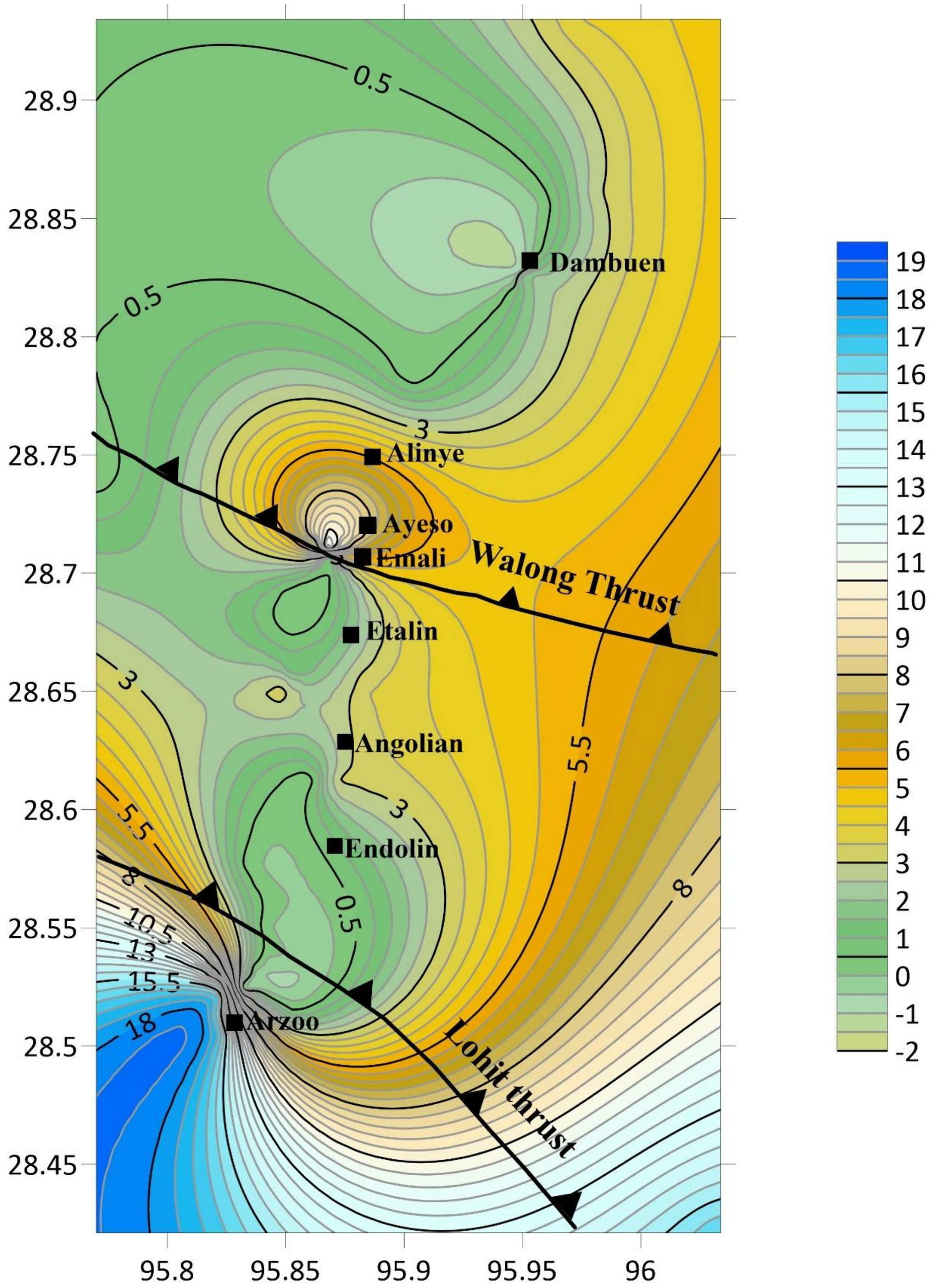

Figure 2.5: Magnetic Susceptibility (MS) contour map showing the spatial variation of MS values recorded from the granitoids of Dibang Valley.

Table 2: Average, and range of Magnetic Susceptibility (MS) values (x 10^{-3} SI unit) obtained from granitoids from Dibang Valley, Arunachal Pradesh

Rock type	**Transect**	**Location**	**Average Magnetic Susceptibility MS values (x10^{-3} SI unit)**	**Range of MS (x10^{-3} SI unit)**	**Inferred Granite Series**
Quartz diorite	Arzoo-Etalin	Arzoo	16.5(6)	14.49-19.29	Magnetite series
		4-5km from Andolin	0.143(14), 0.126(9)	0.077-0.190	Ilmenite series
		Angolian	0.166(10), 0.235(12), 0.117(5), 0.147(5), 0.189(5)	0.113-0.875	Ilmenite series
		2-4km beyond Angolian	0.190(9), 0.174(7)	0.128-0.210	Ilmenite series
		Etalin	0.175(9)	0.121-0.249	Ilmenite series
	Etalin-Anini	10km before Anini	0.098(7), 0.178(8), 0.100(8)	0.069-0.358	Ilmenite series
	Anini-Dambuen	Anini town	0.183(7)	0.152-0.223	Ilmenite series
		Near Alinye	0.653(6), 0.707(16)	0.250-1.082	Ilmenite series
		100m from Dambuen	3.519(7), 3.514(8)	2.763-4.463	Ilmenite to Magnetite series
	Anini-Maroli	Near Maroli village	0.135(9)	0.108-0.183	Ilmenite series
Granodiorite	Arzoo-Etalin	2.5km from Embolin	0.092(15)	0.041-0.131	Ilmenite series
		Andolin	0.097(5), 0.098(5), 0.088(8), 0.072(7), 0.165(5)	0.069-0.188	Ilmenite series
		Angolian	0.138(7)	0.110-0.169	Ilmenite series
	Etalin-Anini	Etalin	0.225(5),0.072(5)	0.035-0.482	Ilmenite series
		7km from Emali	0.324(6), 0.872(5), 1.484(3)	0.039-2.065	Ilmenite series
		10km from Emali	0.856(6), 0.220(6)	0.056-1.051	Ilmenite series
	Anini-Dambuen	Alinye	3.352(6), 3.154(7), 4.029(4), 7.264(5), 9.159(5), 3.783(6)	2.191-10.596	Ilmenite to Magnetite series
		Near Avalley	2.820(7), 3.017(9)	1.638-4.849	Ilmenite to Magnetite series
Granite	Anini-Dambuen	Alinye	0.504(3), 0.041(5)	0.030-0.673	Ilmenite series
		Acheso	3.994(9), 3.516(6), 3.226(8)	2.430-5.397	Ilmenite to Magnetite series
Leucogranite	Etalin-Anini	Etalin	3.021(8)	1.264-4.587	Ilmenite to Magnetite series
		Emali	3.421(5) 3.809(4), 2.259(4), 6.325(7), 4.038(8),	1.597-9.064	Ilmenite to Magnetite series
	Anini-Dambuen	12km from Emali	0.187(6)	0.086-0.444	Ilmenite series
		Ayeso	11.964(4), 4.547(6),	3.018-17.495	Ilmenite to Magnetite series

CHAPTER-3

METHODOLOGY

3.1 INTRODUCTION

In the present study, a comprehensive approach integrating both field-based and laboratory-based analyses was employed to understand the petrogenesis and evolution of the Dibang Valley granitoids. After an initial literature review, detailed fieldwork was conducted and standard geological tools (GPS, hand lens, hammer, Kappameter, notebook etc.) were used to document the study area and collect representative fresh rock samples. These samples were then analysed with the help of various modern laboratory equipment to estimate the key intensive physical and chemical characteristics of the granitoids. A brief overview of the methodologies and instrumentation is provided in this chapter.

3.2 FIELD TECHNIQUES

Detailed geological fieldwork was executed in the Dibang Valley along the transect Hunli-Arzoo-Etalin-Anini-Dambuen taking into account the structural, textural, and mineralogical variations of the various lithologies exposed in the area. Hammers, chisels, a hand lens, Kappameter (KM-7), GPS (Garmin GPS12), digital camera, and field notebook are some of the essential tools and equipment used to successfully carry out and document the field observations. During the intensive field work, datas such as GPS locations (latitude, longitude, and altitude) of the sampling sites, field relations between granitoids and associated lithounits, variations in mineralogy and texture of various granitoids, and Magnetic Susceptibility (MS) measurements have been recorded, and fresh rock samples were collected.

The magnetic susceptibility (MS) of the Dibang granitoids was measured on smooth surfaces in the field using a hand-held Kapameter (model KM-7). The Kapameter, a sensitive instrument with a precision of 10^{-6} SI units, functions at a frequency of 10 kHz and is designed to work in temperatures ranging from 10°C to 60°C. The MS meter is ideally placed on a fresh, smooth rock surface larger than 100×100 mm, and the “measure” button is pressed. The kapameter is then taken at least 30 cm away from the rock surface towards open air, and the measure button is pressed again. The MS meter is finally brought back to the rock surface, and the actual MS value ($\times 10^{-3}$ SI units) is displayed on the LCD screen. To account for surface unevenness, correction of recorded MS values can be done using recommended factors such as: 1 mm = 1.07, 2 mm = 1.15, 3 mm = 1.23, 4 mm = 1.32, 5 mm = 1.41, 6 mm = 1.51, 7 mm = 1.61, 8 mm = 1.72, 9 mm = 1.84, 10 mm = 1.96.

3.3 METHOD OF SAMPLE PREPARATION

After the field investigations and sample collection, representative samples were carefully selected to progress with petrographic studies and further mineralogical and geochemical analyses. For this, rock thin-sections were prepared, and samples were pulverized (powdered) for analytical purposes.

3.3.1 PREPARATION OF THIN SECTIONS

To study and document the petrographic features, thin sections of the representative fresh rock samples were first prepared by cutting the samples from the part of the rock that bears important features as observed in hand specimens. Rock-thin sections were then polished to a desired thickness using suitable grades of corundum powder by mechanical means. The thin section is then glued to the glass slide, and further polished using carborundum powder until the required thickness of 0.03mm is attained. The glass slide is then washed to get it free from grinding powder and dried. The rock-thin section for the present study is not covered with a cover slip, as it will further undergo carbon coating for SEM and EPMA analysis.

3.3.2 FINE POWDERING OF ROCK SAMPLES

Based on the spatial distribution and textural variation, relatively unaltered, fresh granitoid samples were selected for the determination of major, trace, and rare earth elements through XRF and ICP-MS analytical techniques. For these analyses, the selected sample had to be finely powdered. Individual sample weighing about 2 kg or more was first broken down into several smaller pieces and pulverised/ground to coarse grains (< 2mm) in a portable iron mortar. The coarse powder was then homogenized, and about 200g of the sample was separated by the coning and quartering method in several repeated steps. Finally, the 200g sample was ground into a very fine powder using an agate mortar and pestle till it attained a size of 200-mesh. Necessary precautions were taken during sample preparation to avoid contamination. Before processing the next sample, the iron and agate mortars were thoroughly cleaned using isopropyl alcohol.

3.4 ANALYTICAL METHODS

3.4.1 MICROSCOPIC STUDIES AND MODAL MINERAL ANALYSIS

Optical studies of rock thin sections are essential for identifying minerals, mineral assemblages, and classifying granitoids. Petrographic studies were done using a LEICA Polarizing Microscope (DM 750P) in the optical laboratory of the Department of Geology, Nagaland University. About 28 rock thin sections were examined, and key textural variations and mineral assemblages were photographed and documented. Photomicrography was done with a LEICA-DM 2700P microscope equipped with a Leica K3C camera. Modal mineral analysis (volume%) of the samples was carried out for classifying the granitoids, with at least 1,000 points counted for each thin section, allowing determination of the volume percentages of each mineral.

3.4.2 ELECTRON PROBE MICRO-ANALYSIS (EPMA)

For the mineral phase chemistry of feldspars, biotite, amphiboles, and Fe-Ti oxides, representative thin sections of granitoids were selected, and the analysis was carried out using the Electron Probe Micro-Analyzer (EPMA) CAMECA SXFive instrument at DST-SERB National Facility, Department of Geology (Centre of Advanced Study), Institute of Science, Banaras Hindu University. Polished thin sections were coated with a 20 nm layer of carbon using the LEICA-EM ACE200 instrument to prepare them for EPMA analysis. The CAMECA SXFive was operated via SXFive Software at an accelerating voltage of 15 kV and a beam current of 10 nA, utilizing a LaB6 electron source.

Natural silicate mineral andradite was employed as an internal standard to verify the alignment of crystals with respect to the wavelength-dispersive spectrometers (SP1–TAP, SP2–LiF, SP3–LPET, SP4–LTAP, SP5–PET) of the instrument. The following X-ray lines were analyzed: F-Kα, Na-Kα, Mg-Kα, Al-Kα, Si-Kα, P-Kα, Cl-Kα, K-Kα, Ca-Kα, Ti-Kα, Cr-Kα, Mn-Kα, and Fe-Kα. For calibration, X-ray mapping, and quantification, a suite of natural mineral standards supplied by CAMECA-AMETEK was used, including apatite, fluorite, halite, chromite, periclase, wollastonite, corundum, orthoclase, rhodonite, rutile, and hematite.

Data acquisition, calibration, quantification, and processing were performed using CAMECA's SxSAB version 6.1 and SX-Results software. Analytical precision was higher than 1% for major oxides and within 5% for trace elements, as confirmed by repeated standard analyses (e.g., Pandey et al., 2017).

3.4.3 SCANNING ELECTRON MICROSCOPY

Scanning Electron Microscopy (SEM) coupled with Energy Dispersive X-Ray Analysis (EDAX) was employed to identify magnetite and ilmenite from representative Dibang granitoids. Analyses were conducted using Carl Zeiss UK SEM-EVO 18 additionally equipped with an EDAX detector installed at the Geology Department, Kumaun University, Nainital. The instrument operates with a LaB6 source at a voltage of 20 kV and a beam current of 10 nA, ensuring stable beam conditions for high-resolution imaging and elemental analysis. Backscattered electron (BSE) imaging was utilized to distinguish mineral phases based on atomic number contrast, while point analyses and elemental mapping were performed using the EDAX system to determine the chemical composition and spatial distribution of key elements within the opaque minerals.

3.4.4 X-RAY FLUORESCENCE (XRF) SPECTROSCOPY

X-Ray Fluorescence (XRF) spectroscopy is a rapid, non-destructive analytical technique widely used to identify and quantify major oxides and trace elements present in a substance. XRF analysis for major oxides of the Dibang Valley granitoids was carried out using a PANalytical Axios^{maX} at CSIR-National Geophysical Research

Institute (NGRI), Hyderabad, Telangana. The instrument is configured with an SST-maX X-ray tube for superior sensitivity coupled with ZETA technology to eliminate tube aging. It can operate in three power options (2.4, 3.0, and 4.0 kW) at 20 to 60 kV, 10-160mA.

Samples were prepared by pressing 1–2 grams of finely powdered material into pellets using a hydraulic press at 25 tons for 30 seconds. The powdered samples were loaded into collapsible aluminum cups with a boric acid backing. International rock standards JG-2* (Geological Survey of Japan) and G-2 (United States Geological Survey, Reston, CO, USA) were used for calibration and quality control.

3.4.5 HIGH RESOLUTION INDUCTIVELY COUPLED PLASMA MASS SPECTROMETRY (HR-ICP-MS) ANALYSIS

A set of trace and rare earth elements (REE) was determined using a closed vessel digestion method for sample preparation, followed by analysis with the AttoM HR-ICP-MS at CSIR-National Geophysical Research Institute (NGRI), Hyderabad. All quantitative measurements were conducted using the AttoLab instrument software, while datas were processed using Nu Quant (Nu Instrument, UK). The ICP source is powered by a 1.6 kW RF generator operating at 27.12 MHz. A standard Fassel-type plasma torch equipped with a 1.5 mm injector was used for sample introduction.

For preparing the solution to undergo analysis, 0.05 gm of each pulverized rock sample was weighed and transferred to a pressure decomposition vessel called a Savillex Teflon. 10ml acid mixture of 7:3 (HF: HNO_3) was added to the sample. The mixture was swirled gently to make it completely moist. The solution was then kept in a tightly closed vessel and heated on a hot plate at 150˚C for 48 hours. After 48 hours, the sample was allowed to cool, semi-dried at 110˚C, and 1ml of $HClO_4$ was added to it. It was heated again until the liquid evaporated and a semi-solid precipitate was left at the bottom. A mixture of 1:1 HNO_3 and Milipore was prepared, and 10 ml of this mixture was added to each Savilex vessel containing the residue, heated for 10-30 minutes until it dissolved. For the next step, cylindrical vessels and conical flasks were cleaned with a 1:1 HNO_3 and Milipore mixture. 5ml of 1 ppm ^{103}Rh was added to act as an internal standard. The volume of solution was then made to 250ml with deionized water. 1ml conc. HNO_3 was added to 10ml of the solution, and the volume was increased to 100ml again with deionized water. This final solution was stored in 60ml cylindrical bottles and kept for running in the HR-ICP-MS instrument for analysis. JG-1A (Geological Survey of Japan) was the standard used for calibration, and the data obtained for all the analyzed elements have a Relative Standard Deviation (RSD) <5%. The detailed procedures of sample preparation, operating parameters of the instrument, methods for data processing, and quality are all documented in Satyanarayanan et al. (2018).

3.4.6 U-Th-Pb SENSITIVE HIGH-RESOLUTION ION MICRO-PROBE (SHRIMP) ANALYSIS

Three representative samples were selected for age dating through U-Th-Pb SHRIMP analysis. Separation of zircon grains from the samples was accomplished by employing magnetic and heavy liquid separation techniques at the Geology Department, Centre of Advanced Studies, Kumaun University, Nainital, and the U-Th-Pb analysis was carried out by Sensitive High Resolution Ion Micro Probe at SHRIMP Centre, Korea Basic Science Institute (KBSI), Ochang Campus, Korea. Selected grains were mounted in epoxy with FC1 (Duluth gabbroic anorthosite, 1099 Ma; Paces and Miller, 1993) and SL13 (Sri Lankan gem zircon; U = 238 ppm) reference zircons and grounded to expose internal zones. The internal structures of zircons were documented with back-scattered electron (BSE) and cathodoluminescence (CL) images using a JEOL JSM-6610LV scanning electron microscope (SEM) at KBSI. Procedures of SHRIMP analysis are similar to the protocols described in Williams (1998). A 3.0-4.0 nA mass filtered O_2^- primary beam was focused to a spot of approximately 25 μm diameter on the polished surface of target zircon grain. Data processing was conducted using SQUID 2.50 (Ludwig, 2009) and the concordia plots produced using Isoplot 4.15 (Ludwig, 2012) program, developed for Microsoft Excel. Weighted mean ages of zircon were calculated using ^{207}Pb-corrected $^{206}Pb/^{238}U$ ratios after excluding outliers under statistical t-test, and reported at 95% confidence. Common Pb was removed following the ^{207}Pb (for dates < 1000 Ma) or ^{204}Pb (for dates > 1000 Ma) correction method using the model by Stacy and Kramers (1975).

3.4.7 SOFTWARE AND ROCKWARE

The geological map and the transect map were prepared using Google Earth, Global Mapper, and ArcGIS software, and also referring to Survey of India toposheet No. 82P/13 and 82P/14. The Magnetic Susceptibility (MS) contour map was constructed by interpolating onto a grid using a kriging weights algorithm from the Golden Software Surfer (v.23). The acquired data from the mineralogical and bulk-geochemical analyses were further processed, reviewed, and interpreted with the help of a variety of software and spreadsheets tailored for particular calculations. The structural formula of biotite was calculated based on 11 oxygen atoms using the MS-DOS-based software BIOTERM (Yavuz and Öztaş, 1997), the structural formula of plagioclase was calculated based on 8 oxygen atoms with normalization v.17 spreadsheet, and that of amphibole based on 23 oxygen atoms was calculated using WINDOWS-based AMFORM spreadsheet (Ridolfi et al., 2018). Pressure, temperature, oxygen fugacity (fO_2), H_2O melt%, and ΔNNO values of the amphiboles were acquired using software WinAmptb (Yavuz and Döner, 2017) and AmpTB2 (Ridolfi, 2021).

Most of the bulk-rock geochemical data were processed with the help of GCDkit version 5.0 (Janoušek et al., 2006), which facilitates classification and tectonic discrimination through binary, ternary, trace element, REE plots, and CIPW normative mineral calculations. Additional required calculations were performed in **MS Excel** spreadsheet for data calculation, organization, filtering, and plotting. All computed values were manually cross-verified, and graphical outputs were digitized using CorelDRAW Graphics Suite (v. 2021) to produce high-resolution images.

CHAPTER- 4

PETROGRAPHY AND MODAL MINERALOGY

4.1 INTRODUCTION

Petrography is the detailed study and systematic description of rocks and minerals. It includes both megascopic and microscopic observations that can reveal the magmatic processes involved and the nature of melt composition. It is the most significant basic tool and direct method to study the mineral composition, texture, and structure of rocks. Petrographical studies, such as modal mineralogy, mineral assemblage, textural features, and classification of rocks, are of great importance for elucidating the crystallization history and petrogenetic evolution of the rocks under investigation. This chapter describes the petrography and modal mineralogy of the granitoids of Dibang Valley.

4.2 PETROGRAPHY

Based on megascopic observation, the granitoids from Dibang Valley are mesocratic to leucocratic and broadly classified as (i) quartz diorite, (ii) granodiorite, and (iii) granite, and (iv) leucogranite. The granitoids are phaneritic, massive, and compact in nature, and vary in colour from dark grey to light grey depending upon the content of mafic minerals.

The quartz diorites are dark grey in colour, medium to coarse-grained, and equigranular. Biotite and amphibole are the dominant ferromagnesian minerals and are present along with a greyish matrix comprising of quartz, plagioclase, K-feldspar, and other accessory minerals. Random and isolated, sub-rounded to elliptical-shaped mafic enclaves are commonly hosted within the quartz diorites.

The granodiorites are comparatively lighter grey in colour with a greenish tint, medium-grained and foliated. They are mostly gneissic. The gneissosity is defined by alternate bands of quartzo-feldspathic and ferromagnesian minerals in a preferred orientation. They are mostly phenocryst-free. However, small sub-rounded, lenticular, and irregular-shaped enclaves with diffused boundaries are enclosed within them.

The granites are light grey with medium to coarse-grained texture. They contain a moderate amount of biotite, but amphibole is rare or absent. Some granites comprise moderately large phenocrysts of feldspars, while some exhibit a certain degree of foliation defined by the orientation of biotite minerals. They are essentially devoid of mafic enclaves.

The leucogranites are leucocratic, medium to coarse-grained, with comparatively much lesser amounts of ferromagnesian minerals. The distinctive character of the leucogranites from the study area is the presence of muscovite and garnet minerals. They do not host any mafic enclaves within them.

The petrographic observations of Dibang granitoids, such as mineral assemblages, their physical appearance, and mutual relationships in rock thin sections, have been studied under a petrological microscope and documented to establish phase relationships and their genetic significance. The observed textural features and modal mineralogy aid in classifying the particular type of granitoid and contributing to its petrogenetic evolution.

4.2.1 QUARTZ DIORITE

They are medium to coarse-grained and exhibit interlocking hypidiomorphic texture. It has a mineral assemblage of plagioclase, biotite, amphibole (hornblende), quartz, and potash-feldspar as the major minerals (Figure 3.1a). Accessory phases include opaques (Fe-Ti oxides), epidote, apatite, titanite, and zircon. Chlorite, sericite, and epidote are the secondary minerals produced by the breakdown of the major constituent minerals (Figure 3.1b).

Plagioclase grains are medium to coarse, exhibiting characteristic lamellar twinning as well as Carlsbad twinning. The subhedral to anhedral plagioclase contains poikilitic inclusions of stubby apatite, biotite, and quartz grains. Sericitization of the plagioclase grains is frequently observed (Figure 3.1b). Zoning is sporadic but present in a few subhedral grains (figure 3.1c). The Modal abundance of K-feldspar is much lesser than plagioclase and is usually present as interstitial minerals. The K-feldspars in quartz diorite comprise mostly orthoclase and microcline. Intergrowth texture such as myrmekite, is observed at the grain boundaries between quartz and K-feldspar (Figure 3.1b and d).

Biotites are subhedral to euhedral. Both massive and flaky varieties of biotite are observed. The massive biotites are green in colour, anhedral, and lack distinct cleavage. They contain inclusions of quartz, plagioclase, and Fe-Ti oxides (ilmenite and magnetite). This variety of biotite is more abundant in the granitoids from Mipi and is mostly associated with amphibole (Figure 3.1e). The granitoid from Mipi is slightly gneissic megascopically and is microscopically discernible by the alignment of the biotite and amphibole minerals. The flaky biotites are brown in colour, subhedral, have distinct one set cleavage, and exhibit the characteristic “bird’s eye extinction” (Figure 3.1d). Alteration is commonly observed where biotite grains are replaced/altered to epidote or chlorite.

Amphiboles are medium-grained, subhedral to anhedral, and occasionally altered to epidotes. Breakdown of amphibole (Figure 3.1f) and complete replacement by biotite (biotitization) (Figure 3.1g) is commonly observed in the amphibole grains. Subhedral to anhedral magnetite is commonly observed as poikilitic inclusions within the amphibole grains. The ferromagnesian minerals (biotite and amphibole) are present as mafic clusters.

Quartz grains are usually anhedral, showing undulose extinction in some grains, suggesting deformation. Medium-grained quartz often contains inclusions of finer-grained quartz, biotite, felspar, and zircon. Acicular and stubby apatite, anhedral to subhedral epidotes, Fe-Ti oxides, and zircon are present as common accessory minerals (Figure 3.1h). Medium to coarse subhedral epidotes are usually associated with amphiboles and biotite. Zircon occurs as prismatic euhedral crystals enclosed within quartz, plagioclase, or biotite, forming a pleochroic halo when present in biotite. Titanite grains are anhedral to subhedral and are mostly found in association with the mafic clusters.

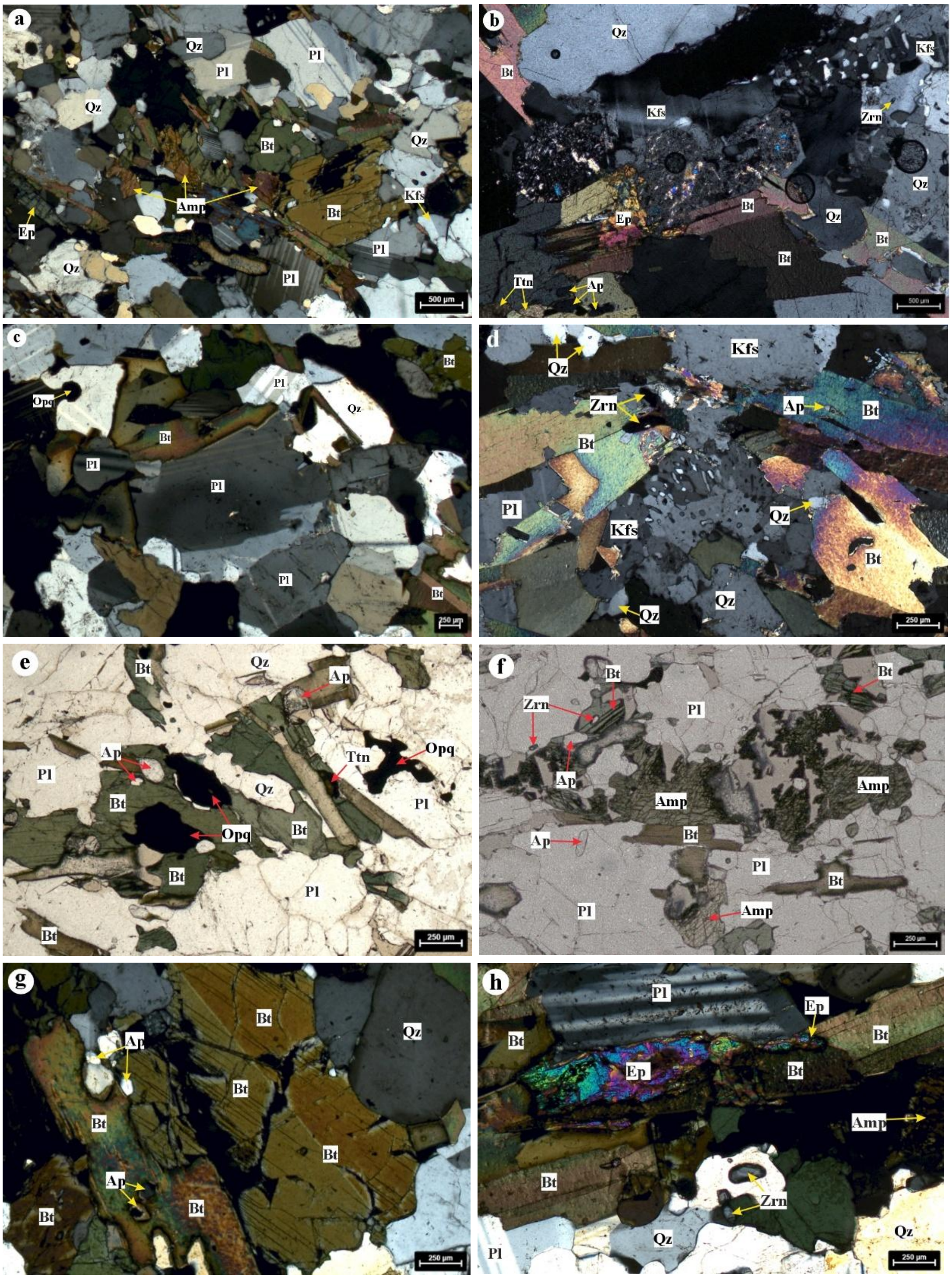

Figure 3.1: Photomicrographs of quartz diorite (a) hypidiomorphic textural relationship of major minerals in quartz diorite; (b) sericitization in plagioclase, alteration of biotite to epidote, and myrmekite texture at grain boundaries of K-feldspar and quartz; (c) feeble zoning in plagioclase; (d) flaky biotites with characteristic bird's eye extinction and myrmekitic intergrowth texture; (e) association of massive green biotite with accessory Fe-Ti oxides, apatite and titanite; (f) partial breakdown of amphibole to biotite; (g) biotitization of amphibole (h) association of common accessory minerals with major minerals

4.2.2 GRANODIORITE

Granodiorites are medium to coarse-grained and display hypidiomorphic granular texture. They essentially consist of plagioclase, K-feldspar, quartz, biotite, and amphibole. Accessory minerals are represented by apatite, epidote, zircon, titanite, and Fe-Ti oxides (Figure 3.2a).

Plagioclase forms subhedral to anhedral prismatic twinned crystals and is the most common constituent mineral in the granodiorites. Some coarse plagioclase grains display both Albite and Carlsbad twins and also exhibit faint zoning (Figure 3.2b). The grain boundaries are often corroded, and myrmekite texture is observed at the contact between plagioclase and quartz. Subhedral plagioclase grains rimmed by biotite are also commonly seen (Figure 3.2c). The K-feldspars are present in subordinate amounts and are represented by orthoclase and microcline, exhibiting Carlsbad (Figure 3.2d) and Pericline twinning, respectively. They are mostly anhedral crystals and fill the interstices between other constituent minerals or are present as inclusions within the coarser grains.

Bitotite represents the majority of the mafic minerals in the granodiorites. Brown flaky biotites are more dominant than the green massive variety. The flaky biotites are subhedral, fine to medium-grained, and strongly pleochroic in shades of light yellow to dark brown with perfect one-set cleavage. They are sometimes partially replaced by chlorite or epidote (Figure 3.2e). The greenish pleochroic biotites are massive, subhedral to anhedral, and lack prominent cleavage. They are often chloritized and accompanied by Fe-Ti oxides. Minor inclusions of zircon and apatite needles are noted within the biotites.

Amphiboles mostly form subhedral, cracked, prismatic crystals and mostly coexist in association with biotite and Fe-Ti oxides. The granodiorites display a stronger foliated fabric shown by the discontinuous alternate layers of the dark coloured ferromagnesian minerals and the light-coloured felsic minerals towards the eastern belt of the LPC. The amphiboles often undergo partial to complete biotitization, with the subsequent breakdown of both amphibole and biotite facilitating the extensive formation of secondary minerals such as epidote and chlorite (Figure 3.2f). These phases collectively impart a characteristic greenish coloration to the altered granodiorites, particularly within the western belt of the LPC.

Zircon typically occurs as small, isolated euhedral crystals, predominantly enclosed within plagioclase and biotite. Apatite is present in stubby, oval forms, commonly included within quartz, feldspar, and biotite. Titanite appears in subhedral to anhedral forms; however, well-formed euhedral rhombic crystals are also observed in association with plagioclase, K-feldspar, and biotite (Figure 3.2g). The presence of euhedral magnetite alongside other mafic mineral assemblages suggests the prevailing oxidising condition during its crystallization (Figure 3.2h).

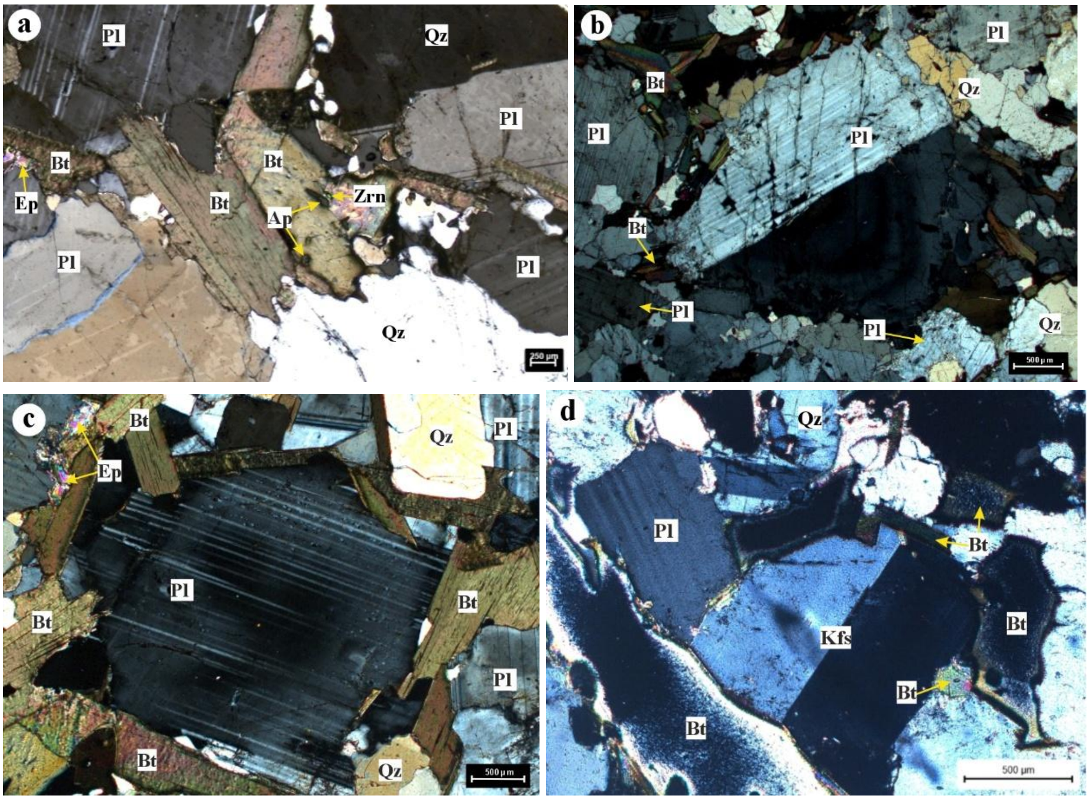

Figure 3.2: Photomicrographs of granodiorite (a) accessory epidote, apatite, and zircon within a biotite cluster associated with plagioclase and quartz; (b) plagioclase showing Albite and Carlsbad twinning as well as faint zoning; (c) subhedral plagioclase with characteristic Albite twins surrounded by flaky biotite grains; (d) K-feldspar with Carlsbad twin.

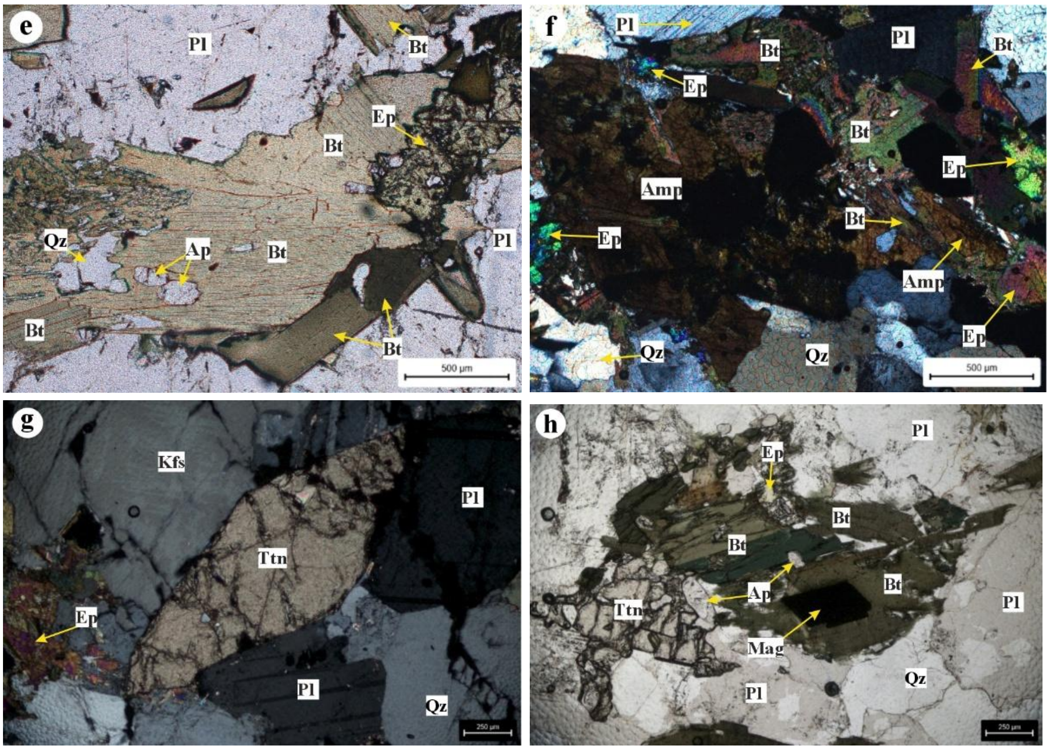

Figure 3.2: Photomicrographs of granodiorite (e) Flaky brown biotites partially replaced by epidotes; (f) alteration of amphibole and biotite to secondary epidote; (g) euhedral rhombic titanite (sphene) associated with plagioclase and K-feldspar; (h) euhedral magnetite associated with amphibole and biotite

4.2.3 GRANITE

Granites are medium to coarse-grained, light grey to pinkish in colour. They possess an equigranular hypidiomorphic texture and are observed only in the eastern belt of the plutonic complex (Alinye and Dambuen areas). They possess a mineral assemblage of pl-kfs -qtz-bt±hbl-ttn-ep-ap-zr (Figure 3.3a). Plagioclase, K-feldspar, and quartz are the major phases, while biotite, amphibole, and titanite are the minor phases. Zircon, apatite, and Fe-Ti oxides are the common accessory minerals. Chlorite, epidote, and sericite are the secondary minerals produced as a result of the alteration of ferromagnesian minerals and feldspars.

K-feldspar grains are mostly coarse-grained, subhedral to anhedral, and consist of both microcline with its characteristic cross-hatch twinning (Figure 3.3b). and orthoclase with simple twinning. The granites from Dambuen are comparatively coarse-grained with large phenocrysts of K-feldspar and plagioclase. Plagioclase grains are medium to coarse-grained, subhedral to anhedral, and exhibit typical albitic twinning and occasionally exhibit simple twinning. Some coarse feldspar grains poikilitically enclose smaller plagioclase, biotite and quartz crystals. Sericitization of feldspar is also observed (Figure 3.3c). Quartz crystals are usually anhedral, interstitial grains, exhibiting first-order grey to pale-yellow interference colours, and are commonly intergrown with feldspar in vermicular patterns, characteristic of myrmekite texture (Figure 3.3d). Faint zoning in some plagioclase crystals is also observed.

Biotites present in the granites are of both massive and flaky variants and are often found in clusters with Fe-Ti oxides (Figure 3.3e). Amphiboles are not common and are often altered. Secondary epidotes are commonly observed at the boundaries of ferromagnesian minerals and also crystallize along the fractures of larger feldspar grains (Figure 3.3f). Accessory minerals such as apatite, epidote, zircon, titanite, and Fe-Ti oxides are present in association with the other major minerals.

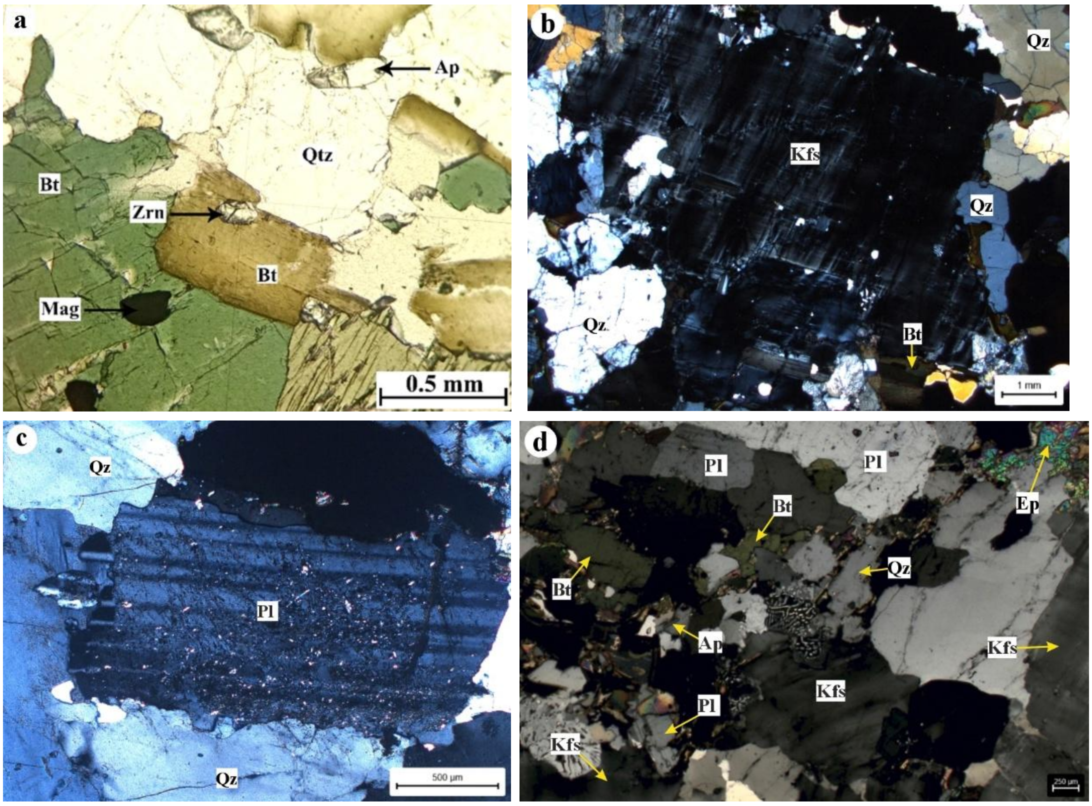

Figure 3.3: Photomicrographs of granite (a) accessory euhedral zircon and apatite enclosed within biotite and quartz; (b) cross-hatched twinning in microcline; (c) plagioclase with sericitized core; (d) myrmekite texture developed at grain boundaries.

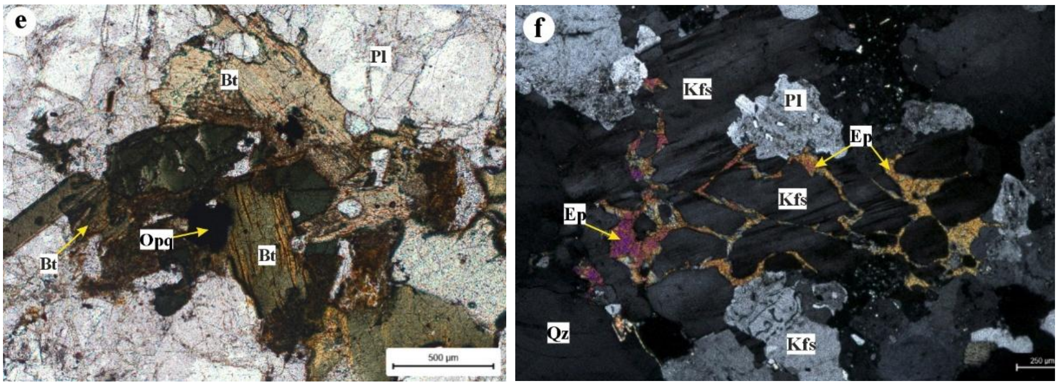

Figure 3.3: Photomicrographs of granite (e) massive and flaky biotite cluster associated with magnetite and plagioclase; (f) development of epidote along the fractures of feldspar grain.

4.2.4 LEUCOGRANITE

Leucogranites are medium to coarse-grained, leucocratic, and are distributed in the vicinity of the Walong Thrust in and around Etalin and Ayeso. They possess an equigranular hypidiomorphic texture and have a mineral assemblage of qtz-pl-kfs-bt-ms-grt-ep-zr (Figure 3.4a). In addition to the major minerals viz., quartz, plagioclase, and K-feldspar, these leucogranites contain two-mica (biotite and muscovite) and garnet in their mineral assemblage. Zircon, apatite, and Fe-Ti oxides are the common accessory minerals.

Plagioclase grains occur as coarse, subhedral to anhedral grains with a tabular habit and show the characteristic polysynthetic twinning. K-feldspars are mostly microcline, subhedral to anhedral, exhibiting pericline twinning (Figure 3.4b). Alteration to sericite is observed in some grains. Quartz grains occur as medium to fine subhedral to anhedral intergranular grains. They show first-order grey interference colours with wavy extinction.

Biotites are euhedral with prismatic form and exhibit reddish-brown to light yellow pleochroism in plane-polarized light (PPL) and second-order interference colour under cross-polarized light (Figure 3.4c). Muscovite, characterized by its perfect one-set cleavage, lack of pleochroism, and bright blue to pink interference colors, is commonly found in association with biotite (Figure 3.4d). Most of these muscovites may have formed due to the interaction of hydrothermal fluid with biotites and K-feldspar. The biotites are mostly primary magmatic crystals and fill the interstices between quartz and feldspar grains. Magmatic epidotes are observed in some samples (Figure 3.4e), pointing to their emplacement at shallow crustal levels, i.e., <30 km (Zen and Hammarstrom, 1984; Schmidt and Poli, 2004), but most epidotes are the result of the breakdown of mica minerals. Euhedral to subhedral garnet with tiny inclusions of quartz is commonly present in these leucogranites, advocating to its peraluminous nature (Figure 3.4f). Other accessory phases include apatite, sphene, zircon, and Fe-Ti oxides.

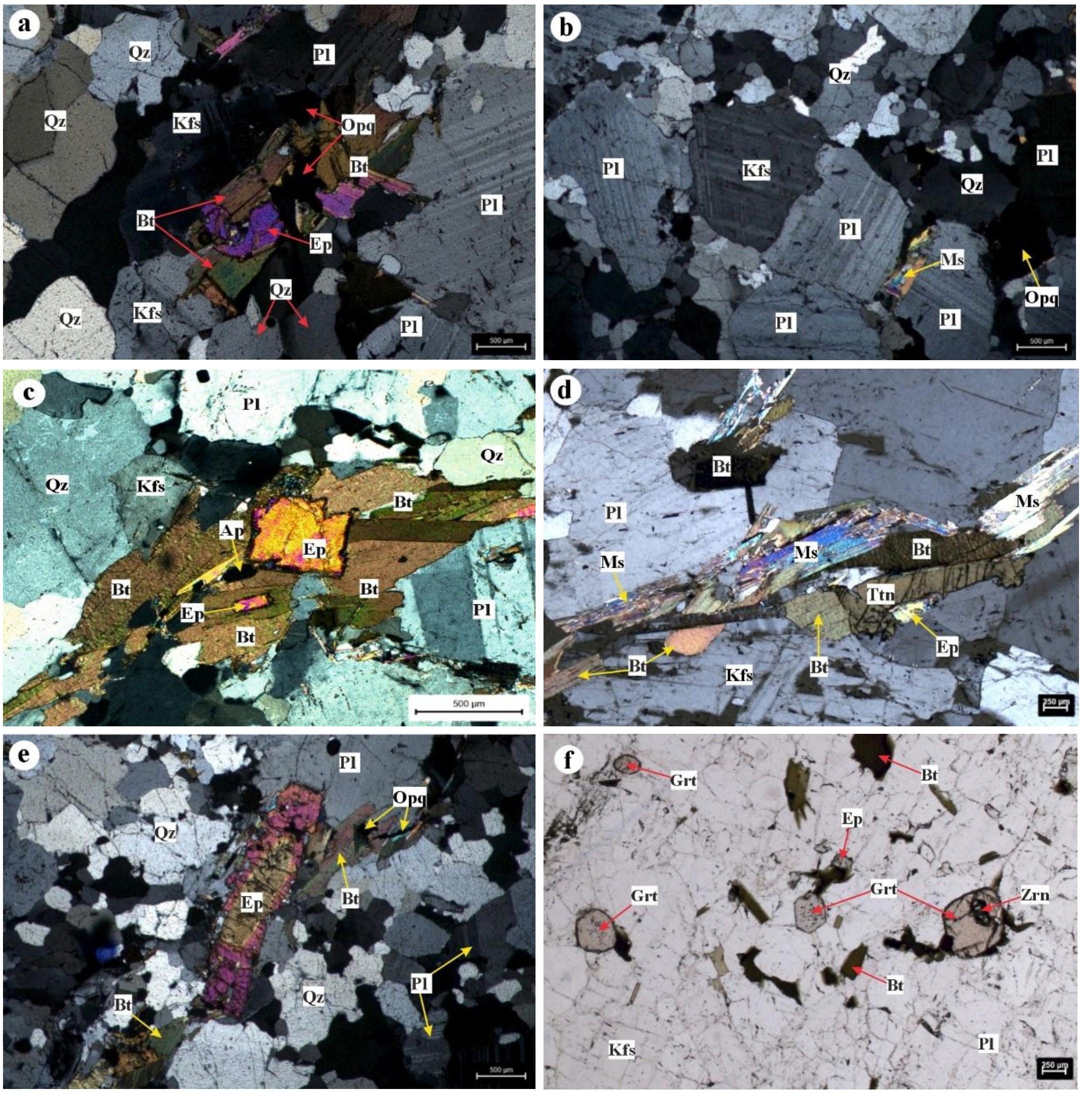

Figure 3.4: Photomicrographs of leucogranite (a) Hypidiomorphic textural assemblage of major minerals with accessory epidote and iron oxides within biotite cluster; (b) association of subhedral K-feldspar with Pericline twin and plagioclase with Albite twin and interstitial muscovite and iron oxide; (c) subhedral, platy, pleochroic biotite with interstitial epidote; (d) non-pleochroic muscovite associated with pleochroic biotite and present alongside plagioclase, quartz and titanite; (e) magmatic zoned epidote; (f) abundant subhedral garnet with quartz and zircon inclusion.

4.3 MODAL MINERALOGY AND IUGS CLASSIFICATION

Modal analysis, i.e., the quantitative determination of the relative proportions (by volume percentage) of the different mineral constituents in a rock, is a key method used to classify and understand the composition of rocks (igneous plutonic rocks in this case). Based on the petrographic studies, modal analysis (point counting) has been carried out for 28 granitoid thin sections. Acquired results (in volume percentage) for each mineral are given in Table 3. The percentage of Q-quartz, A-alkali feldspar, and P-plagioclase is then recalculated to 100% (Le Maitre, 2002) and plotted in the QAP-diagram (Streckeisen, 1976) (Figure 3.5) recommended by the International Union of Geological Sciences (IUGS).

The modal mineralogy of the phaneritic quartz diorite is 35-62 vol.% plagioclase, 2-5% k-feldspar, 19-35% biotite, 5-18% amphibole, 4-14% quartz, and 2-11% accessories consisting of opaques, epidote, apatite, titanite, zircon and they modally correspond to quartz diorite and quartz monzodiorite. Granodiorites have a modal percentage of 42-55% plagioclase, 2-16% K-feldspar, 5-18% biotite, 2-10% amphibole, 12-30% quartz, and 2-12% opaques and accessory minerals. Modally, they largely correspond to granodiorite and a few to tonalite/trondhjemite. The granites have a modal mineralogy of 35-40% quartz, 27-31% plagioclase, 25-30% K-feldspar, 2-5% biotite, 1% amphibole, and 1-3% accessory minerals. Based on this modal mineralogy, they plot within the monzogranite field in the QAP diagram. The modal mineralogy of leucogranites is 22-42% quartz, 32-55% plagioclase, 8-20% K-feldspar, 2-13% mica (biotite ± muscovite), 1% amphibole, and 1-7% opaques and accessory minerals. Modally, these two-mica leucogranites classify as monzogranite and granodiorite in the QAP classification diagram.

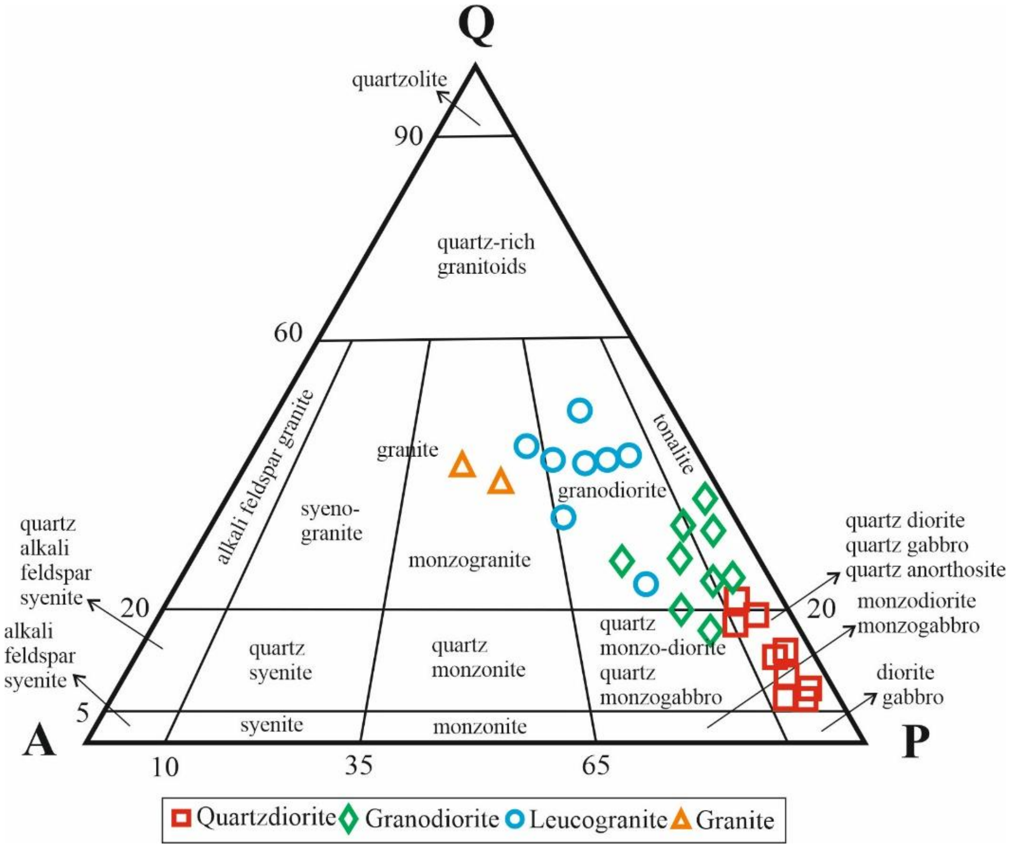

Figure 3.5: Quartz (Q), Alkali-feldspar (A), Plagioclase (P) triangular plot representing the modal composition of quartz diorite, granodiorite, granite, and leucogranite (after Streckeisen, 1973; Le Maitre, 2002).

Table 3: Modal mineral constituents (volume %) of representative granitoids from Dibang Valley, Arunachal Pradesh

QUARTZ DIORITE							
Sample No.	**Quartz**	**K-feldspar**	**Plagioclase**	**Biotite**	**Amphibole**	**Accessories***	**Total**
D2	5	2	53	25	10	5	100
M1	4	3	56	20	15	2	100
AN20	5	5	62	20	5	3	100
E5	7	2	42	30	12	7	100
E6	9	6	34	22	18	11	100
E11	12	3	48	24	9	4	100
E12	6	3	50	23	11	7	100
E13	5.50	2.50	35	35	15	7	100
E14	12	6	45	19	12	6	100

GRANODIORITE							
Sample No.	**Quartz**	**K-feldspar**	**Plagioclase**	**Biotite**	**Amphibole**	**Accessories***	**Total**
D3	25	16	50	5	2	2	100
D4	17	5	48	18	7	5	100
D5	22	8	49	13	3	5	100
D6	25	3	51	11	5	5	100
E3	30	2	50	8	2	8	100
E4	23	5	42	13	5	12	100
ET7	19	4	55	14	3	5	100
E2	14	10	47	16	5	8	100
E8	12	8	50	15	10	5	100

GRANITE							
Sample No.	**Quartz**	**K-feldspar**	**Plagioclase**	**Biotite**	**Amphibole**	**Accessories***	**Total**
D1	40	30	27	2	0	1	100
D7B	35	25	31	5	1	3	100

LEUCOGRANITE							
Sample No.	**Quartz**	**K-feldspar**	**Plagioclase**	**Biotite**	**Amphibole**	**Accessories***	**Total**
E15	40	15	42	2	0	1	100
ET22	35	10	38	13	0	4	100
ET24	22	15	55	7	0	1	100
ET9	42	20	33	2	1	2	100
ET12	42	10	33	8	0	7	100
ET14	30	20	40	5	0	5	100
ET15	35	16	32	10	0	7	100
ET16	37	8	42	10	0	3	100

*Epidote, titanite, apatite, magnetite, ilmenite, zircon

CHAPTER- 5

MINERAL CHEMISTRY

5.1 INTRODUCTION

Igneous rock-forming minerals hold valuable insights into the deep interior of the Earth, which cannot be directly accessed from the Earth's surface. Each mineral records the physico-chemical conditions under which various magmatic processes have taken place across a broad range of depths, ranging from the upper mantle to shallow crustal levels. All the magmatic processes involved in the genesis of the studied granitoids are subtly inscribed in the phase chemistry of its constituent minerals.

Mineral chemistry provides insights into the composition, structure, textural relationships, and geochemical behaviour of minerals, which are critical in understanding the nature and origin of magmatic rocks. The naturally occurring crystalline substances, composed of one or more chemical elements broadly termed "minerals," are also ionic in nature and are made up of anions and cations of variable charge and sizes in systematic arrangements.

The variations in mineral composition and stability fields of minerals can reveal information about pressure, temperature, fugacity of oxygen and water, and fluid interactions during rock formation. Detailed study of mineral chemistry thus allows us to estimate physical and chemical conditions and assess the protoliths, magmatic processes, and tectonic settings of magmas.

The chemical analyses of major rock-forming minerals (amphibole, biotite, and feldspar) from the granitoids of Dibang Valley, Arunachal Pradesh, have been done by using the analytical technique of Electron Probe Micro Analysis (EPMA) as given in Chapter 3. The analytical results were processed using different proxies to infer the prevailing physico-chemical conditions at the time of their crystallization in the respective host magma.

Electron Probe Micro Analysis data on 53 amphibole, 61 biotite, and 109 feldspar mineral grains are presented in Tables 4.1, 4.2, and 4.3, respectively.

5.2 AMPHIBOLE

Amphibole group of minerals occur in a wide range of P-T environments and are common constituents of igneous and metamorphic rocks. In igneous rocks, they are particularly common constituents of intermediate members of the calc-alkali series. Structurally, they are double-chain ionosilicates consisting of Si and Al at the tetrahedral site and have the composition ratio of Si:O = 4:11. The general formula of amphibole is $A_{0\text{-}1}B_2C_5T_8O_{22}$ (OH, F)$_2$. The site-A is occupied by highly mobile alkalies (Na^+, K^+), whereas site-B is for the cation at M_4 site (Ca^{2+}, Na^+, Mn^{2+}, Fe^{2+}, Mg^{2+} and Li^+); C-site usually filled by medium-size cation in the M_1, M_2, and M_3 sites (Al^{VI}, Mn^{2+},Fe^{2+},Mg^{2+},Fe^{3+},Ti^{4+}). The T-site is occupied by Si^{4+} and Al^{IV} up to a maximum total of eight, coordinated by $O_3(OH)$ in an octahedral manner. Calculation of the structural formula was determined using 23 oxygen ions.

5.2.1 COMPOSITION AND CLASSIFICATION OF AMPHIBOLE

Amphibole, with its complex chemical compositions, represents a crucial mineral in magmatic system, particularly in subduction zones, where it records the role of differentiation of calc-alkaline melts under hydrous conditions. The chemical composition of amphibole varies widely in differentiating magma and thus has great potential to contribute to the magmatic process. Couple and cation substitution at various sites (A, B, C) affect the Al-Si proportion at T-site in the amphibole structure, and hence, these are useful indicators for determining the factors controlling the crystallization conditions of amphiboles (e.g., Bachmann & Dungan, 2002; de Angelis et al., 2013). Active substitutions in magmatic amphiboles determine the variations in physicochemical parameters (temperature, pressure, oxygen, and water fugacities) during magmatic differentiation (e.g., Fabries et al., 1984). Hence, a comprehensive investigation of the amphibole assemblage is aimed at understanding the chemical and thermal evolution, including the depth of emplacement of the LPC. The calculated structural formulae and chemical composition of the amphiboles analysed are given in Table 4.1

Based on the IMA (International Mineralogical Association) approved nomenclature (Hawthorne et al., 2012), all the analyzed amphiboles belong to the calcic group. The ^{A}(Na+K+2Ca) atom per formula unit (apfu) increases progressively in the amphiboles of quartz diorite (0.22-0.57), granodiorite (0.44-0.65), and leucogranite (0.57-0.67) while the ^{C}(Al+Fe^{3+}+ 2Ti) apfu values are variable in the amphiboles of quartz diorite (0.80-1.51), granodiorite (0.87-1.36) and leucogranite (1.11-1.41). The Si apfu values in the quartz diorite (6.30-7.06), granodiorite (6.30-6.81), and leucogranite (6.29-6.43) amphiboles are resulted from the magmatic differentiation as also supported by their observed higher Ca+Al^{IV}>2.4. A similar range of aluminium mole fraction ($I = Al^{t}/(Al^{t} + Si + Mg + Fe^{t})$ =0.10-0.19) can be observed for quartz diorite and granodiorite amphiboles (Table 4.1). According to the classification given by Hawthorne et al. (2012) where ^{A}(Na+K+2Ca) apfu is plotted against ^{C}(Al+Fe^{3+}+2Ti) apfu (Figure 4.1) the calcic amphiboles of quartz diorite and granodiorite can largely be classified as magnesio-hornblende and a few to pargasite, while granite amphiboles largely plot in the pargasite field.

All amphiboles from the Dibang granitoids have been identified as magmatic amphiboles (Figure 4.2) by the relationship between (Ca+Na+K) and Si (Leake, 1971, 1978). Al^{IV} and Mg# [Mg/(Mg+Fe^{t})] are particularly sensitive to the environment in which the amphiboles grew. Negatively correlated Mg vs Al^{IV} (Figure 4.3a), positively correlated Al^{IV} vs (Na+K)^{A} (Figure 4.3b), and positively correlated Al^{IV} vs A+2Ti+Fe^{3+}+Al^{VI} (Figure 4.3c), indicate that pargasite and tschermak substitutions were primarily involved during crystallization of amphiboles in the Dibang Valley granitoids. The varying degree of tschermak substitution is one of the factors responsible for the redox state of the magmas (Phillips et al., 1988). The observed linear correlation between Si and Al^{IV} + (Na + K)^{A} (Figure 4.3d), Fe^{2+} and Mg (Figure 4.3e), and the absence of correlation between Na^{B} and Fe^{3+} (Figure 4.3f) strongly point to the predominance of pargasite and tschermak substitutions over the other substitutions during the evolution of amphiboles from Dibang Valley granitoids.

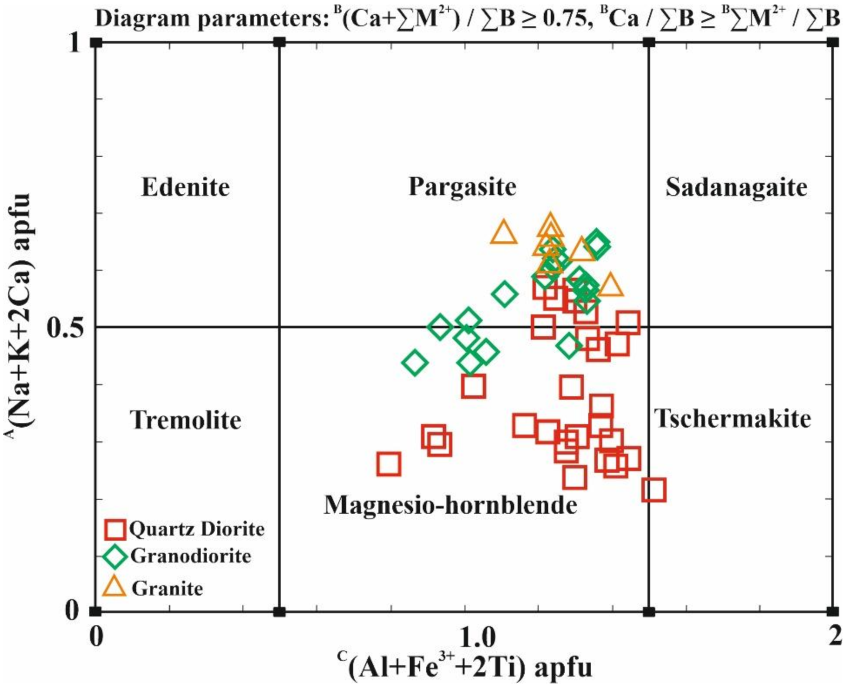

Figure 4.1: ^{C}(Al+Fe^{3+}+2Ti) vs ^{A}(Na+K+2Ca) amphibole classification diagram for calcic amphiboles from granitoids of Dibang Valley (after Hawthorne et al., 2012).

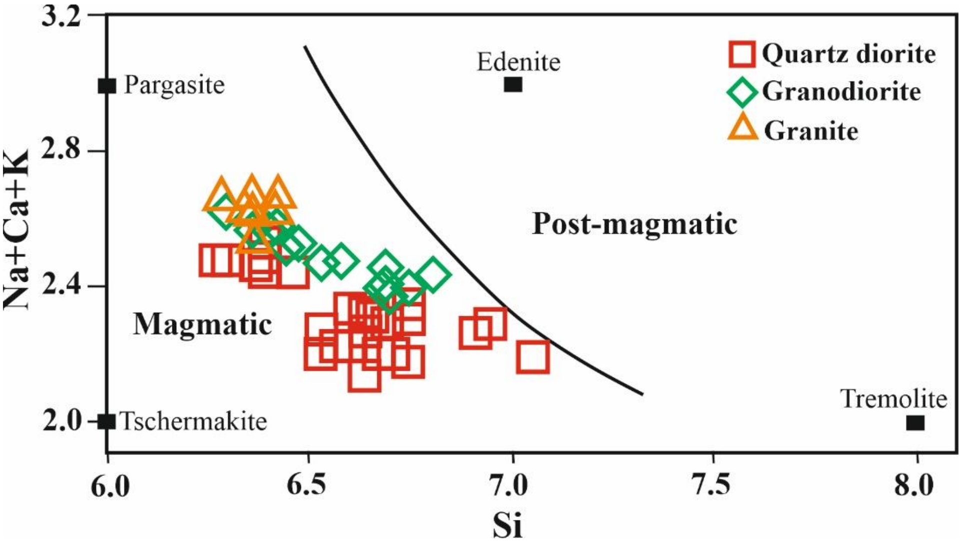

Figure 4.2: Si vs Na+Ca+K diagram of Leake (1971) applied to the studied amphiboles. The curve separates the composition of magmatic from post-magmatic amphiboles.

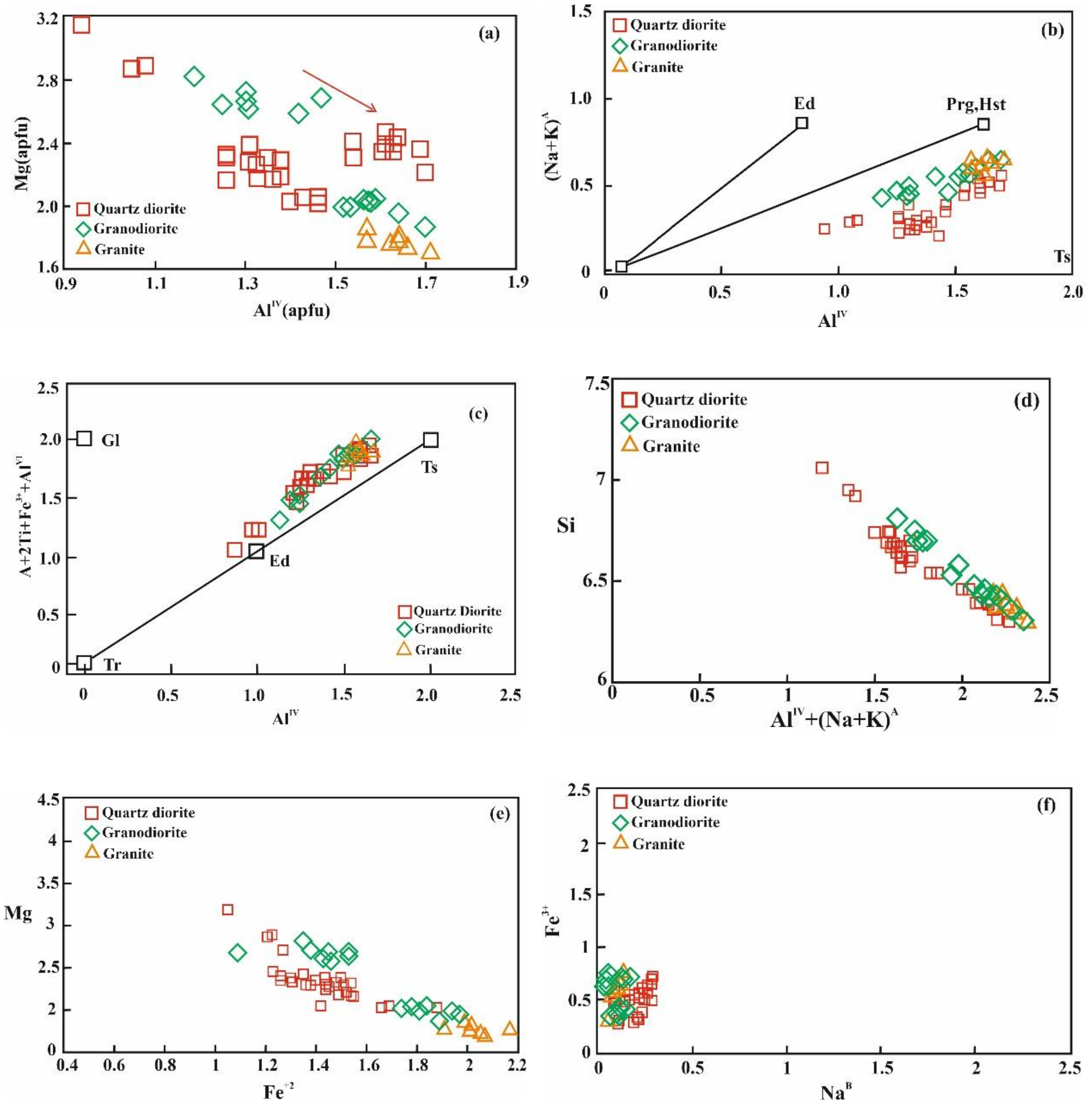

Figure 4.3: Chemical substitutions in the amphiboles of Dibang Valley granitoids (a) Al^{IV} vs Mg apfu; (b) Al^{IV} vs $(Na+K)^{A}$; (c) Al^{IV} $A+2Ti+Fe^{3+}+Al^{VI}$; (d) $Al^{IV}+(Na+K)^{A}$ vs Si; (e) Fe^{2+} vs Mg; (f) Na^{B} vs Fe^{3+}

5.3 BIOTITE:

The mica group of minerals are sheet silicates/phyllosilicates and has a platy morphology with perfect basal cleavage (Deer et al., 1992). General formula of mica is $IM_{2-3} \square_{1-0} T_4 O_{10} X_2$ where, I is an interlayered cation (K, Na, Ca, Ba, Cs, NH_4); M is an octahedral layered cation (Al, Mg, Fe^{2+}, Fe^{3+}, Li, Ti, Mn^{2+}, Mn^{3+}, Zn, Cr, V, Na); $\square$ is a vacancy in the octahedral layer; T is a tetrahedral layer cation (Si, Al, Fe^{3+}, Be, B); O is oxygen; and *X* is an anion (OH, F, Cl, O, S), not bonded to T (Deer et al., 1966). Structurally, they consist of a sheet of octahedrally coordinated M cation (mainly Al, Mg, Fe) wedged between two similar tetrahedral sheets $(Si, Al)O_4$. These sheets are superimposed and linked by the M cations. The hydroxyl ions (OH), along with the apical oxygens of the terahedra, complete the octahedral coordination.

Biotite is a trioctahedral mica with brucite-like structure having $M_3^{2+}(OH)_6$ (Deer et al., 1992). Most biotite exhibits an appreciable amount of Tschermak substitution whereby Al substitutes Mg^{2+}, Fe^{2+} cations from octahedral site and another Al substitutes tetrahedral Si^{4+}, trending toward the end-member compositions of eastonite and siderophyllite. It is a ferromagnesian mineral commonly found in mafic and felsic rocks and has compositional similarities with other Fe-Mg-rich minerals like olivine, pyroxene, and amphiboles. The biotites from the present study exhibit affinity with amphiboles.

Electron microprobe analysis of a total of 61 spots of biotite has been obtained: 20 from quartz diorite, 20 from granodiorite, 10 from granite, and 11 from leucogranite. The structural formulae and chemical composition of the biotites analysed are given in Table 4.2.

5.3.1 COMPOSITION AND CLASSIFICATION OF BIOTITE

The chemistry of biotite is classically used to classify the granitoid and determine the physico-chemical condition of the host magma. The biotites of Dibang Valley granitoids have compositional affinity with other Fe-Mg-rich minerals like olivine, pyroxene, and amphiboles.

The analysed biotites are either completely devoid of calcium or calcium-poor, ranging from 0.00 to 0.15 wt. % (Table 4.2). Nachit et al, (2005) proposed a ternary diagram (TiO_2-FeO*-MgO; where, FeO*= FeO+MnO) to distinguish primary magmatic biotites and reequilibrated biotites. The biotites from quartz diorite, granodiorite, and granite mostly belong to re-equilibrated biotites with a few exceptions, suggesting post-magmatic alteration by hydrothermal fluids. While the biotites from the garnet-bearing leucogranite are mostly primary biotite.

Al_2O_3 content of quartz diorite (14.7-16.1wt%), granodiorite (14.42-16.15wt%), granite (14.11-15.34 wt%), and leucogranites (15-86-16.86 wt%) are similar and hence have a similar Al^t value ranging from 1.38 to 1.47 wt% for quartz diorite, 1.32 to 1.47 wt% for granodiorite, 1.32 to 1.38 wt% in granite, and 1.46-1.53 wt% in leucogranite. The TiO_2 content of biotite in quartz diorite (1.18-2.77wt%) and granodiorite (1.8-3.37 wt%) is slightly lower than in granite (2.13-3.36 wt%) and leucogranite (2.65-3.51 wt%). The quartz diorite has higher SiO_2 and lower FeO^t content varying within a range (SiO_2=35.84-38.38 wt%, FeO^t=15.97-18.55 wt%) as compared to granodiorite (SiO_2=35.07-36.78 wt%, FeO^t=16.38-21.15 wt%), granite (SiO_2=35.90-36.73 wt%, FeO^t=18.74-20.45 wt%) and leucogranite (SiO2=35.24-36.13 wt%, FeO^t=21.54-23.36 wt%). The Ti_{apfu} in quartz diorite (0.07-0.16 wt%) is slightly lower than in granodiorite, granite, and leucogranite (Ti_{apfu} = 0.1-0.2, 0.12-0.20, and 0.15-0.21, respectively).

According to the ternary plot with end members Mg^{+2} – Fe^{+2} – Fe^{+3+} (Beane, 1974), biotites from Dibang Valley granitoids mostly lie within or close to the field of primary biotite. Biotite can be classified on the quadrilateral classification diagram based on end-members annite [$KFe^{2+}3AlSi_3O_{10}(OH)_2$], siderophyllite [$KFe^{2+}AlAl_2Si_2O_{10}(OH)_2$], phlogopite [$KMg\ 3AlSi_3O_{10}(OH)_2$], and eastonite [$KMg\ _2AlAl_2Si_2O_{10}(OH)_2$] siderophyllite-phlogopite-eastonite. On plotting the analyzed biotites in terms of Al^{IV} vs. Fe/Fe+Mg (Deer et al., 1963), the biotites of Dibang Valley granitoids plot close to the siderophyllite–eastonite boundary (Figure 4.4). The biotites of granite and leucogranite, including a few biotite samples of granodiorite, show enrichment in the siderophyllite component, which is more akin to crustally-derived, peraluminous felsic melts. Mg_{apfu} values of quartz diorite (1.21-1.44) and granodiorite (Mg_{apfu} = 1.14-1.49) are higher than those of leucogranite. In terms of (Al^{IV}+Fe^{+3})-Mg-(Fe^{+2}+Mn) components (Foster, 1960), biotites of quartz diorite and granodiorite plot in closer proximity to the Mg-biotite field, whereas leucogranites have compositional affinity with Fe^{+2}- biotite (Figure 4.5).

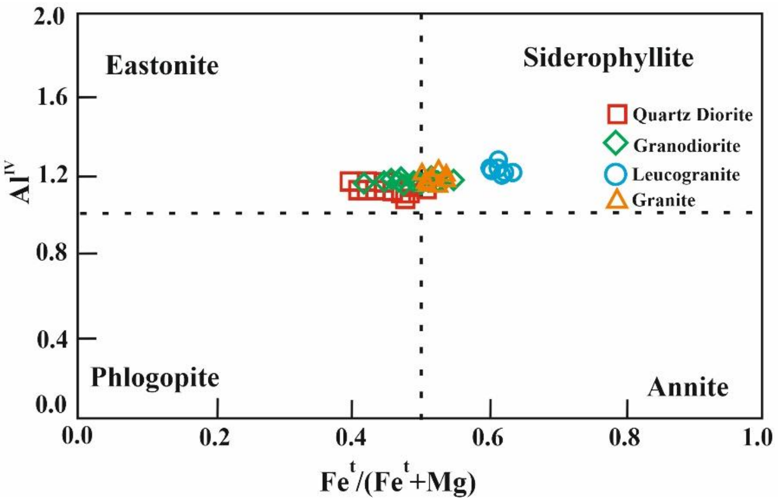

Figure 4.4: Al^{IV} vs. Fe/Fe+Mg biotite classification diagram of Dibang Valley granitoids after Deer et al. (1963).

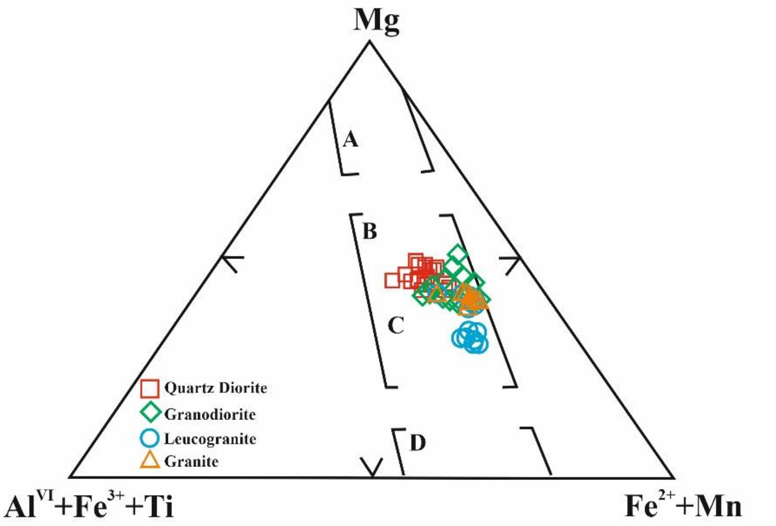

Figure 4.5: (Al^{IV}+Fe^{+3}+Ti)-Mg-(Fe^{+2}+Mn) ternary diagram after Foster, 1960. The fields of A-Phlogopite, B-Mg-biotite, C-Fe^{2+} biotite, D-Siderophyllites, and Lepidomelane.

5.3.2 NATURE OF HOST MAGMA

The X_{Mg} ($Mg/Mg+Fe^t$) of biotite (Table 4.2) is suggestive of the redox condition of the crystallizing magma (Czamanske and Wones, 1973). Hence, the oxidizing or reducing nature of the host magma from which the Dibang granitoids crystallized can be determined by the X_{Mg} of biotites. The quartz diorite (X_{Mg}= 0.50-0.59) and granodiorite (X_{Mg}= 0.47-0.58) records higher X_{Mg} content, while granite (X_{Mg}= 0.46-0.49) and leucogranite (X_{Mg}= 0.36-0.39) have the least values, indicating that they crystallized from a primary melt of varying compositions (Ishihara et al., 2002; Kumar and Pathak, 2010; Bora and Kumar, 2015; Singh et al., 2016; Kumar et al., 2021). The comparatively higher X_{Mg} of biotites from quartz diorite and granodiorite indicates that they crystallized in an oxidizing environment relative to the biotites of granite and leucogranite, which crystallized in a more reducing environment. FeO^t/MgO ratio of biotites from quartz diorite (1.26-1.78; average 1.50), granodiorite (1.27-2.04; average 1.77), and granite (1.86-2.11; average 1.99) is lower than leucogranites (2.74-3.18; average 2.93).

Relatively low Al^{VI} abundances of biotites of quartz diorite (0.26-0.35), granodiorite (0.15-0.28), granite (0.15-0.22), and leucogranites (0.24-0.31), indicate their nature similar to metaluminous (I-type) granitoid melts. In the studied samples, the X_{Fe} (Fe^t/Fe^t+Mg) and X_{Mg} ($Mg/Mg+Fe^t$) show an inverse relationship. The X_{Fe} of biotites in quartz diorite (X_{Fe} = 0.41-0.50) and granodiorite (X_{Fe} = 0.42-0.53) has lower variation and values, whereas biotites from granite and leucogranite (X_{Fe} = 0.51-0.64) has a wider variation and higher Fe content. Such differences can be a result of the influence of other crustal materials during the genesis of the magma, along with differentiation in the degree of fractionation (Kumar and Pathak, 2010; Bora and Kumar, 2015). The higher and equivocal values of X_{Mg} values of quartz diorite (0.50-0.59) and granodiorite (0.47-0.58) with an average of 0.55 and 0.50, respectively imply the high Mg character of studied samples characteristic of metaluminous (I-type) granites while the relatively lower X_{Mg} values of granite (0.46-0.49), and leucogranites (0.36-0.39) with an average value of 0.47 and 0.38 suggest their affinity to peraluminous (S-type) granites. According to Abdel-Rahman (1994), biotites in alkaline anorogenic suites are generally Fe-rich, biotites in peraluminous (including S-type) suites tend to be siderophyllitic in composition, while those in calc-alkaline suites are Mg-rich, and are related to orogenic suites from subduction settings. The variable FeO^t/MgO ratio of the Dibang granitoids is characteristic of their crystallization in transitional form between peraluminous (S-type) and metaluminous (I-type) granitoid melts.

In the ternary MgO-FeO^t-Al_2O_3 diagram (Figure 4.6) after Albuquerque (1973), the biotites from quartz diorite, granodiorite, and granite have shown compositional similarity with the biotites typically crystallized in association with pyroxene, amphibole, and biotite, characteristics of calc-alkaline, metaluminous (I-type) granitoid melts of subduction origin. The biotites from leucogranite, however, show more affinity with biotite and muscovite. This is also consistent in the biotite discrimination diagrams based on Al_2O_3 vs FeO^t, Al_2O_3 vs MgO, and MgO vs FeO^t (Abdel-Rahman, 1994), wherein biotites of Dibang Valley granitoids plot in the calc-alkaline field and leucogranites are closer to the peraluminous field (Figure 4.7 a-c). The $Fe^t/(F^te+Mg)$ ratios of biotite in Dibang Valley granitoids decrease with increasing ΣAl. Although there is an overlap, the $Fe^t/(Fe^t+Mg)$ ratio of quartz diorite (0.41-0.50), granodiorite (0.42-0.53), and granite (0.51-0.54) is slightly lower than the leucogranite (0.61-0.64). These transitional (I- and S-type) granitoid melts may represent hybrid magma, evidenced by the presence of microgranular enclaves in host granitoids. However, the effect of assimilation or mixing of a deeper-seated mafic melt into the felsic magmatic reservoir, other than the sole influence of source rock, cannot be ruled out. In the chemical classification (Figure 4.8) as proposed by Nachit et al. (2005), biotites from Dibang granitoids evolved from the field of primary biotite to re-equilibrated primary biotite, which may be due to late subsolidus reactions or deformation that variably affected their host rocks during the Himalayan orogeny.

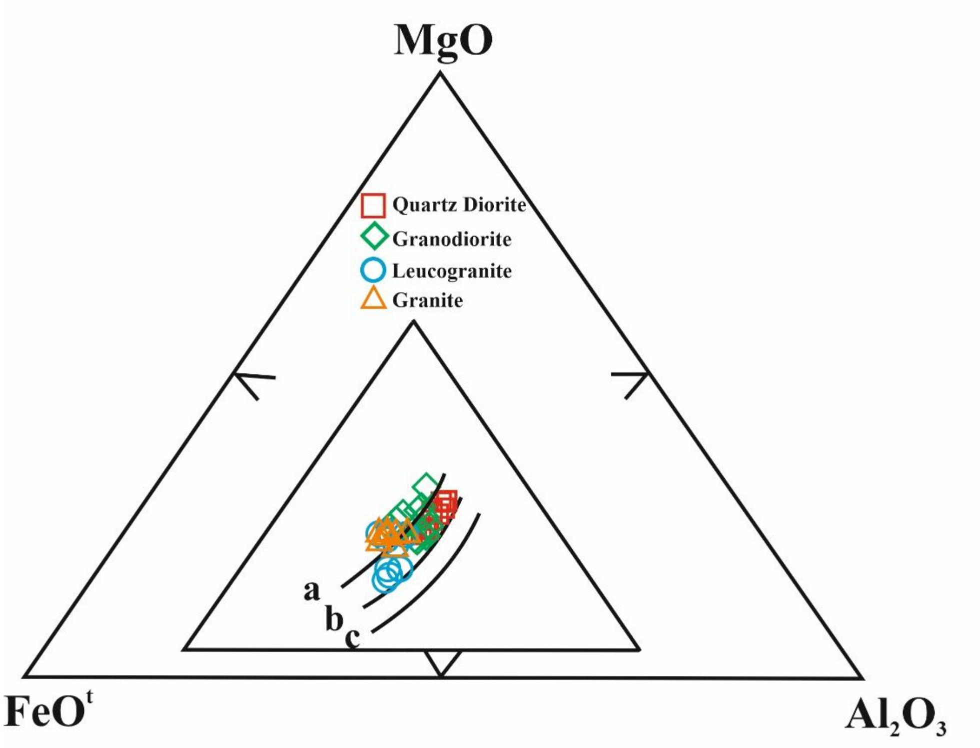

Figure 4.6: Ternary diagram of MgO-FeO^t-Al_2O_3 after Albuquerque (1973) (a) Biotite coexisting with amphibole (b) Biotite coexisting with ferro-magnesian minerals (c) Biotite coexisting with muscovite

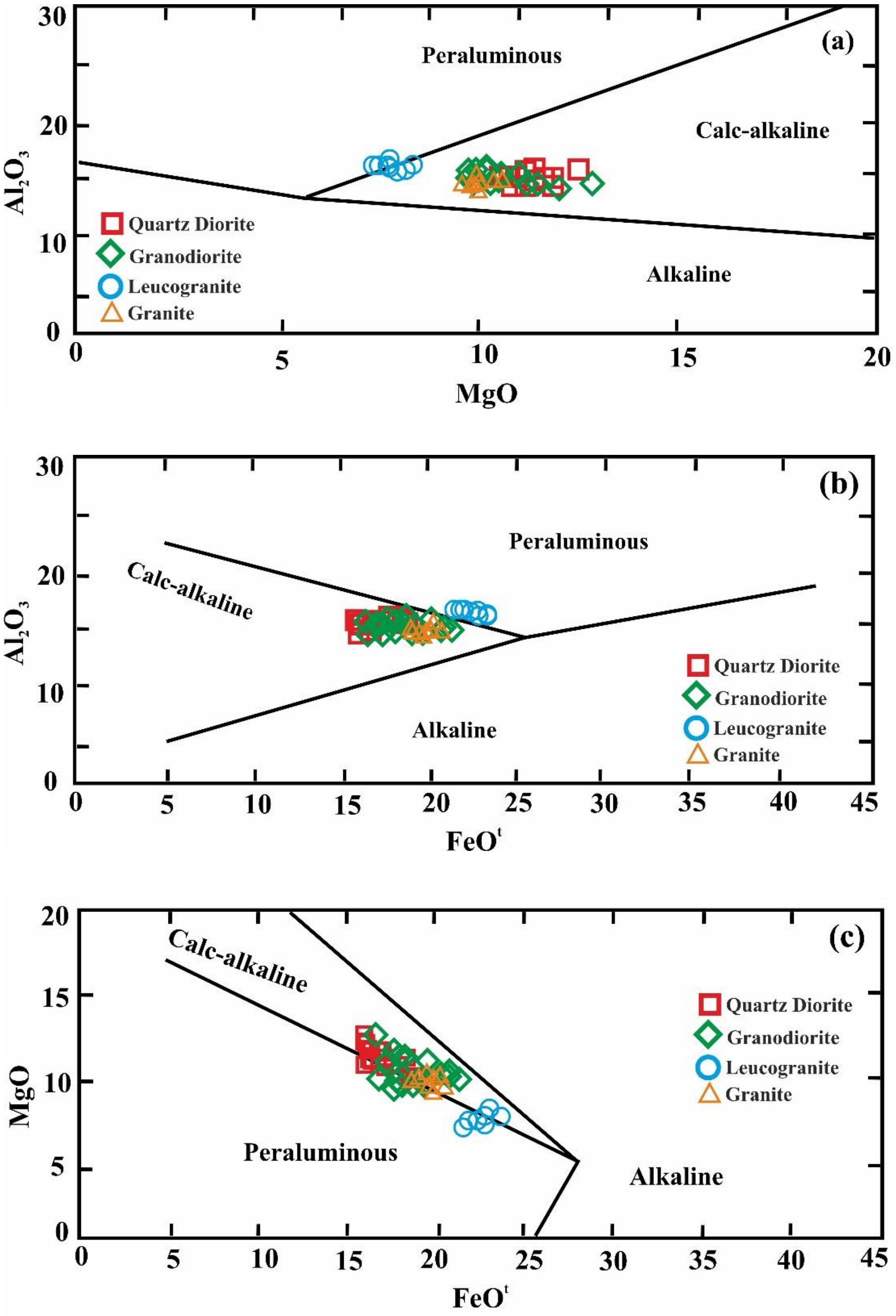

Figure 4.7: Tectonic discrimination diagrams of Abdel-Rahman (1994). (a) MgO vs Al_2O_3 (b) FeO^t vs Al_2O_3 (c) FeO^t vs MgO

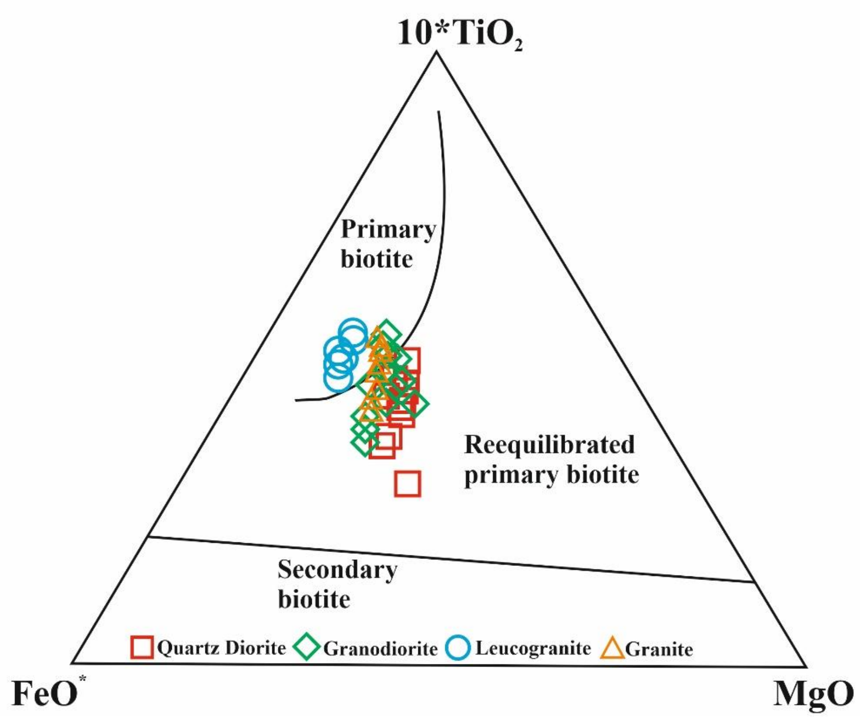

Figure 4.8: TiO_2-FeO*-MgO (FeO*= FeO+MnO) ternary diagram after Nachit et al. (2005).

5.3.3 OXYGEN FUGACITY (fO_2)

Oxygen fugacity (fO_2) represents the effective partial pressure of oxygen in a system and is a key factor in determining oxidation states of elements, especially iron (Fe^{2+} /Fe^{3+}) and other redox-sensitive elements in minerals. Biotite incorporates iron in both ferrous (Fe^{2+}) and ferric (Fe^{3+}) states, the ratio of which can be used to estimate fO_2 conditions during crystallization, whereby higher Fe^{3+} content signifies higher fO_2 conditions and vice versa. Biotite stability is influenced by the fO_2, and its coexistence with minerals such as magnetite (Fe_3O_4), ilmenite ($FeTiO_3$), and amphiboles can indicate oxidation-reduction conditions.

Oxygen fugacity is thus an essential parameter constraining the chemistry of biotites and calcic amphiboles (Anderson, 1996; Anderson and Smith, 1995). The chemistry of these hydrous ferromagnesian minerals (biotite and amphibole) can possibly be used to infer the redox condition, tectonic environments, and associated mineralization, if any (Ishihara 1979; 2004; Hart, Goldfarb, Lewis and Mair, 2004; Singh & Kumar 2005; Kumar and Pathak 2009).

In the Fe^{2+}(annite)-Mg(phlogopite)-Fe^{3+}(oxyannite) ternary diagram (Figure 4.9), the comparison of biotite compositions stabilized at different oxygen buffers viz., FMQ (fayalite-magnetite-quartz), NNO (nickel-nickel oxide), and HM (hematite-magnetite) shows that the biotites of quartz diorite, granodiorite, and granite mostly stabilized between FMQ and NNO buffer with an increasing trend, which suggests their crystallization in a moderately oxidizing environment as compared to the leucogranite, which mostly plots away from the other granitoids in the FMQ buffer. Biotite compositions (100×Fe/Fe+Mg) from the quartz diorite and granodiorite projected onto experimental isobaric (2,070 bar) fO_2-T section (Wones and Eugster, 1965) to illustrate the progressive changes in fO_2 with decreasing temperatures (Figure 4.10) shows that the estimated log fO_2 for the quartz diorite and granodiorite samples range from log fO_2^{-13} to log fO_2^{-12} MPa suggesting crystallization of these granitoids from relatively oxidized magmas within a temperature range of 800-880ºC, granite have fugacity of log fO_2^{-13} MPa indicating moderate oxidizing condition within a temperature of 800-820ºC, while leucogranite have a lower value with log fO_2^{-15} MPa within a temperature range of 755-780ºC indicating a more reducing magmatic environment.

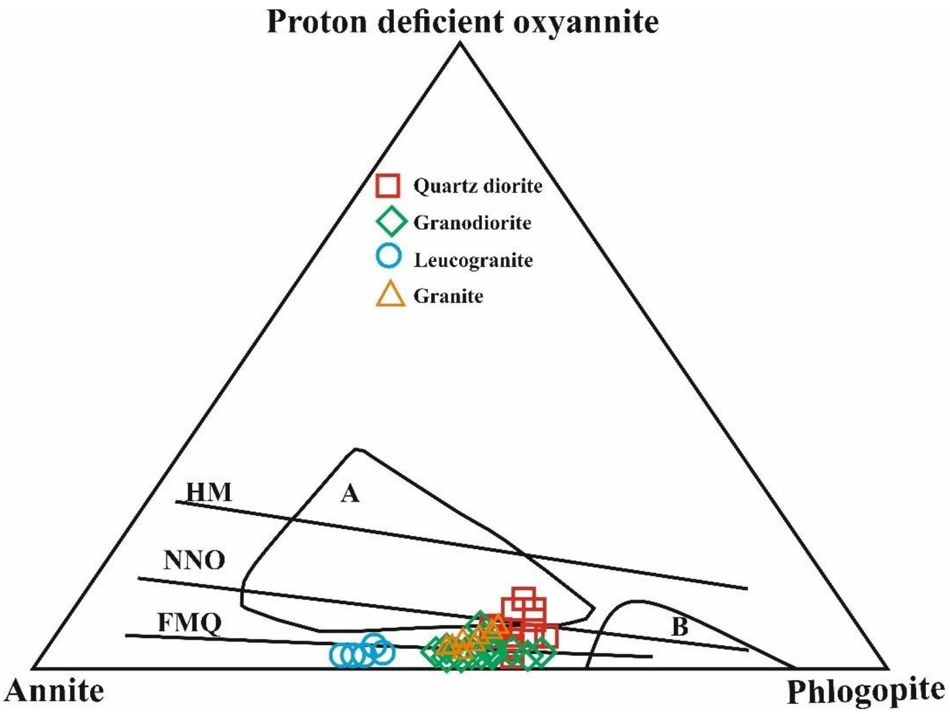

Figure 4.9: Fe^{2+} - Fe^{3+} - Mg^{2+} ternary plot after Beane (1974). A: Field of primary biotite; B: Field of hydrothermal biotites.

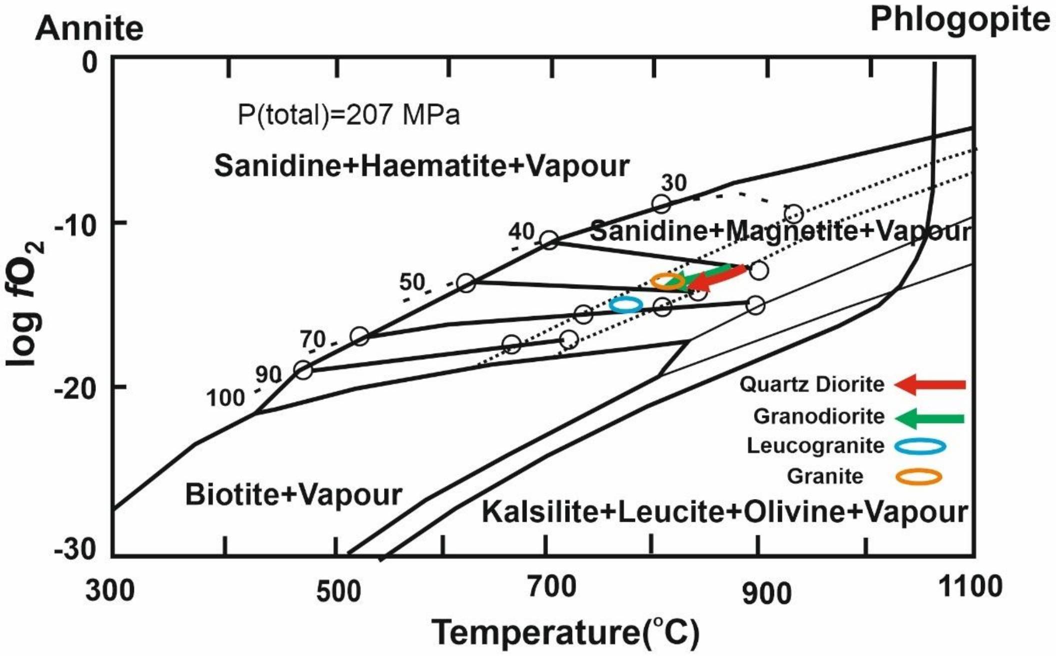

Figure 4.10: Temperature vs fO_2 binary diagram of experimentally calibrated biotite equilibria at constant P=2070 bars (Wones & Eugster, 1965).

5.4 FELDSPAR

The feldspar group of minerals has a wide thermo-chemical variation and, owing to its ubiquitous nature in almost all igneous rocks, they are inevitably fundamental in understanding the genesis and evolution as well as categorization/classification of the igneous rocks. Structurally, feldspars are tectosilicates based on aluminosilicate tetrahedra, whereby each tetrahedron consists of an aluminum or silicon ion linked by four oxygen ions to form a three-dimensional network. Chemically, the composition of feldspars can be expressed in terms of its three endmembers: orthoclase ($KAlSi_3O_8$), albite ($NaAlSi_3O_8$), anorthite ($CaAl_2Si_2O_8$). Solid solution occurs between the end-members, where solid solutions between orthoclase and albite are called alkali feldspars, and those between albite and anorthite are called plagioclase feldspars. The general formula of feldspar is XZ_4O_8, where X= Ca, Na, K, and Z = Si, Al.

5.4.1 COMPOSITION AND CLASSIFICATION OF FELDSPAR

The obtained chemical composition and calculated structural formulae (based on 8 oxygen atoms) for plagioclase feldspars from the representative samples are summarised in Table 4.3. The compositions of plagioclase and K-feldspar are classified and plotted in terms of end-members Or-An-Ab (Figure 4.11)

Composition of plagioclase in the quartz diorite varies from $An_{29.87}Ab_{63.55}Or_{0}$–$An_{36.34}Ab_{69.62}Or_{0.69}$, and that of granodiorite varies between $An_{22.31}Ab_{67.41}Or_{0.0}$-$An_{32.09}Ab_{75.82}Or_{2.11}$), mostly classifying as oligoclase and andesine with the exception of two albitic granitoids (E13 & E4). The plagioclases in the albitic field are comparably more altered and sericitized than the plagioclases in the oligoclase-andesine field. Plagioclase of granite and leucogranite also classifies as oligoclase and andesine with An-Ab-Or values varying from $An_{26.81}Ab_{65.92}Or_{0.66}$-$An_{32.41}Ab_{72.3}Or_{1.90}$ and $An_{20.78}Ab_{71.47}Or_{0.41}$-$An_{27.56}Ab_{78.88}Or_{1.48}$, respectively. Plagioclase of leucogranite also classifies as oligoclase and andesine with An-Ab-Or values varying from $An_{18.27}Ab_{65.92}Or_{0}$-$An_{32.41}Ab_{78.88}Or_{1.90}$. Plagioclases of quartz diorite are mostly andesine, while those of granodiorite, granite, and leucogranite are mostly oligoclase. A generally consistent range of $An_{18.27}$ (oligoclase) to $An_{36.34}$ (andesine) has been observed for all the granitoids except for a notably low An content of An_0 to $An_{5.64}$ (albitic) observed in the highly altered samples. Compositions of K-feldspars of quartz diorite, granodiorite, and leucogranites are generally equivocally orthoclase in composition, and the Or-Ab-An values range from $Or_{84.31}Ab_{3.42}An_0$ to $Or_{96.58}Ab_{14.73}An_{0.01}$.

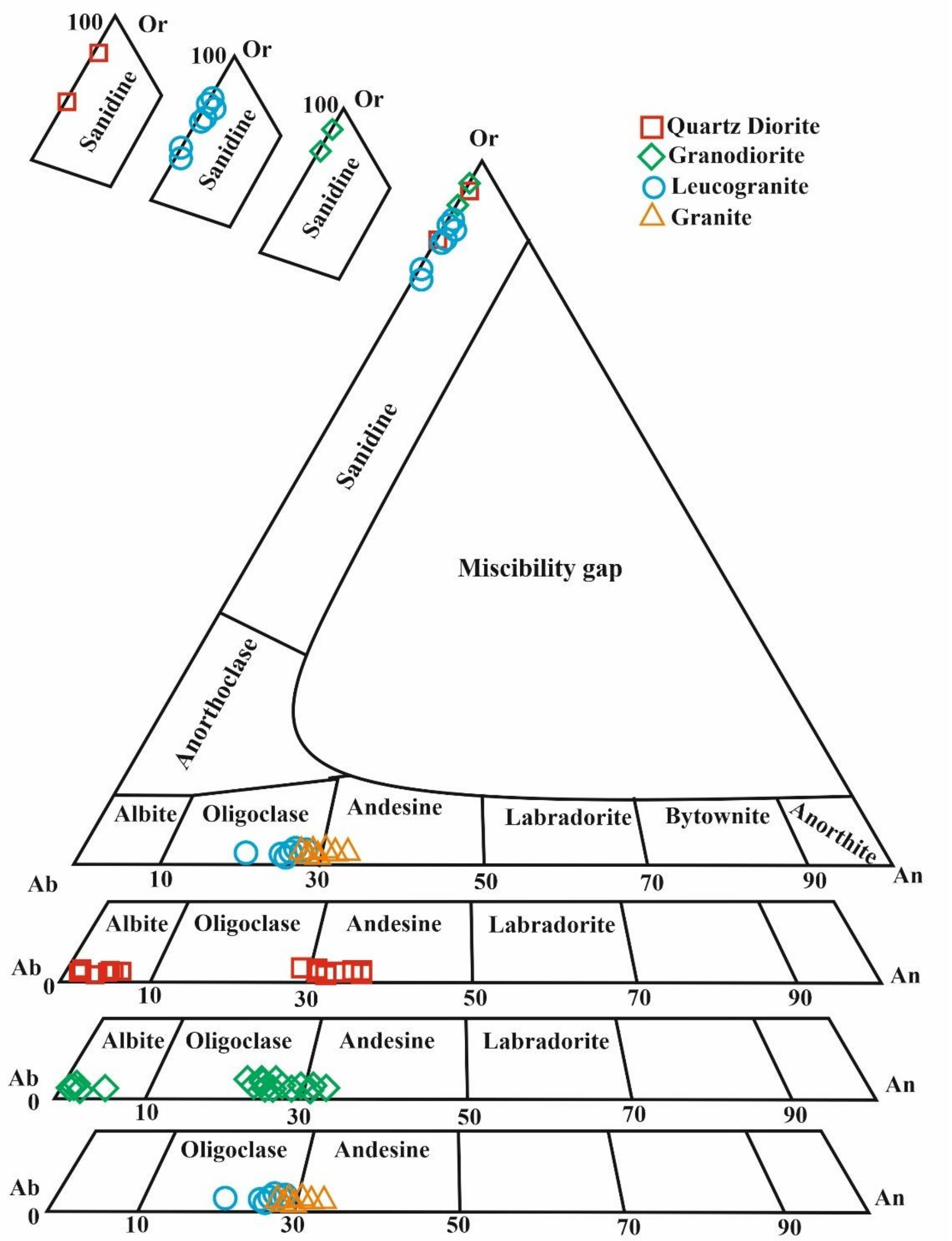

Figure 4.11: Compositional variation of plagioclase from Dibang Valley granitoids in terms of Ab-An-Or components.

Table 4.1: Electron micro probe analysis (wt %) and structural formulae of amphiboles from granitoids of Dibang Valley, Arunachal Pradesh

	QUARTZ DIORITE															
Sample no.	**D2 (2)**	**D2 (6)**	**D2 (7)**	**D2 (8)**	**D2 (9)**	**D2 (10)**	**D2 (11)**	**D2 (12)**	**M1 (1)**	**M1 (2)**	**M1 (3)**	**M1 (4)**	**M1 (6)**	**M1 (7)**	**M1 (9)**	**M1 (15)**
SiO_2	43.12	42.68	43.11	44.16	43.75	43.35	44.68	42.66	43.95	43.65	43.69	43.24	44.02	43.92	43.27	43.66
TiO_2	0.73	0.88	0.80	0.69	0.63	0.40	0.28	0.18	0.35	0.34	0.68	0.64	0.56	0.46	0.50	0.53
Al_2O_3	11.94	11.48	11.42	11.39	11.73	11.34	11.12	11.87	11.05	11.14	10.94	11.17	10.75	10.65	10.69	10.83
V_2O_3	0.08	0.08	0.09	0.00	0.00	0.00	0.00	0.00	0.00	0.00	0.00	0.00	0.00	0.07	0.00	0.00
Cr_2O_3	0.03	0.00	0.03	0.00	0.00	0.00	0.00	0.00	0.00	0.00	0.00	0.00	0.00	0.00	0.00	0.00
FeO	18.40	17.50	17.38	16.36	16.73	16.56	16.39	16.75	15.43	15.78	15.41	15.38	15.49	16.18	14.51	14.51
MnO	0.52	0.49	0.48	0.26	0.25	0.48	0.57	0.37	0.34	0.35	0.32	0.20	0.20	0.24	0.24	0.16
MgO	8.96	8.97	8.89	9.62	9.57	9.60	9.62	8.92	10.03	9.87	10.14	10.01	10.52	10.03	10.00	10.14
CaO	10.17	10.60	10.34	10.43	9.90	10.29	10.21	10.32	10.68	10.60	10.76	10.72	10.10	10.78	10.69	10.62
Na_2O	1.58	1.44	1.38	1.49	1.49	1.40	1.46	1.44	1.44	1.47	1.37	1.52	1.52	1.51	1.44	1.46
K_2O	0.49	0.59	0.64	0.43	0.50	0.53	0.50	0.45	0.61	0.73	0.67	0.61	0.53	0.52	0.59	0.65
F	0.02	0.00	0.05	0.00	0.00	0.11	0.15	0.05	0.17	0.18	0.23	0.24	0.10	0.26	0.18	0.17
Cl	0.01	0.00	0.01	0.00	0.00	0.04	0.02	0.00	0.00	0.00	0.00	0.00	0.00	0.00	0.00	0.00
O=F,Cl	0.01	0.00	0.02	0.00	0.00	0.06	0.07	0.02	0.07	0.08	0.10	0.10	0.04	0.11	0.08	0.07
Total	**96.04**	**94.71**	**94.60**	**94.83**	**94.52**	**94.04**	**94.93**	**92.99**	**93.99**	**94.03**	**94.12**	**93.64**	**93.75**	**94.51**	**92.04**	**92.66**
Structural formula based on 23 oxygen																
Si	6.54	6.54	6.60	6.67	6.64	6.62	6.74	6.57	6.69	6.66	6.65	6.62	6.69	6.68	6.74	6.74
Al^{IV}	1.46	1.46	1.40	1.33	1.36	1.38	1.26	1.43	1.31	1.34	1.35	1.38	1.31	1.32	1.26	1.26
ΣT=8.00	**8.00**	**8.00**	**8.00**	**8.00**	**8.00**	**8.00**	**8.00**	**8.00**	**8.00**	**8.00**	**8.00**	**8.00**	**8.00**	**8.00**	**8.00**	**8.00**
Al^{VI}	0.67	0.61	0.66	0.70	0.73	0.66	0.72	0.73	0.67	0.66	0.62	0.64	0.62	0.59	0.70	0.71
Ti	0.08	0.10	0.09	0.08	0.07	0.05	0.03	0.02	0.04	0.04	0.08	0.07	0.06	0.05	0.06	0.06
Cr	0.00	0.00	0.00	0.00	0.00	0.00	0.00	0.00	0.00	0.00	0.00	0.00	0.00	0.00	0.00	0.00
Fe^{3+}	0.46	0.56	0.56	0.53	0.58	0.63	0.52	0.74	0.53	0.57	0.60	0.59	0.67	0.60	0.35	0.40
Mg	2.03	2.05	2.03	2.17	2.17	2.18	2.16	2.05	2.28	2.24	2.30	2.29	2.38	2.27	2.32	2.33
Fe^{2+}	1.88	1.69	1.66	1.54	1.54	1.49	1.55	1.42	1.44	1.44	1.36	1.38	1.30	1.45	1.54	1.48
Mn	0.07	0.06	0.06	0.03	0.03	0.06	0.07	0.05	0.04	0.05	0.04	0.03	0.03	0.03	0.03	0.02
ΣC=5.00	**5.00**	**5.00**	**5.00**	**5.00**	**5.00**	**5.00**	**5.00**	**5.00**	**5.00**	**5.00**	**5.00**	**5.00**	**5.00**	**5.00**	**5.00**	**5.00**
ΔC	0.19	0.07	0.07	0.05	0.12	0.06	0.06	0.00	0.00	0.00	0.00	0.00	0.06	0.00	0.00	0.00

Ca	1.65	1.74	1.70	1.69	1.61	1.68	1.65	1.70	1.74	1.73	1.76	1.76	1.64	1.76	1.78	1.76
Na	0.16	0.19	0.23	0.26	0.27	0.25	0.29	0.30	0.26	0.27	0.24	0.24	0.29	0.24	0.22	0.24
ΣB=2.00	**2.00**	**2.00**	**2.00**	**2.00**	**2.00**	**2.00**	**2.00**	**2.00**	**2.00**	**2.00**	**2.00**	**2.00**	**2.00**	**2.00**	**2.00**	**2.00**
Na	0.30	0.24	0.18	0.18	0.17	0.16	0.14	0.13	0.17	0.17	0.16	0.21	0.16	0.20	0.22	0.19
K	0.09	0.12	0.12	0.08	0.10	0.10	0.10	0.09	0.12	0.14	0.13	0.12	0.10	0.10	0.12	0.13
ΣA=0.00-1.00	**0.40**	**0.36**	**0.30**	**0.26**	**0.27**	**0.27**	**0.24**	**0.22**	**0.29**	**0.31**	**0.29**	**0.33**	**0.26**	**0.30**	**0.33**	**0.32**
Total cations	15.40	15.36	15.30	15.26	15.27	15.27	15.24	15.22	15.29	15.31	15.29	15.33	15.26	15.30	15.33	15.32
Na^B	0.16	0.19	0.23	0.26	0.27	0.25	0.29	0.30	0.26	0.27	0.24	0.24	0.29	0.24	0.22	0.24
(Na+K)^A	0.40	0.36	0.30	0.26	0.27	0.27	0.24	0.22	0.29	0.31	0.29	0.33	0.26	0.30	0.33	0.32
Ca^B	1.65	1.74	1.70	1.69	1.61	1.68	1.65	1.70	1.74	1.73	1.76	1.76	1.64	1.76	1.78	1.76
(Ca+Na)^B	1.81	1.93	1.93	1.95	1.88	1.94	1.94	2.00	2.00	2.00	2.00	2.00	1.94	2.00	2.00	2.00
Al mol fraction (I)	0.16	0.16	0.16	0.16	0.16	0.16	0.15	0.17	0.15	0.16	0.15	0.16	0.15	0.15	0.15	0.15
Fe#	0.54	0.52	0.52	0.49	0.50	0.49	0.49	0.51	0.46	0.47	0.46	0.46	0.45	0.48	0.45	0.45
Mg#	0.46	0.48	0.48	0.51	0.50	0.51	0.51	0.49	0.54	0.53	0.54	0.54	0.55	0.52	0.55	0.55
R	0.20	0.25	0.25	0.26	0.27	0.30	0.25	0.34	0.27	0.28	0.31	0.30	0.34	0.29	0.18	0.21
Mg/(Mg+Fe^{2+})	0.52	0.55	0.55	0.58	0.58	0.60	0.58	0.59	0.61	0.61	0.63	0.62	0.65	0.61	0.60	0.61
Al^t	2.13	2.07	2.06	2.03	2.09	2.04	1.98	2.15	1.98	2.00	1.96	2.02	1.93	1.91	1.96	1.97

** I= $Al^t/(Al^t+Si+Mg+Fe^t)$; Fe# = $Fe^t/(Mg+Fe^t)$; Mg# = $Mg/(Mg+Fe^t)$; R= $Fe^{3+}/(Fe^{3+}+Fe^{2+})$; $Al^t= (Al^{IV}+Al^{VI})$

Contd…Table 4.1: Electron micro probe analysis (wt %) and structural formulae of amphiboles from granitoids of Dibang Valley, Arunachal Pradesh

	QUARTZ DIORITE														
Sample no.	**E13 (1)**	**E13 (3)**	**E13 (4)**	**E13 (5)**	**E13 (6)**	**E13 (7)**	**E13 (9)**	**E13 (11)**	**E13 (15)**	**E13 (16)**	**E13 (19)**	**E13 (20)**	**E13 (21)**	**E13 (22)**	**E13 (26)**
SiO$_2$	48.45	45.33	47.24	47.52	42.21	42.16	42.79	42.87	42.68	42.62	42.26	41.73	42.70	41.94	42.73
TiO$_2$	0.27	0.49	0.40	0.42	0.63	0.66	0.67	0.65	0.63	0.63	0.70	0.66	0.69	0.63	0.68
Al$_2$O$_3$	7.32	10.38	9.20	8.84	12.84	12.35	13.00	13.04	12.93	12.64	12.93	13.39	13.03	13.66	12.32
V$_2$O$_3$	0.05	0.06	0.12	0.11	0.17	0.06	0.11	0.02	0.12	0.08	0.14	0.08	0.17	0.09	0.00
Cr$_2$O$_3$	0.05	0.12	0.03	0.05	0.00	0.00	0.01	0.06	0.00	0.03	0.01	0.03	0.01	0.60	0.02
FeO	12.08	13.64	12.27	13.24	14.99	14.44	15.14	14.36	15.64	15.40	14.81	14.74	15.45	15.62	14.46

MnO	0.37	0.23	0.18	0.34	0.29	0.35	0.24	0.27	0.38	0.24	0.32	0.30	0.11	0.34	0.33
MgO	14.67	12.29	13.08	13.32	10.80	10.86	10.50	10.23	10.68	10.63	10.38	10.40	10.53	9.85	10.70
CaO	11.63	11.67	11.39	11.52	11.29	11.32	11.47	11.65	11.34	11.68	11.08	11.15	11.73	11.30	10.84
Na_2O	0.20	0.47	0.30	0.36	0.64	0.59	0.60	0.68	0.59	1.86	1.83	1.86	1.82	1.76	1.92
K_2O	0.20	0.47	0.30	0.36	0.64	0.59	0.60	0.68	0.59	0.58	0.59	0.66	0.61	0.85	0.66
F	0.00	0.01	0.00	0.00	0.03	0.00	0.01	0.03	0.03	0.04	0.03	0.13	0.00	0.00	0.00
Cl	0.04	0.05	0.04	0.04	0.02	0.04	0.07	0.06	0.04	0.02	0.03	0.07	0.03	0.03	0.04
O=F,Cl	0.01	0.02	0.01	0.01	0.02	0.01	0.02	0.02	0.02	0.02	0.02	0.07	0.01	0.01	0.01
Total	**96.38**	**96.34**	**95.83**	**97.18**	**95.63**	**94.58**	**96.55**	**95.56**	**96.93**	**96.42**	**95.07**	**95.12**	**96.86**	**96.67**	**94.70**
Structural formula based on 23 oxygen															
Si	7.06	6.70	6.95	6.92	6.36	6.39	6.39	6.46	6.37	6.39	6.39	6.31	6.37	6.30	6.46
Al^{IV}	0.94	1.30	1.05	1.08	1.64	1.61	1.61	1.54	1.63	1.61	1.61	1.69	1.63	1.70	1.54
ΣT=8.00	**8.00**	**8.00**	**8.00**	**8.00**	**8.00**	**8.00**	**8.00**	**8.00**	**8.00**	**8.00**	**8.00**	**8.00**	**8.00**	**8.00**	**8.00**
Al^{VI}	0.32	0.51	0.55	0.44	0.64	0.60	0.68	0.78	0.64	0.62	0.69	0.70	0.66	0.72	0.65
Ti	0.03	0.05	0.04	0.05	0.07	0.07	0.08	0.07	0.07	0.07	0.08	0.07	0.08	0.07	0.08
Cr	0.01	0.01	0.00	0.01	0.00	0.00	0.00	0.01	0.00	0.00	0.00	0.00	0.00	0.07	0.00
Fe^{3+}	0.42	0.42	0.31	0.38	0.54	0.60	0.49	0.30	0.45	0.49	0.56	0.60	0.50	0.44	0.56
Mg	3.19	2.71	2.87	2.89	2.43	2.46	2.34	2.30	2.38	2.37	2.34	2.35	2.34	2.21	2.41
Fe^{2+}	1.05	1.27	1.21	1.23	1.35	1.23	1.40	1.51	1.50	1.44	1.31	1.26	1.43	1.52	1.26
Mn	0.05	0.03	0.02	0.04	0.04	0.05	0.03	0.03	0.05	0.03	0.04	0.04	0.01	0.04	0.04
ΣC=5.00	**5.00**	**5.00**	**5.00**	**5.00**	**5.00**	**5.00**	**5.00**	**5.00**	**5.00**	**5.00**	**5.00**	**5.00**	**5.00**	**5.00**	**5.00**
ΔC	0.06	0.00	0.00	0.04	0.07	0.01	0.02	0.00	0.09	0.02	0.03	0.03	0.02	0.08	0.01
Ca	1.82	1.85	1.80	1.80	1.82	1.84	1.84	1.88	1.81	1.87	1.79	1.81	1.87	1.82	1.76
Na	0.13	0.15	0.20	0.16	0.11	0.15	0.15	0.12	0.10	0.10	0.18	0.16	0.10	0.11	0.23
ΣB=2.00	**2.00**	**2.00**	**2.00**	**2.00**	**2.00**	**2.00**	**2.00**	**2.00**	**2.00**	**2.00**	**2.00**	**2.00**	**2.00**	**2.00**	**2.00**
Na	0.23	0.31	0.25	0.24	0.40	0.36	0.41	0.37	0.45	0.44	0.36	0.38	0.43	0.41	0.33
K	0.04	0.09	0.06	0.07	0.12	0.12	0.11	0.13	0.11	0.11	0.11	0.13	0.12	0.16	0.13
ΣA=0.00-1.00	**0.26**	**0.40**	**0.30**	**0.31**	**0.53**	**0.48**	**0.53**	**0.50**	**0.57**	**0.55**	**0.47**	**0.51**	**0.54**	**0.57**	**0.46**
Total cations	15.26	15.40	15.30	15.31	15.53	15.48	15.53	15.50	15.57	15.55	15.47	15.51	15.54	15.57	15.46
Na^B	0.13	0.15	0.20	0.16	0.11	0.15	0.15	0.12	0.10	0.10	0.18	0.16	0.10	0.11	0.23
$(Na+K)^A$	0.26	0.40	0.30	0.31	0.53	0.48	0.53	0.50	0.57	0.55	0.47	0.51	0.54	0.57	0.46
Ca^B	1.82	1.85	1.80	1.80	1.82	1.84	1.84	1.88	1.81	1.87	1.79	1.81	1.87	1.82	1.76
$(Ca+Na)^B$	1.94	2.00	2.00	1.96	1.93	1.99	1.98	2.00	1.91	1.98	1.97	1.97	1.98	1.92	1.99

Al mol fraction (I)	0.10	0.14	0.12	0.12	0.18	0.17	0.18	0.18	0.18	0.17	0.18	0.18	0.18	0.19	0.17
Fe#	0.32	0.38	0.34	0.36	0.44	0.43	0.45	0.44	0.45	0.45	0.44	0.44	0.45	0.47	0.43
Mg#	0.68	0.62	0.66	0.64	0.56	0.57	0.55	0.56	0.55	0.55	0.56	0.56	0.55	0.53	0.57
R	0.29	0.25	0.20	0.24	0.29	0.33	0.26	0.17	0.23	0.25	0.30	0.32	0.26	0.22	0.31
$Mg/(Mg+Fe^{+2})$	0.75	0.68	0.70	0.70	0.64	0.67	0.63	0.60	0.61	0.62	0.64	0.65	0.62	0.59	0.66
Al^t	1.26	1.81	1.60	1.52	2.28	2.21	2.29	2.32	2.27	2.23	2.30	2.39	2.29	2.42	2.19

** I= $Al^t/(Al^t+Si+Mg+Fe^t)$; Fe# = $Fe^t/(Mg+Fe^t)$; Mg# = $Mg/(Mg+Fe^t)$; R= $Fe^{3+}/(Fe^{3+}+Fe^{2+})$; $Al^t= (Al^{IV}+Al^{VI})$

Contd… Table 4.1: Electron micro probe analysis (wt %) and structural formulae of amphiboles from granitoids of Dibang Valley, Arunachal Pradesh

	GRANODIORITE														
Sample no.	**E4 (1)**	**E4 (2)**	**E4 (5)**	**E4 (11)**	**E4 (13)**	**E4 (14)**	**E4 (15)**	**E4 (19)**	**D6a (1)**	**D6a (2)**	**D6a (3)**	**D6a (4)**	**D6a (6)**	**D6a (10)**	**D6a (11)**
SiO_2	45.01	44.80	43.96	45.42	45.07	44.62	46.01	42.84	41.62	41.18	41.21	40.27	40.80	41.78	40.82
TiO_2	1.27	0.86	1.24	1.43	1.56	1.08	0.83	0.76	1.40	1.38	1.21	1.12	1.36	1.24	1.18
Al_2O_3	9.04	9.55	10.29	9.00	9.13	9.59	8.79	10.27	10.01	10.00	10.21	11.15	10.12	10.18	10.61
V_2O_3	0.00	0.00	0.00	0.00	0.00	0.00	0.00	0.18	0.12	0.05	0.12	0.25	0.07	0.07	0.00
Cr_2O_3	0.05	0.00	0.01	0.00	0.00	0.00	0.01	0.02	0.04	0.02	0.02	0.07	0.04	0.02	0.02
FeO	15.24	14.41	15.25	15.29	14.78	14.83	13.69	14.40	19.79	19.23	19.44	20.15	18.62	19.40	19.97
MnO	0.54	0.51	0.44	0.51	0.39	0.53	0.34	0.20	0.47	0.44	0.34	0.25	0.55	0.27	0.58
MgO	12.11	12.15	11.59	11.94	12.16	11.67	12.79	11.78	8.62	8.76	8.84	8.01	8.61	8.61	8.38
CaO	11.46	11.33	11.22	11.28	11.59	11.20	11.83	11.14	11.20	10.79	11.38	11.37	11.08	11.12	11.20
Na_2O	1.38	1.35	1.62	1.37	1.43	1.41	1.41	1.59	1.35	1.52	1.39	1.45	1.50	1.40	1.42
K_2O	0.91	0.90	1.09	1.05	1.02	1.05	0.84	0.96	1.25	1.18	1.30	1.41	1.30	1.31	1.30
F	0.00	0.08	0.12	0.17	0.14	0.03	0.00	0.19	0.30	0.17	0.21	0.16	0.38	0.32	0.21
Cl	0.07	0.07	0.11	0.08	0.06	0.09	0.09	0.11	0.07	0.08	0.06	0.07	0.08	0.10	0.06
O=F,Cl	0.02	0.05	0.08	0.09	0.07	0.03	0.02	0.10	0.14	0.09	0.10	0.08	0.18	0.16	0.10
Total	**97.08**	**95.97**	**96.87**	**97.46**	**97.24**	**96.06**	**96.60**	**94.32**	**96.10**	**94.71**	**95.62**	**95.66**	**94.33**	**95.65**	**95.65**
Structural formula based on 23 oxygen															
Si	6.70	6.70	6.58	6.75	6.70	6.69	6.81	6.53	6.46	6.44	6.41	6.30	6.42	6.48	6.36

Al^{IV}	1.30	1.30	1.42	1.25	1.30	1.31	1.19	1.47	1.54	1.56	1.59	1.70	1.58	1.52	1.64
ΣT=8.00	**8.00**	**8.00**	**8.00**	**8.00**	**8.00**	**8.00**	**8.00**	**8.00**	**8.00**	**8.00**	**8.00**	**8.00**	**8.00**	**8.00**	**8.00**
Al^{VI}	0.29	0.39	0.39	0.32	0.30	0.39	0.35	0.37	0.29	0.28	0.28	0.35	0.29	0.34	0.31
Ti	0.14	0.10	0.14	0.16	0.17	0.12	0.09	0.09	0.16	0.16	0.14	0.13	0.16	0.14	0.14
Cr	0.01	0.00	0.00	0.00	0.00	0.00	0.00	0.00	0.00	0.00	0.00	0.01	0.00	0.00	0.00
Fe^{3+}	0.37	0.43	0.45	0.37	0.38	0.43	0.34	0.74	0.62	0.73	0.69	0.75	0.71	0.71	0.64
Mg	2.69	2.71	2.58	2.64	2.69	2.61	2.82	2.68	1.99	2.04	2.05	1.87	2.02	1.99	1.95
Fe^{2+}	1.53	1.38	1.46	1.53	1.45	1.43	1.35	1.09	1.94	1.78	1.84	1.89	1.74	1.81	1.97
Mn	0.07	0.07	0.06	0.06	0.05	0.07	0.04	0.03	0.06	0.06	0.04	0.03	0.07	0.04	0.08
ΣC=5.00	**5.00**	**5.00**	**5.00**	**5.00**	**5.00**	**5.00**	**5.00**	**5.00**	**5.00**	**5.00**	**5.00**	**5.00**	**5.00**	**5.00**	**5.00**
ΔC	0.09	0.06	0.08	0.09	0.06	0.05	0.00	0.00	0.08	0.06	0.04	0.03	0.00	0.02	0.08
Ca	1.83	1.82	1.80	1.79	1.85	1.80	1.88	1.82	1.86	1.81	1.90	1.90	1.87	1.85	1.87
Na	0.08	0.12	0.12	0.12	0.10	0.16	0.12	0.18	0.06	0.13	0.06	0.07	0.13	0.13	0.05
ΣB=2.00	**2.00**	**2.00**	**2.00**	**2.00**	**2.00**	**2.00**	**2.00**	**2.00**	**2.00**	**2.00**	**2.00**	**2.00**	**2.00**	**2.00**	**2.00**
Na	0.32	0.27	0.35	0.28	0.32	0.25	0.28	0.29	0.34	0.33	0.36	0.37	0.32	0.29	0.38
K	0.17	0.17	0.21	0.20	0.19	0.20	0.16	0.19	0.25	0.24	0.26	0.28	0.26	0.26	0.26
ΣA=0.00-1.00	**0.50**	**0.44**	**0.56**	**0.48**	**0.51**	**0.46**	**0.44**	**0.47**	**0.59**	**0.56**	**0.62**	**0.65**	**0.58**	**0.55**	**0.64**
Total cations	15.50	15.44	15.56	15.48	15.51	15.46	15.44	15.47	15.59	15.56	15.62	15.65	15.58	15.55	15.64
Na^{B}	0.08	0.12	0.12	0.12	0.10	0.16	0.12	0.18	0.06	0.13	0.06	0.07	0.13	0.13	0.05
$(Na+K)^{A}$	0.50	0.44	0.56	0.48	0.51	0.46	0.44	0.47	0.59	0.56	0.62	0.65	0.58	0.55	0.64
Ca^{B}	1.83	1.82	1.80	1.79	1.85	1.80	1.88	1.82	1.86	1.81	1.90	1.90	1.87	1.85	1.87
$(Ca+Na)^{B}$	1.91	1.94	1.92	1.91	1.94	1.95	2.00	2.00	1.92	1.94	1.96	1.97	2.00	1.98	1.92
Al mol fraction (I)	0.12	0.13	0.14	0.12	0.12	0.13	0.12	0.14	0.14	0.14	0.15	0.16	0.15	0.14	0.15
Fe#	0.41	0.40	0.42	0.42	0.41	0.42	0.38	0.41	0.56	0.55	0.55	0.59	0.55	0.56	0.57
Mg#	0.59	0.60	0.58	0.58	0.59	0.58	0.62	0.59	0.44	0.45	0.45	0.41	0.45	0.44	0.43
R	0.19	0.24	0.23	0.19	0.21	0.23	0.20	0.41	0.24	0.29	0.27	0.28	0.29	0.28	0.24
$Mg/(Mg+Fe^{+2})$	0.64	0.66	0.64	0.63	0.65	0.65	0.68	0.71	0.51	0.53	0.53	0.50	0.54	0.52	0.50
Al^{t}	1.59	1.68	1.81	1.58	1.60	1.70	1.53	1.85	1.83	1.84	1.87	2.05	1.88	1.86	1.95

** $I= Al^{t}/(Al^{t}+Si+Mg+Fe^{t})$; $Fe\# = Fe^{t}/(Mg+Fe^{t})$; $Mg\# = Mg/(Mg+Fe^{t})$; $R= Fe^{3+}/(Fe^{3+}+Fe^{2+})$; $Al^{t}= (Al^{IV}+Al^{VI})$

Contd…Table 4.1: Electron micro probe analysis (wt %) and structural formulae of amphiboles from granitoids of Dibang Valley, Arunachal Pradesh.

	GRANITE						
Sample no.	**D7b (1)**	**D7b (2)**	**D7b (3)**	**D7b (5)**	**D7b (6)**	**D7b (7)**	**D7b (8)**
SiO_2	40.83	40.76	40.88	41.08	41.18	40.75	40.39
TiO_2	1.22	1.25	1.04	1.27	1.18	1.03	1.10
Al_2O_3	11.17	11.12	11.00	10.78	10.32	11.31	11.36
V_2O_3	0.23	0.35	0.00	0.03	0.13	0.00	0.08
Cr_2O_3	0.06	0.05	0.01	0.02	0.00	0.00	0.00
FeO	19.70	18.87	20.56	20.64	19.96	20.18	20.54
MnO	0.59	0.69	0.46	0.54	0.54	0.82	0.92
MgO	7.76	7.53	7.62	7.65	7.94	7.46	7.31
CaO	11.52	11.50	10.97	11.17	11.29	11.44	11.45
Na_2O	1.45	1.39	1.36	1.43	1.41	1.37	1.44
K_2O	1.58	1.48	1.54	1.59	1.49	1.59	1.60
F	0.47	0.43	0.45	0.31	0.25	0.29	0.25
Cl	0.19	0.21	0.24	0.20	0.17	0.21	0.25
O=F,Cl	0.24	0.23	0.24	0.18	0.14	0.17	0.16
Total	**96.53**	**95.40**	**95.87**	**96.55**	**95.71**	**96.29**	**96.54**
Structural formula based on 23 oxygen							
Si	6.36	6.43	6.37	6.38	6.43	6.34	6.29
Al^{IV}	1.64	1.57	1.63	1.62	1.57	1.66	1.71
ΣT=8.00	**8.00**	**8.00**	**8.00**	**8.00**	**8.00**	**8.00**	**8.00**
Al^{VI}	0.41	0.49	0.39	0.35	0.33	0.41	0.38
Ti	0.14	0.15	0.12	0.15	0.14	0.12	0.13
Cr	0.01	0.01	0.00	0.00	0.00	0.00	0.00
Fe^{3+}	0.55	0.32	0.77	0.67	0.62	0.57	0.60
Mg	1.80	1.77	1.77	1.77	1.85	1.73	1.70
Fe^{2+}	2.02	2.17	1.91	2.01	1.99	2.06	2.07
Mn	0.08	0.09	0.06	0.07	0.07	0.11	0.12
ΣC=5.00	**5.00**	**5.00**	**5.00**	**5.00**	**5.00**	**5.00**	**5.00**

ΔC	0.00	0.00	0.03	0.02	0.00	0.00	0.00
Ca	1.92	1.94	1.83	1.86	1.89	1.91	1.91
Na	0.08	0.06	0.14	0.12	0.11	0.09	0.09
ΣB=2.00	**2.00**	**2.00**	**2.00**	**2.00**	**2.00**	**2.00**	**2.00**
Na	0.36	0.37	0.27	0.31	0.32	0.32	0.34
K	0.31	0.30	0.31	0.32	0.30	0.31	0.32
ΣA=0.00-1.00	**0.67**	**0.66**	**0.57**	**0.63**	**0.61**	**0.64**	**0.66**
Total cations	15.67	15.66	15.57	15.63	15.61	15.64	15.66
Na^B	0.08	0.06	0.14	0.12	0.11	0.09	0.09
$(Na+K)^A$	0.67	0.66	0.57	0.63	0.61	0.64	0.66
Ca^B	1.92	1.94	1.83	1.86	1.89	1.91	1.91
$(Ca+Na)^B$	2.00	2.00	1.97	1.98	2.00	2.00	2.00
Al mol fraction (I)	0.16	0.16	0.16	0.15	0.15	0.16	0.16
Fe#	0.59	0.58	0.60	0.60	0.59	0.60	0.61
Mg#	0.41	0.42	0.40	0.40	0.41	0.40	0.39
R	0.21	0.13	0.29	0.25	0.24	0.22	0.23
$Mg/(Mg+Fe^{+2})$	0.47	0.45	0.48	0.47	0.48	0.46	0.45
Al^t	2.05	2.07	2.02	1.97	1.90	2.07	2.09

** I= $Al^t/(Al^t+Si+Mg+Fe^t)$; Fe# = $Fe^t/(Mg+Fe^t)$; Mg# = $Mg/(Mg+Fe^t)$; R= $Fe^{3+}/(Fe^{3+}+Fe^{2+})$; $Al^t= (Al^{IV}+Al^{VI})$

Table 4.2: Representative electron probe micro-analysis (wt%) and structural formulae of biotites from granitoids of Dibang Valley, Arunachal Pradesh

	QUARTZ DIORITE														
Sample No.	**D2 (1)**	**D2 (2)**	**D2 (3)**	**D2 (4)**	**D2 (5)**	**D2 (6)**	**D2 (7)**	**D2 (8)**	**D2 (9)**	**D2 (10)**	**M1 (1)**	**M1 (2)**	**M1 (3)**	**M1 (4)**	**M1 (5)**
SiO_2	36.69	36.13	37.11	37.66	36.49	37.44	36.64	37.29	37.01	37.07	37.15	37.40	37.95	37.55	36.99
Al_2O_3	15.46	15.27	15.86	16.04	15.36	15.74	15.95	16.10	15.65	15.40	15.33	15.32	16.04	15.69	15.19
TiO_2	2.26	2.54	2.31	2.20	2.17	1.66	2.15	1.66	1.95	2.11	2.15	1.95	1.18	2.37	2.27
Cr_2O_3	0.01	0.04	0.01	0.21	0.03	0.14	0.11	0.13	0.13	0.16	0.11	0.01	0.15	0.13	0.11
FeO	18.55	17.79	17.99	17.61	17.72	16.82	17.21	18.25	16.94	17.05	16.63	16.19	15.98	15.97	16.44
MnO	0.16	0.20	0.16	0.06	0.14	0.19	0.12	0.01	0.08	0.14	0.01	0.18	0.05	0.07	0.12
MgO	10.43	10.73	11.08	11.12	10.41	10.97	10.79	11.35	11.52	10.97	11.85	12.05	12.65	12.13	11.74
CaO	0.02	0.02	0.04	0.04	0.15	0.02	0.02	0.00	0.03	0.03	0.06	0.08	0.07	0.00	0.10
Na_2O	0.06	0.20	0.15	0.20	0.17	0.23	0.14	0.17	0.20	0.21	0.19	0.16	0.20	0.12	0.16
BaO	0.00	0.00	0.00	0.00	0.00	0.00	0.00	0.00	0.00	0.00	0.00	0.00	0.00	0.00	0.00
K_2O	8.48	8.51	8.34	8.15	8.09	8.21	8.63	7.76	8.21	8.64	8.26	8.47	7.74	8.56	8.28
Total	**91.57**	**91.87**	**92.84**	**91.75**	**91.85**	**91.57**	**91.87**	**92.84**	**91.75**	**91.85**	**91.87**	**91.86**	**92.13**	**92.77**	**91.63**
Structural formula based on 11 oxygen															
Si	2.87	2.84	2.86	2.88	2.88	2.91	2.85	2.87	2.87	2.89	2.88	2.89	2.90	2.87	2.87
Al^{IV}	1.13	1.16	1.14	1.12	1.12	1.09	1.15	1.13	1.13	1.11	1.12	1.11	1.10	1.13	1.13
$\sum Z$	4.00	4.00	4.00	4.00	4.00	4.00	4.00	4.00	4.00	4.00	4.00	4.00	4.00	4.00	4.00
Al^{VI}	0.29	0.26	0.29	0.32	0.30	0.35	0.32	0.32	0.30	0.30	0.28	0.29	0.35	0.28	0.26
Fe^{3+}	0.03	0.00	0.00	0.07	0.12	0.22	0.12	0.02	0.07	0.16	0.07	0.10	0.12	0.08	0.08
Ti	0.13	0.15	0.13	0.13	0.13	0.10	0.13	0.10	0.11	0.12	0.12	0.11	0.07	0.14	0.13
Cr	0.00	0.00	0.00	0.01	0.00	0.01	0.01	0.01	0.01	0.01	0.01	0.00	0.01	0.01	0.01
Mg	1.21	1.26	1.27	1.27	1.22	1.27	1.25	1.30	1.33	1.27	1.37	1.39	1.44	1.38	1.36
Fe^{2+}	1.18	1.17	1.16	1.06	1.05	0.87	1.00	1.16	1.03	0.95	1.01	0.94	0.90	0.94	0.99
Mn	0.01	0.01	0.01	0.00	0.01	0.01	0.01	0.00	0.01	0.01	0.00	0.01	0.00	0.00	0.01
$\sum Y$	2.86	2.85	2.87	2.85	2.83	2.83	2.83	2.90	2.86	2.82	2.85	2.85	2.89	2.84	2.84
Na	0.01	0.03	0.02	0.03	0.03	0.03	0.02	0.03	0.03	0.03	0.03	0.02	0.03	0.02	0.02
K	0.85	0.85	0.82	0.79	0.81	0.81	0.86	0.76	0.80	0.86	0.82	0.84	0.76	0.83	0.82

$\sum X$	0.86	0.89	0.84	0.83	0.85	0.85	0.88	0.79	0.84	0.89	0.85	0.87	0.79	0.85	0.85
Fe^t/Fe^t+Mg	0.50	0.48	0.48	0.47	0.49	0.46	0.47	0.47	0.45	0.47	0.44	0.43	0.41	0.42	0.44
$Mg/Mg+Fe^t$	0.50	0.52	0.52	0.53	0.51	0.54	0.53	0.53	0.55	0.53	0.56	0.57	0.59	0.58	0.56
$Fe^{2+}/Fe^{2+}+Fe^{3+}$	0.97	1.00	1.00	0.94	0.90	0.80	0.89	0.99	0.93	0.86	0.94	0.90	0.88	0.92	0.92
$Fe^{3+}/Fe^{2+}+Fe^{3+}$	0.03	0.00	0.00	0.06	0.10	0.20	0.11	0.01	0.07	0.14	0.06	0.10	0.12	0.08	0.08
FeO^t/MgO	1.78	1.66	1.62	1.69	1.70	1.53	1.59	1.61	1.47	1.55	1.40	1.34	1.26	1.32	1.40
Al^t	1.42	1.42	1.43	1.44	1.42	1.44	1.47	1.45	1.43	1.41	1.4	1.4	1.45	1.41	1.39

**Fe^t= total iron per formula unit (pfu); FeO^t= total iron; $Al^t = (Al^{IV} + Al^{VI})$ pfu

Contd… Table 4.2: Representative electron probe micro-analysis (wt%) and structural formulae of biotites from granitoids of Dibang Valley, Arunachal Pradesh

	QUARTZ DIORITE					**GRANODIORITE**									
Sample No.	**M1 (6)**	**M1 (7)**	**M1 (8)**	**M1 (9)**	**M1 (10)**	**D4 (1)**	**D4 (2)**	**D4 (3)**	**D4 (4)**	**D4 (5)**	**D4 (6)**	**D4 (7)**	**D4 (8)**	**D4 (9)**	**D4 (10)**
SiO_2	38.38	36.91	36.95	35.84	36.91	36.78	36.36	35.98	36.06	35.43	35.07	36.67	36.25	35.93	36.29
Al_2O_3	15.51	15.16	15.00	14.70	15.09	15.80	16.15	15.71	15.32	15.66	15.59	16.15	15.88	15.63	15.83
TiO_2	2.77	2.31	2.37	2.00	1.93	2.84	2.75	2.84	2.88	2.76	2.75	2.68	3.02	3.04	2.62
Cr_2O_3	0.04	0.14	0.14	0.11	0.15	0.02	0.01	0.02	0.03	0.03	0.02	0.01	0.03	0.02	0.00
FeO	16.33	16.40	15.99	15.98	16.38	17.98	18.31	17.64	17.26	17.65	16.63	19.02	18.76	18.76	17.92
MnO	0.24	0.19	0.08	0.24	0.07	0.36	0.51	0.28	0.40	0.32	0.44	0.37	0.53	0.46	0.37
MgO	11.91	11.72	11.59	10.93	11.19	10.14	10.25	10.28	11.14	9.87	10.27	10.24	9.91	9.94	10.38
CaO	0.01	0.05	0.05	0.03	0.05	0.02	0.00	0.01	0.00	0.01	0.05	0.06	0.02	0.02	0.01
Na_2O	0.18	0.16	0.16	0.13	0.16	0.13	0.13	0.19	0.09	0.18	0.10	0.12	0.12	0.06	0.12
BaO	0.00	0.00	0.00	0.00	0.00	0.00	0.00	0.00	0.00	0.00	0.00	0.00	0.00	0.00	0.00
K_2O	8.19	8.39	8.59	8.46	8.39	9.31	9.00	8.97	8.78	8.78	8.83	9.14	8.99	9.25	9.31
Total	**93.65**	**91.52**	**91.07**	**88.71**	**90.49**	**93.54**	**93.60**	**92.12**	**92.18**	**90.87**	**89.92**	**94.60**	**93.65**	**93.30**	**92.98**
Structural formula based on 11 oxygen															
Si	2.90	2.87	2.89	2.88	2.90	2.84	2.81	2.82	2.81	2.81	2.81	2.81	2.81	2.80	2.82
Al^{IV}	1.10	1.13	1.11	1.12	1.10	1.16	1.19	1.18	1.19	1.19	1.19	1.19	1.19	1.20	1.18
$\sum Z$	4.00	4.00	4.00	4.00	4.00	4.00	4.00	4.00	4.00	4.00	4.00	4.00	4.00	4.00	4.00
Al^{VI}	0.28	0.26	0.27	0.28	0.30	0.28	0.28	0.26	0.22	0.28	0.28	0.27	0.25	0.23	0.27

Fe^{3+}	0.03	0.05	0.13	0.20	0.20	0.13	0.03	0.08	0.03	0.08	0.08	0.04	0.00	0.01	0.09
Ti	0.16	0.14	0.14	0.12	0.11	0.16	0.16	0.17	0.17	0.16	0.17	0.15	0.18	0.18	0.15
Cr	0.00	0.01	0.01	0.01	0.01	0.00	0.00	0.00	0.00	0.00	0.00	0.00	0.00	0.00	0.00
Mg	1.34	1.36	1.35	1.31	1.31	1.17	1.18	1.20	1.30	1.17	1.22	1.17	1.14	1.15	1.20
Fe^{2+}	1.00	1.02	0.91	0.87	0.88	1.03	1.15	1.07	1.09	1.09	1.03	1.18	1.21	1.21	1.07
Mn	0.02	0.01	0.01	0.02	0.00	0.02	0.03	0.02	0.03	0.02	0.03	0.02	0.03	0.03	0.02
∑ Y	2.83	2.85	2.82	2.81	2.82	2.79	2.83	2.81	2.84	2.81	2.81	2.83	2.82	2.82	2.82
Na	0.03	0.02	0.02	0.02	0.02	0.02	0.02	0.03	0.01	0.03	0.01	0.02	0.02	0.01	0.02
K	0.79	0.83	0.86	0.87	0.84	0.92	0.89	0.90	0.87	0.89	0.90	0.89	0.89	0.92	0.92
∑ X	0.82	0.86	0.89	0.89	0.87	0.94	0.91	0.92	0.89	0.92	0.92	0.92	0.91	0.93	0.94
Fe^t/Fe^t+Mg	0.43	0.44	0.44	0.45	0.45	0.50	0.50	0.49	0.47	0.50	0.48	0.51	0.52	0.51	0.49
$Mg/Mg+Fe^t$	0.57	0.56	0.56	0.55	0.55	0.50	0.50	0.50	0.53	0.50	0.52	0.49	0.48	0.49	0.51
$Fe^{2+}/Fe^{2+}+Fe^{3+}$	0.97	0.96	0.87	0.81	0.82	0.89	0.97	0.93	0.97	0.93	0.93	0.97	1.00	0.99	0.92
$Fe^{3+}/Fe^{2+}+Fe^{3+}$	0.03	0.04	0.13	0.19	0.18	0.11	0.03	0.07	0.03	0.07	0.07	0.03	0.00	0.01	0.08
FeO^t/MgO	1.37	1.40	1.38	1.46	1.46	1.77	1.79	1.72	1.55	1.79	1.62	1.86	1.89	1.89	1.73
Al^t	1.38	1.39	1.38	1.4	1.4	1.44	1.47	1.44	1.41	1.47	1.47	1.46	1.44	1.43	1.45

** Fe^t= total iron per formula unit (pfu); FeO^t= total iron; Al^t = (Al^{IV} + Al^{VI}) pfu

Contd… Table 4.2: Representative electron probe micro-analysis (wt%) and structural formulae of biotites from granitoids of Dibang Valley, Arunachal Pradesh

	GRANODIORITE										**LEUCOGRANITE**				
Sample No.	**D6a (1)**	**D6a (2)**	**D6a (3)**	**D6a (4)**	**D6a (5)**	**D6a (6)**	**D6a (7)**	**D6a (8)**	**D6a (9)**	**D6a (10)**	**ET22 (1)**	**ET22 (2)**	**ET22 (3)**	**ET22 (4)**	**ET22 (5)**
SiO_2	36.18	35.88	36.11	36.67	36.32	36.23	36.68	36.37	36.21	36.57	36.00	36.13	35.62	35.78	35.79
Al_2O_3	14.68	14.42	15.04	15.66	14.82	15.02	14.95	14.64	15.00	14.68	16.35	16.14	16.52	16.52	15.96
TiO_2	2.49	2.57	2.01	1.80	3.37	3.20	2.64	2.22	2.13	2.30	3.13	2.77	2.65	3.45	3.51
Cr_2O_3	0.02	0.05	0.03	0.02	0.04	0.04	0.02	0.01	0.05	0.03	0.10	0.07	0.22	0.00	0.00
FeO	17.89	17.29	20.53	20.10	18.89	19.19	21.15	16.38	20.43	19.36	22.82	23.36	23.11	21.75	22.34
MnO	0.40	0.33	0.25	0.37	0.23	0.37	0.21	0.24	0.32	0.37	0.09	0.10	0.32	0.15	0.27
MgO	11.50	12.06	10.55	10.56	9.79	9.98	10.38	12.88	10.32	11.35	7.34	8.14	8.09	7.66	7.77
CaO	0.00	0.02	0.06	0.11	0.03	0.03	0.07	0.02	0.07	0.00	0.01	0.06	0.04	0.00	0.00

Na_2O	0.14	0.15	0.10	0.16	0.20	0.13	0.17	0.13	0.15	0.11	0.16	0.18	0.00	0.15	0.11
BaO	0.00	0.00	0.00	0.00	0.00	0.00	0.00	0.00	0.00	0.00	0.00	0.00	0.00	0.00	0.00
K_2O	9.02	9.10	9.20	8.90	8.91	9.17	9.08	9.14	8.99	9.32	8.62	8.80	8.73	8.96	8.80
Total	**92.57**	**92.15**	**94.05**	**94.61**	**92.87**	**93.51**	**95.62**	**92.34**	**93.86**	**94.42**	**94.71**	**95.96**	**95.58**	**94.51**	**94.79**
Structural formula based on 11 oxygen															
Si	2.83	2.81	2.81	2.82	2.84	2.82	2.81	2.83	2.82	2.82	2.80	2.78	2.75	2.78	2.78
Al^{IV}	1.17	1.19	1.19	1.18	1.16	1.18	1.19	1.17	1.18	1.18	1.20	1.22	1.25	1.22	1.22
$\sum$ Z	4.00	4.00	4.00	4.00	4.00	4.00	4.00	4.00	4.00	4.00	4.00	4.00	4.00	4.00	4.00
Al^{VI}	0.18	0.15	0.19	0.24	0.20	0.20	0.16	0.17	0.20	0.16	0.29	0.24	0.26	0.29	0.24
Fe^{3+}	0.02	0.06	0.03	0.06	0.03	0.02	0.07	0.00	0.01	0.02	0.01	0.04	0.08	0.01	0.06
Ti	0.15	0.15	0.12	0.10	0.20	0.19	0.15	0.13	0.12	0.13	0.18	0.16	0.15	0.20	0.21
Cr	0.00	0.00	0.00	0.00	0.00	0.00	0.00	0.00	0.00	0.00	0.01	0.00	0.01	0.00	0.00
Mg	1.34	1.41	1.22	1.21	1.14	1.16	1.19	1.49	1.20	1.31	0.85	0.93	0.93	0.89	0.90
Fe^{2+}	1.15	1.08	1.31	1.24	1.20	1.23	1.29	1.06	1.32	1.23	1.47	1.47	1.42	1.41	1.39
Mn	0.03	0.02	0.02	0.02	0.01	0.02	0.01	0.02	0.02	0.02	0.01	0.01	0.02	0.01	0.02
$\sum$ Y	2.86	2.87	2.89	2.88	2.79	2.82	2.87	2.87	2.88	2.87	2.82	2.85	2.87	2.80	2.81
Na	0.02	0.02	0.02	0.02	0.03	0.02	0.02	0.02	0.02	0.02	0.02	0.03	0.00	0.02	0.02
K	0.90	0.91	0.91	0.87	0.89	0.91	0.89	0.91	0.89	0.92	0.85	0.86	0.86	0.89	0.87
$\sum$ X	0.92	0.94	0.93	0.91	0.92	0.93	0.92	0.93	0.92	0.93	0.88	0.90	0.86	0.91	0.89
Fe^t/Fe^t+Mg	0.47	0.45	0.52	0.52	0.52	0.52	0.53	0.42	0.53	0.49	0.64	0.62	0.62	0.61	0.62
$Mg/Mg+Fe^t$	0.53	0.55	0.48	0.48	0.48	0.48	0.47	0.58	0.47	0.51	0.36	0.38	0.38	0.39	0.38
$Fe^{2+}/Fe^{2+}+Fe^{3+}$	0.98	0.95	0.98	0.96	0.97	0.98	0.95	1.00	0.99	0.98	0.99	0.97	0.95	1.00	0.96
$Fe^{3+}/Fe^{2+}+Fe^{3+}$	0.02	0.05	0.02	0.04	0.03	0.02	0.05	0.00	0.01	0.02	0.01	0.03	0.05	0.00	0.04
FeO^t/MgO	1.56	1.43	1.95	1.90	1.93	1.92	2.04	1.27	1.98	1.71	3.11	2.87	2.86	2.84	2.88
Al^t	1.35	1.32	1.38	1.42	1.36	1.38	1.35	1.34	1.38	1.34	1.49	1.46	1.51	1.51	1.46

** Fe^t= total iron per formula unit (pfu); FeO^t= total iron; Al^t = (Al^{IV} + Al^{VI}) pfu

Contd… Table 4.2: Representative electron probe micro-analysis (wt%) and structural formulae of biotites from granitoids of Dibang Valley, Arunachal Pradesh

	LEUCOGRANITE						**GRANITE**									
Sample No.	**ET22 (6)**	**ET22 (7)**	**ET22 (8)**	**ET22 (9)**	**ET22 (10)**	**ET22 (11)**	**D7b (1)**	**D7b (2)**	**D7b (3)**	**D7b (4)**	**D7b (5)**	**D7b (6)**	**D7b (7)**	**D7b (8)**	**D7b (9)**	**D7b (10)**
SiO_2	35.24	35.43	35.25	35.26	35.76	35.60	35.94	36.65	36.12	36.00	36.28	36.12	35.90	36.28	36.64	36.73
Al_2O_3	16.43	16.19	15.86	16.12	16.17	16.86	14.68	15.34	14.58	14.64	14.70	14.31	14.11	14.42	15.06	14.70
TiO_2	3.39	2.74	2.86	3.00	3.23	3.06	3.09	3.34	3.35	2.50	2.39	2.57	2.95	3.36	2.13	2.86
Cr_2O_3	0.06	0.13	0.15	0.12	0.06	0.03	0.09	0.06	0.06	0.01	0.01	0.01	0.00	0.03	0.02	0.02
FeO	21.54	22.89	22.64	21.88	21.71	22.67	20.03	20.19	20.45	19.16	18.74	19.72	19.38	19.97	20.23	20.09
MnO	0.28	0.00	0.00	0.00	0.19	0.27	0.49	0.38	0.27	0.55	0.46	0.49	0.49	0.34	0.49	0.50
MgO	7.51	7.19	7.46	7.58	7.92	7.71	9.61	9.98	9.71	10.21	10.10	9.78	9.93	9.62	10.47	10.22
CaO	0.01	0.01	0.01	0.00	0.04	0.06	0.02	0.05	0.05	0.02	0.06	0.00	0.02	0.04	0.02	0.01
Na_2O	0.00	0.09	0.11	0.10	0.10	0.15	0.13	0.15	0.10	0.04	0.07	0.04	0.07	0.06	0.04	0.05
BaO	0.00	0.00	0.00	0.00	0.00	0.00	0.00	0.00	0.00	0.00	0.00	0.00	0.00	0.00	0.00	0.00
K_2O	8.77	8.65	8.84	8.76	8.91	8.64	9.21	9.34	8.89	9.15	8.92	9.13	8.97	9.11	8.26	9.10
Total	**93.38**	**93.34**	**93.20**	**92.85**	**94.29**	**95.10**	**93.81**	**95.94**	**94.03**	**92.76**	**92.20**	**92.65**	**92.19**	**93.59**	**93.76**	**94.74**
Structural formula based on 11 oxygen																
Si	2.77	2.80	2.79	2.79	2.79	2.76	2.81	2.79	2.81	2.83	2.86	2.85	2.84	2.83	2.84	2.83
Al^{IV}	1.23	1.20	1.21	1.21	1.21	1.24	1.19	1.21	119	1.17	1.14	1.15	1.16	1.17	1.16	1.17
∑ Z	4.00	4.00	4.00	4.00	4.00	4.00	4.00	4.00	4.00	4.00	4.00	4.00	4.00	4.00	4.00	4.00
Al^{VI}	0.29	0.31	0.27	0.29	0.27	0.29	0.16	0.17	0.15	0.19	0.22	0.18	0.16	0.16	0.21	0.17
Fe^{3+}	0.04	0.00	0.01	0.01	0.01	0.08	0.03	0.00	0.06	0.07	0.14	0.08	0.00	0.01	0.05	0.00
Ti	0.20	0.16	0.17	0.18	0.19	0.18	0.18	0.19	0.20	0.15	0.14	0.15	0.18	0.20	0.12	0.17
Cr	0.00	0.01	0.01	0.01	0.00	0.00	0.01	0.00	0.00	0.00	0.00	0.00	0.00	0.00	0.00	0.00
Mg	0.88	0.85	0.88	0.89	0.92	0.89	1.12	1.13	1.13	1.20	1.19	1.15	1.17	1.12	1.21	1.17
Fe^{2+}	1.38	1.51	1.49	1.44	1.40	1.38	1.27	1.29	1.28	1.19	1.09	1.22	1.28	1.29	1.26	1.29
Mn	0.02	0.00	0.00	0.00	0.01	0.02	0.03	0.02	0.02	0.04	0.03	0.03	0.03	0.02	0.03	0.03
∑ Y	2.81	2.84	2.83	2.82	2.81	2.85	2.81	2.81	2.82	2.83	2.81	2.82	2.83	2.81	2.89	2.83
Na	0.00	0.01	0.02	0.02	0.02	0.02	0.02	0.02	0.01	0.01	0.01	0.01	0.01	0.01	0.01	0.01
K	0.88	0.87	0.89	0.88	0.89	0.85	0.92	0.91	0.88	0.92	0.90	0.92	0.91	0.91	0.82	0.89

$\sum X$	0.88	0.89	0.91	0.90	0.90	0.88	0.94	0.93	0.90	0.93	0.91	0.93	0.92	0.92	0.83	0.90
Fe^t/Fe^t+Mg	0.62	0.64	0.63	0.62	0.61	0.62	0.54	0.53	0.54	0.51	0.51	0.53	0.52	0.54	0.52	0.52
$Mg/Mg+Fe^t$	0.38	0.36	0.37	0.38	0.39	0.38	0.46	0.47	0.46	0.49	0.49	0.47	0.48	0.46	0.48	0.48
$Fe^{2+}/Fe^{2+}+Fe^{3+}$	0.97	1.00	0.99	1.00	0.99	0.94	0.97	1.00	0.96	0.95	0.88	0.94	1.00	0.99	0.97	1.00
$Fe^{3+}/Fe^{2+}+Fe^{3+}$	0.03	0.00	0.01	0.00	0.01	0.06	0.03	0.00	0.04	0.05	0.12	0.06	0.00	0.01	0.03	0.00
FeO^t/MgO	2.87	3.18	3.03	2.89	2.74	2.94	2.08	2.02	2.11	1.88	1.86	2.02	1.95	2.08	1.93	1.97
Al^t	1.52	1.51	1.48	1.50	1.48	1.53	1.35	1.38	1.34	1.36	1.36	1.33	1.32	1.33	1.37	1.34

**Fe^t= total iron per formula unit (pfu); FeO^t= total iron; $Al^t = (Al^{IV} + Al^{VI})$ pfu

Table 4.3: Electron probe micro analysis (wt%) and structural formulae of feldspars from granitoids of Dibang Valley, Arunachal Pradesh.

QUARTZ DIORITE											
Plagioclase											
Sample no.	**D2 (1)**	**D2 (2)**	**D2 (3)**	**D2 (4)**	**D2 (5)**	**D2 (6)**	**D2 (8)**	**D2 (11)**	**D2 (13)**	**D2 (14)**	**D2 (15)**
SiO_2	59.24	58.78	60.04	59.72	59.61	60.16	59.99	58.39	60.16	60.09	60.28
Al_2O_3	25.24	25.19	25.37	25.38	25.34	25.30	25.24	24.85	25.32	25.73	25.73
CaO	7.36	7.17	7.15	7.23	7.32	7.32	6.72	6.75	6.71	7.05	6.69
Na_2O	7.22	7.34	7.15	7.19	7.29	7.56	7.49	7.25	7.55	7.51	7.36
K_2O	0.07	0.12	0.07	0.04	0.03	0.01	0.00	0.02	0.00	0.00	0.00
FeO	0.06	0.07	0.11	0.02	0.46	0.50	0.53	0.55	0.58	0.55	0.47
Total	**98.78**	**98.24**	**99.37**	**99.22**	**98.29**	**98.96**	**97.96**	**95.67**	**98.17**	**98.86**	**98.67**
Structural formula based on 8 oxygen											
Si	2.68	2.67	2.70	2.69	2.70	2.70	2.72	2.71	2.72	2.70	2.72
Al	1.35	1.35	1.35	1.35	1.35	1.34	1.35	1.36	1.35	1.36	1.37
Z	4.02	4.01	4.05	4.04	4.05	4.04	4.07	4.07	4.07	4.06	4.08
Ca	0.36	0.35	0.35	0.35	0.36	0.35	0.33	0.35	0.34	0.36	0.34
Na	0.63	0.65	0.62	0.63	0.64	0.66	0.66	0.65	0.66	0.65	0.64
K	0.00	0.01	0.00	0.00	0.00	0.00	0.00	0.00	0.00	0.00	0.00
X	1.00	1.01	0.98	0.98	1.00	1.01	0.98	1.01	1.00	1.01	0.98
Fe	0.00	0.00	0.00	0.00	0.02	0.02	0.02	0.02	0.02	0.02	0.02

An%	**36.34**	**35.11**	**36.05**	**35.88**	**35.62**	**34.84**	**33.17**	**34.95**	**34.22**	**35.22**	**34.30**
Ab%	**63.26**	**64.20**	**63.55**	**63.89**	**64.20**	**65.11**	**66.89**	**64.93**	**66.01**	**64.78**	**65.70**
Or%	**0.40**	**0.69**	**0.41**	**0.23**	**0.17**	**0.06**	**0.00**	**0.12**	**0.00**	**0.00**	**0.00**

** Z=Si+Al; X=Ca+Na+K

Contd…Table 4.3: Electron probe micro analysis (wt%) and structural formulae of feldspars from granitoids of Dibang Valley, Arunachal Pradesh

QUARTZ DIORITE ***Plagioclase***													
Sample no.	**M1 (1)**	**M1 (2)**	**M1 (3)**	**M1 (4)**	**M1 (5)**	**M1 (6)**	**M1 (7)**	**M1 (8)**	**M1 (9)**	**M1 (10)**	**M1 (11)**	**M1 (12)**	**M1 (13)**
SiO_2	60.01	60.95	60.16	59.98	60.22	61.01	60.42	60.40	61.08	60.52	61.09	60.27	60.69
Al_2O_3	24.88	24.93	24.84	24.71	24.95	25.01	24.62	24.61	24.90	24.71	24.43	25.17	24.73
CaO	6.42	6.17	6.34	6.58	6.13	6.08	6.35	6.02	6.01	6.20	6.07	6.77	6.23
Na_2O	7.73	7.91	7.83	7.81	7.78	8.06	7.75	8.01	7.85	7.82	8.03	7.37	7.84
K_2O	0.07	0.05	0.06	0.01	0.00	0.00	0.08	0.09	0.00	0.02	0.03	0.11	0.00
FeO	0.50	0.47	0.54	0.66	0.55	0.57	0.46	0.47	0.52	0.46	0.53	0.53	0.58
Total	**97.61**	**98.57**	**97.79**	**97.39**	**97.55**	**98.73**	**97.82**	**97.59**	**98.41**	**97.83**	**98.22**	**98.20**	**97.98**
Structural formula based on 8 oxygen													
Si	2.73	2.74	2.73	2.73	2.74	2.74	2.74	2.74	2.75	2.74	2.76	2.73	2.75
Al	1.33	1.32	1.33	1.33	1.34	1.32	1.32	1.32	1.32	1.32	1.30	1.34	1.32
Z	4.06	4.06	4.05	4.05	4.07	4.06	4.06	4.05	4.08	4.06	4.06	4.07	4.07
Ca	0.33	0.31	0.31	0.34	0.32	0.31	0.33	0.30	0.31	0.32	0.31	0.35	0.32
Na	0.68	0.69	0.69	0.69	0.69	0.70	0.68	0.70	0.69	0.69	0.70	0.65	0.69
K	0.00	0.00	0.00	0.00	0.00	0.00	0.01	0.01	0.00	0.00	0.00	0.01	0.00
X	1.01	1.00	1.00	1.03	1.00	1.01	1.01	1.01	0.99	1.00	1.02	1.00	1.01
Fe	0.02	0.02	0.02	0.03	0.02	0.02	0.02	0.02	0.02	0.02	0.20	0.02	0.02
An%	**32.29**	**31.01**	**30.81**	**33.17**	**31.63**	**30.99**	**32.12**	**29.87**	**31.11**	**31.44**	**30.76**	**34.56**	**31.97**
Ab%	**67.31**	**68.70**	**68.85**	**66.78**	**68.43**	**69.12**	**67.42**	**69.62**	**69.01**	**68.45**	**69.08**	**64.80**	**68.15**
Or%	**0.40**	**0.29**	**0.35**	**0.06**	**0.00**	**0.00**	**0.46**	**0.52**	**0.00**	**0.12**	**0.17**	**0.64**	**0.00**

** Z=Si+Al; X=Ca+Na+K

Contd…Table 4.3: Electron probe micro analysis (wt%) and structural formulae of feldspars from granitoids of Dibang Valley, Arunachal Pradesh

GRANODIORITE *Plagioclase*													
Sample no.	**E4 (2)**	**E4 (4)**	**E4 (5)**	**E4 (6)**	**E4 (8)**	**E4 (9)**	**E4 (10)**	**E4 (11)**	**D4 (1)**	**D4 (2)**	**D4 (3)**	**D4 (4)**	**D4 (5)**
SiO_2	67.92	68.30	69.17	68.62	69.26	68.56	67.28	67.17	61.89	59.51	60.78	60.06	59.71
Al_2O_3	20.52	19.11	19.48	19.57	19.05	19.26	19.13	19.13	23.35	24.55	23.86	24.91	24.25
CaO	1.02	0.01	0.00	0.00	0.02	0.30	0.09	0.00	5.51	6.74	6.07	6.35	6.15
Na_2O	11.46	11.96	11.94	12.03	12.18	12.02	11.99	11.92	8.74	7.90	8.24	7.94	8.07
K_2O	0.04	0.04	0.08	0.08	0.07	0.05	0.04	0.06	0.17	0.09	0.16	0.17	0.10
FeO	0.00	0.00	0.00	0.00	0.00	0.00	0.00	0.00	0.00	0.00	0.00	0.00	0.00
Total	**100.81**	**100.13**	**100.48**	**100.07**	**100.37**	**99.96**	**98.31**	**98.07**	**99.66**	**98.42**	**98.72**	**99.18**	**97.82**
Structural formula based on 8 oxygen													
Si	2.95	2.98	3.00	2.99	3.01	2.99	2.98	2.98	2.75	2.69	2.73	2.69	2.71
Al	1.05	0.98	1.00	1.00	0.98	0.99	1.00	1.00	1.22	1.31	1.26	1.32	1.30
Z	4.00	3.97	4.00	3.99	3.98	3.98	3.97	3.98	3.97	3.99	4.00	4.01	4.01
Ca	0.06	0.01	0.01	0.01	0.01	0.02	0.00	0.00	0.26	0.33	0.29	0.31	0.30
Na	0.96	1.01	1.01	1.03	1.03	1.02	1.03	1.02	0.75	0.69	0.72	0.69	0.71
K	0.00	0.00	0.00	0.00	0.00	0.00	0.00	0.00	0.01	0.01	0.01	0.01	0.01
X	1.02	1.02	1.03	1.04	1.04	1.04	1.03	1.02	1.03	1.03	1.02	1.01	1.02
Fe	0.00	0.00	0.00	0.00	0.01	0.00	0.00	0.00	0.00	0.00	0.00	0.00	0.00
An%	**5.64**	**0.94**	**0.78**	**1.00**	**1.15**	**2.22**	**0.00**	**0.00**	**25.59**	**32.09**	**28.74**	**30.83**	**29.59**
Ab%	**94.14**	**98.85**	**98.79**	**98.58**	**98.48**	**97.52**	**99.82**	**100.30**	**73.47**	**67.41**	**70.36**	**68.21**	**69.84**
Or%	**0.22**	**0.22**	**0.43**	**0.43**	**0.37**	**0.27**	**0.22**	**0.33**	**0.94**	**0.51**	**0.90**	**0.96**	**0.57**

** Z=Si+Al; X=Ca+Na+K

Contd…Table 4.3: Electron probe micro analysis (wt%) and structural formulae of feldspars from granitoids of Dibang Valley, Arunachal Pradesh

GRANODIORITE ***Plagioclase***														
Sample no.	**D4 (6)**	**D4 (7)**	**D4 (11)**	**D4 (12)**	**D4 (13)**	**D6a (1)**	**D6a (2)**	**D6a (3)**	**D6a (7)**	**D6a (8)**	**D6a (9)**	**D6a (11)**	**D6a (14)**	**D6a (15)**
SiO_2	60.56	61.10	60.61	61.19	61.75	60.61	60.39	59.82	59.86	60.01	61.64	61.42	60.58	61.16
Al_2O_3	24.67	24.23	24.41	23.85	23.64	23.38	23.50	23.73	23.69	23.72	23.65	22.83	23.82	23.70
CaO	6.09	5.79	6.43	6.07	5.59	5.24	5.25	5.35	5.37	5.34	5.12	4.78	5.51	5.38
Na_2O	8.15	8.39	8.23	8.21	8.52	8.48	8.72	8.36	8.56	8.57	8.66	8.95	8.35	8.53
K_2O	0.07	0.14	0.07	0.18	0.06	0.22	0.18	0.31	0.21	0.18	0.13	0.38	0.22	0.20
FeO	0.10	0.00	0.00	0.00	0.00	0.00	0.00	0.00	0.00	0.00	0.00	0.00	0.00	0.00
Total	**99.64**	**99.71**	**99.36**	**99.23**	**99.27**	**98.03**	**98.16**	**97.62**	**97.71**	**97.83**	**99.32**	**98.39**	**98.50**	**98.98**
Structural formula based on 8 oxygen														
Si	2.70	2.72	2.71	2.74	2.76	2.74	2.72	2.72	2.71	2.71	2.75	2.76	2.73	2.74
Al	1.30	1.27	1.29	1.26	1.25	1.25	1.25	1.27	1.26	1.26	1.24	1.21	1.26	1.25
Z	4.00	3.99	3.99	4.00	4.00	3.99	3.97	3.98	3.98	3.98	3.99	3.97	3.99	3.99
Ca	0.29	0.28	0.31	0.30	0.27	0.25	0.25	0.26	0.26	0.26	0.24	0.23	0.27	0.26
Na	0.71	0.72	0.71	0.71	0.74	0.74	0.76	0.74	0.75	0.75	0.75	0.78	0.73	0.74
K	0.00	0.01	0.00	0.01	0.00	0.01	0.01	0.02	0.01	0.01	0.01	0.02	0.01	0.01
X	1.00	1.01	1.03	1.02	1.01	1.01	1.03	1.01	1.02	1.02	1.00	1.03	0.74	1.01
Fe	0.00	0.00	0.00	0.00	0.00	0.00	0.00	0.00	0.00	0.00	0.00	0.00	0.00	0.00
An%	**29.11**	**27.39**	**30.29**	**29.07**	**26.71**	**25.13**	**24.71**	**25.66**	**25.44**	**25.35**	**24.44**	**22.31**	**26.39**	**25.55**
Ab%	**70.49**	**71.82**	**69.32**	**69.92**	**72.96**	**73.61**	**74.28**	**72.57**	**73.38**	**73.63**	**74.82**	**75.58**	**72.36**	**73.32**
Or%	**0.40**	**0.79**	**0.39**	**1.01**	**0.34**	**1.26**	**1.01**	**1.77**	**1.18**	**1.02**	**0.74**	**2.11**	**1.25**	**1.13**

** Z=Si+Al; X=Ca+Na+K

Contd…Table 4.3: Electron probe micro analysis (wt%) and structural formulae of feldspars from granitoids of Dibang Valley, Arunachal Pradesh

	GRANODIORITE ***Plagioclase***						**GRANITE** ***Plagioclase***							
Sample no.	**D6a (17)**	**D6a (18)**	**D6a (20)**	**D6a (21)**	**D6a (22)**	**D6a (127)**	**D7b (1)**	**D7b (2)**	**D7b (3)**	**D7b (4)**	**D7b (5)**	**D7b (7)**	**D7b (8)**	**D7b (9)**
SiO_2	61.46	60.32	62.11	61.27	60.40	60.37	59.85	60.84	60.02	60.85	60.80	60.59	60.27	61.80
Al_2O_3	23.90	23.78	23.47	23.53	23.99	23.81	24.84	24.57	24.69	24.36	23.96	23.79	23.95	23.96
CaO	5.31	5.38	5.20	5.26	5.33	5.07	6.08	6.48	6.93	5.91	6.30	6.29	6.19	5.75
Na_2O	8.55	8.47	8.73	8.71	8.72	8.68	8.25	7.97	7.79	8.13	8.34	8.10	8.16	8.57
K_2O	0.18	0.14	0.25	0.23	0.08	0.17	0.22	0.30	0.30	0.24	0.12	0.34	0.23	0.16
FeO	0.00	0.00	0.00	0.00	0.00	0.00	0.00	0.00	0.00	0.00	0.00	0.00	0.00	0.00
Total	**99.58**	**98.22**	**100.01**	**99.12**	**98.76**	**98.05**	**99.28**	**100.21**	**99.85**	**99.64**	**99.66**	**99.14**	**98.90**	**100.54**
Structural formula based on 8 oxygen														
Si	2.74	2.72	2.75	2.74	2.71	2.72	2.67	2.70	2.68	2.71	2.71	2.72	2.71	2.73
Al	1.25	1.26	1.23	1.24	1.27	1.27	1.31	1.29	1.30	1.28	1.26	1.26	1.27	1.25
Z	3.99	3.99	3.98	3.98	3.97	3.99	3.98	3.99	3.97	4.00	3.97	3.97	3.97	3.98
Ca	0.25	0.26	0.25	0.25	0.26	0.24	0.29	0.31	0.33	0.28	0.30	0.30	0.30	0.27
Na	0.74	0.74	0.75	0.75	0.76	0.76	0.71	0.69	0.67	0.70	0.72	0.70	0.71	0.73
K	0.01	0.01	0.01	0.01	0.00	0.01	0.01	0.02	0.02	0.01	0.01	0.02	0.01	0.01
X	1.00	1.01	1.01	1.02	1.02	1.01	1.02	1.01	1.02	1.00	1.03	1.03	1.02	1.01
Fe	0.01	0.00	0.01	0.00	0.01	0.00	0.00	0.00	0.00	0.01	0.00	0.00	0.00	0.01
An%	**25.29**	**25.77**	**24.42**	**24.70**	**25.14**	**24.17**	**28.58**	**30.48**	**32.41**	**28.27**	**29.25**	**29.46**	**29.16**	**26.81**
Ab%	**73.69**	**73.43**	**74.18**	**74.01**	**74.42**	**74.87**	**70.19**	**67.84**	**65.92**	**70.37**	**70.08**	**68.65**	**69.55**	**72.30**
Or%	**1.02**	**0.80**	**1.40**	**1.29**	**0.45**	**0.96**	**1.23**	**1.68**	**1.67**	**1.37**	**0.66**	**1.90**	**1.29**	**0.89**
$^{Pl}X_{ab}$	-	-	-	-	-	-	0.70	0.68	0.66	0.71	0.70	0.69	0.70	0.72
$^{Kfs}X_{ab}$	-	-	-	-	-	-	-	-	-	-	-	-	-	-

** Z=Si+Al; X=Ca+Na+K

Contd…Table 4.3: Electron probe micro analysis (wt%) and structural formulae of feldspars from granitoids of Dibang Valley, Arunachal Pradesh

	LEUCOGRANITE *Plagioclase*													
Sample no.	**ET22 (82)**	**ET22 (83)**	**ET22 (84)**	**ET22 (85)**	**ET22 (86)**	**ET22 (87)**	**ET22 (88)**	**ET22 (93)**	**ET22 (94)**	**ET22 (95)**	**ET22 (97)**	**ET22 (107)**	**ET22 (108)**	**ET22 (109)**
SiO_2	61.79	61.82	61.41	61.84	60.34	61.51	61.88	62.52	61.78	61.69	62.18	62.64	60.85	61.97
Al_2O_3	23.33	23.70	23.45	23.71	23.43	23.71	23.42	22.34	23.55	23.66	23.80	23.97	23.16	23.86
CaO	5.08	5.14	5.35	5.56	5.36	5.32	5.28	4.29	5.04	5.43	5.33	5.14	5.28	5.42
Na_2O	8.34	8.29	8.67	7.97	8.49	8.49	8.18	9.00	8.38	7.93	8.43	7.80	8.48	8.19
K_2O	0.17	0.07	0.08	0.16	0.17	0.17	0.17	0.06	0.25	0.25	0.14	0.17	0.04	0.17
FeO	0.10	0.09	0.00	0.00	0.00	0.06	0.06	0.00	0.06	0.00	0.04	0.00	0.00	0.10
Total	**98.81**	**99.11**	**98.96**	**99.24**	**97.79**	**99.26**	**98.99**	**98.21**	**99.06**	**98.96**	**99.92**	**99.72**	**97.81**	**99.71**
Structural formula based on 8 oxygen														
Si	2.778	2.778	2.725	2.774	2.729	2.745	2.777	2.815	2.676	2.776	2.763	2.809	2.755	2.764
Al	1.236	1.252	1.227	1.253	1.249	1.247	1.239	1.185	1.243	1.255	1.246	1.251	1.236	1.254
Z	4.014	4.039	3.952	4.027	3.978	3.992	4.016	4.00	3.919	4.031	4.009	4.06	3.991	4.018
Ca	0.245	0.247	0.254	0.267	0.260	0.254	0.254	0.207	0.242	0.262	0.254	0.247	0.256	0.259
Na	0.727	0.721	0.746	0.693	0.744	0.735	0.712	0.786	0.728	0.692	0.726	0.678	0.744	0.708
K	0.01	0.004	0.005	0.009	0.010	0.010	0.010	0.003	0.014	0.014	0.008	0.010	0.002	0.010
X	0.982	0.972	1.005	0.969	1.014	0.999	0.976	0.996	0.984	0.968	0.988	0.935	1.002	0.977
Fe	0.004	0.003	0.00	0.00	0.00	0.002	0.002	0.00	0.002	0.00	0.001	0.00	0.00	0.004
An%	**24.93**	**25.41**	**25.31**	**27.56**	**25.61**	**25.47**	**26.03**	**20.78**	**24.58**	**27.04**	**25.68**	**26.42**	**25.54**	**26.51**
Ab%	**74.07**	**74.17**	**74.24**	**71.49**	**73.42**	**73.56**	**72.97**	**78.88**	**73.97**	**71.47**	**73.51**	**72.54**	**74.23**	**72.50**
Or%	**0.99**	**0.41**	**0.45**	**0.94**	**0.97**	**0.97**	**1.00**	**0.35**	**1.45**	**1.48**	**0.80**	**1.04**	**0.23**	**1.00**
$^{Pl}X_{ab}$	0.74	0.74	0.74	0.72	0.73	0.74	0.73	0.79	0.74	0.71	0.73	0.73	0.74	0.72
$^{Kfs}X_{ab}$	-	-	-	-	-	-	-	-	-	-	-	-	-	-

** Z=Si+Al; X=Ca+Na+K

Contd…Table 4.3: Electron probe micro analysis (wt%) and structural formulae of feldspars from granitoids of Dibang Valley, Arunachal Pradesh

LEUCOGRANITE ***Plagioclase***														
Sample no.	**ET22 (110)**	**ET22 (111)**	**ET22 (112)**	**ET22 (113)**	**ET22 (114)**	**ET22 (117)**	**ET22 (118)**	**ET22 (119)**	**ET22 (120)**	**ET22 (124)**	**ET22 (125)**	**ET22 (130)**	**ET22 (138)**	**ET22 (139)**
SiO_2	61.93	61.92	61.99	61.78	61.37	61.33	60.52	60.93	60.26	60.89	61.43	62.75	61.07	60.85
Al_2O_3	23.83	23.89	23.89	23.70	23.74	22.96	23.53	23.83	23.34	23.38	23.19	21.78	23.55	23.74
CaO	5.20	5.43	5.21	5.34	5.50	5.01	5.41	5.12	5.61	5.37	5.01	3.80	5.44	5.42
Na_2O	8.15	8.42	8.34	8.21	8.16	8.74	8.57	8.61	8.50	8.51	8.58	9.34	8.68	8.54
K_2O	0.18	0.18	0.14	0.14	0.14	0.00	0.11	0.09	0.10	0.05	0.08	0.08	0.06	0.09
FeO	0.07	0.07	0.16	0.03	0.10	0.00	0.00	0.00	0.00	0.00	0.00	0.00	0.00	0.00
Total	**99.36**	**99.91**	**99.73**	**99.2**	**99.01**	**98.04**	**98.14**	**98.58**	**97.81**	**98.2**	**98.29**	**97.75**	**98.8**	**98.64**
Structural formula based on 8 oxygen														
Si	2.772	2.751	2.762	2.767	2.756	2.769	2.730	2.735	2.729	2.748	2.769	2.832	2.735	2.730
Al	1.257	1.251	1.254	1.251	1.256	1.222	1.251	1.261	1.246	1.244	1.232	1.159	1.243	1.255
Z	4.029	4.002	4.016	4.018	4.012	3.991	3.981	3.996	3.975	3.992	4.001	3.991	3.978	3.985
Ca	0.249	0.258	0.249	0.256	0.265	0.242	0.261	0.246	0.272	0.260	0.242	0.184	0.261	0.261
Na	0.707	0.725	0.720	0.713	0.710	0.765	0.749	0.749	0.746	0.745	0.750	0.817	0.754	0.743
K	0.010	0.010	0.008	0.008	0.008	0.00	0.006	0.005	0.006	0.003	0.005	0.005	0.003	0.005
X	0.966	0.993	0.977	0.977	0.983	1.007	1.016	1.00	1.024	1.008	0.997	1.006	1.018	1.009
Fe	0.003	0.003	0.006	0.001	0.004	0.00	0.00	0.00	0.00	0.00	0.00	0.00	0.00	0.00
An%	**25.79**	**26.00**	**25.45**	**26.22**	**26.92**	**24.06**	**25.70**	**24.61**	**26.57**	**25.78**	**24.28**	**18.27**	**25.64**	**25.83**
Ab%	**73.15**	**72.97**	**73.73**	**72.96**	**72.27**	**75.94**	**73.68**	**74.88**	**72.86**	**73.93**	**75.26**	**81.27**	**74.03**	**73.66**
Or%	**1.06**	**1.03**	**0.81**	**0.89**	**0.82**	**0.00**	**0.62**	**0.52**	**0.56**	**0.29**	**0.46**	**0.46**	**0.34**	**0.51**
$^{Pl}X_{ab}$	**0.73**	**0.73**	**0.74**	**0.73**	**0.72**	**0.75**	**0.74**	**0.75**	**0.73**	**0.74**	**0.75**	**0.81**	**0.74**	**0.74**
$^{Kfs}X_{ab}$	-	-	-	-	-	-	-	-	-	-	-	-	-	-

** Z=Si+Al; X=Ca+Na+K

Contd…Table 4.3: Electron probe micro analysis (wt%) and structural formulae of feldspars from granitoids of Dibang Valley, Arunachal Pradesh

	GRANITE *k-feldspar*												**GRANODIORITE** *k-feldspar*		**QUARTZDIROITE** *k-feldspar*	
Sample no.	**D7b (31)**	**D7b (32)**	**D7b (33)**	**D7b (34)**	**D7b (35)**	**D7b (36)**	**D7b (37)**	**D7b (38)**	**D7b (39)**	**D7b (40)**	**D7b (42)**	**D7b (44)**	**E4 (1)**	**E4 (2)**	**E13 (1)**	**E13 (2)**
SiO_2	64.20	64.38	64.56	64.27	63.60	64.53	64.99	64.79	64.59	65.08	65.04	65.30	50.16	49.51	46.06	47.69
Al_2O_3	18.42	18.48	18.47	18.30	18.78	18.52	18.66	18.48	18.23	18.19	17.95	18.02	26.52	27.35	33.65	29.26
CaO	0.00	0.00	0.00	0.00	0.00	0.00	0.00	0.00	0.00	0.00	0.01	0.00	0.00	0.00	0.00	0.00
Na_2O	1.07	1.18	0.94	0.86	1.13	1.20	1.12	1.71	1.11	1.22	1.29	1.58	0.40	0.24	0.80	0.27
K_2O	14.52	14.70	14.46	14.53	14.44	14.23	14.18	13.97	14.34	14.84	14.25	13.90	10.36	10.26	10.03	10.10
FeO	0.03	0.09	0.15	0.05	0.03	0.06	0.02	0.01	0.05	0.06	0.06	0.13	0.00	0.00	0.00	0.00
Total	**98.25**	**98.84**	**98.58**	**98.01**	**97.98**	**98.56**	**98.99**	**98.99**	**98.34**	**99.41**	**98.60**	**98.93**	**94.48**	**93.77**	**92.67**	**91.88**
Structural formula based on 8 oxygen																
Si	3.01	3.00	3.03	3.03	2.99	3.02	3.03	3.01	3.03	3.02	3.04	3.04	2.43	2.42	2.25	2.37
Al	1.02	1.02	1.02	1.02	1.04	1.02	1.03	1.01	1.01	0.99	0.99	0.99	1.52	1.57	1.93	1.71
Z	4.03	4.02	4.05	4.05	4.03	4.04	4.06	4.02	4.04	4.01	4.03	4.03	3.95	3.99	4.18	4.08
Ca	0.00	0.00	0.00	0.00	0.00	0.00	0.00	0.00	0.00	0.00	0.00	0.00	0.00	0.00	0.00	0.00
Na	0.10	0.11	0.09	0.08	0.10	0.11	0.10	0.15	0.10	0.11	0.12	0.14	0.04	0.02	0.08	0.03
K	0.87	0.87	0.86	0.87	0.87	0.85	0.84	0.83	0.86	0.88	0.85	00.83	0.64	0.64	0.62	0.64
X	0.97	0.98	0.95	0.95	0.97	0.96	0.94	0.98	0.96	0.99	0.97	0.97	0.68	0.66	0.70	0.67
Fe	0.00	0.00	0.01	0.00	0.00	0.00	0.00	0.00	0.00	0.00	0.00	0.00	0.00	0.00	0.00	0.00
An%	0.00	0.00	0.00	0.00	0.00	0.00	0.00	0.00	0.00	0.00	0.05	0.01	0.00	0.00	0.00	0.00
Ab%	10.07	10.87	8.99	8.25	10.63	11.36	10.72	15.69	10.53	11.11	12.09	14.73	5.54	3.42	10.81	3.90
Or%	89.93	89.13	91.01	91.75	89.37	88.64	89.28	84.31	89.47	88.89	87.86	85.27	94.46	96.58	89.19	96.10
$^{Pl}X_{ab}$	-	-	-	-	-	-	-	-	-	-	-	-	0.70	0.68	0.70	0.69
$^{Kfs}X_{ab}$	0.10	0.11	0.09	0.08	0.11	0.11	0.11	0.16	0.11	0.11	0.12	0.15	-	-	-	-

** Z=Si+Al; X=Ca+Na+K

CHAPTER-6

GEOCHEMISTRY

6.1 MAJOR ELEMENT GEOCHEMISTRY

6.1.1 INTRODUCTION

The chemical composition and mineralogy of the source region exert a fundamental control over the chemistry of magmatic rocks. For a better understanding of the different processes that operated during the journey of magma from its source through magma chambers and conduit systems to its final emplacement on the Earth's surface, detailed study of the bulk geochemistry (major and trace elements) of the plutonic rocks of interest is critical.

The major and trace element composition of a melt is influenced by the type of melting process and the degree of partial melting. However, the melt composition can be substantially modified en route to the surface. Whole-rock geochemistry serves as an effective tool for deciphering the petrogenesis of granitoids and related igneous rocks. Geochemical studies help identify key processes such as partial melting, fractionation, magma mingling and mixing, assimilation, or a combination of these dynamic mechanisms. The geochemical characteristics of a rock significantly influence its nature, reflecting its source and the processes that acted on the melt, thereby aiding in assessing its tectonic discrimination and protolith evolution. Major element data play a crucial role in classifying individual rocks and rock associations, constructing variation diagrams, and comparing compositions with experimentally determined rock samples formed under known conditions. This geochemical review aims to analyze the behavior and relationships of major elements in different granitoids of Dibang Valley, shedding light on their petrogenesis and tectonic setting.

Twenty-two representative granitoid samples of the Dibang Valley granitoids have been analysed for whole-rock major oxide (wt%), trace element (ppm), and rare earth element concentrations. 8 samples of quartz diorite, 9 granodiorite samples, 2 granite samples, and 3 leucogranite samples have been analysed and studied for whole-rock geochemistry. The representative whole-rock geochemical data of the 22 granitoids are presented in Table 5.1

6.1.2 MAJOR OXIDES AND CIPW NORM

QUARTZ DIORITE

The quartz diorite of Dibang Valley exhibits variation in SiO_2 (52.00-61.22 wt%), Na_2O (3.07-4.20 wt%), and K_2O (0.81-2.32 wt%), and has a more sodic nature with Na_2O/K_2O values ranging from 1.33-4.78 wt% (Table 5.1). They have moderate values of Al_2O_3 (14.71-16.20 wt%), higher Fe_2O_3 (6.21-9.60 wt%), MgO (4.09-8.96 wt%), and CaO (6.54-7.69 wt%) and low content of TiO_2 (0.66-0.98 wt%), P_2O_5 (0.20-0.40 wt%), and MnO (0.11-0.17 wt%). They are primarily magnesian with FeO^t/FeO^t+MgO (0.45-0.62 wt%) and Mg# (53.42-69.83 wt%) and also characterized by high ferromagnesian oxides (FeO^t +MgO+MnO+TiO_2, (FMMT) = 10.50-17.91 wt%). They possess an Alumina Saturation Index [ASI= Al_2O_3/(CaO + Na_2O + K_2O)] of 0.72-0.82 wt%. According to the CIPW norm after Janousek et al., 2006, the CIPW values in order of abundance of normative minerals are albite (26.01-35.57), anorthite (20.34-24.71), hypersthene (7.07-17.88), quartz (2.48-16.08), diopside (4.15-10.23), orthoclase (4.79-13.68), and haematite (6.21-9.60). In the feldspar triangle diagram (O'Connor, 1965), the quartz diorites plot in the tonalite field, except for Sample E12, which plots in the granodiorite field (Figure 5.1).

GRANODIORITE

The granodiorites of Dibang Valley contain relatively higher content of SiO_2 (57.99-65.77 wt%), Na_2O (3.63-4.75 wt%) and K_2O (1.24-3.37 wt%) as compared to the quartz diorites, but exhibit similar sodic nature with Na_2O/K_2O values of 1.09-3.07. Fe_2O_3 varies from 4.02-7.32 wt%, MgO ranges from 1.98-5.92 wt% and CaO from 3.78-6.59 wt%. The granodiorites are also magnesian-rich with FeO^t/FeO^t+MgO (0.49-0.66 wt%) and Mg# (51.14-65.72 wt%) but comparatively lower ferromagnesian content (FMMT= 6.38-12.90 wt%). They have low to moderate Al_2O_3 (14.47-17.22 wt%) and are metaluminous (I-type) with molar Al_2O_3/CaO+Na_2O+K_2O values between 0.78-0.98 wt%. The content of TiO_2 (0.40-0.81 wt%), P_2O_5 (0.19-0.49

wt%) and MnO (0.07-0.12 wt%) is comparatively lower than quartz diorite. The dominant normative minerals are albite (30.60-40.21), anorthite (14.18-20.93), quartz (9.55-21.56), orthoclase (7.30-19.92), hypersthene (4.87-14.70), and haematite (4.02-9.21) and the rest are in minor amounts. They also fall within the tonalite and granodiorite domains in the normative An-Ab-Or feldspar diagram (Figure 5.1).

GRANITE

The granites of Dibang Valley contain high amounts of SiO_2 (66.70-70.09 wt%), Na_2O (2.65-3.12 wt%) and K_2O (4.33-4.85 wt%) as compared to the quartz diorites and granodiorites, but comparably lower Na_2O/K_2O values of 0.55-0.72 wt% radiating towards slightly more potassic nature. Fe_2O_3 varies from 2.62-3.60 wt%, MgO ranges from 1.22-1.17 wt% and CaO from 2.49-2.89 wt%. The granites are also magnesian-rich with FeO^t/FeO^t+MgO (0.66-0.74 wt%) and Mg# (40.75-50.75 wt%), but the ferromagnesian content (FMMT= 3.98-4.85 wt%) is notably very low. Al_2O_3 (14.41-15.89 wt%) content is moderate, and they are weakly peraluminous (S-type) with molar $Al_2O_3/CaO+Na_2O+K_2O$ values between 1.02-1.05 wt%. The contents of TiO_2 (0.35-0.38 wt%), P_2O_5 (0.17-0.21 wt%), and MnO (0.05-0.06 wt%) are significantly lower than those of quartz diorite and granodiorites. The dominant normative minerals are quartz (24.64-29.45), orthoclase (25.58-28.69), albite (22.40-26.43), anorthite (11.26-12.97), corundum (0.67-1.31), hypersthene (2.91-3.03), and haematite (2.62-3.60) and the rest are in minor amounts. They classify as quartz monzonite in the normative An-Ab-Or feldspar diagram (Figure 5.1).

LEUCOGRANITE

Amongst the Dibang Valley granitoids, the leucogranites have the highest SiO_2 content (66.73-76.94 wt%), and very low content of Fe_2O_3 (2.34-4.52 wt%), MgO (0.18-0.59 wt%) and CaO (3.06-4.11 wt%). These leucogranites are rich in aluminosilicate minerals (e.g., muscovite and garnet) and hence, have the highest Al_2O_3 (10.71-16.98 wt%) amongst all granitoids in the present study. These leucogranites have the lowest K_2O content (0.24-0.69 wt%), higher Na_2O (4.14-5.06 wt%), and consequently, they are more sodic, with Na_2O/K_2O values varying from

7.16-21.08 wt%. Mg# varies from 7.09-25.71 wt%, and ferromagnesian oxides (FMMT) vary from 2.73-4.42 wt%. They are mildly peraluminous with ASI values ranging from 0.84-1.06. In CIPW norm, quartz (27.42-45.80) and albite (35.05-42.82) are the most dominant normative minerals, and the rest of the minerals in decreasing order of dominance are anorthite (9.69-20.13), haematite (2.34-4.52), orthoclase (1.42-4.08), diopside (0-1.94), and corundum (0.00-0.75). In the feldspar triangle diagram, these samples plot within the tonalite-trondhjemite field (Figure 5.1).

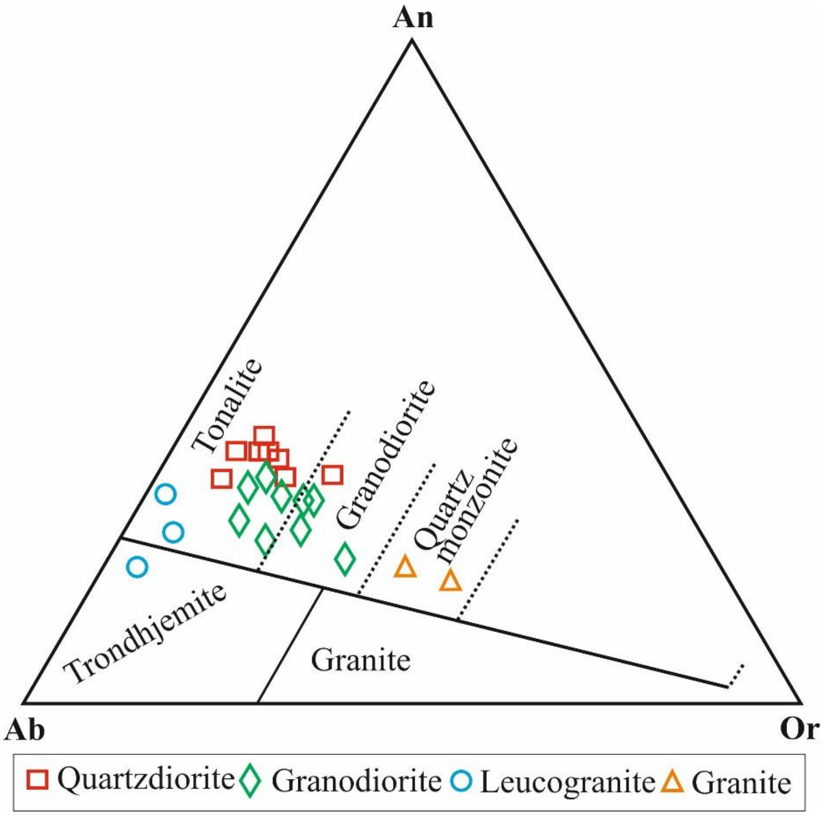

Figure 5.1: Normative An-Ab-Or ternary diagram (after O' Connor, 1965).

6.1.3 CLASSIFICATION

The ternary AFM diagram ($Na_2O+K_2O-FeO^t-MgO$) after Irvine and Baragar (1971) has been employed to distinguish between the calc-alkaline and tholeiite differentiation trends in the sub-alkaline magma series. Generally, the tholeiitic magma series exhibits a strong trend of iron enrichment during the early stages of differentiation. In contrast, a progressive suppression of iron by the early crystallisation of oxides of Fe-Ti oxides leads to an alkalic trend in the calc-alkaline series. The granitoids of Dibang Valley mostly belong to the calc-alkaline field, with a few quartz diorites in the tholeiitic field (Figure 5.2). It exhibits a linear variation trend with leucogranites closest to the AF side of the plot, granodiorites in the middle, and quartz diorite closest to the tholeiitic field.

The petrogenetic parameter introduced by Shand (1927), i.e., the Alumina Saturation Index (ASI), expressed as the molar ratio $Al_2O_3/(CaO+Na_2O+K_2O)$ or A/CNK, uses aluminosity as a key characteristic of granitoids and remains one of the most widely applied geochemical discriminators for their classification. According to Chapell and White (1974), granitoids with A/CNK <1 are termed as metaluminous (I-type) and those with A/CNK >1 are considered peraluminous (S-type). According to the ASI index (Figure 5.3), quartz diorites are classified as metaluminous (I-type) with A/CNK values ranging from 0.72-0.82 wt%; granodiorites also suggest metaluminous (I-type) nature with molar A/CNK values between 0.78-0.98 wt% whereas granites and leucogranites are peraluminous (S-type) with molar A/CNK values ranging from 1.02-1.06 wt%, except for one sample with A/CNK 0.84 wt%.

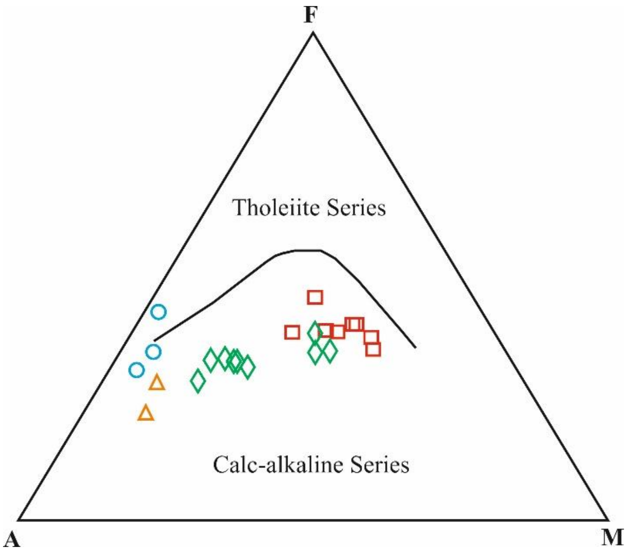

Figure 5.2: $Na_2O+K_2O-FeO^t-MgO$ (AFM) diagram after Irvine and Baragar (1971)

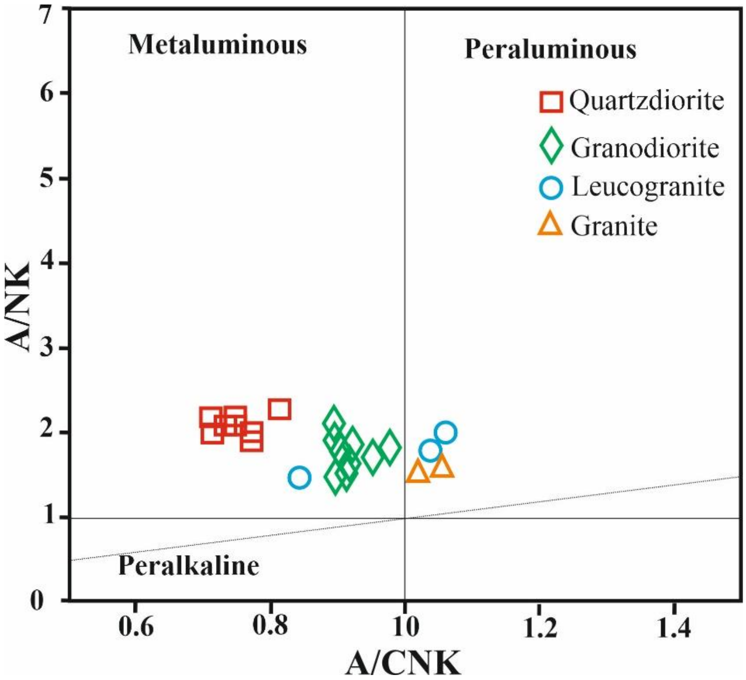

Figure 5.3: Alumina Saturation Index (ASI) of Dibang granitoids according to Shand (1943). Boundary between the fields of I-type and S-type granite according to Maniar and Piccoli (1989)

Relative to the composition of SiO_2 vs K_2O plot (Peccerillo and Taylor, 1976), the granitoids dominantly plot within the calc-alkaline rock series, with granites extending into the high-K calc-alkaline rock series (Figure 5.4), as per the classification scheme of Le Maitre et al. (1989). According to the Total Alkali Saturation (TAS) diagram (Middlemost, 1994), quartz diorites are mostly restricted to the gabbroic diorite field, granodiorites are scattered across the diorite, granodiorite, and monzonite fields, granites and leucogranites fall within the granodiorite and granite fields (Figure 5.5).

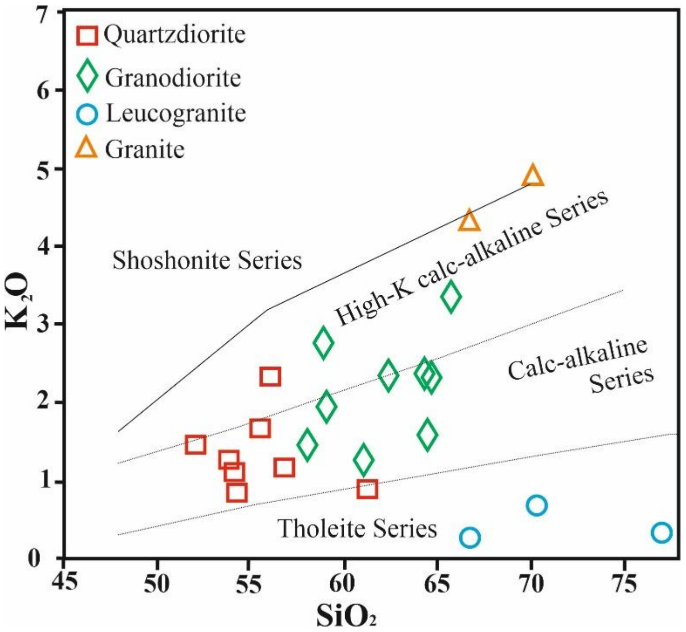

Figure 5.4: SiO_2 vs KO_2 plot (Peccerillo and Taylor, 1976)

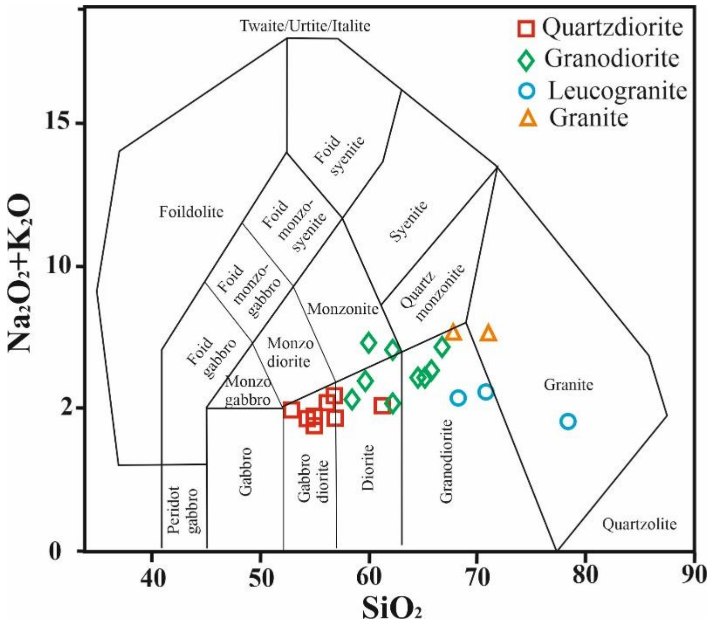

Figure 5.5: Na2O + K2O Vs SiO2 classification diagram after Middlemost (1994).

In the B-A plot of Debon Le Fort (1988), where B = (Fe+Mg+Ti) measures the maficity and A= Al – (K+Na+2Ca) indicates the aluminium balance to Ca and alkalis, separating the peraluminous and metaluminous fields and thus is analogous to the A/CNK index of Shand. Villaseca et al. (1998) modified the plot and further subdivided the peraluminous field into low, moderate, high and felsic peraluminous suites. The metaluminous field is occupied by the quartz diorites and granodiorites, while the leucogranites lie in the low-peraluminous field (weakly peraluminous) (Figure 5.6). The metaluminous nature of quartz diorites and granodiorites can be attributed to the presence of abundant ferromagnesian minerals as well as the occurrence of Fe-Ti oxides, titanite, and apatite, which are Ca-rich minerals. Meanwhile, the peraluminous nature of the granites and leucogranites can arise from some degree of fractionation trailed by hydrothermal or supra-crustal assimilation.

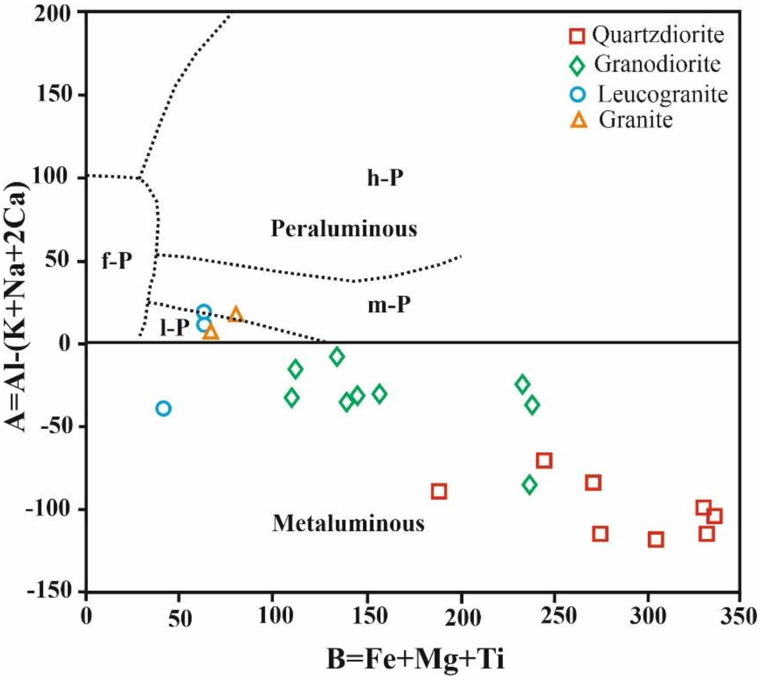

Figure 5.6: Discrimination plot of A = Al - (K + Na + 2Ca) vs. B = Fe + Mg + Ti with field boundaries from Debon and Le Fort (1983) and modified after Villaseca et al. (1998).

In the modified alkali lime index (MALI) diagram (Frost et al., 2001), the Dibang granitoids are mostly calcic to calc-alkalic (Figure 5.7a). The Fe# (FeO^t/FeO^t+MgO) of quartz diorites varies from 0.45-0.62 wt%, 0.49-0.66 wt% in granodiorites, 0.66-0.74 wt% in granites, and 0.84-0.96 wt% in leucogranites. The FeO^t/FeO^t+MgO vs SiO_2 classification diagram proposed by Frost et al. (2001) delineates a clear compositional trend that differentiates between iron-enriched and magnesian-enriched granite fields. This Fe-index plot (Figure 5.7b) indicates that the quartz diorites, granodiorites, and granites are predominantly magnesian. The leucogranites are ferroan, indicative of iron-enriched granite. This corresponds to the quartz diorites and granodiorites belonging to the metaluminous and the leucogranites to the peraluminous field in the A/NK vs. A/CNK diagram (Shand, 1943) (Figure 5.3).

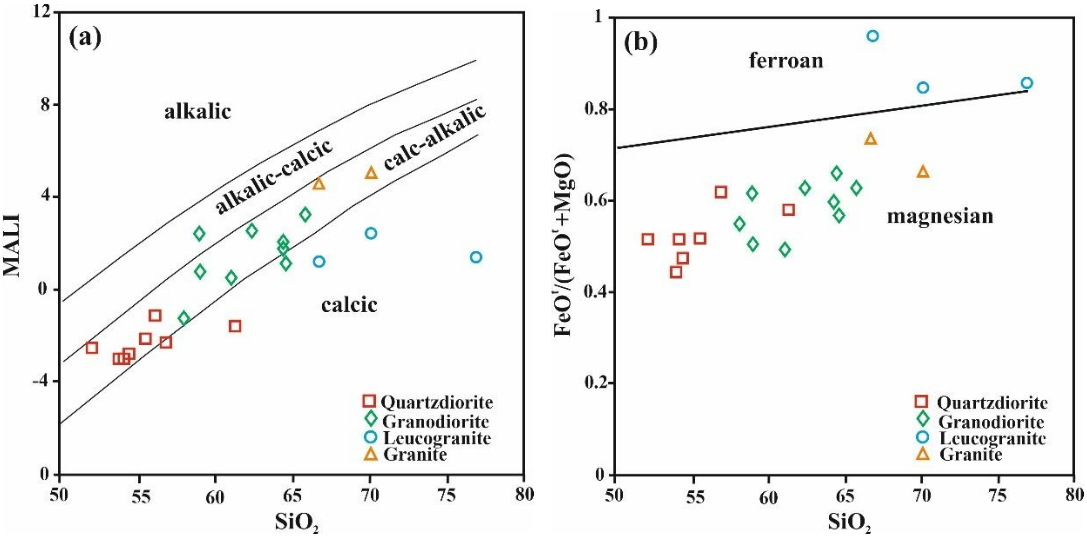

Figures 5.7: Classification diagrams of Frost et al. (2001) (a) SiO_2 vs MALI (Na_2O+K_2O-CaO); (b) (FeO^t/FeO^t+MgO) vs SiO_2.

Following the SiO_2 vs $Al_2O_3/(CaO+Na_2O+K_2O)$ classification of granitoids into I-type (igneous origin) and S-type (sedimentary origin) as proposed by White and Chappell (1977), the quartz diorites and granodiorites fall in the I-type granite field and granites and leucogranites lie very close to the S-type boundary (Figure 5.8) corresponding to metaluminous and weakly peraluminous granites. The I-type geochemical signature of the granitoids is supported by the mineralogy, where mafic silicate minerals (biotite and amphibole) are predominant, along with the presence of titanite, apatite, sphene and Fe-Ti oxides as accessory minerals. Correspondingly, the magmatic source is evident from the P_2O_5/ TiO_2 vs MgO/ CaO after Werner (1987), where the granitoids cluster in the field of magmatic rocks (Figure 5.9).

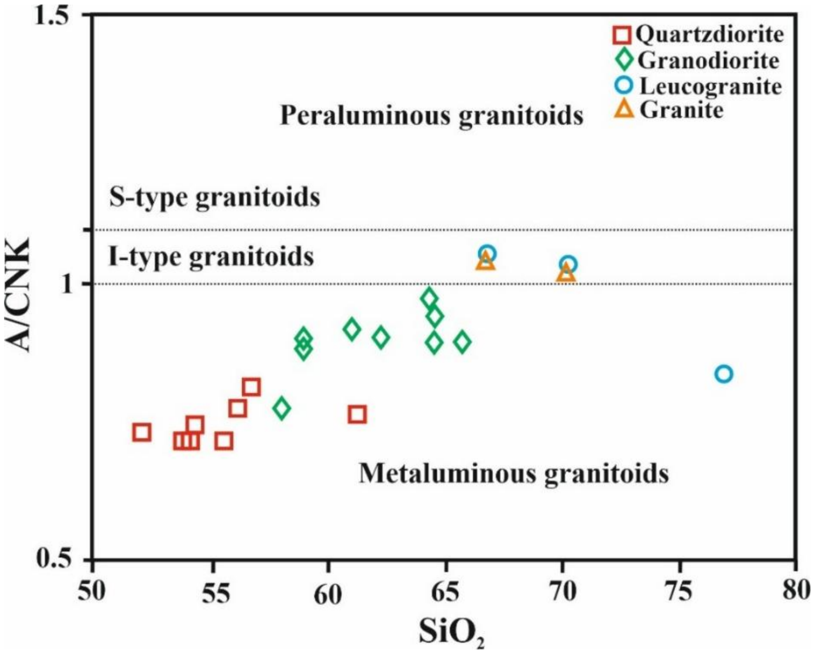

Figure 5.8: Classification scheme of molar ratio $Al_2O_3/(CaO + Na_2O+K_2O)$ vs SiO_2. Peraluminous and meta-aluminous granite fields after Chappell and White (1974); I (igneous) and S (sedimentary) origin fields after White and Chappell (1977)

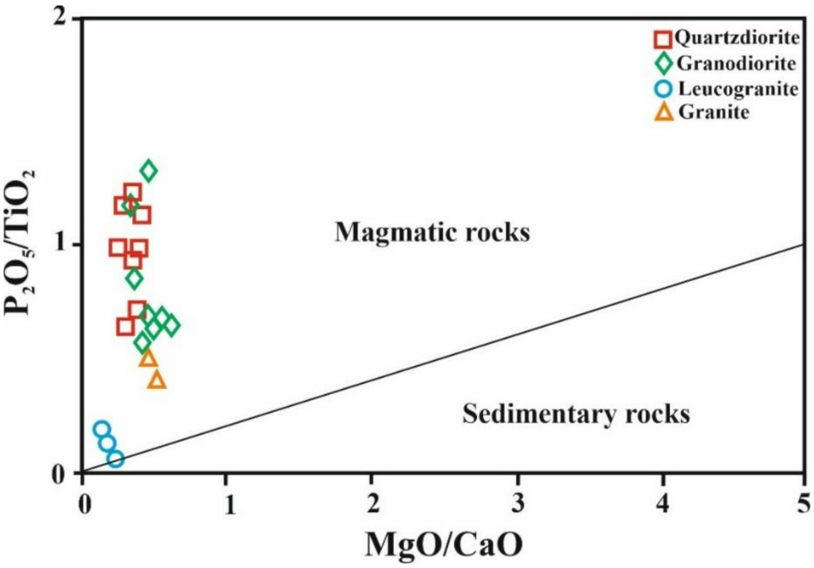

Figure 5.9: P_2O_5/TiO_2 vs MgO/CaO discrimination diagram of Ortho-para source after Werner (1987).

Bivariate Harker variation diagrams are an extensively employed and best-known graphical method of representing geochemical trends. It is based on the correlation of constituent major oxides in weight percentage plotted against SiO_2 wt.%. SiO_2 is selected to be plotted on the x-axis due to its broad compositional range and maximum variability observed in the granitoids. Most of the major elements, such as TiO_2, MgO, CaO, P_2O_5, and Fe_2O_3, display a continuous trend and decrease with increasing SiO_2 (Figure 5.10), exhibiting a negative correlation. Na_2O and K_2O have a positive correlation with SiO_2. Al_2O_3 shows large data scatter against SiO_2, lacking a systematic correlation. Depleting Fe_2O_3, MgO, and TiO_2 with an increase in SiO_2 could be a probable result of the fractionation of ferromagnesian (biotite, amphibole) minerals during magma evolution (through the process of magma differentiation and mixing).

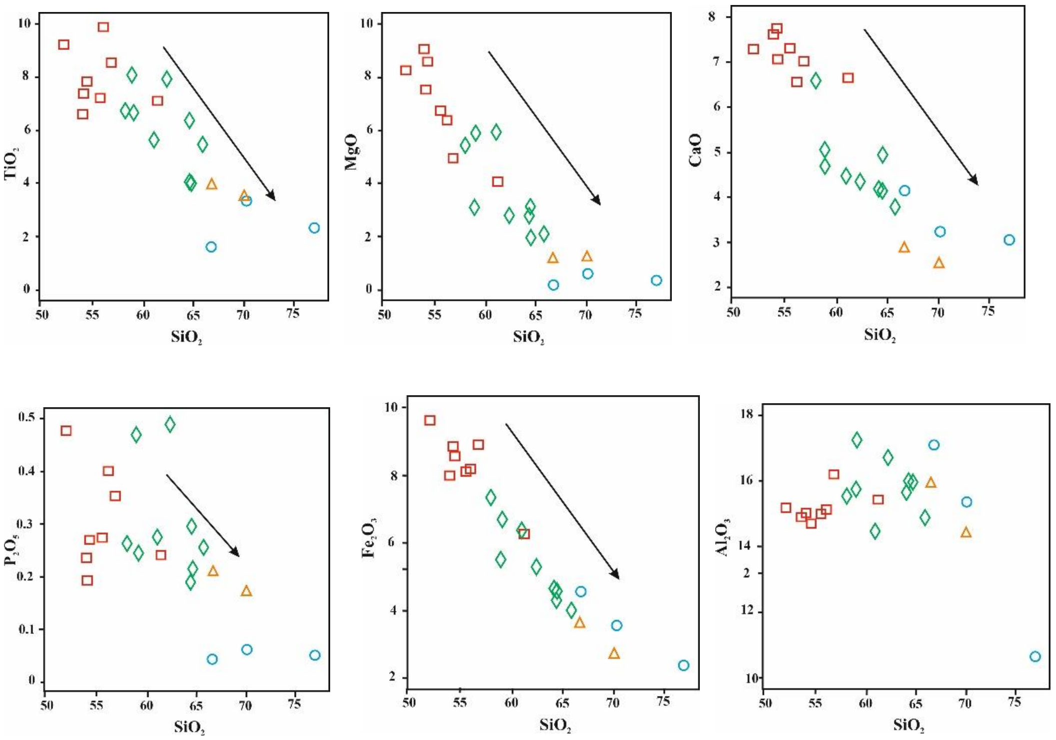

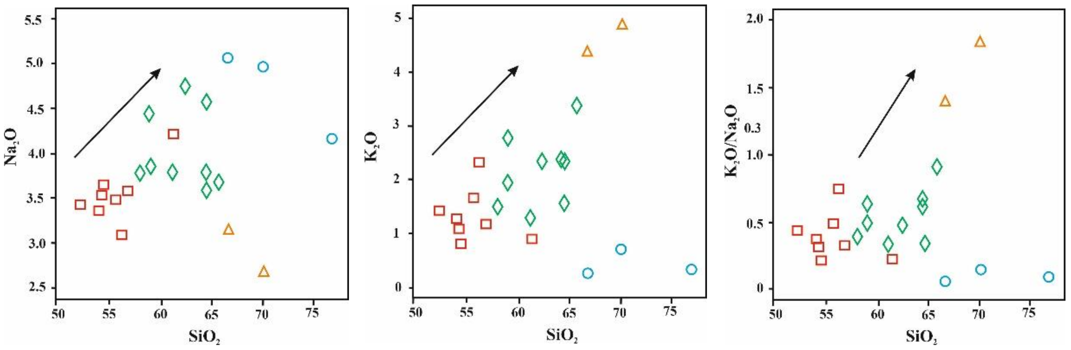

Figure 5.10: Bivariate Harker diagrams of major oxides vs SiO_2 for the Dibang granitoids. Symbols: Red square- quartz diorite; Green diamond- granodiorite; Orange triangle- granite; Blue circle- leucogranite.

6.2 TRACE ELEMENT GEOCHEMISTRY

6.2.1 INTRODUCTION

A trace element can be defined as an element present in a rock in concentrations of less than 0.1 wt %, i.e., <1000 ppm. Despite their low concentration, trace element geochemistry has become a vital part of petrologic studies as it helps in understanding geological processes from magma genesis and differentiation to the concentration of ore deposits and the evolution of the Earth as a whole. There is wide variation in the behaviour of trace elements, and they are collectively sensitive to processes to which major elements are insensitive. An example will be the depth at which partial melting occurs in the mantle.

Trace elements are preferentially partitioned or excluded by specific minerals based on their ionic radius, charge particles and electronegativity. According to their phase-specific activities and partition coefficients within an equilibrium melt-crystal system, the trace element redistributes between the melt and coexisting solid phases. In granitoids, trace elements can exist in different ways; some are found concentrated in the accessory minerals, while some substitute for major elements. While some of the rarer trace elements are sufficiently abundant to constitute accessory minerals of their own. Trace elements tend to display a preference either for the melt phase or the early-crystallising mineral phase. Based on their partition affinity to either one of the phases, they are grouped as incompatible (bulk distribution coefficient, i.e., D<<1) and compatible (D≥1) elements, respectively.

In the following section, an attempt has been made to study the nature and characteristics of trace elements, including Rare Earth Elements (REEs) of the representative granitoids of Dibang Valley. Analytical results of trace element content (in ppm), including REE, and vital element ratios of petrogenetic significance such as Ga/Al, K/Rb, Rb/Sr, Nb/Ta, Eu/Eu*, etc., for the representative Dibang Valley granitoids are given in Table 5.2

6.2.2 TRACE ELEMENT CHARACTERISTICS

QUARTZ DIORITE

Quartz diorites of Dibang Valley have a lower concentration of transitional elements (e.g., Ni= 6.91-10.99 ppm, Cr= 15.76-113.76 ppm, Co= 16.85-33.95 ppm) and higher content of Sc= 12.50-19.02 ppm, V= 106.60-210.50 ppm. They are enriched in incompatible elements like Ba (143.01-378.83 ppm), Sr (414.83-659.13 ppm), with low Rb (16.52-54.53 ppm). They have a moderate concentration of Zr (103.88-138.75 ppm), and Y (15.38-31.35 ppm) and low contents of U (0.90-2.50 ppm) and Th (1.11-12.40 ppm). Ga/Al values range from 2.06-2.64 ppm. Primitive mantle normalized trace element patterns (Sun and McDonough, 1989) show that the quartz diorites are enriched in large-ion-lithophile elements (LILEs) (e.g., Rb, Ba, Sr, Pb, Nd, Sm) and depleted in high field strength elements (HFSE) (e.g., Nb, Ta, P, Ti) (Figure 5.11a). The strongly depleted negative Nb anomaly and enrichment in LILEs are consistent with their origin in a subduction-related environment.

GRANODIORITE

The Dibang granodiorites are also enriched in incompatible elements (Ba= 297.35-a1163-01 ppm, Sr= 572.89-775.71 ppm, Rb= 27.06-67.69 ppm). Reduced concentration of transitional elements (Ni= 4.32-15.56 ppm, Cr= 11.16-33.53 ppm, Co= 8.45-21.20 ppm) and modest abundance of Sc (5.35-14.82 ppm), and V (59.30-154.67 ppm). Moderate enrichment of Zr (88.08-130.32 ppm), Y (10.21-26.04 ppm), with low U (0.93-2.03 ppm) and Th (1.21-7.94 ppm) is recorded. The Ga/Al values vary in a narrow range between 2.15-2.48 ppm. REEs normalized to Primitive mantle values (Sun and McDonough, 1989) show that the granodiorites are enriched in large-ion-lithophile elements (LILEs) (e.g., Rb, Ba, Sr, Pb, Nd, Sm) and depleted in high field strength elements (HFSE) (e.g., Nb, Ta, P, Ti) (Figure 5.11b)

GRANITE

The biotite-rich granites of Dibang Valley bear a high content of incompatible elements (Ba=777.39-2652.42 ppm, Rb=93.42-194.99 ppm, Sr=440.25-611.90 ppm) and a low concentration of transitional elements (Ni=4.67-4.87 ppm, Cr=17.59-19.73 ppm, Co=6.42-6.69 ppm, Sc=6.32-11.35, V=5.24-48.36). The value of Y ranges from 19.80-34.07 ppm and that of Zr range from 116.63-120.23 ppm. The concentration of Th (9.55-42.47 ppm) and U (1.74-5.80 ppm) is slightly higher than the other granitoids. (Ga/Al ranges from 2.10-2.38 ppm. Primitive mantle normalized REE distribution patterns (Sun and McDonough, 1989) indicate that these granites are enriched in large-ion-lithophile elements (LILEs) (e.g., Ba, Sr, Pb, Nd, Sm) and depleted in high field strength elements (HFSE) (e.g., Nb, Ti) (Figure 5.11c) The high Sr (440.25-611.90) values, along with the slightly depleted HREE, may suggest the involvement of mantle as well as crustal source.

LEUCOGRANITE

The garnet bearing two-mica leucogranites have comparatively much lower concentration of incompatible elements (Ba=40.47-119.32 ppm, Rb=2.18-11.28 ppm, Sr=146.71-451.61 ppm) and a similar low concentration of transitional elements (Ni=5.19-5.69 ppm, Cr=9.85-14.01 ppm, Co=1.73-2.66 ppm, Sc= 6.32-11.35 ppm, V= 5.24-27.04 ppm). Th (0.50-1.01 ppm) and U (0.16-0.93 ppm) is also very low. The Ga/Al values vary between 1.57-2.51 ppm. REE spidergrams of leucogranites normalized to Primitive mantle values (Sun and McDonough, 1989) show that they are slightly enriched in LILE (e.g., Ba, Sr, Pb, Nd, Sm) and depleted in high field strength elements (HFSE) (e.g., Nb, Zr, Ti) (Figure 5.11d).

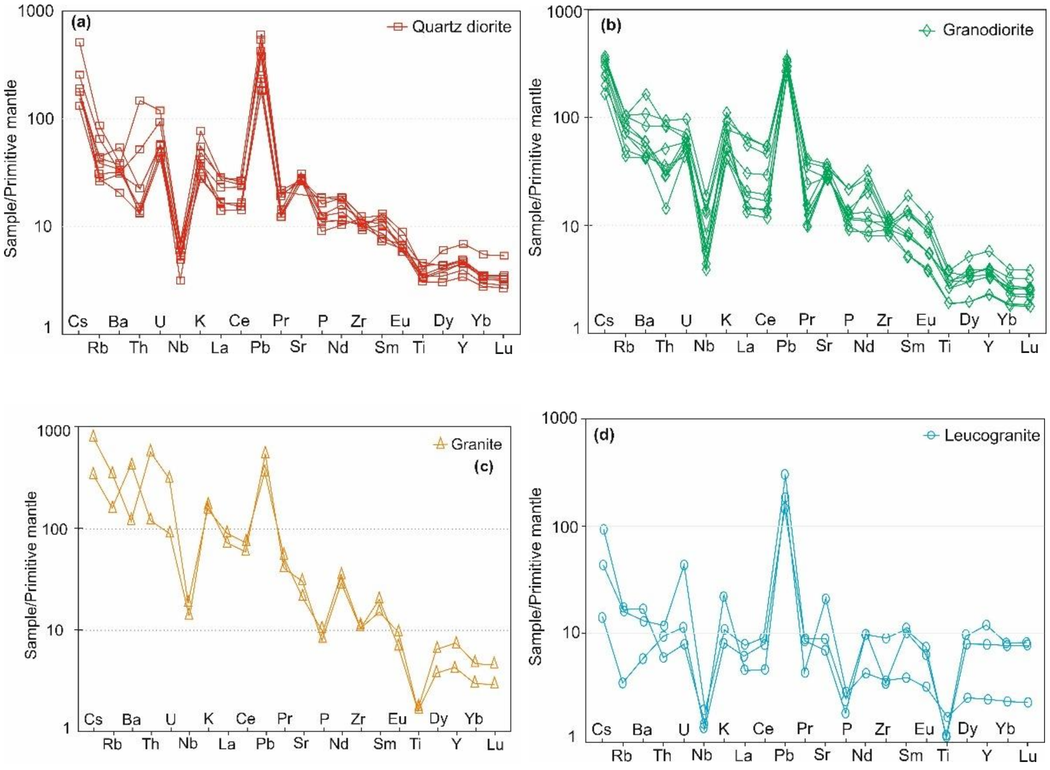

Figure 5.11: Chondrite-normalized (Sun and Mc Donough, 1989) rare earth elements (REE) patterns of (a) quartz diorite; (b) granodiorite; (c) granite; and (d) leucogranite

6.2.3 BEHAVIOUR OF TRACE ELEMENTS

Variation of trace elements plotted against SiO_2 are shown in the bivariate Harker's diagram (Figure 5.12). Progressive enrichment of Rb, Nb, Ta, and Cs with increasing SiO_2 is observed, while Ti, V, Co, Ni, Cu, La, Ga, Hf, and Zr display a distinct negative trend. SiO_2 versus the elements Ba, Sr, Y, U, and Th do not show any trend but rather define a field. The granitoids exhibit a trace element composition characterized by a high content of Sr (av. 529.70) and a low content of Yb (av. 1.86). An increase in the concentration of Ba, Pb and Sr and a decrease Nb concentration is observed. The distinct negative anomalies identified for Nb, and Ti and positive anomaly observed for Pb is consistent with the calc-alkaline nature of the granitoids. The positive Sr anomaly points to a limited degree of plagioclase fractionation. The granitoids are rich in LILEs (Rb, Ba and Sr) and strongly depleted in HFSEs (Nb, Ta), suggesting obvious characteristics of arc magmatic rocks and emplacement in a subduction environment.

Whalen et al. (1987) proposed several diagrams to geochemically distinguish A-type granites from the other granite types (S-, I-, and M-type) and also differentiate fractionated and unfractionated I- and S-type granites. On the Zr+Nb+Y+Ce vs (Na_2O+K_2O)/CaO diagram (Figure 5.13a), all the granitoids from the present study fall within the unfractionated I- and S-type granite field. On the Zr vs. 10000Ga/Al plot (Figure 5.13b), all samples fall in the I- and S-type granite field. The concentration of Zr+Nb+Y+Ce in the granitoids varies between 57.95-288.06 ppm, which is typical of calc-alkaline I-type granites (<350 ppm threshold) (e.g., Whalen et al., 1987; Frost and Frost, 2008).

The evolutionary nature of the granitoids is expressed in the ternary relationship diagram of Rb-Ba-Sr (Figure 5.14) proposed by El Bouseily and El Sokkary (1975). All the granitoids from this study plot close to the Ba-Sr boundary, indicating that these granitoids have undergone limited fractional crystallization and are moderately evolved. This is consistent with the high Ba and Sr values, low Rb/Sr (av. 0.09), moderate to negligible europium anomalies with minimal plagioclase fractionation and its metaluminous to weakly peraluminous character.

Primitive mantle normalized spidergrams of the granitoids display pronounced spikes at Ba, U, K, Pb, Sr, Y and prominent troughs at Rb, Nb, Zr and Ti. A distinguished positive Pb anomaly present with a marked negative Nb anomaly is typical of magma derived from a subduction-related setting (e.g., Zartman and Doe, 1981; Saunders et al., 1991). Thus, inclusion of crustal component is anticipated in the genesis of Dibang granitoids.

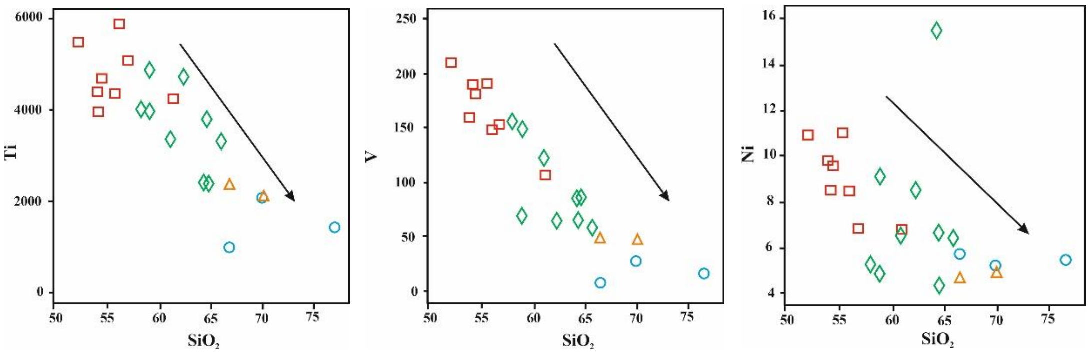

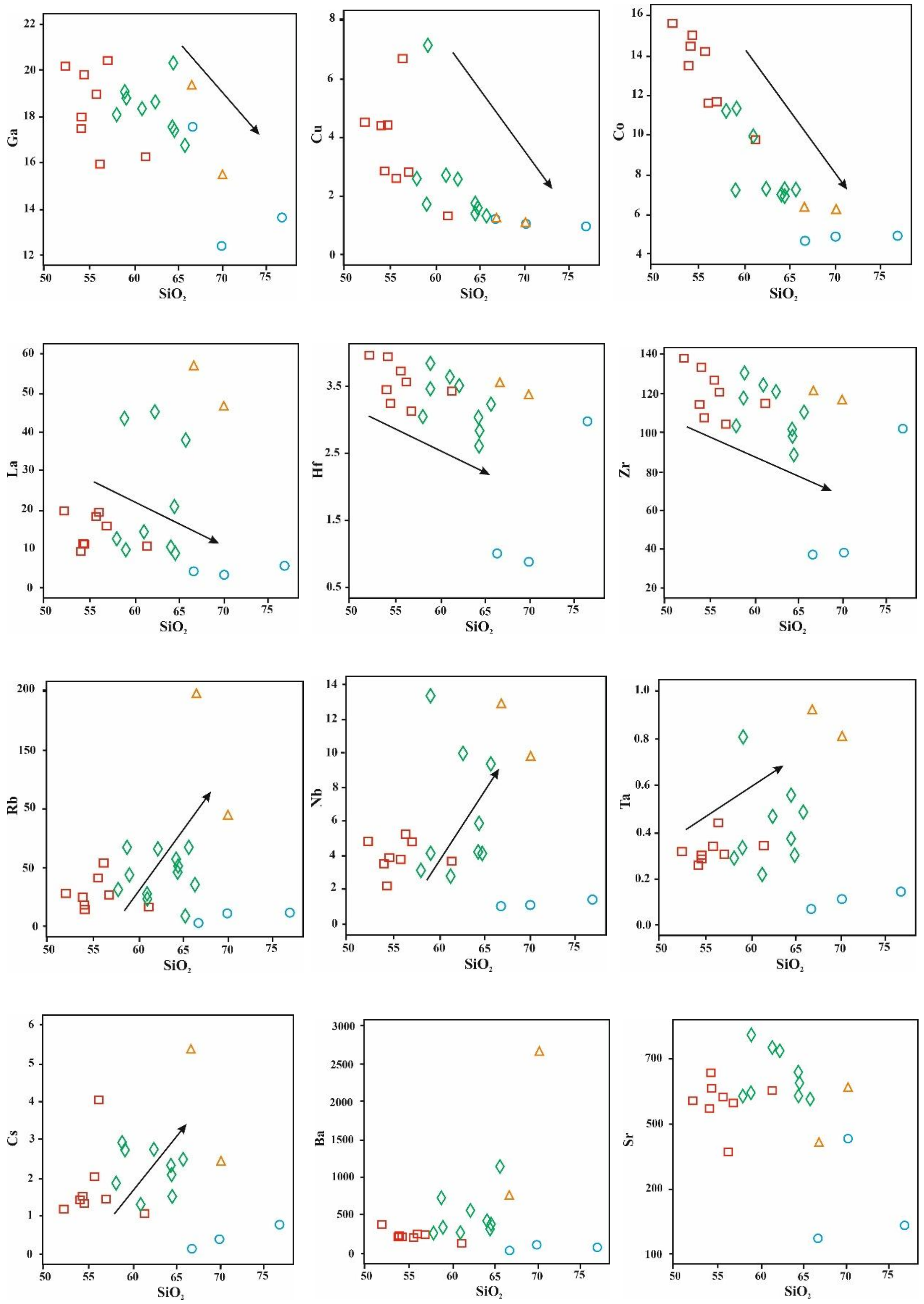
Ga
22
20
18
16
14
12
50
55
60
65
70
75
SiO₂
Cu
8
6
4
2
0
SiO₂
Co
16
14
12
10
8
6
4
SiO₂
La
60
50
40
30
20
10
0
SiO₂
Hf
3.5
2.5
1.5
0.5
SiO₂
Zr
140
120
100
80
60
40
20
SiO₂
Rb
200
150
50
50
0
SiO₂
Nb
14
12
10
8
6
4
2
0
SiO₂
Ta
1.0
0.8
0.6
0.4
0.2
0.0
SiO₂
Cs
6
5
4
3
2
1
0
SiO₂
Ba
3000
2500
2000
1500
1000
500
0
SiO₂
Sr
700
500
200
100
SiO₂

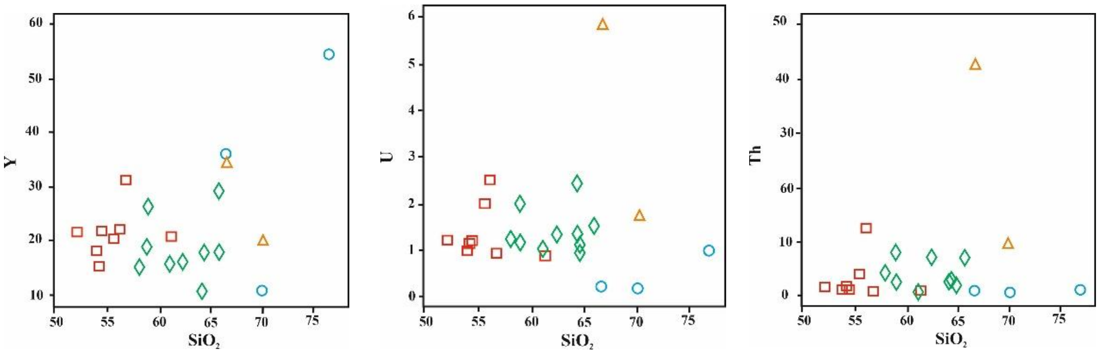

Figure 5.12: Bivariate Harker diagrams of trace elements vs SiO_2 for the Dibang granitoids. Symbols: Red square- quartz diorite; Green diamond- granodiorite; Orange triangle- granite; Blue circle- leucogranite.

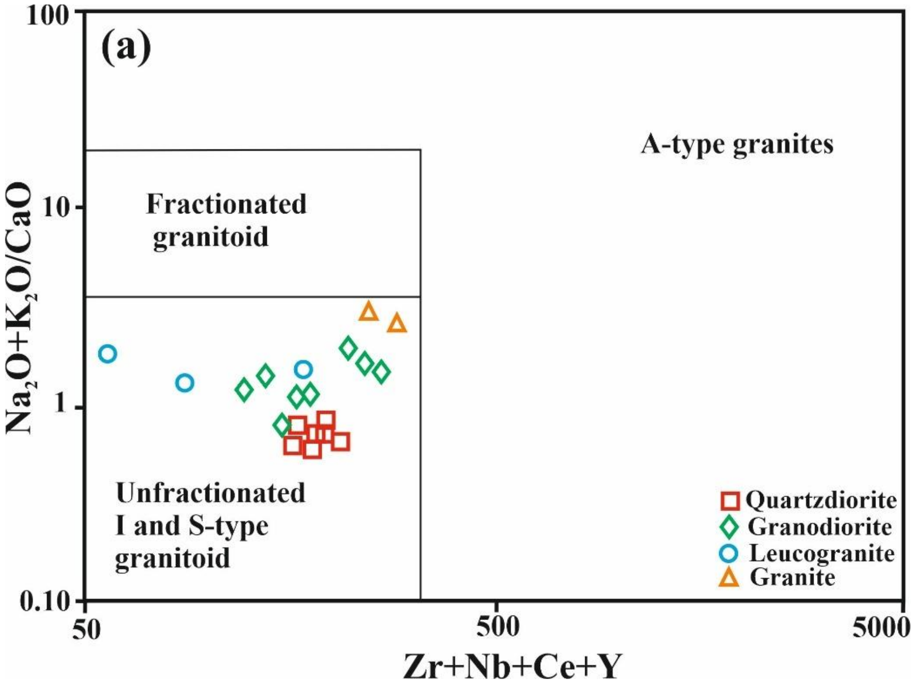

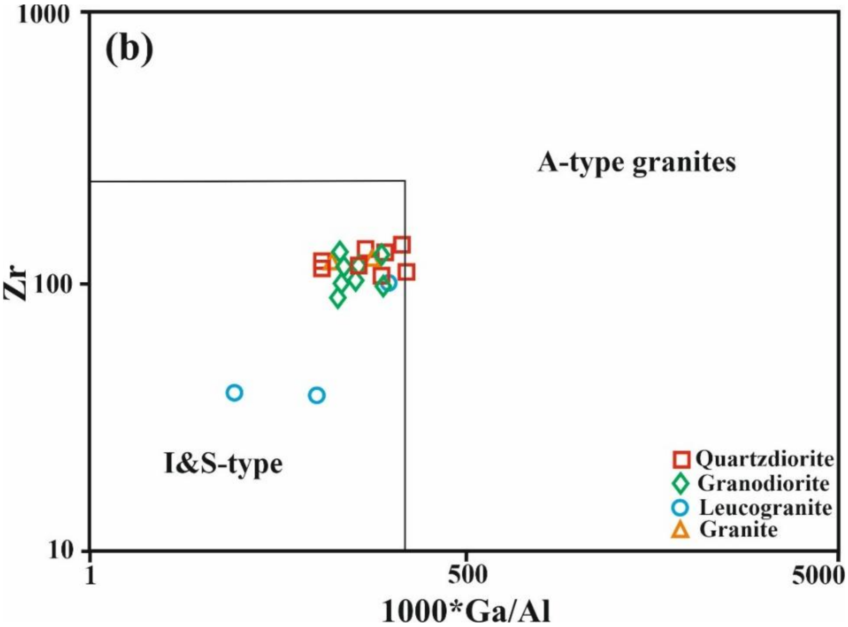

Figure 5.13: (a) Zr+Nb+Ce+Y vs Na_2O+K_2O/CaO discrimination diagram for fractionated, unfractionated I- and S-type, and A-type granitoids. (b) Discrimination diagram for I- and S-type, and A-type granites (Whalen et al., 1987).

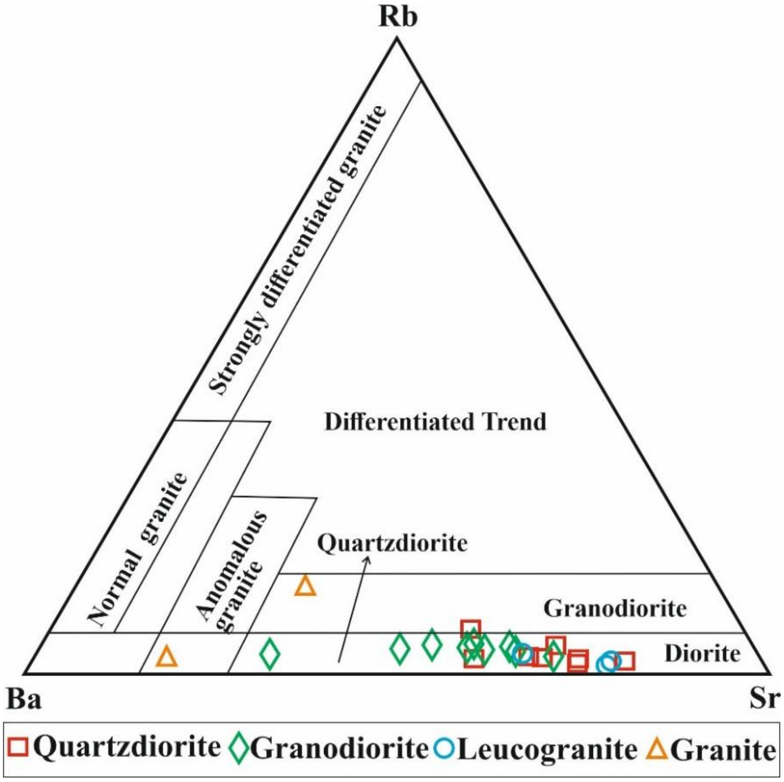

Figure 5.14: Ba-Rb-Sr ternary diagram for Dibang granitoids. Fields of composition and differentiation trends after El Bouseily and El Sokkary, 1975.

6.3 RARE EARTH ELEMENS (REE)

Rare Earth Elements (REE) are the most useful of all trace elements and comprise the series of metals with atomic numbers 57-71, i.e., La-Lu. Rare Earth Elements (REEs) have important applications in petrogenetic studies because they all have very similar chemical and physical attributes and are relatively unaffected by hydrothermal processes. The small difference in sizes and behaviour is used by several petrological processes, which causes the REE series to become fractionated relative to each other. The chemical similarity in REE is because they all form stable 3+ ions under most geological conditions. However, Europium (Eu) can occur in two oxidation states, Eu^{2+} and $Eu^{3+,}$ and it is this peculiar property of Eu that makes it particularly interesting in interpreting geochemical processes. REE concentrations in rocks are normalised to a standard value using values for chondrite meteorites. In the present study, the REEs are normalised after Sun and McDonough 1989. Observed chondrite-normalised REE patterns are used to deduce the minerals involved either in fractional crystallisation or partial melting. The presence or absence of Europium anomalies are chiefly controlled by the role of feldspars. Detailed examination of the behaviour of REE and its distribution pattern is used extensively in geochemistry to probe into the genesis of rock suites and unravel petrological processes

The obtained values of rare earth elements (La to Lu) in ppm from the representative granitoids, along with the chondrite-normalised values (after Sun and McDonough, 1989) and calculated LREE to HREE fractionation (La_N/Lu_N or Ce_N/Yb_N), Eu* (=Sm_N+Gd_N/2) and Eu-anomaly (Eu_N/Eu*) are given in Table 5.3.

QUARTZ DIORITE

Compared to the average total REE concentration of about 250 ppm recorded in common granitic rocks (Emmermann et al., 1975), the studied quartz diorites record comparatively lower concentrations (ΣREE = 68.13-116.95 ppm; av. 92.15). Chondrite-normalized spidergram (Sun and McDonough, 1989) show moderately fractionated REE patterns (Figure 5.15a) characterized by $(La/Yb)_N$ = 4.19-8.96 ppm and $(Ce/Yb)_N$ = 4.27-8.31 ppm with reasonable enrichment of LREE [$(La/Sm)_N$ = 1.60-2.57 ppm, $(La/Lu)_N$ = 4.30-9.19 ppm] and depleted HREE pattern [$(Gd/Yb)_N$ =

1.29-2.01 ppm] suggesting involvement of mantle source. The moderate to weak negative Eu anomalies with Eu/Eu* values of 0.64-1.11 ppm suggest minimal plagioclase fractionation and are typical of continental arc-related igneous rocks.

GRANODIORITE

The granodiorites are characterized by higher REE concentration compared to quartz diorite (ΣREE = 51.12-220.44 ppm, av. 117.92 ppm). Chondrite-normalized REE patterns (Sun and McDonough, 1989) show enrichment in LREE [$(La/Sm)_N$ = 1.52-4.81 ppm, $(La/Lu)_N$ = 4.65-28.85] with respect to HREE [$(Gd/Yb)_N$ = 1.38-3.06 ppm] and exhibit a moderately fractionated REE pattern (Figure 5.15b) characterized by $(La/Yb)_N$ = 4.08-28.13 ppm and $(Ce/Yb)_N$ = 4.42-22.89 ppm suggesting involvement of mantle source. The negligible Eu anomaly (Eu/Eu* = 0.81-0.95 ppm) indicates that no significant fractionation of plagioclase occurred.

GRANITE

The biotite-rich granites have a similar REE composition to the granodiorites. Total REE range between 213.94-264.30 ppm. REE patterns in the chondrite-normalized spidergram show highly fractionated REEs (Figure 5.15c) characterized by $(La/Yb)_N$ = 17.11-21.86 ppm and $(Ce/Yb)_N$ = 14.06-17.96 ppm with enrichment of LREE [$(La/Sm)_N$ = 4.26-4.48 ppm, $(La/Lu)_N$ = 17.54-22.41 ppm] and depleted HREE pattern [$(Gd/Yb)_N$ = 1.95-2.14 ppm]. Eu/Eu* value varies from 0.49-0.90 ppm, indicating a negative to moderate Eu anomaly with significant fractionation of plagioclase taking place.

LEUCOGRANITE

Total REE for the garnet-bearing two-mica leucogranite is comparatively low (ΣREE= 36.10-96.03 ppm). In the chondrite-normalized diagram (Figure 5.15d), these leucogranites exhibit more HREE enrichment [$(Gd/Yb)_N$ = 1.01-1.21 ppm] relative to the depleted LREE [$(La/Sm)_N$ = 0.61-1.19 ppm, $(La/Lu)_N$ = 0.79-2.02 ppm] giving an almost flat REE pattern suggesting less fractionation also characterized by [$(La/Yb)_N$ = 0.79-2.04 ppm and $(Ce/Yb)_N$ = 1.01-2.08 ppm]. The moderate degree of Eu anomalies (Eu/Eu* = 0.71-0.96 ppm) indicates that no significant fractionation of plagioclase occurred.

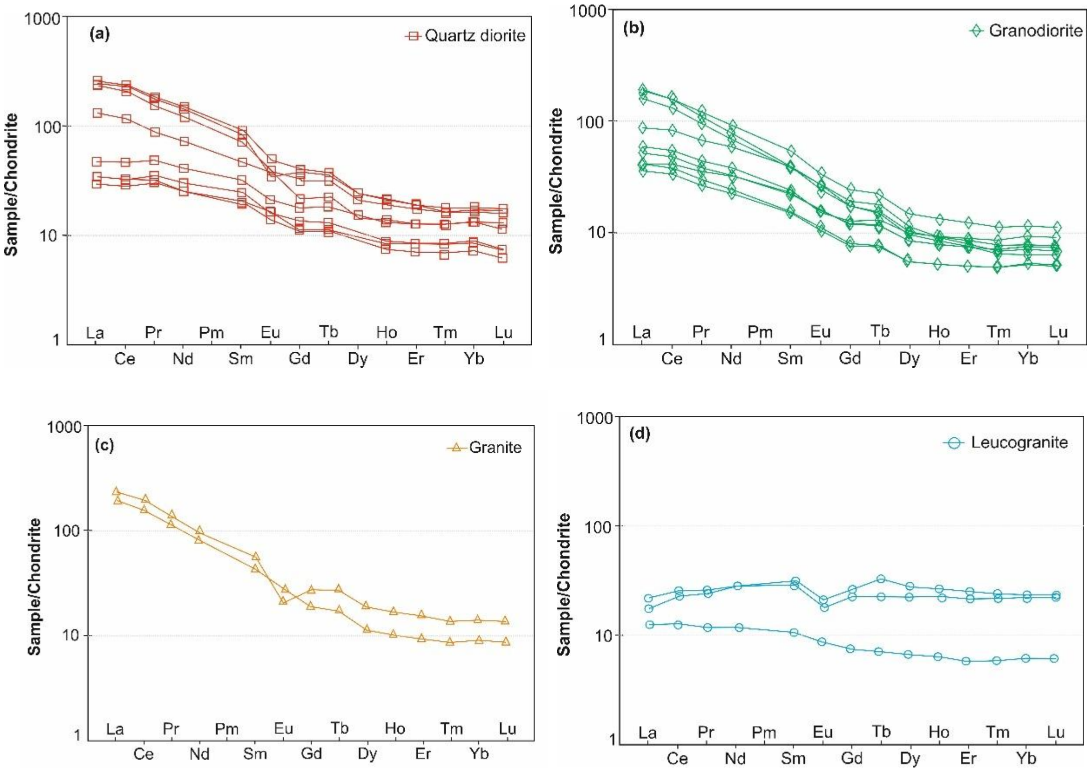

Figure 15.5: Chondrite-normalized (Sun and McDonough, 1989) rare earth elements (REE) patterns of the Dibang Valley granitoids (a) Quartz diorite; (b) Granodiorite; (c) Granite; (d) Leucogranite.

6.4 TECTONIC ENVIRONMENT

Whole-rock geochemistry plays a crucial role in understanding the tectonic setting of granitic rocks (Förster et al., 1997; Pearce et al., 1984). Numerous geochemical parameters have been suggested by various researchers (e.g., Pitcher, 1983; Pearce et al., 1984; Batchelor and Bowden, 1985; Harris et al., 1986; Maniar and Piccoli, 1989; Barbarin, 1996, 1999) to determine the tectono-magmatic environment of these rocks.

Pearce et al. (1984) proposed several tectonic discrimination diagrams based on the values of Y, Nb, Ta, and Rb. Concentration Y, Nb, and Ta are typically more enriched in normal ocean ridge settings and within-plate granites compared to volcanic arc granites. Rb serves as a highly effective discriminator between the oceanic ridge granites (ORG) and within-plate granites (WPG), as well as between volcanic arc granites (VAG) and syn-collisional granites (syn-COLG). Consequently, these trace elements are particularly valuable for tectonic discrimination (Pearce et al., 1984). The studied Dibang Valley granitoids fall within the VAG + syn-COLG field in the Nb vs Y plot (Figure 5.16a) and within the VAG field in the Rb vs Y+Nb plot (Figure 5.16b), indicating arc-related origin.

This is supported by the FeO^t/FeO^t+MgO vs SiO_2 plot (Figure 5.16c) from Maniar and Piccoli (1989), showing most granitoids in the island arc, continental arc, and continental collision granite fields. the leucogranites, however, fall within the rift-related, continental uplift, and post-orogenic granite fields. These leucogranites exhibit higher A/CNK values (>1.04), indicating they are S-type granites, which suggests a crustal or continental origin linked to syn- or post-orogenic tectonic processes.

The muti-cationic R_1-R_2 [$R_1 = 4Si-11(Na + K)- 2(Fe + Ti) – R_2 = 6Ca + 2Mg = Al$] diagram (Batchelor and Bowden, 1985; De la Roche et al., 1980) has geotectonic and petrogenetic implications for granitoid suites. In this diagram, it is observed that the quartz diorite and granodiorite are mostly compatible with pre-plate collision (i.e. I-type) whereas granites and leucogranites plot in closer proximity to the syn-collision orogenic setting (i.e. S- type) (Figure 5.16d).

In the A-B multicationic diagram (Figure 5.17) of Debon and Le Fort (1988), six fields are recognised depending upon the aluminosity of the rock. The quartz diorite and granodiorite belong to field IV (i.e., Bt, Amp, ± Px), whereas the granites and leucogranites belong to field III (Bt, ± minor Amp), suggestive of both mantle and crustal sources for the generation of LPC magma.

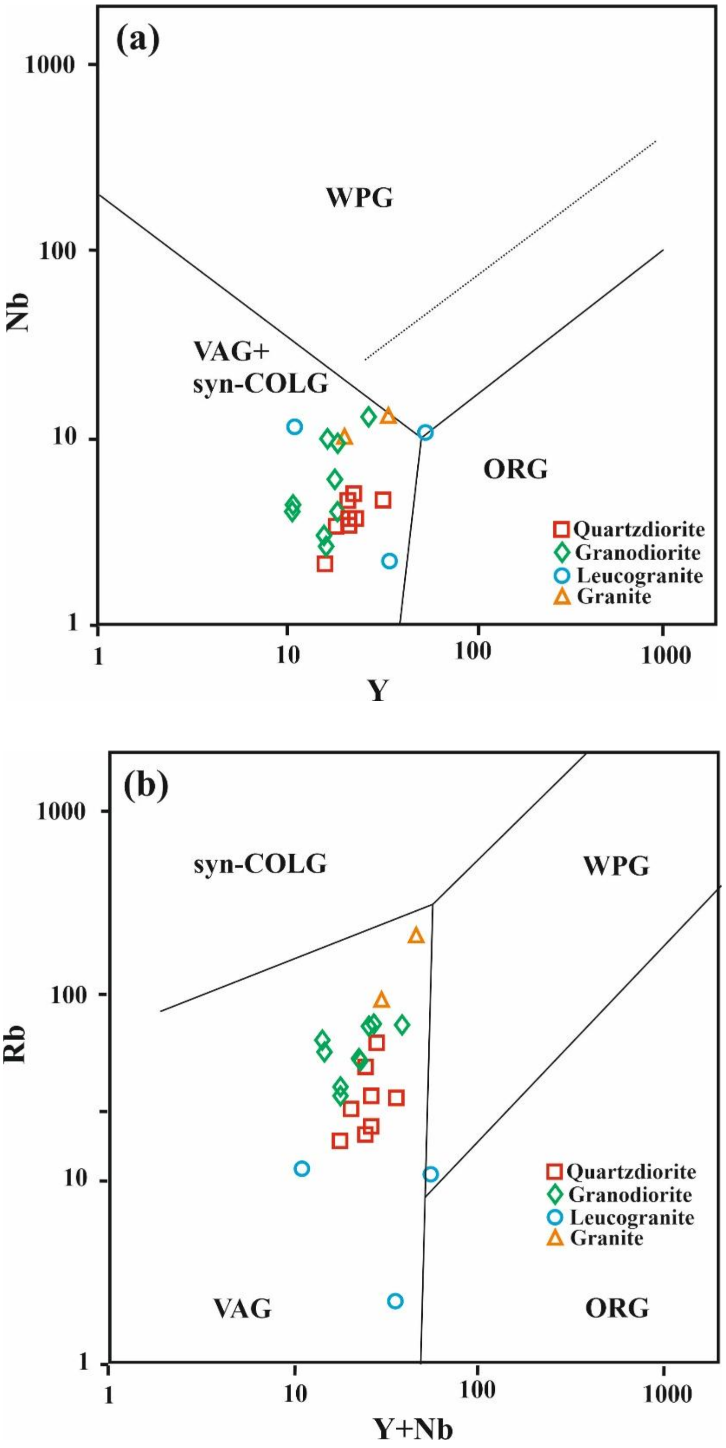

Figure 5.16: Tectonic discrimination diagram (a) Nb vs Y; (b) Rb vs Y+Nb (Pearce et al., 1984)

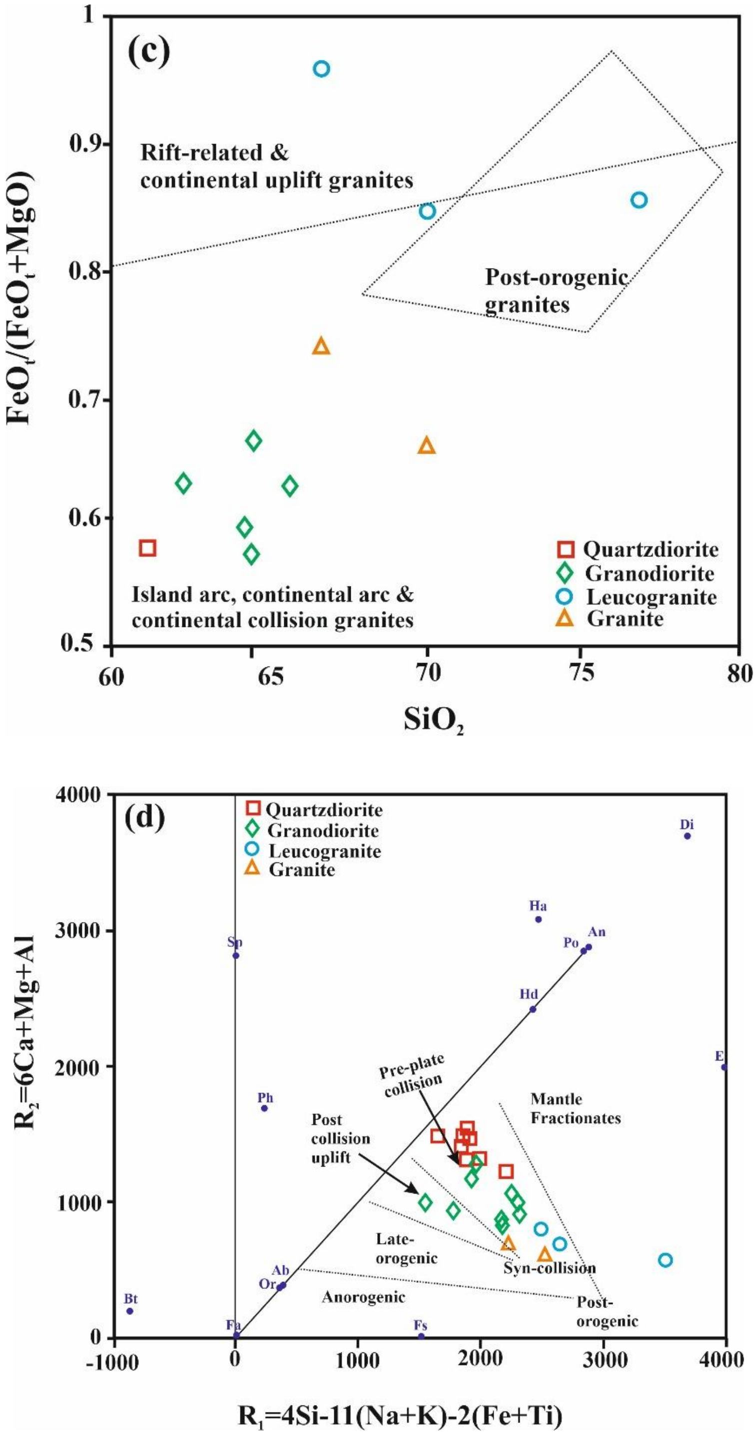

Figure 5.16: Tectonic discrimination diagram (c) FeO^t/FeO^t+MgO vs SiO$_2$ plot (Maniar and Piccoli, 1989); (d) R1 vs R2 multicationic plot (Batchelor and Bowden, 1985)

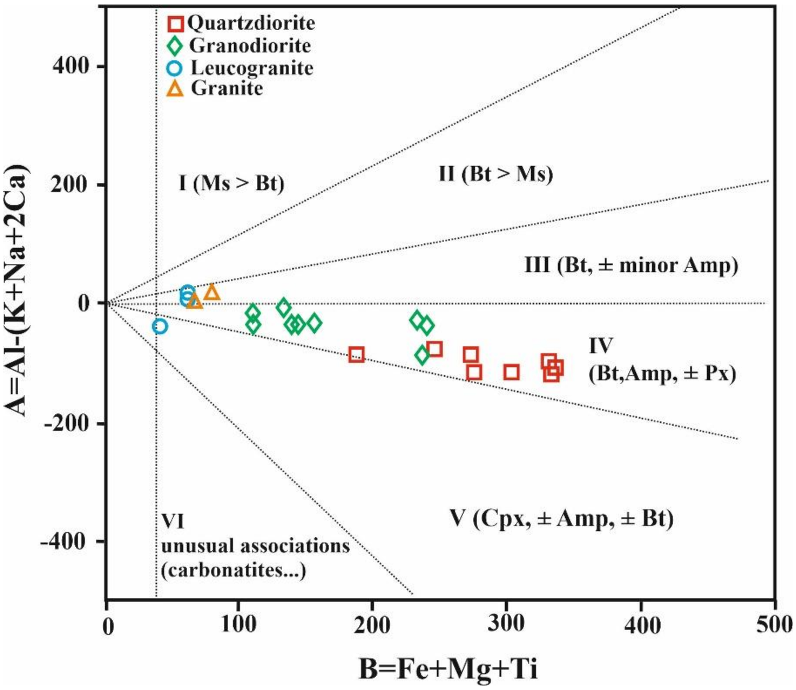

Figure 5.17: Multicationic A-B (characteristic minerals) diagram of Debon Le Fort (1988). Six fields are represented by Field I=(Ms>Bt); II=(Bt>Ms); III=(Bt, ± minor Amp); IV=(Bt, Amp, ± Px); V=(Cpx, ± Amp, ± Bt); VI= unusual associations (carbonatites).

Table 5.1: Major oxides (wt%) and CIPW normative (wt%) values of representative Dibang Valley Granitoids

	Quartz diorite							
Sample No.	**D2**	**M1**	**E5**	**E6**	**E11**	**E12**	**E13**	**E14**
SiO_2	56.79	61.22	53.87	54.32	55.53	56.09	54.12	52.00
TiO_2	0.85	0.71	0.74	0.78	0.72	0.98	0.66	0.92
Al_2O_3	16.20	15.45	14.88	14.71	15.01	15.14	15.03	15.12
Fe_2O_3	8.93	6.21	8.00	8.56	8.11	8.17	8.83	9.60
MnO	0.17	0.11	0.14	0.15	0.12	0.12	0.14	0.14
MgO	4.92	4.09	8.96	8.58	6.72	6.38	7.48	8.21
CaO	6.99	6.64	7.61	7.08	7.30	6.54	7.69	7.28
Na_2O	3.58	4.20	3.36	3.62	3.49	3.07	3.53	3.41
K_2O	1.16	0.88	1.25	0.81	1.68	2.32	1.09	1.45
P_2O_5	0.36	0.24	0.24	0.27	0.27	0.40	0.20	0.39
Total	**99.95**	**99.77**	**99.06**	**98.90**	**98.96**	**99.22**	**98.75**	**98.52**
FeO^t	8.03	5.59	7.20	7.71	7.30	7.35	7.94	8.64
FeO	7.65	5.15	6.90	7.39	7.02	6.69	7.84	8.22
Fe_2O_3*	1.28	1.07	1.10	1.17	1.09	1.47	0.99	1.38
Na_2O/ K_2O	3.08	4.78	2.68	4.46	2.08	1.33	3.24	2.35
K_2O/Na_2O	0.32	0.21	0.37	0.22	0.48	0.75	0.31	0.43
K_2O+Na_2O	4.74	5.08	4.62	4.43	5.17	5.39	4.61	4.85
Al_2O_3/TiO_2	19.04	21.69	20.24	18.78	20.73	15.40	22.77	16.49
P2O5/TiO_2	0.42	0.34	0.32	0.35	0.38	0.41	0.30	0.43
MgO/CaO	0.70	0.62	1.18	1.21	0.92	0.98	0.97	1.13
FeO^t/MgO	1.63	1.37	0.80	0.90	1.09	1.15	1.06	1.05
TiO_2/MgO	0.17	0.17	0.08	0.09	0.11	0.15	0.09	0.11
CaO/Na_2O	1.95	1.58	2.26	1.95	2.09	2.13	2.18	2.14
A/NK	2.27	1.96	2.16	2.15	1.99	2.00	2.15	2.11
A/CNK	0.82	0.77	0.72	0.75	0.72	0.78	0.72	0.74
Mg#	53.42	58.60	69.83	67.42	63.02	62.96	62.96	64.01

FeO^t/FeO^t+MgO	0.62	0.58	0.45	0.47	0.52	0.54	0.52	0.51
FMMT	13.97	10.50	17.04	17.22	14.86	14.84	16.21	17.91
CIPW norm								
Q	11.87	16.08	3.62	5.53	6.97	8.94	5.59	2.48
C	0	0	0	0	0	0	0	0
Or	6.86	5.20	7.41	4.79	9.90	13.68	6.42	8.56
Ab	30.29	35.57	28.47	30.63	29.54	26.01	29.84	28.82
An	24.71	20.68	21.78	21.48	20.34	20.67	21.97	21.69
Di	4.15	6.73	9.67	7.54	9.40	4.81	10.23	7.19
Hy	10.34	7.07	17.85	17.88	12.38	13.67	13.88	17.12
Mt	0	0	0	0	0	0	0	0
Il	0.36	0.23	0.30	0.32	0.26	0.26	0.29	0.30
Hm	8.93	6.21	8.00	8.57	8.11	8.17	8.83	9.60
Tn	1.63	1.45	1.42	1.51	1.44	2.08	1.24	1.86
Ru	0	0	0	0	0	0	0	0
Ap	0.84	0.57	0.56	0.65	0.65	0.96	0.46	0.93
Sum	99.97	99.78	99.07	98.91	98.98	99.24	98.76	98.55

$FeO^t = Fe_2O_3*0.9$; $Fe_2O_3* = TiO2*1.5$; $FeO = Fe_2O_3 - Fe_2O_3*$; A/CNK=molar $Al_2O_3/(CaO+Na_2O+K_2O)$; Fe_2O_3: total iron; Mg# = (Mg/Mg+Fe); FMMT= FeO^t +MgO+MnO+TiO_2

Contd…Table 5.1: Major oxides (wt%) and CIPW normative (wt%) values of representative Dibang Valley Granitoids

					Granodiorite				
Sample No.	**D3**	**D4**	**D5**	**D6**	**E2**	**E3**	**E4**	**E8**	**E9**
SiO_2	65.77	64.44	62.37	58.92	64.30	64.52	57.99	61.04	58.97
TiO_2	0.55	0.63	0.78	0.81	0.40	0.40	0.67	0.56	0.66
Al_2O_3	14.89	15.99	16.68	17.22	15.76	15.90	15.52	14.47	15.71
Fe_2O_3	4.02	4.32	5.27	5.57	4.65	4.58	7.32	6.34	6.71
MnO	0.07	0.08	0.08	0.09	0.08	0.09	0.12	0.10	0.12
MgO	2.14	1.98	2.81	3.12	2.87	3.09	5.51	5.91	5.92

CaO	3.78	4.14	4.38	4.72	4.20	4.95	6.59	4.49	5.05
Na_2O	3.68	4.59	4.75	4.41	3.63	3.77	3.78	3.79	3.86
K_2O	3.37	1.56	2.33	2.77	2.38	2.31	1.50	1.24	1.94
P_2O_5	0.26	0.30	0.49	0.47	0.19	0.22	0.26	0.28	0.24
Total	98.53	98.03	99.94	98.12	98.46	99.84	99.28	98.24	99.18
FeO^t	3.61	3.89	4.74	5.02	4.19	4.12	6.59	5.71	6.04
FeO	3.19	3.37	4.09	4.36	4.05	3.98	6.32	5.50	5.72
Fe_2O_3*	0.83	0.95	1.17	1.22	0.60	0.60	1.01	0.84	0.99
Na_2O/ K_2O	1.09	2.94	2.04	1.59	1.53	1.63	2.52	3.07	1.99
K_2O/Na_2O	0.92	0.34	0.49	0.63	0.65	0.61	0.40	0.33	0.50
K_2O+Na_2O	7.05	6.15	7.08	7.17	6.00	6.08	5.28	5.03	5.80
Al_2O_3/TiO_2	26.93	25.34	21.33	21.21	39.41	39.75	23.16	25.74	23.80
P2O5/TiO_2	0.46	0.47	0.63	0.58	0.48	0.54	0.39	0.50	0.37
MgO/CaO	0.56	0.48	0.64	0.66	0.68	0.62	0.84	1.32	1.17
FeO^t/MgO	1.69	1.96	1.69	1.61	1.46	1.34	1.20	0.96	1.02
TiO_2/MgO	0.26	0.32	0.28	0.26	0.14	0.13	0.12	0.10	0.11
CaO/Na_2O	1.03	0.90	0.92	1.07	1.16	1.31	1.74	1.18	1.31
A/NK	1.54	1.73	1.61	1.68	1.84	1.83	1.98	1.91	1.86
A/CNK	0.90	0.95	0.91	0.91	0.98	0.90	0.78	0.92	0.89
Mg#	54.45	51.14	55.00	56.08	55.76	58.01	60.85	65.72	64.81
FeO^t/FeO^t+MgO	0.63	0.66	0.63	0.62	0.59	0.57	0.54	0.49	0.51
FMMT	6.38	6.58	8.41	9.04	7.53	7.69	12.90	12.28	12.73
CIPW Norm									
Q	21.56	20.84	13.89	9.55	21.30	19.91	10.82	16.97	10.96
C	0	0	0	0	0.06	0	0	0	0
Or	19.92	9.21	13.77	16.35	14.04	13.68	8.88	7.30	11.47
Ab	31.10	38.82	40.21	37.29	30.68	31.88	31.99	32.08	32.62
An	14.18	18.43	17.30	19.04	19.56	19.64	20.93	18.80	19.82
Di	0.99	0	0	0	0	1.90	6.40	0.08	1.40
Hy	4.87	4.94	7.00	7.78	7.14	6.81	10.76	4.70	14.09

Mt	0	0	0	0	0	0	0	0	0
Il	0.15	0.18	0.17	0.20	0.18	0.19	0.27	0.22	0.25
Hm	4.02	4.32	5.27	5.57	4.65	4.58	7.32	6.34	6.72
Tn	1.16	0.11	0.88	0.92	0	0.74	1.30	1.10	1.30
Ru	0	0.50	0.33	0.33	0.31	0	0	0	0
Ap	0.61	0.71	1.16	1.12	0.45	0.51	0.62	0.66	0.58
Sum	98.55	98.05	99.97	98.15	98.46	99.83	99.29	98.25	99.19

$FeO^t = Fe_2O_3*0.9$; $Fe_2O_3* = TiO2*1.5$; $FeO = Fe_2O_3 - Fe_2O_3*$; A/CNK=molar $Al_2O_3/(CaO+Na_2O+K_2O)$; Fe_2O_3: total iron; Mg# = (Mg/Mg+Fe); FMMT= $FeO^t + MgO + MnO + TiO_2$

Contd…Table 5.1: Major oxides (wt%) and CIPW normative (wt%) values of representative Dibang Valley Granitoids

GRANITE			**LEUCOGRANITE**		
Sample No.	**D1**	**D7**	**E15**	**ET12**	**ET22**
SiO_2	70.09	66.70	76.94	70.18	66.73
TiO_2	0.35	0.38	0.23	0.34	0.16
Al_2O_3	14.41	15.89	10.71	15.38	16.98
Fe_2O_3	2.62	3.60	2.34	3.56	4.52
MnO	0.05	0.06	0.03	0.02	0.01
MgO	1.22	1.17	0.36	0.59	0.18
CaO	2.49	2.89	3.06	3.23	4.11
Na_2O	2.65	3.12	4.14	4.95	5.06
K_2O	4.85	4.33	0.32	0.69	0.24
P_2O_5	0.17	0.21	0.05	0.06	0.04
Total	98.91	99.03	98.20	99.24	98.34
FeO^t	2.36	3.24	2.10	3.20	4.07
FeO	2.10	3.02	1.99	3.05	4.27
Fe_2O_3*	0.52	0.58	0.35	0.51	0.24
Na_2O/K_2O	0.55	0.72	12.86	7.16	21.08
K_2O/Na_2O	1.83	1.39	0.08	0.14	0.05
K_2O+Na_2O	7.50	7.45	4.46	5.64	5.30

Al_2O_3/TiO_2	41.28	41.37	45.98	45.64	104.18
$P2O5/TiO_2$	0.49	0.54	0.22	0.18	0.26
MgO/CaO	0.49	0.40	0.12	0.18	0.04
FeO^t/MgO	1.94	2.78	5.85	5.40	22.22
TiO_2/MgO	0.29	0.33	0.65	0.57	0.89
CaO/Na_2O	0.94	0.93	0.74	0.65	0.81
A/NK	1.50	1.62	1.50	1.73	1.98
A/CNK	1.02	1.05	0.84	1.04	1.06
Mg#	50.75	40.75	24.39	25.71	7.09
FeO^t/FeO^t+MgO	0.66	0.74	0.85	0.84	0.96
FMMT	3.98	4.85	2.73	4.15	4.42
CIPW Norm					
Q	29.45	24.64	45.80	31.12	27.42
C	0.67	1.31	0	0.76	1.02
Or	28.69	25.58	1.90	4.08	1.42
Ab	22.40	26.43	35.05	41.89	42.82
An	11.26	12.97	9.69	15.63	20.13
Di	0	0	1.94	0	0
Hy	3.03	2.91	0	1.47	0.45
Mt	0	0	0	0	0
Il	0.11	0.14	0.06	0.04	0.02
Hm	2.62	3.60	2.34	3.56	4.52
Tn	0	0	0	0	0
Ru	0.29	0.31	0	0.32	0.15
Ap	0.40	0.50	0.12	0.14	0.10
Sum	98.92	98.37	98.20	99.01	98.04

$FeO^t = Fe_2O_3*0.9$; $Fe_2O_3* = TiO2*1.5$; $FeO= Fe_2O_3 - Fe_2O_3*$; A/CNK=molar $Al_2O_3/(CaO+Na_2O+K_2O)$; Fe_2O_3: total iron; Mg# = (Mg/Mg+Fe); FMMT= $FeO^t +MgO+MnO+TiO_2$

Table 5.2: Trace elements (ppm) and important elemental ratios of representative granitoids from Dibang Valley

	QUARTZ DIORITE							
Sample No.	**D2**	**M1**	**E5**	**E6**	**E11**	**E12**	**E13**	**E14**
Sc	13.52	12.50	17.68	17.71	17.35	12.51	19.02	17.20
V	152.46	106.60	157.76	180.81	189.84	147.51	188.54	210.50
Cr	15.76	19.36	113.76	81.78	78.21	30.13	55.01	111.07
Co	22.53	16.85	27.75	32.04	29.64	22.23	30.56	33.95
Ni	6.91	6.92	9.86	9.58	10.99	8.46	8.49	10.91
Cu	2.83	1.34	4.42	4.43	2.59	6.70	2.84	4.54
Zn	77.94	23.03	47.43	46.61	73.94	68.25	23.03	57.80
Ga	20.39	16.27	17.47	19.78	19.00	15.92	17.99	20.22
Rb	27.39	17.56	24.32	19.37	41.15	54.53	16.52	28.12
Sr	561.76	600.32	550.37	659.13	581.92	414.83	610.59	570.55
Y	31.35	20.76	17.89	21.78	20.34	22.25	15.38	21.51
Zr	103.88	114.79	114.80	107.84	127.12	120.59	133.31	138.75
Nb	4.73	3.68	3.49	3.84	3.74	5.21	2.20	4.82
Cs	1.44	1.04	1.42	1.39	2.02	4.05	1.51	1.22
Ba	261.96	143.01	234.72	225.14	221.09	271.20	213.26	378.83
La	15.78	11.51	9.55	11.22	18.36	19.07	11.45	19.76
Ce	41.53	28.42	25.24	29.23	42.94	46.02	26.83	47.34
Pr	5.53	3.61	3.39	3.96	5.27	5.76	3.35	5.96
Nd	25.05	15.35	15.49	18.32	21.31	23.98	13.92	25.06
Sm	5.86	3.44	3.76	4.53	4.61	5.21	3.25	5.48
Eu	1.48	1.16	0.97	1.12	1.07	0.97	1.04	1.29
Gd	4.46	2.76	2.84	3.37	3.24	3.68	2.40	3.85
Tb	0.86	0.53	0.52	0.62	0.58	0.64	0.44	0.66
Dy	4.41	2.80	2.57	3.07	2.87	3.19	2.22	3.17
Ho	0.92	0.59	0.52	0.62	0.59	0.65	0.46	0.64
Er	2.57	1.69	1.42	1.71	1.60	1.75	1.28	1.70
Tm	0.38	0.26	0.20	0.25	0.23	0.25	0.19	0.24

Yb	2.70	1.77	1.45	1.71	1.64	1.69	1.35	1.58
Lu	0.39	0.26	0.21	0.25	0.24	0.25	0.20	0.23
Hf	3.15	3.45	3.44	3.24	3.73	3.56	3.95	3.98
Ta	0.30	0.34	0.26	0.30	0.34	0.44	0.26	0.32
Pb	36.79	16.46	12.95	18.22	26.49	43.29	16.56	30.45
TH	1.11	1.17	1.26	1.29	4.31	12.40	1.92	1.90
U	0.96	0.90	1.00	1.22	1.97	2.50	1.16	1.21
ΣLREE	108.76	75.99	76.08	86.10	110.90	113.51	78.85	122.09
ΣHREE	48.05	31.42	27.62	33.39	31.34	34.34	23.92	33.57
ΣREE	156.81	107.41	103.70	119.49	142.24	147.86	102.77	155.66
REE Chondrite normalized (after Sun and Mc Donough, 1989)								
La$_N$	66.59	48.57	40.29	47.34	77.46	80.47	48.30	83.37
Ce$_N$	67.86	46.45	41.24	47.76	70.16	75.20	43.84	77.36
Pr$_N$	58.23	37.98	35.66	41.70	55.43	60.60	35.26	62.74
Nd$_N$	53.65	32.86	33.17	39.24	45.62	51.35	29.80	53.65
Sm$_N$	38.32	22.48	24.59	29.62	30.13	34.06	21.24	35.84
Eu$_N$	25.54	20.02	16.75	19.35	18.53	16.69	18.00	22.16
Ti$_N$	11.46	9.59	9.90	10.55	9.75	13.24	8.89	12.35
Gd$_N$	21.72	13.45	13.82	16.39	15.77	17.91	11.66	18.72
Tb$_N$	22.90	14.23	13.97	16.67	15.57	17.14	11.80	17.60
Dy$_N$	17.38	11.01	10.11	12.09	11.31	12.54	8.75	12.48
Yb$_N$	15.88	10.41	8.50	10.05	9.65	9.95	7.94	9.30
Lu$_N$	15.48	10.15	8.29	9.80	9.41	9.70	7.74	9.07
Pb$_N$	14.89	6.67	5.24	7.37	10.72	17.53	6.70	12.33
Th$_N$	38.30	40.40	43.54	44.43	148.60	427.48	66.37	65.63
U$_N$	120.16	113.09	125.53	152.21	246.77	311.94	145.39	151.87
Elemental ratios and calculations								
Eu*	30.02	17.96	19.21	23.00	22.95	25.99	16.45	27.28
Zr+Nb+Ce+Y	181.49	167.65	161.43	162.69	194.14	194.07	177.72	212.42
Ti/Zr	49.11	37.19	38.38	43.53	34.14	48.87	29.68	39.62
Sr/Zr	5.41	5.23	4.79	6.11	4.58	3.44	4.58	4.11
Th/Yb	0.41	0.66	0.87	0.75	2.63	7.33	1.43	1.20

Ba/La	16.60	12.42	24.58	20.07	12.04	14.22	18.63	19.17
Ba/Zr	2.52	1.25	2.04	2.09	1.74	2.25	1.60	2.73
Th/Zr	0.01	0.01	0.01	0.01	0.03	0.10	0.01	0.01
Ba/Th	235.85	122.07	185.90	174.73	51.30	21.88	110.80	199.03
Th/Nb	0.23	0.32	0.36	0.34	1.15	2.38	0.88	0.40
Sr/La	35.60	52.16	57.64	58.74	31.70	21.75	53.34	28.88
La/Yb	5.85	6.50	6.61	6.57	11.19	11.27	8.48	12.49
Rb/Sr	0.05	0.03	0.04	0.03	0.07	0.13	0.03	0.05
Rb/Ba	0.10	0.12	0.10	0.09	0.19	0.20	0.08	0.07
Sr/Y	17.92	28.92	30.76	30.26	28.61	18.64	39.69	26.53
Rb/Zr	0.26	0.15	0.21	0.18	0.32	0.45	0.12	0.20
Ba+Sr	823.71	743.34	785.09	884.28	803.00	686.04	823.85	949.38
Zr/Nb	21.95	31.23	32.87	28.11	34.03	23.14	60.63	28.81
Rb/Nb	5.79	4.78	6.96	5.05	11.02	10.47	7.51	5.84
Y/Nb	6.62	5.65	5.12	5.68	5.45	4.27	7.00	4.47
Ga/Al	2.47	2.07	2.30	2.64	2.48	2.06	2.35	2.62
K/Rb	351.00	414.52	426.87	346.67	337.06	351.52	544.75	426.38
Ba/Nb	55.36	38.91	67.20	58.69	59.18	52.05	96.99	78.67
Ce_N/Yb_N	4.27	4.46	4.85	4.75	7.27	7.56	5.52	8.31
Ce_N/Pb_N	4.56	6.97	7.87	6.48	6.54	4.29	6.54	6.28
Th_N/Nb_N	1.99	2.70	3.07	2.85	9.79	20.18	7.43	3.35
La_N/Nb_N	3.46	3.25	2.84	3.04	5.10	3.80	5.40	4.26
La_N/Lu_N	4.30	4.79	4.86	4.83	8.23	8.29	6.24	9.19
La_N/Yb_N	4.19	4.67	4.74	4.71	8.02	8.09	6.08	8.96
La_N/Sm_N	1.74	2.16	1.64	1.60	2.57	2.36	2.27	2.33
Gd_N/Yb_N	1.37	1.29	1.63	1.63	1.63	1.80	1.47	2.01
Hf_N/Sm_N	0.68	0.83	0.66	1.84	1.60	1.28	1.41	1.40
Ta_N/La_N	0.45	0.18	0.31	0.62	0.59	0.39	0.27	0.57
Eu/Eu*	0.85	1.11	0.87	0.84	0.81	0.64	1.09	0.81

Contd... Table 5.2: Trace elements (ppm) and important elemental ratio of representative granitoids from Dibang Valley, Arunachal Pradesh

				Granodiorite					
Sample No.	**D3**	**D4**	**D5**	**D6**	**E2**	**E3**	**E4**	**E8**	**E9**
Sc	7.35	5.35	6.23	9.20	9.74	9.01	13.50	12.18	14.82
V	59.30	65.57	64.08	68.97	86.21	84.99	154.67	121.94	149.50
Cr	23.21	11.16	13.14	13.45	26.66	23.10	16.61	24.21	33.53
Co	9.61	8.45	9.44	9.15	9.03	9.56	21.01	17.38	21.20
Ni	6.52	6.72	8.61	4.91	15.56	4.32	5.37	6.62	9.10
Cu	1.28	1.36	2.60	1.74	1.66	1.57	2.58	2.73	7.15
Zn	42.99	66.17	36.04	42.08	54.60	27.61	30.92	55.56	69.60
Ga	16.72	20.26	18.63	19.08	17.54	17.41	18.10	18.31	18.71
Rb	67.69	44.20	64.42	67.01	57.28	50.48	31.56	27.06	44.32
Sr	572.89	593.15	722.36	775.71	661.59	629.30	583.68	738.97	599.06
Y	17.86	17.49	15.91	26.04	10.21	10.34	15.08	15.44	18.61
Zr	111.26	97.78	120.39	130.32	102.14	88.08	101.72	124.45	117.77
Nb	9.38	5.97	10.06	13.42	4.26	4.12	3.14	2.73	4.05
Cs	2.52	1.52	2.77	2.90	2.35	2.09	1.91	1.31	2.72
Ba									
La	38.01	20.83	45.22	43.74	10.17	8.74	12.62	14.14	10.04
Ce	81.18	51.22	95.01	97.13	23.57	20.65	29.56	33.93	25.29
Pr	9.20	6.51	10.60	11.40	2.88	2.57	3.68	4.26	3.32
Nd	32.61	27.73	36.47	42.96	11.58	10.63	15.27	17.79	14.80
Sm	5.78	6.06	6.08	8.31	2.40	2.33	3.41	3.73	3.57
Eu	1.42	1.39	1.54	1.95	0.66	0.62	0.95	0.90	0.93
Gd	3.57	4.03	3.63	5.07	1.68	1.58	2.45	2.56	2.65
Tb	0.57	0.66	0.55	0.83	0.29	0.28	0.44	0.45	0.49

Dy	2.60	2.87	2.47	3.77	1.42	1.42	2.19	2.17	2.53
Ho	0.51	0.53	0.48	0.76	0.30	0.30	0.45	0.45	0.53
Er	1.38	1.29	1.25	2.02	0.84	0.83	1.25	1.23	1.49
Tm	0.20	0.16	0.17	0.29	0.13	0.12	0.18	0.18	0.22
Yb	1.35	1.09	1.15	1.92	0.88	0.91	1.31	1.28	1.59
Lu	0.20	0.16	0.17	0.28	0.13	0.13	0.19	0.19	0.23
Hf	3.25	2.85	3.53	3.82	3.06	2.60	3.05	3.66	3.48
Ta	0.49	0.56	0.47	0.81	0.37	0.30	0.29	0.22	0.34
Pb	23.53	19.62	20.86	24.66	27.05	20.21	17.79	27.84	28.05
Th	7.29	3.01	6.98	7.94	2.64	2.42	4.45	1.21	2.50
U	1.52	0.93	1.34	2.03	1.37	1.10	1.24	1.01	1.19
ΣLREE	175.55	119.09	201.15	214.69	60.98	54.54	79.00	86.92	72.78
ΣHREE	28.23	28.29	25.78	40.98	15.87	15.93	23.54	23.94	28.33
ΣREE	203.78	147.38	226.93	255.67	76.85	70.46	102.54	110.86	101.11
REE Chondrite normalized (after Sun and Mc Donough, 1989)									
La$_N$	160.37	87.90	190.78	184.56	42.89	36.86	53.24	59.66	42.38
Ce$_N$	132.65	83.68	155.25	158.71	38.51	33.74	48.30	55.44	41.32
Pr$_N$	96.86	68.52	111.60	119.97	30.31	27.06	38.79	44.79	34.98
Nd$_N$	69.83	59.38	78.10	91.99	24.79	22.76	32.70	38.09	31.69
Sm$_N$	37.76	39.62	39.72	54.34	15.66	15.20	22.32	24.39	23.33
Eu$_N$	24.55	23.99	26.61	33.67	11.31	10.67	16.31	15.43	16.02
Ti$_N$	7.45	8.50	10.54	10.94	5.39	5.39	9.03	7.57	8.89
Gd$_N$	17.36	19.62	17.66	24.69	8.16	7.71	11.92	12.46	12.88
Tb$_N$	15.27	17.74	14.84	22.24	7.63	7.57	11.72	11.93	13.05
Dy$_N$	10.25	11.31	9.71	14.86	5.59	5.59	8.60	8.53	9.95
Yb$_N$	7.92	6.41	6.78	11.32	5.19	5.38	7.70	7.52	9.36
Lu$_N$	7.72	6.26	6.61	11.04	5.05	5.24	7.51	7.33	9.12

Pb$_N$	9.53	7.94	8.44	9.98	10.95	8.18	7.20	11.27	11.35
Th$_N$	251.32	103.64	240.84	273.84	91.18	83.44	153.50	41.61	86.33
U$_N$	189.94	115.99	167.52	253.73	170.80	138.07	154.72	126.60	149.14
Elemental ratios and calculations									
Eu*	27.56	29.62	28.69	39.51	11.91	11.46	17.12	18.42	18.11
Zr+Nb+Ce+Y	219.68	172.46	241.37	266.91	140.17	123.20	149.50	176.55	165.71
Ti/Zr	29.80	38.69	38.94	37.36	23.48	27.22	39.49	27.07	33.60
Sr/Zr	5.15	6.07	6.00	5.95	6.48	7.14	5.74	5.94	5.09
Th/Yb	5.41	2.76	6.06	4.13	3.00	2.65	3.40	0.94	1.57
Ba/La	30.60	14.79	13.02	17.23	42.31	48.05	23.67	21.03	36.13
Ba/Zr	10.45	3.15	4.89	5.78	4.21	4.77	2.94	2.39	3.08
Th/Zr	0.07	0.03	0.06	0.06	0.03	0.03	0.04	0.01	0.02
Ba/Th	159.57	102.52	84.32	94.88	162.68	173.50	67.09	246.39	144.95
Th/Nb	0.78	0.50	0.69	0.59	0.62	0.59	1.42	0.44	0.62
Sr/La	15.07	28.47	15.98	17.73	65.08	72.04	46.26	52.27	59.64
La/Yb	28.23	19.10	39.21	22.73	11.53	9.56	9.64	11.06	6.32
Rb/Sr	0.12	0.07	0.09	0.09	0.09	0.08	0.05	0.04	0.07
Rb/Ba	0.06	0.14	0.11	0.09	0.13	0.12	0.11	0.09	0.12
Sr/Y	32.09	33.91	45.41	29.79	64.81	60.86	38.71	47.85	32.20
Rb/Zr	0.61	0.45	0.54	0.51	0.56	0.57	0.31	0.22	0.38
Ba+Sr	1735.90	901.27	1311.27	1529.15	1091.72	1049.10	882.31	1036.32	961.96
Zr/Nb	11.86	16.37	11.97	9.71	23.99	21.38	32.39	45.58	29.10
Rb/Nb	7.22	7.40	6.40	4.99	13.45	12.25	10.05	9.91	10.95
Y/Nb	1.90	2.93	1.58	1.94	2.40	2.51	4.80	5.66	4.60
Ga/Al	2.20	2.48	2.19	2.17	2.18	2.15	2.29	2.48	2.34
K/Rb	412.34	292.07	299.48	341.91	343.31	379.54	394.34	378.19	362.46
Ba/Nb	123.98	51.58	58.54	56.15	101.02	101.89	95.09	108.91	89.69

Ce_N/Yb_N	16.75	13.05	22.89	14.02	7.42	6.28	6.27	7.37	4.42
Ce_N/Pb_N	13.92	10.54	18.39	15.90	3.52	4.12	6.71	4.92	3.64
Th_N/Nb_N	6.59	4.27	5.89	5.02	5.27	4.98	12.02	3.75	5.25
La_N/Nb_N	4.21	3.62	4.67	3.38	2.48	2.20	4.17	5.38	2.58
La_N/Lu_N	20.77	14.05	28.85	16.72	8.49	7.03	7.09	8.14	4.65
La_N/Yb_N	20.25	13.70	28.12	16.30	8.27	6.86	6.91	7.93	4.53
La_N/Sm_N	4.25	2.22	4.80	3.40	2.74	2.42	2.39	2.45	1.82
Gd_N/Yb_N	2.19	3.06	2.60	2.18	1.57	1.43	1.55	1.66	1.38
Hf_N/Sm_N	0.81	0.68	0.83	0.66	1.84	1.60	1.28	1.41	1.40
Ta_N/La_N	0.22	0.45	0.18	0.31	0.62	0.59	0.39	0.27	0.57
Eu/Eu*	0.89	0.81	0.93	0.85	0.95	0.93	0.95	0.84	0.88

Contd... Table 5.2: Trace elements (ppm) and important elemental ratio of representative granitoids from Dibang Valley, Arunachal Pradesh

	GRANITE		LEUCOGRANITE		
Sample No.	**D1**	**D7**	**E15**	**ET12**	**ET22**
Sc	7.24	9.14	11.35	6.32	9.13
V	45.13	48.36	13.98	27.04	5.24
Cr	19.73	17.59	9.85	13.48	14.01
Co	6.42	6.69	2.66	2.45	1.73
Ni	4.87	4.67	5.43	5.19	5.69
Cu	1.07	1.25	0.96	1.04	1.25
Zn	48.17	26.79	41.10	42.47	58.25
Ga	15.45	19.29	13.69	12.33	17.51
Rb	93.42	194.99	10.39	11.28	2.18
Sr	611.90	440.25	186.85	451.61	146.71
Y	19.80	34.07	54.00	10.32	35.79
Zr	116.63	120.23	100.69	38.77	37.88
Nb	9.75	12.91	1.34	1.01	0.93
Cs	2.40	5.34	0.76	0.36	0.11
Ba	2652.42	777.39	91.29	119.32	40.74
La	46.38	56.95	5.30	2.98	4.18
Ce	98.40	120.85	15.98	7.86	13.92
Pr	11.03	13.38	2.48	1.12	2.33
Nd	38.27	45.28	13.18	5.52	13.25
Sm	6.69	8.64	4.84	1.62	4.44
Eu	1.64	1.20	1.23	0.50	1.06
Gd	3.93	5.64	5.40	1.53	4.63
Tb	0.64	1.00	1.23	0.27	0.85

Dy	2.87	4.80	7.04	1.71	5.78
Ho	0.57	0.96	1.49	0.36	1.29
Er	1.55	2.53	4.15	0.94	3.56
Tm	0.22	0.35	0.61	0.15	0.56
Yb	1.52	2.39	4.06	1.05	3.81
Lu	0.22	0.35	0.59	0.16	0.57
Hf	3.36	3.54	2.96	0.88	0.99
Ta	0.80	0.92	0.15	0.11	0.07
Pb	33.65	23.24	22.05	14.49	9.79
Th	9.55	42.47	1.01	0.50	0.78
U	1.74	5.80	0.93	0.16	0.24
ΣLREE	209.64	255.43	54.36	25.92	48.31
ΣHREE	31.34	52.07	78.57	16.49	56.85
ΣREE	240.98	307.50	132.93	42.42	105.15
REE Chondrite normalized (after Sun and Mc Donough, 1989)					
La$_N$	195.68	240.31	22.36	12.56	17.62
Ce$_N$	160.78	197.47	26.11	12.84	22.75
Pr$_N$	116.10	140.80	26.07	11.82	24.54
Nd$_N$	81.95	96.95	28.22	11.82	28.37
Sm$_N$	43.72	56.45	31.65	10.60	29.04
Eu$_N$	28.31	20.63	21.25	8.67	18.27
Ti$_N$	4.70	5.17	3.14	4.54	2.20
Gd$_N$	19.14	27.44	26.27	7.47	22.55
Tb$_N$	17.17	26.66	32.91	7.14	22.78
Dy$_N$	11.31	18.88	27.70	6.74	22.77
Yb$_N$	8.95	14.05	23.86	6.17	22.44
Lu$_N$	8.73	13.70	23.27	6.22	22.34

Pb_N	13.62	9.41	8.93	5.87	3.96
Th_N	329.17	1464.46	34.88	17.23	26.96
U_N	217.75	725.00	116.36	20.20	29.82
Elemental ratios and calculations					
Eu*	31.43	41.94	28.96	9.03	25.79
Zr+Nb+Ce+Y	244.58	288.06	172.00	57.95	88.52
Ti/Zr	17.94	19.15	13.87	52.11	25.80
Sr/Zr	5.25	3.66	1.86	11.65	3.87
Th/Yb	6.27	17.78	0.25	0.48	0.20
Ba/La	57.19	13.65	17.23	40.08	9.76
Ba/Zr	22.74	6.47	0.91	3.08	1.08
Th/Zr	0.08	0.35	0.01	0.01	0.02
Ba/Th	277.86	18.30	90.25	238.82	52.11
Th/Nb	0.98	3.29	0.76	0.50	0.84
Sr/La	13.19	7.73	35.26	151.69	35.13
La/Yb	30.47	23.85	1.31	2.84	1.09
Rb/Sr	0.15	0.44	0.06	0.02	0.01
Rb/Ba	0.04	0.25	0.11	0.09	0.05
Sr/Y	30.90	12.92	3.46	43.77	4.10
Rb/Zr	0.80	1.62	0.10	0.29	0.06
Ba+Sr	3264.32	1217.64	278.14	570.92	187.46
Zr/Nb	11.97	9.31	75.28	38.47	40.66
Rb/Nb	9.58	15.10	7.77	11.20	2.34
Y/Nb	2.03	2.64	40.37	10.24	38.43
Ga/Al	2.10	2.38	2.51	1.57	2.02
K/Rb	430.25	183.83	256.65	507.12	911.59
Ba/Nb	272.15	60.21	68.25	118.40	43.74

Ce_N/Yb_N	17.96	14.06	1.09	2.08	1.01
Ce_N/Pb_N	11.80	20.99	2.92	2.19	5.74
Th_N/Nb_N	8.31	27.90	6.42	4.21	7.12
La_N/Nb_N	4.94	4.58	4.11	3.07	4.65
La_N/Lu_N	22.41	17.54	0.96	2.02	0.79
La_N/Yb_N	21.86	17.11	0.94	2.04	0.79
La_N/Sm_N	4.48	4.26	0.71	1.19	0.61
Gd_N/Yb_N	2.14	1.95	1.10	1.21	1.01
Hf_N/Sm_N	0.72	0.59	0.88	0.78	0.32
Ta_N/La_N	0.29	0.27	0.47	0.64	0.28
Eu/Eu*	0.90	0.49	0.73	0.96	0.71

CHAPTER-7

U-Pb ZIRCON GEOCHRONOLOGY

7.1 INTRODUCTION

Geochronology is a fundamental tool in petrology as it provides absolute age constraints on magmatic events such as emplacement, crystallization, and evolutionary history. These age determinations aid in reconstructing the geological history of igneous bodies and linking magmatic activity with regional tectonic processes. When combined with geochemical and isotopic data, geochronology provides deeper insights into magma source characteristics, evolution, and the timing of crustal formation or recycling.

Representative samples of 1 quartz diorite and 2 granites have been selected, and the Pb-Th-U isotopes of the zircons from each sample have been analyzed using a SHRIMP IIe/MC ion microprobe. A detailed description of the analytical methods is given in Chapter 3. The obtained geochronological data are summarised in Table 6.

7.2 ZIRCON U-Pb GEOCHRONOLOGICAL RESULTS

The zircon grains in the quartz diorite and granite samples are variable from sub-rounded stubby prisms to elongated euhedral prisms and range between 100 to 400µm in length and 50-100µm in width, with length-to-width ratios from 2:1 to 4:1. Most of the zircon crystals are transparent and colourless, but some have a pale yellowish tint. Oscillatory zonings are exhibited by some grains, while in some grains, only a faint zoning is visible or is absent altogether. Uranium and thorium contents of these zircons range from 77.06-1945.56 ppm and 23.55-1360.45 ppm, respectively, with a high Th/U ratio of 0.12-1.96 (Table 6). Hoskin and Schaltegger (2003) suggested a magmatic origin for zircon crystals if the Th/U is >0.1. Accordingly, the euhedral morphology, distinct oscillatory zoning, and elevated Th/U values (>0.1) observed in most of the grains attest to their magmatic origin.

7.2.1 QUARTZ DIORITE: MZ-1

A total of 45 spots were analysed from 23 zircons, from which 21 analytical spots are most concordant (Table 6). 4 zircon spots did not give valid data due to very high Pb-loss and hence were discarded. Most of the zircons are rounded to subrounded and subhedral. The zircons exhibit variation in growth zoning. Faint and broad zoning are common; typical oscillatory zonings with magmatic growth zones are rare, and occasional grains exhibiting sector zoning are also present (Figure 6.1a). Most of the rounded to subrounded zircon grains exhibit a dark structureless metamorphic rim, while the smaller subrounded zircons exhibit irregular and chaotic growth zones. The length of the zircons varies from 150 to 400µm, and the width varies from 50 to 100µm. Analysed zircons have a wide range of Th/U values between 0.12 to 0.60, consistent with values typical of magmatic origin. The concordant spots of zircons provided a multimodal distribution of ^{206}Pb/^{238}U ages of Late Cretaceous, ranging from 143±8 Ma to 92.3±1 Ma, and around 47.1±4 to 59.7±1 Ma of Mid-Eocene age (Figure 6.2b). 16 spot analyses of zircon from the older age cluster gave a weighted mean ^{206}Pb/^{238}U age of

This sample gives a high MSWD, which is probably due to high lead loss, but it provides a probable age of ~104.8 Ma, which is similar to the age of LPC granitoids estimated by other workers (Pebam et al., 2019; Bikramaditya et al., 2020; Mukherjee et al., 2025) and also consistent with the ages of Gangdese Batholith. The low Th/U ratio (0.01-0.45 ppm) and disruptions of the inner texture, occasionally with internal cracks or overgrowth rims suggestive of a hydrothermal imprint, are exhibited by zircon populations from the younger units. The younger age population thus reflects a later event of zircon overgrowth as a function of fluid-induced condition. or recrystallization and/or alteration age.

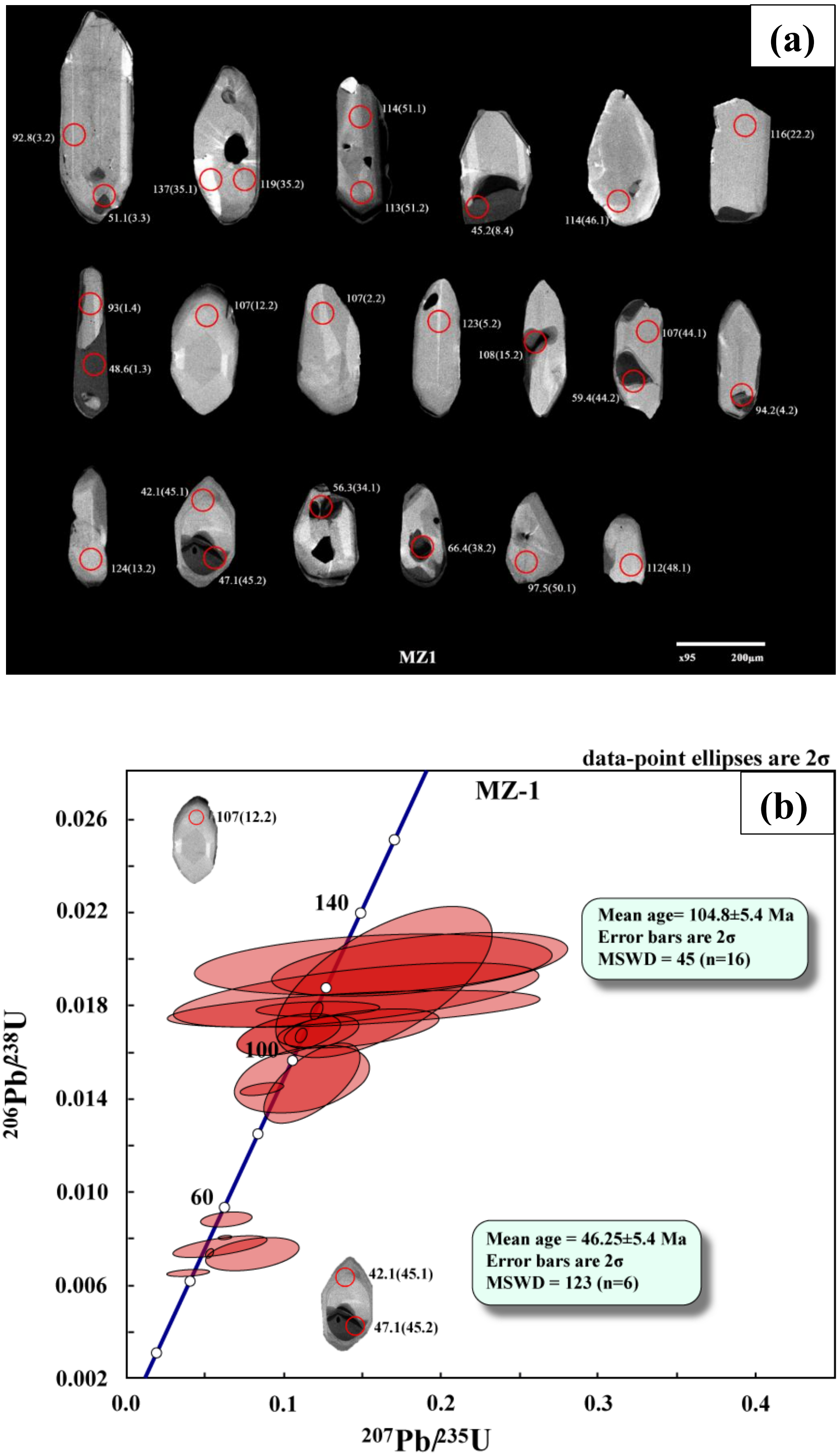

Figure 6.1: (a) Cathodoluminiscence (CL) images of representative zircons from quartz diorite (sample MZ-1); (b) Zircon U-Pb age and concordia diagram of quartz diorite (sample MZ-1).

7.2.2 GRANITE: DZ-1 (GRANITE)

Thirty-six spots are analysed on 22 individual zircons (Table 6). Most of the zircons vary in length and width from 100-300 μm and 50-100 μm, respectively, with a length-to-width ratio of 2:1 to 3:1, giving rise to an elongated and tabular habit. Oscillatory zonings with magmatic growth zones can be observed (Figure 6.2a). The core of some of the zircons shows irregular and chaotic growth zones over which oscillatory and normal growth zones are developed. The Th/U ratio of analysed zircon spots ranges between 0.1 to 1.96, typical of magmatic origin of zircon, with the exception of one spot (15.2) of zircon which shows a low Th/U ratio (0.09). The isotopic ratios of zircon U-Pb for both rim (Figure 6.2b) and core (Figure 6.2c) are plotted on the concordia diagram. Most of the grains are concordant, and the ^{206}Pb/^{238}U age obtained is considered to represent the crystallization age. 20 spot analyses of zircon rims with high concordance provide a weighted mean ^{206}Pb/^{238}U age of 44.82±0.91 Ma (MSWD 1.18) and 12 spot analyses of zircon cores with high concordance provide a weighted mean ^{206}Pb/^{238}U age of 48.78±00.70 Ma (MSWD 1.18) with a 95% confidence level yielding an Early-Late Eocene age for the granite sample.

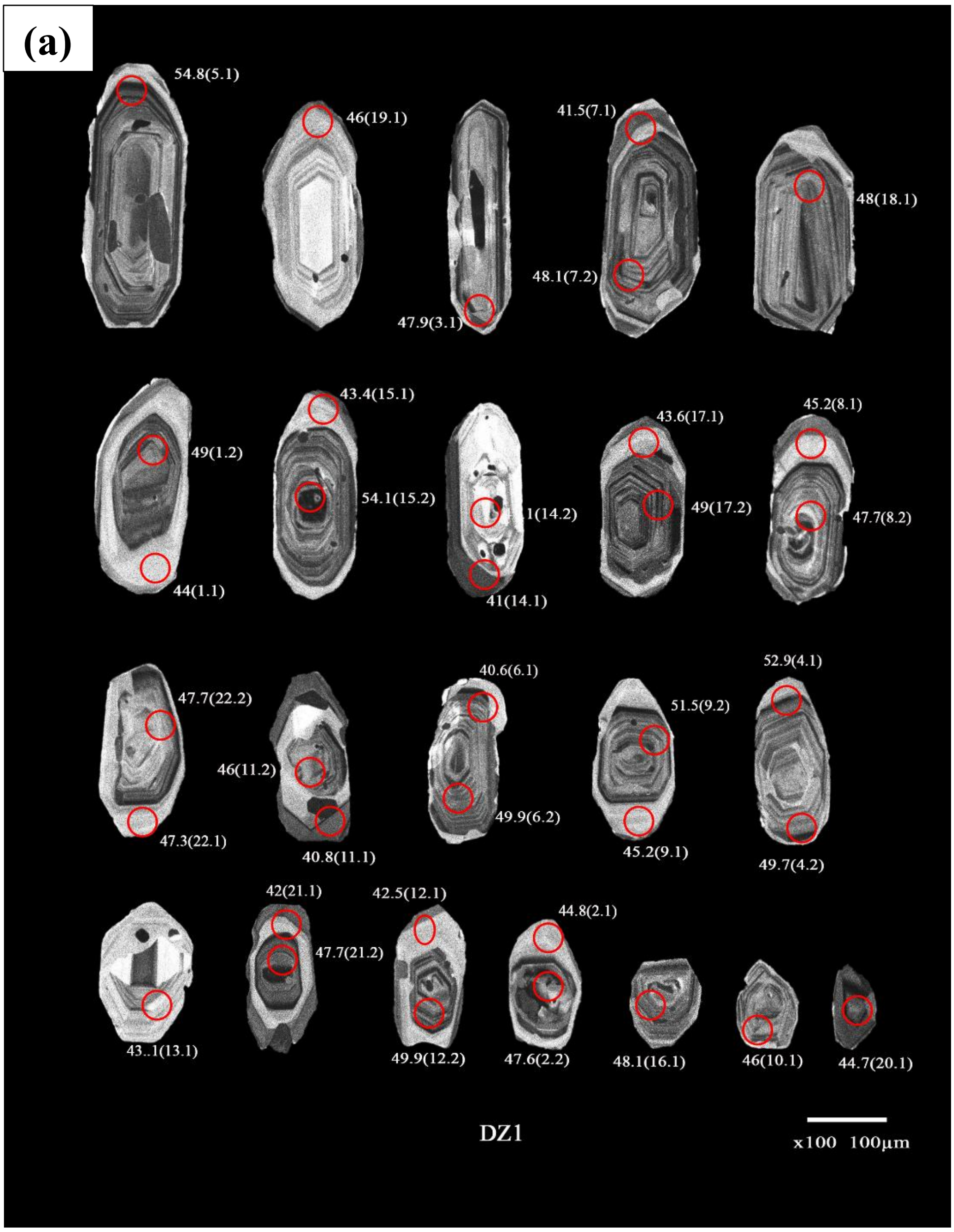

Figure 6.2: (a) Cathodoluminiscence (CL) images of representative zircons from granite (sample DZ-1).

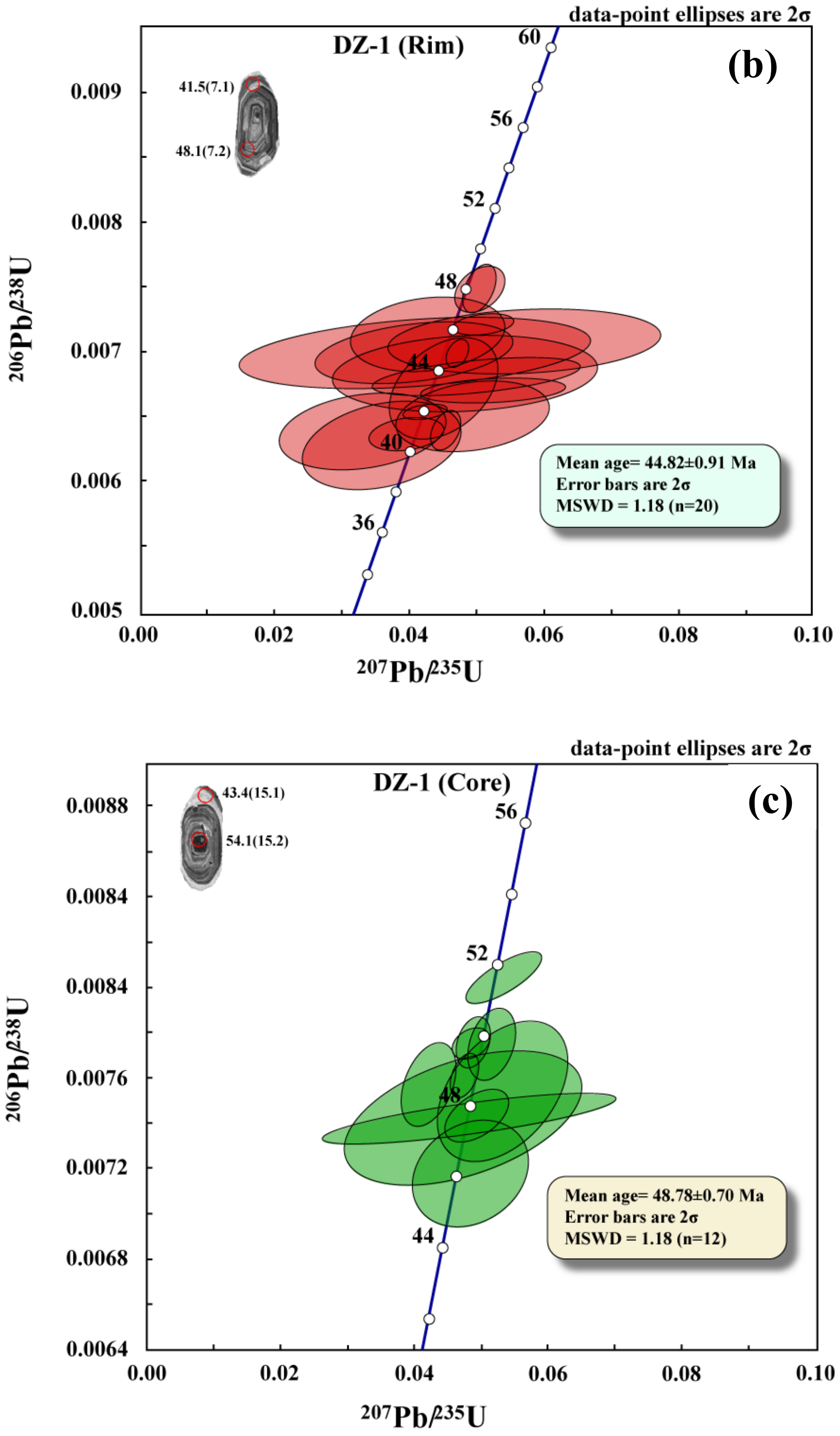

Figure 6.2: (b) Zircon U-Pb age and concordia diagram of granite from the rim of zircons in sample DZ-1; (c) from cores of zircon in sample DZ-1.

7.2.4 GRANITE: DZ7

A total of 23 spots were analysed from 14 zircons (Table 6). Most of the zircons are euhedral to subhedral and rarely rounded. The width and length of the zircons varies from 50-150 μm and from 150-300 μm, respectively, giving rise to a tabular to elongated shape of the zircon crystal The zircon crystals mostly contain distinct core-mantle rims, and a systematic trend of younger ages in zircon rims (high-luminescent domains) can be observed (Figure 6.3a). Oscillatory zonings with magmatic growth zones and polychronous rims are commonly observed. The overgrowth rims exhibit clear oscillatory zoning, indicative of late-stage magmatic crystallization. The cores of a few zircons show irregular or chaotic patterns, which may be attributed to metamictization. Th/U ratio of analysed zircon spots ranges between 0.13 -0.70, which indicates a typical magmatic origin of zircon. 15 spot analyses of zircons plotted on the concordia diagram (Figure 6.3b) provide a weighted mean $^{206}Pb/^{238}U$ age of 55.20±0.38 Ma (MSWD 2.5) with a 95% confidence level and is considered the crystallization age for this granite sample.

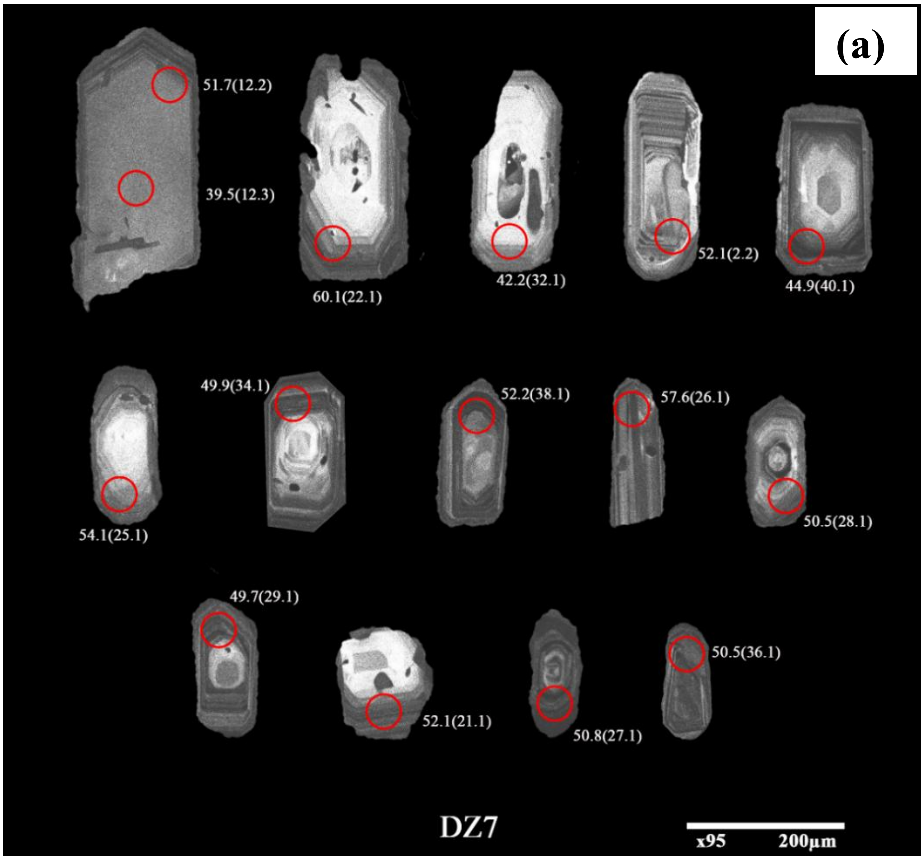

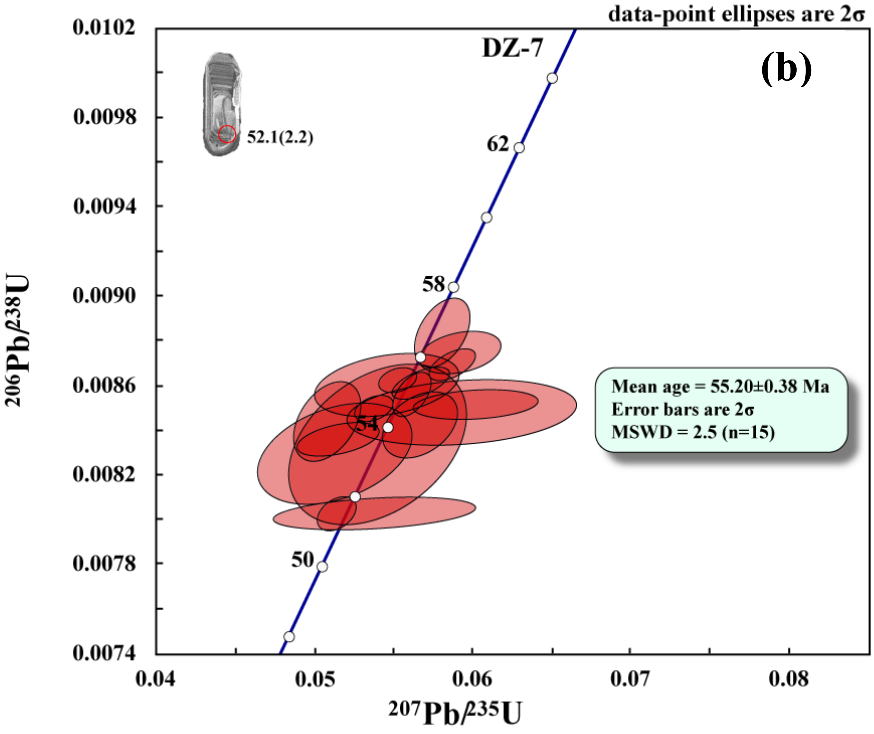

Figure 6.3: (a) Cathodoluminiscence (CL) images of representative zircons from granite (sample DZ-7); (b) Zircon U-Pb age and concordia diagram of granite (sample DZ-7).

Table 6: The U-Pb isotopic data of zircons from the granitoids of Dibang Valley, Arunachal Pradesh

QUARTZ DIORITE (MZ-1)									
Sample no.	**Th ppm**	**U ppm**	**Th/U ppm**	**^{206}Pb/^{238}U (age)**	**±%**	**^{207}Pb*/^{235}U**	**±%**	**^{206}Pb*/^{238}U**	**±%**
MZ-1_2.2	7.6	20	0.39	108	4	0.128	13	0.0169	3.5
MZ-1_3.2	16.4	35	0.47	92.3	1	0.086	13	0.0144	1.6
MZ-1_3.3	28.4	118	0.24	51.8	0.4	0.063	6	0.0081	0.9
MZ-1_1.3	23.4	88	0.27	49.2	3	0.060	41	0.0077	5.2
MZ-1_1.4	11.4	30	0.38	94.3	9	0.118	21	0.0147	9.3
MZ-1_34.1	7.7	214	0.04	56.7	2	0.064	21	0.0088	3.0
MZ-1_4.2	11.1	90	0.12	95	8	0.112	31	0.0149	8.0
MZ-1_8.4	35.6	124	0.29	47.1	4	0.080	30	0.0073	8.1
MZ-1_35.1	17.4	32	0.54	142	8	0.229	50	0.0222	5.5
MZ-1_35.2	10.7	19	0.56	121	17	0.164	34	0.0190	13.8
MZ-1_38.2	18.6	277	0.07	67.3	4	0.084	48	0.0105	5.9
MZ-1_44.1	26.6	44	0.60	107	2	0.108	6	0.0167	1.7
MZ-1_44.2	1.3	112	0.01	59.7	1	0.065	4	0.0093	1.9
MZ-1_45.1	11.2	25	0.05	42.0	0.8	0.040	28	0.0065	1.8
MZ-1_45.2	27.7	112	0.25	47.4	0.9	0.053	5	0.0074	2.0
MZ-1_46.1	18.4	41	0.45	114	1	0.122	26	0.0178	1.3
MZ-1_5.2	10.6	18	0.57	126	7	0.186	41	0.0197	5.3
MZ-1_12.2	8.9	22	0.41	109	4	0.148	29	0.0170	3.9
MZ-1_13.2	8.0	19	0.43	125	7	0.157	59	0.0196	5.6
MZ-1_15.2	7.8	40	0.20	107	5	0.103	26	0.0168	4.5
MZ-1_48.1	14.8	28	0.52	114	4	0.145	67	0.0178	3.7
MZ-1_50.1	18.5	41	0.45	102	4	0.192	26	0.0160	3.6

MZ-1_51.1	14.2	27	0.53	121	7	0.252	40	0.0190	5.8
MZ-1_51.2	139	553	0.25	113	2	0.121	3	0.0177	1.9
MZ-1_22.2	13.1	22	0.59	118	7	0.146	65	0.0184	5.9

Contd… Table 6: The U-Pb isotopic data of zircons from the granitoids of Dibang Valley, Arunachal Pradesh

GRANITE (DZ-1 RIM)									
Sample no.	**Th ppm**	**U ppm**	**Th/U ppm**	**^{206}Pb/^{238}U (age)**	**±%**	**^{207}Pb*/^{235}U**	**±%**	**^{206}Pb*/^{238}U**	**±%**
DZ-1_1.1	28	77	0.36	44.0	2	0.069	58	0.00706	7.0
DZ-1_2.1	44	108	0.41	44.8	1	0.043	85	0.00696	4.9
DZ-1_3.1	115	312	0.37	47.9	0.9	0.052	22	0.00749	2.2
DZ-1_4.1	26	171	0.15	52.9	3	0.056	72	0.00827	5.0
DZ-1_5.1	168	1418	0.12	54.8	0.3	0.055	4	0.00853	0.7
DZ-1_6.1	44	107	0.41	40.6	2	0.002	1579	0.00594	6.3
DZ-1_7.1	24	116	0.20	41.5	1	0.011	324	0.00619	5.8
DZ-1_8.1	45	109	0.41	45.2	2	0.024	173	0.00684	5.2
DZ-1_9.1	39	131	0.30	45.2	1	0.103	28	0.00753	4.0
DZ-1_10.1	174	292	0.60	46.0	0.4	0.041	31	0.00712	1.7
DZ-1_11.1	40	356	0.11	40.8	0.8	0.056	16	0.00648	2.3
DZ-1_12.1	30	118	0.25	42.5	0.7	0.053	60	0.00670	4.3
DZ-1_13.1	61	86	0.71	43.1	2	0.022	209	0.00652	7.3
DZ-1_14.1	58	469	0.12	41.0	0.7	0.041	21	0.00637	1.9
DZ-1_15.1	35	116	0.30	43.4	0.9	0.046	63	0.00677	3.6
DZ-1_16.1	244	441	0.55	48.1	0.6	0.054	14	0.00753	1.5
DZ-1_17.1	36	94	0.38	43.6	2	0.026	130	0.00664	5.1

DZ-1_18.1	359	596	0.60	48.0	0.9	0.055	12	0.00752	2.0
DZ-1_19.1	59	131	0.45	46.0	1	0.077	31	0.00743	4.0
DZ-1_20.1	186	721	0.26	44.7	0.6	0.043	12	0.00695	1.4
DZ-1_21.1	74	434	0.17	42.0	0.3	0.036	23	0.00648	1.2
DZ-1_22.2	61	159	0.38	47.7	3	0.044	70	0.00739	6.0

Contd… Table 6: The U-Pb isotopic data of zircons from the granitoids of Dibang Valley, Arunachal Pradesh

GRANITE (DZ-1 CORE)									
Sample no.	**Th ppm**	**U ppm**	**Th/U ppm**	**^{206}Pb/^{238}U (age)**	**±%**	**^{207}Pb*/^{235}U**	**±%**	**^{206}Pb*/^{238}U**	**±%**
DZ-1_1.2	171	290	0.59	49.0	0.9	0.046	26	0.00760	2.2
DZ-1_2.2	1360	931	1.46	47.6	0.3	0.056	13	0.00748	1.0
DZ-1_4.2	200	372	0.54	49.7	0.7	0.054	19	0.00777	1.9
DZ-1_6.2	257	551	0.47	49.9	0.5	0.057	11	0.00783	1.3
DZ-1_7.2	92	231	0.40	48.1	1	0.052	30	0.00753	3.3
DZ-1_8.2	114	191	0.60	47.7	1	0.024	108	0.00722	3.7
DZ-1_9.2	220	393	0.56	51.5	0.4	0.057	14	0.00807	1.0
DZ-1_11.2	95	191	0.49	46.0	1	0.052	36	0.00721	3.2
DZ-1_12.2	248	547	0.45	49.9	0.3	0.038	19	0.00766	1.0
DZ-1_14.2	210	155	1.36	47.1	2	0.048	55	0.00734	5.9
DZ-1_15.2	179	1946	0.09	54.1	0.6	0.056	4	0.00844	1.2
DZ-1_17.2	343	537	0.64	49.0	0.4	0.044	14	0.00757	1.2
DZ-1_21.2	821	949	0.87	47.7	0.5	0.057	7	0.00750	1.1
DZ-1_22.2	61	159	0.38	47.7	3	0.044	70	0.00739	6.0

Contd…Table 6: The U-Pb isotopic data of zircons from the granitoids of Dibang Valley, Arunachal Pradesh

GRANITE (DZ-7)									
Sample no.	**Th ppm**	**U ppm**	**Th/U ppm**	**^{206}Pb/^{238}U (age)**	**±%**	**^{207}Pb*/^{235}U**	**±%**	**^{206}Pb*/^{238}U**	**±%**
DZ-7_21.1	313.0	935	0.33	54.6	0.3	0.054	2	0.0085	0.6
DZ-7_22.1	252.4	1114	0.23	55.4	0.3	0.055	2	0.0086	0.6
DZ-7_2.2	112.7	427	0.26	54.4	0.4	0.060	5	0.0085	0.6
DZ-7_25.1	304.3	575	0.53	53.4	1	0.051	8	0.0083	2.2
DZ-7_26.1	807.5	1150	0.70	54.4	0.8	0.051	3	0.0084	1.7
DZ-7_27.1	247.1	1920	0.13	54.9	0.5	0.056	2	0.0086	0.9
DZ-7_28.1	233.7	702	0.33	55.2	0.3	0.057	3	0.0086	0.7
DZ-7_29.1	426.5	1295	0.33	55.9	0.3	0.062	3	0.0088	0.6
DZ-7_32.1	177.7	375	0.47	54.2	0.8	0.059	10	0.0085	1.4
DZ-7_34.1	263.7	968	0.27	56.7	0.7	0.058	2	0.0088	1.4
DZ-7_12.2	330.7	1198	0.28	54.0	0.7	0.057	3	0.0084	1.4
DZ-7_12.3	100.1	418	0.24	53.5	2	0.054	9	0.0083	3.5
DZ-7_36.1	179.5	773	0.23	55.3	0.7	0.055	7	0.0086	1.3
DZ-7_38.1	628.1	1519	0.41	56.0	0.5	0.059	4	0.0087	0.9
DZ-7_40.1	291.5	1095	0.27	55.7	0.3	0.059	2	0.0087	0.7

CHAPTER 8

DISCUSSION AND CONCLUSION

8.1 INTRODUCTION

The Tibet, Pamir, and Karakoram ranges were long since considered to be a single orogenic belt during the amalgamation of the Gondwana supercontinent (e.g., Burtman and Molnar, 1993; Robinson et al., 2012; Chapman et al., 2018). Collision of the Indian plate with the Asian plate during the Tertiary period gave rise to the active young mountain belt- the Himalaya. Before the collision, the southern margin of the Asian plate experienced extensive calc-alkaline, Andean-type magmatism associated with the northward subduction of the Neo-Tethyan oceanic lithosphere (e.g., Sharma and Kumar, 1978; Rai, 1980), forming the Trans-Himalayan magmatic arc of which the Lohit Plutonic Complex (LPC) is a part. Consequently, it is studied to understand the evolution and mode of formation of the said magmatic arc.

Previous chapters (1 to 7) have recounted in detail about the field observations, occurrences of the granitoids, and their relationship with other lithounits, magnetic susceptibility, petrography, phase chemistry, whole-rock geochemistry, and U-Pb SHRIMP zircon geochronology of representative granitoids from Dibang Valley. The present chapter attempts to synthesize the obtained results to infer the physico-chemical conditions of magma, the nature of magma, the timing of magmatism, and tectonic setting of the Lohit Plutonic Complex.

8.2 FIELD PETROGRAPHY

8.2.1 TEXTURAL VARIATIONS AND THEIR SIGNIFICANCE

The granitoids, along with the gabbro, diorite, and migmatites, are an integral part of the Lohit Plutonic Complex. Megascopically, the studied granitoids from Dibang Valley of the LPC are commonly coarse to medium-grained, leucocratic to mesocratic, and occasionally gneissic in some outcrops. Although not abundant, the quartz diorite host small mafic enclaves of rounded to lenticular size often exhibiting sharp and diffused contacts with host granites (Figure 2.2d) which attest to minor contribution of mafic magma in the petrogenesis of felsic host magma as opined by various workers (Barbarin and Didier, 1992; Kumar et al., 2004, Kumar, 2010). The quartz diorites are mostly phenocryst-free and are relatively undeformed, while the granodiorites often exhibit varying degrees of gneissosity, indicative of post-magmatic deformation. These granitoids are frequently crosscut by quartz or pegmatite veins, as well as leucogranites, suggestive of a younger magmatic activity relative to the host granitoids. The leucocratic granites from Alinye and Dambuen are relatively undeformed and contain phenocrysts of K-feldspar and plagioclase, while the leucogranites from Ayeso often exhibit foliation by the accumulation and orientation of mica minerals, and often grade to migmatitic texture, a signature of ductile deformation and localization of strain.

Biotite is the most abundant mafic silicate in quartz diorite, granodiorite, and granite, followed by amphibole, whereas in leucogranite, alumino-silicate minerals (such as garnet and muscovite) typical of peraluminous granite are observed. Biotites in quartz diorite, granodiorite, and granite are mostly found as small subhedral flakes of reddish brown and greenish colour, usually clustered with opaque minerals (magnetite and ilmenite) and other accessory phases such as epidote, zircon, apatite, and titanite (Figure 3.1 h), typical of their crystallization from a magmatic melt. Ilmenite and magnetite constitute the dominant opaque minerals, which are primarily observed as inclusions within biotite and/or amphibole. Euhedral to subhedral magnetite (Figure 3.2h) and titanite (Figure 3.2g) occur in close association with biotite and amphiboles that attest to its magmatic origin under a relatively oxidised magma.

8.3 GRANITE SERIES EVALUATION

8.3.1 MAGNETIC SUSCEPTIBILITY (MS) AND GRANITE SERIES

The bulk magnetic susceptibility (MS) of rocks is the sum of the contributions from all Fe-bearing minerals (Aydin et al., 2007; Thomson and Oldfield, 1986; Verosub and Roberts, 1995) and varies with concentration and composition of rock forming minerals which may include diamagnetic (quartz and feldspar), paramagnetic (hornblende and biotite) and ferromagnetic (magnetite, and pyrrhotite). The main carriers of MS are paramagnetic (iron-bearing silicates) and ferromagnetic (magnetite, along with accessory monoclinic pyrrhotite) minerals.

The Dibang Valley granitoids host diamagnetic (quartz and feldspars), paramagnetic (hornblende and biotite), and Fe-Ti oxides (magnetite and ilmenite) minerals in varied proportions. The presence of Fe-Ti oxides results in an increase in magnetic susceptibility, which is a typical signature of I-type granite suites (Chappell and White 1974; Ishihara 1977; Pitcher 1993). In the present study, the majority of the granitoids exhibit a wide range of modal compositions from quartz diorite–tonalite/trondhjemite-granodiorite-monzogranite and contain mineral assemblages of hornblende, biotite, magnetite, plagioclase, K-feldspar, and quartz comparable in petrographic characteristics with the metaluminous (I-type) granites of Chappell and White (1974), while the leucogranite usually contains aluminium-bearing minerals, such as garnet and muscovite, akin to crustally-derived, peraluminous (S-type) felsic melts. Despite Fe-Ti oxides being the dominant opaque minerals in the studied granitoids, most of the measured MS values are low and fall within the domain of nonmagnetic, weakly magnetic, or paramagnetic granites. This is in apparent contradiction with the results of the amphibole and biotite mineral chemistry and whole-rock geochemistry, which identified not only S-type (granite and leucogranite), but also I-type granites (quartz diorite and granodiorite). Low MS values in I-type granites are not uncommon (Gleizes et al., 1998; Gregorová et al., 2003; Kopf, 1966), and the apparent contradiction between magnetic susceptibility values and the mineral phase chemistry, including geochemistry in the present study, may be attributed to a modified magnetic mineralogy as a result of post-magmatic processes and deformational events that operated during Himalayan and Trans-Himalayan orogenesis.

The spatial distribution pattern of magnetic susceptibility in Dibang valley (Figure 2.5) reveals high MS values in the western belt in close proximity to the Lohit thrust. The granitoids are deformed and sheared to a certain extent, often exhibiting foliations, and are traversed by several shear zones parallel to the NW-SE regional trend.

Extensive ductile deformation associated with retrogressive metamorphism has been suggested for the LPC granitoids (e.g., Thakur and Jain, 1975; Choudhuri et al., 2009). The observed wide MS variations in the studied granitoids within the same granite variant and given region can be attributed to the large modal variations and grain size of ferromagnesian minerals (mainly amphibole and biotite), Fe-Ti oxides, and the presence or absence of ME in them. The presence of ME in the quartz diorites and granodiorites suggest the contribution of mantle-derived mafic magma in the evolution of the granitoids through mixing and mingling (open magmatic system) and hence is capable to enhance the MS value leading to increased oxidizing condition of the granitoids, as opined elsewhere (e.g., Kumar, 2008; Kumar, 2010 a, 2010b; Kumar and Rino, 2006; Kumar and Singh, 2008; Kumar et al., 2004a, 2004b). Accordingly, in Dibang Valley, the high MS values (3.049 to 19.29 $\times 10^{-3}$SI units) are commonly recorded from ME bearing granitoids that reflect the abundance of ferromagnetic and paramagnetic minerals, classifying them as magnetite series (oxidized) granites. Additionally, depending on the proportion of relatively coarse-grained primary titanomagnetite microphenocrysts and the degree of alteration of Fe-Ti oxides, variation in MS value from high to low was observed. The main Fe-Ti oxides observed in the Dibang Valley granitoids are magnetite and ilmenite. The studied granitoids exhibit re-equilibration textures in Fe-Ti oxides and amphibole replacement by biotite, indicating the influence of metamorphic processes.

The back-scattered electron (BSE) images obtained through SEM EDAX analysis confirm the presence of euhedral to subhedral Fe-Ti oxides (Figures 7.1a-f) in the Dibang Valley granitoids, often in close association with plagioclase, amphibole, and biotite. The euhedral magnetite, poikilitically enclosed within biotite (Figure 7.1a), and interstitial subhedral magnetite (Figure 7.1b) associated with stubby apatite, biotite and plagioclase attest to its magmatic origin under relatively oxidized (high fO_2) magmatic conditions, which is consistent with the recorded MS values (≥ 3 × 10^ (-3) SI units) characteristic of the magnetite (oxidized) series granite. The opaque Fe-Ti oxides include titanomagnetite with variable Ti content, forming a rim of ilmenite around some magnetite (Figure 7.1b), or exsolving blobs of ilmenite (Figure 7.1c-d) within magnetite. These are interpreted to have formed as a result of oxy-exsolution of primary titanomagnetite during post-magmatic cooling below 600-700 °C, a process facilitated by elevated oxygen fugacity (Tan et al., 2016). Magnetite rimmed by titanite is observed in few granodiorites (Figure 7e), suggesting subsolidus or low-grade metamorphic overprinting, while complete replacement of titanite by ilmenite, leaving behind titanite pseudomorphs (Figure 7f) observed in an altered granodiorite, likely contributed to the demagnetization of the granitoid, consequently giving it a low MS value (Meyase et al., 2023).

The replacement of titanite by ilmenite may have been facilitated by widespread hydrothermal fluid activity under high fO_2 during the subsolidus cooling phase. Secondary titanite, associated with amphibole and biotite, further supports the occurrence of late-stage, fluid-driven reactions. These mineralogical changes reflect both retrograde metamorphism and deformation-related processes.

Retrograde metamorphism and hydrothermal alterations can lead to the breakdown of magnetite by the oxidizing role of water (Airo, 1999). Alternatively, significant input of reducing sedimentary material (C- and S-rich) could lead to the production of reduced arc magmas and ilmenite-series plutonism (Takagi, 2004). Hence, deformation of the granitoids accompanied by alteration and destruction/breakdown of original magnetite fabrics that may have existed in the original I-type granites cannot be overlooked. Elevated fO_2 conditions in intensely deformed shear zones can result in the breakdown of magnetite and be replaced by biotite (Clark 1997). The LPC granitoids have undergone extensive ductile deformation, evident in their sheared, foliated, and jointed nature. Previous studies (e.g., Thakur and Jain, 1975; Choudhuri et al., 2009) opined that this region experienced widespread retrogressive metamorphism. Consequently, the low to moderate MS values observed in the Dibang Valley granitoids of LPC are best explained by fluid-enhanced post-magmatic modifications associated with Himalayan and Trans-Himalayan orogenic processes (e.g., Kumar, 2008). It is therefore plausible that the range of MS values measured from the granitoids reflects proportionate impacts from subsequent tectono-metamorphic and thermal events, including deformation, metamorphism, and hydrothermal alteration.

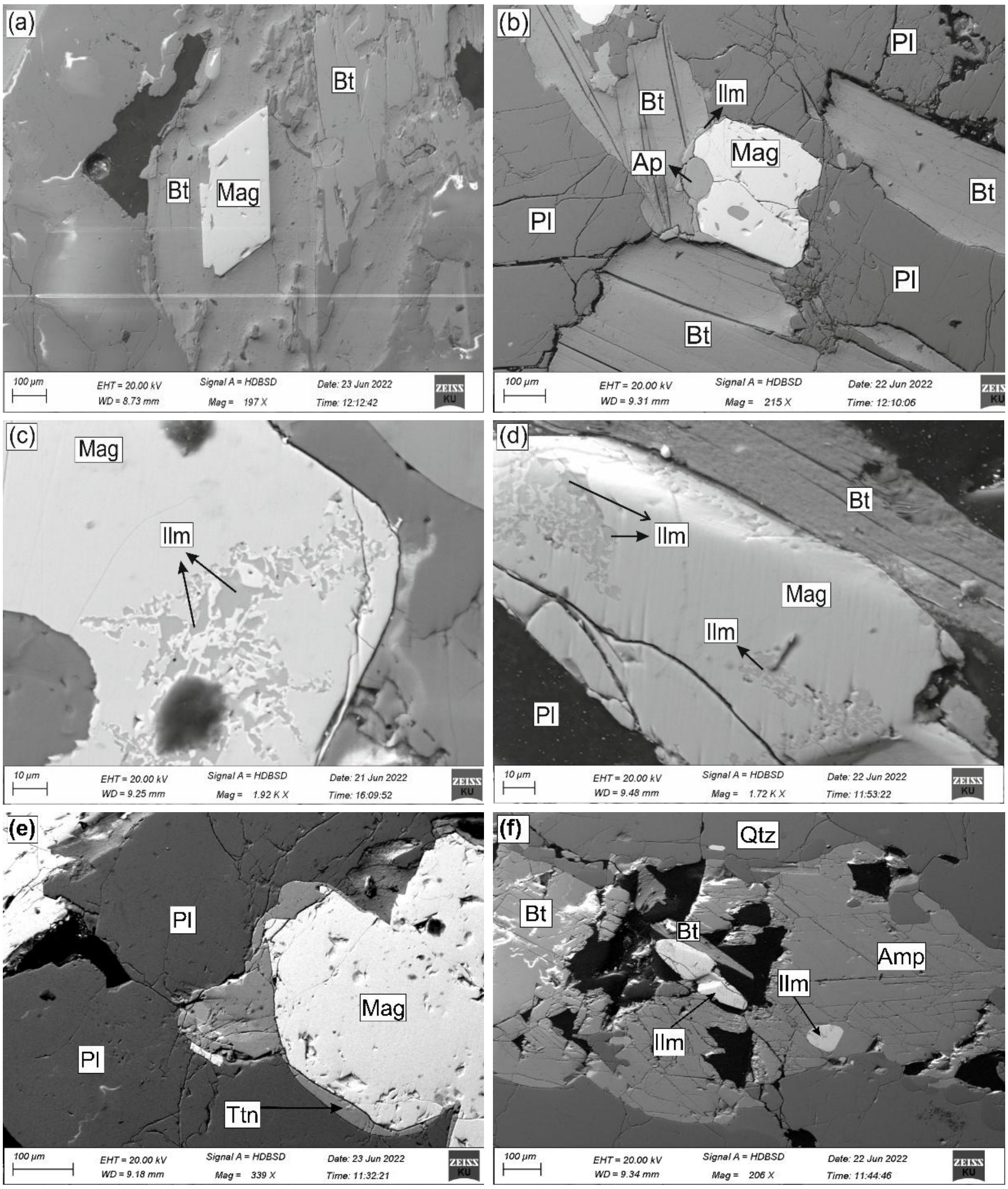

Figure 7.1: Backscattered Electron (BSE) images of Fe-Ti oxides obtained using SEM EDAX (a) euhedral magnetite in association with biotite; (b) interstitial subhedral magnetite with thin ilmenite rim associated with apatite and biotite; (c) & (d) exolution of ilmenite in magnetite; (e) magnetite rimmed with titanite; (f) ilmenite pseudomorph of remnant titanite within amphibole.

8.3.2 MODAL COMPOSITION, NOMENCLATURE, AND INFERRED GRANITE SERIES

Following the nomenclature scheme of felsic plutonic rocks given by the International Union of Geological Sciences (IUGS), the granitoids from Dibang Valley of LPC show wide variation in modal mineralogical composition. The ferromagnesian-rich granitoids are classified as quartz diorite and quartz monzodiorite; granodiorites fall within the granodiorite and tonalite/trondhjemite fields, while the granite and leucogranite modally correspond to monzogranite and granodiorite.

Based on the measured magnetic susceptibility (MS) of the felsic granitoids in Dibang Valley, which range from 0.030 to 19.29 x 10^{-3} SI units, a bi-modal distribution is inferred, comprising approximately 64% ilmenite-series, and 36% magnetite-series granite. These granitoids show a closer affinity to ilmenite series (S-type) and a lesser extent to the magnetite series (I-type).

8.4 VARIATION IN MINERAL COMPOSITION

Quartz diorite and granodiorite have similar mineral composition, with biotite and amphibole being the dominant ferromagnesian minerals present alongside plagioclase, quartz, and a minor amount of K-feldspar. Secondary epidotes are abundant due to mineral breakdown. Other accessory minerals are euhedral to subhedral titanite, stubby apatite, zircon, and magmatic as well as secondary Fe-Ti oxides. The granites and leucogranites possess lesser mineralogical variation, with dominant minerals being quartz, plagioclase, and K-feldspar. A fair amount (~25%) of biotite is present in the granite, but relatively less in leucogranite. Muscovite and garnet are observed only in the leucogranites. Common accessories are epidote, zircon, titanite, and opaques.

The presence of magmatic amphibole, flaky biotite, and coarse plagioclase grains in association with magnetite and titanite infers crystallization from a less fractionated magma for the quartz diorite and granodiorite. In contrast, the granite and leucogranite, characterized by the rare occurrence of magmatic amphibole and limited mineralogical variation, suggest crystallization from a more evolved magma. Additionally, the presence of garnet and muscovite indicates the involvement of crustal materials, likely due to assimilation during magma ascent.

8.4.1 AMPHIBOLE COMPOSITION

The composition of amphibole is influenced by the magma's bulk composition, as well as temperature, pressure, and oxygen fugacity during crystallization. Consequently, amphibole, being a characteristic phase of felsic hydrous magma (Arculus and Wills 1980; Cawthorn et al., 1973; Davidson et al., 2007), can be utilized to infer the magmatic processes and intensive parameters of crystallization (Bachmann and Dungan, 2002; Ridolfi et al., 2008, 2010; De Angelis et al., 2013; Turner et al., 2013). It is most commonly employed to infer the magmatic crystallization pressure and temperature and determine the emplacement depth of batholiths (e.g., Ague and Brandon, 1992; Anderson and Smith, 1995).

The amphiboles present in the granitoids of the present study are all calcic and largely classify as magnesio-hornblende and pargasite. The pargasite and tschermakite substitutions present in these amphiboles, in conjunction with the varying Al and Fe#, help in deducing the redox condition of the magma.

8.4.2 BIOTITE COMPOSITION

The dominant ferromagnesian mineral in the granitoids of Dibang Valley is biotite- a trioctahedral member of the quadrilateral isomorphic system comprising annite, phlogopite, siderophyllite, eastonite (Rieder et al., 1998). The role of biotite in assessing the physico-chemical conditions (P, T, fO_2, H_2O melt) and nature of magma is crucial (e.g., Wones and Eugster 1965; Czamanske et al., 1981; Abdel-Rahman, 1994; Kumar et al., 2005, 2006; Kumar and Singh, 2008; Kumar and Pathak, 2010; Bora and Kumar, 2015; Singh et al., 2016). The composition of biotite is used to infer elemental substitutions, which reflect the nature of host felsic magma (A-, I-, or S-type), which, in turn, corresponds to specific tectonic settings such as extensional/anorogenic environment, subduction-related, and syn-collisional settings (Abdel-Rahman, 1994).

Moreover, biotite is widely recognized as a reliable indicator of the redox conditions prevailing in magmatic systems (Wones and Eugster, 1965; Burkhard, 1991, 1993). In this context, it plays a significant role as a discriminative tool for identifying tectono-magmatic processes associated with granitoid petrogenesis (Barrière and Cotton, 1979; El Sheshtawi et al., 1993; Lalonde and Bernard, 1993; Abdel-Rahman, 1994; Machev et al., 2004, and references therein).

8.4.2.1 NATURE OF FELSIC MAGMA AND ELEMENTAL SUBSTITUTION

Based on the ternary diagram of Nachit et al. (2005), biotites from granitoids of Dibang Valley (except leucogranite biotites) reflect that their composition is more akin to hydrothermally re-equilibrated biotite. Although biotite undergo significant re-equilibration, it can nonetheless preserve and reflect the original physico-chemical conditions of the primary melt (Bónová et al., 2010).

The Ti content of biotite is primarily controlled by temperature (Patiño Douce, 1993; Stussi and Cuney, 1996). Biotite grains that have re-equilibrated or formed anew due to low temperature hydrothermal alteration contain less titanium compared to primary magmatic biotites. Consequently, low TiO_2 (1.18-3.36 wt%) and Ti content (0.07-0.20 wt%) for most of the granitoids are consistent with the re-equilibrated nature of biotite. While a relatively higher TiO_2 (2.74-3.51 wt%) and Ti (0.15-0.21 wt%) for the leucogranite support its primary nature.

A negative correlation between MgO and Al_2O_3 (Table 4.2) suggests elemental substitution between Mg and Al ($3Mg \rightleftharpoons 2Al$) in these calc-alkaline and peraluminous suites. The well-defined negative correlation between MgO and FeO^t in the granitoids (except leucogranite) reflects that the $FeO^t \rightleftharpoons MgO$ substitution influences the composition of biotite in calc-alkaline melts (Abdel-Rahman, 1994).

Compositional variation of biotite from the MgO-FeO^t-Al_2O_3 diagram (Albuquerque, 1973) shows most granitoids having compositional affinity with pyroxene and ferromagnesian minerals, pointing to a contribution of mafic mantle source, while the biotites of leucogranite having compositional affinity with biotite and muscovite, advocates an involvement/addition of crustal source during the collision. The variation diagram of $FeO^t/(FeO^t+MgO)$ vs. MgO (Figure 7.2) after Zhou (1986), shows a perfectly negative correlation, suggesting mixed mantle- and crust (hybrid) sources for the origin of Dibang granitoid melts. Although there is an overlap between the biotites of quartz diorite, granodiorite, and granite with $FeO^t/(FeO^t + MgO)$ varying between 0.56-0.68 wt%, they are slightly lower than that of leucogranite biotite (0.73-0.76 wt%), which attests to the involvement of a crustal component for the leucogranites and a mantle component for the other granitoids. These transitional (I- and S-type) granitoid melts may represent hybrid magma, evidenced by the presence of microgranular enclaves in host granitoids. However, the effect of assimilation or mixing of a deeper-seated mafic melt into the felsic magmatic reservoir, other than the sole influence of source rock, cannot be ruled out.

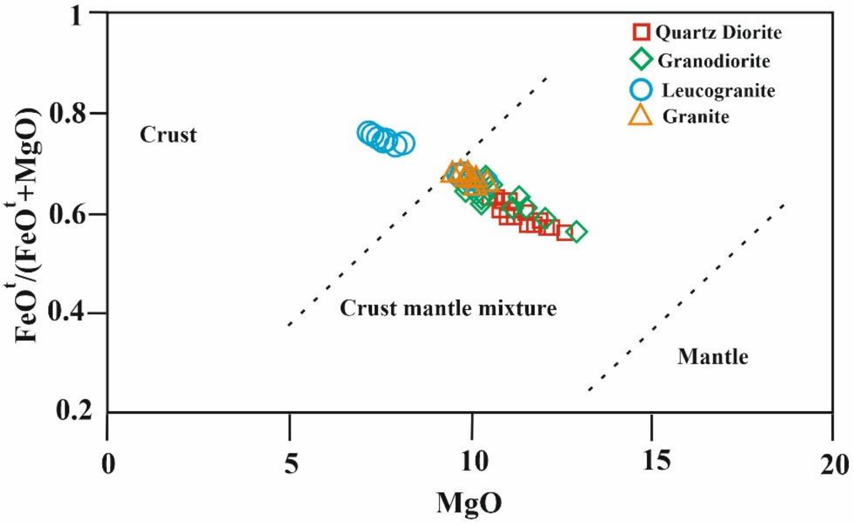

Figure 7.2: Variation diagram of biotites in terms of $FeO^t/(FeO^t + MgO)$ vs MgO (Zhou, 1986) suggests varying proportions of crust and mantle mixed (hybrid) sources for the origin of Dibang granitoids

8.4.2.2 REDOX CONDITION OF FELSIC MAGMA

The Mg# ($Mg/Mg+Fe^t$) ratio of biotite is widely applied for the approximation of the redox condition during mineral crystallization, whereby higher Mg# indicates an oxidized magmatic environment (Ishihara et al., 2002; Kumar and Pathak, 2010; Bora and Kumar, 2015). Accordingly, the quartz diorites, granodiorites, and granites having higher Mg# (0.47-0.58 wt%; average 0.51) imply an oxidizing condition during crystallization, while the biotites of leucogranite with lower Mg# (0.36-0.39 wt%; average 0.38) relate to a reducing environment.

The occurrence of titanite + magnetite + quartz assemblage, along with the presence of clinopyroxene or amphibole with intermediate or higher Mg# [(Mg/(Mg+Fe^t)] ratios, suggests crystallization from felsic magma under relatively high oxygen fugacity (fO_2) conditions (e.g., Enami et al., 1993; Wones, 1989). Similarly, the Fe# [Fe^t/(Fe^t+Mg)] of amphibole and biotite is used to constrain the oxygen fugacity of the magma system (e.g., Spear, 1981; Wones, 1981; Anderson and Smith, 1995; Anderson et al., 2008). Accordingly, the oxidizing or reducing nature of the magmatic environment had been deciphered using Fe# [Fe^t/(Fe^t+Mg)] and Mg# [(Mg/(Mg+Fe^t)] of biotite and amphibole (e.g., Czamanske and Wones, 1973; Wones, 1981; Anderson and Smith, 1995; Anderson et al., 2008).

Amphiboles and biotites that crystallized under oxidizing conditions tend to show higher Mg# values compared to those formed in a reducing environment (e.g., Wones, 1981; Bora & Kumar, 2015). Mg# of amphibole and biotite from quartz diorite, and granodiorite are significantly higher compared to those of granite and leucogranite (Table 5.1&5.2) and therefore, might be consistent with their moderately to strongly oxidized nature. However, the molar ratio $R=Fe^{3+}/(Fe^{3+}+Fe^{2+})$ of the calcic amphiboles from the Dibang Valley granitoids is variable (0.17 to 0.41 wt%), suggesting a range of fO_2 below and above the FMQ buffer, corresponding to low to moderate oxidizing conditions. Amphiboles with high Fe# [Fe^t/(Fe^t+Mg)] are believed to have been formed under low oxygen fugacity (Anderson and Smith, 1995). Most of the amphiboles of quartz diorite and granodiorite have low Fe# (0.32-0.59 wt%) as compared to granite (0.58-0.61 wt%) and correlate with high to moderate oxidizing conditions (Figure 7.3a). The calculated Fe^t/Fe^t+Mg ratios of biotite from the quartz diorite, granodiorite, and granite vary between 0.41-0.54 wt% and a slightly higher value of 0.61-0.64 wt% for leucogranite, suggesting their crystallization under moderate to high oxidising conditions with oxygen fugacity conditions between ΔFMQ+1 and ΔFMQ+3 (Figure 7.3b). Furthermore, the commonly observed dark brown to greenish-brown biotites along with the co-existence of euhedral Fe-Ti oxide, biotite, quartz, and K-feldspar (Figure 3.2h) as well as the presence of magmatic epidote, amphibole, and euhedral wedge shaped titanite (Figure 3.2g) documented in the present study collectively indicate an oxidizing magmatic environment (e.g., Wones, 1989; Lalonde & Bernard, 1993) comparable to those documented in the Mesoproterozoic Laurentia magnetite-series granites (Anderson et al., 2008).

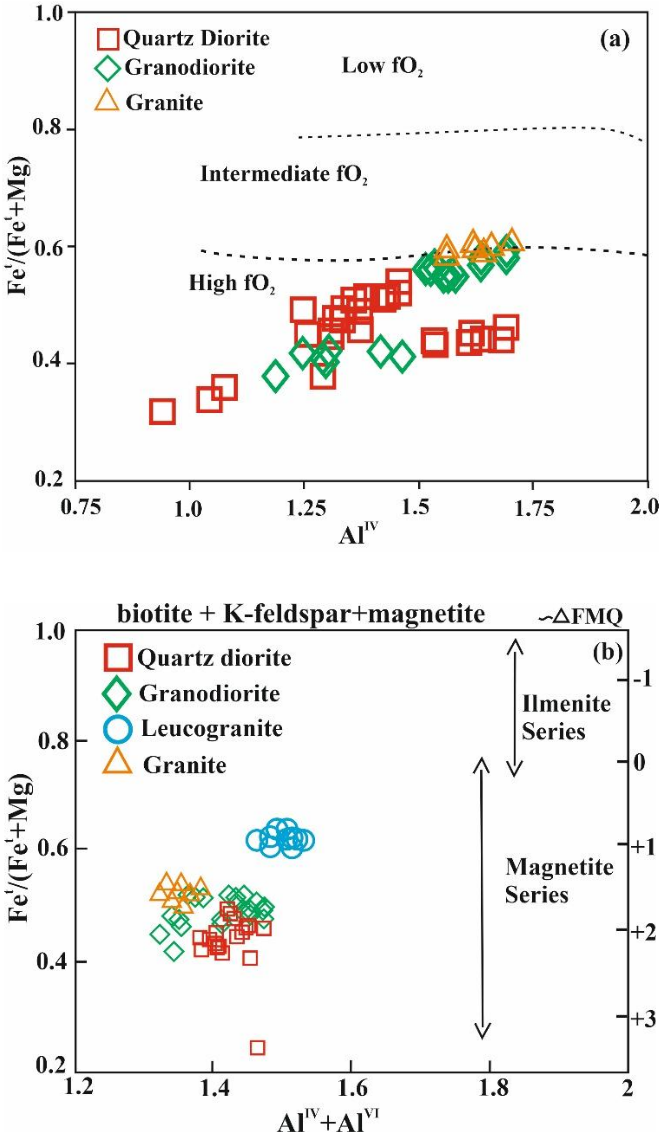

Figure 7.3: Constraining the redox conditions of Dibang granitoids during crystallization. (a) Fe^t/(Fe^t+Mg) vs Al^{IV} plot for amphibole (different fO_2 fields are shown after Anderson and Smith, 1995); (b) Fe^t/(Fe^t+Mg) vs Al^{IV} + Al^{VI} plot for biotite (after Anderson et al., 2008) comparable with the Mesoproterozoic Laurentia

magnetite-series granites, with approximate fO_2 relative to FMQ buffer ($P_{H2O} = P_{total}$) based on the calibration of Wones (1981).

Estimation of fO_2 of felsic melt using the annite-oxyannite-phlogopite (Fe^{2+}-Fe^{2+}-Mg^{2+}) content of biotite occurring together with magnetite and K-feldspar was carried out based on the calibration method of Wones and Eugster (1965). According to this ternary plot, biotites from most of the granitoids stabilized between the FMQ and NNO buffer. While biotites from leucogranite stabilized around the FMQ buffer zone, corroborating the oxidized nature of most of the granitoids and slightly reduced conditions of leucogranites as deduced from the previous parameters discussed above. Projection of biotite compositions (100×Fe/Fe+Mg), when projected onto an isobaric experimental calibration (P = 2,070 bar) of fO_2-Temperature binary section (Wones and Eugster, 1965) for biotite equilibria under various redox buffers (FMQ, NNO, HM) for granitoid melts indicates an oxidizing trend (fO_2^{-13} to log fO_2^{-12} MPa) with crystallizing temperature of 800-880˚C for most granitoids to a moderate to relatively reducing trend (fO_2^{-15} to log fO_2^{-13} MPa) for granite and leucogranite within temperature range of 755-820ºC.

Fugacities, and H_2O melt% values estimated through different calibrations are given in Table 8. Fugacity (log fO_2) values of amphiboles calculated using calibration of Ridolfi et al. (2010) yield an average value of -12.06 in quartz diorite, -12.14 in granodiorite, and -12.62 in granite, implying moderate oxidizing conditions. Crystallization of hydrous ferromagnesian minerals requires a certain amount of water to be present in the system. Experimental studies by eminent workers (Eggler, 1972; Helz, 1973; Naney, 1983; Merzbacher and Eggler, 1984) have suggested a threshold value of ≥ 5 wt% H_2O to stabilize amphiboles at high pressure. The elevated values of H_2O melt% of amphiboles from quartz diorite (8.17-10.73 wt%), granodiorite (5.18-6.53 wt%), and granite (6.08-7.12 wt%) imply a water-saturated magmatic system typical of a subduction-related tectonic setting. The abundant occurrence of magmatic amphibole and biotite in the said granitoids strongly supports this inference.

8.4.2.3 TECTONIC IMPLICATION

The composition of biotite is a reliable parameter in assessing the origin of parental melt (e.g., Burkhard 1993; Lalonde and Bernard 1993; Aydin et al., 2003; Machev et al., 2004; Kumar et al., 2006; Kumar and Pathak, 2010; Bora and Kumar, 2015). Based on the tectonic discrimination diagrams of Abdel-Rahman (1994), the Dibang granitoids are classified as I-type calc-alkaline to slightly peraluminous S-type characteristic of a subduction-related tectonic setting.

High Mg# (0.46-0.59 wt%), low Ti (<0.1 apfu), moderate Al^t (1.35-1.53 apfu), low FeO^t/MgO (< 2.11 wt%) ratio with enhanced Mg exhibited by the granitoids (except leucogranite) of Dibang Valley, is typical of biotites that crystallized in a subduction setting. Moreover, the enhanced H_2O melt% and abundant presence of magmatic ferromagnesian minerals point to its crystallization in a subduction-related setting, where slab-derived fluids flux the overlying mantle and/or crust, initiating partial melting.

8.4.3 PLAGIOCLASE COMPOSITION

The composition of plagioclases, ranging from $An_{18.27}$ to $An_{32.09}$ (oligoclase-andesine), $Ab_{63.55}$ to $Ab_{78.88}$ (andesine), and Or_0 to $Or_{2.11}$ (orthoclase), has been observed in all the granitoids of Dibang Valley. Most quartz diorite plagioclases are andesine in composition, while most granodiorites, granites, and leucogranites belong to oligoclase.

8.5 GEOCHEMISTRY

8.5.1 MAJOR AND TRACE ELEMENT VARIATION AS PROCESS DIAGNOSIS

Geochemically, the majority of the granitoids of Dibang valley possess characteristics that indicate a moderately evolved parental melt, which is reflected by the moderate SiO_2 content (52.00-65.77 wt%) except for the granites, which show a more evolved signature with SiO_2 (66.70-70.09 wt%). From the ternary plot Na_2O-K_2O-CaO (Hassan and Hashad, 1990) (Figure 7.4), the quartz diorite and granodiorites lie within the calc-alkaline (CA) field, indicating a moderately evolved, transitional calc-alkaline melt, while the granites plot closer to the Egyptian Younger Granites field, reflecting a more evolved and fractionated nature. The Molar A/NK vs A/CNK plot also indicates a metaluminous (I-type) character, typical of moderately fractionated calc-alkaline magma (Chappell and White, 1992), while the slight peraluminosity of granites suggests a higher degree of fractionation of residual melt. The peraluminosity of leucogranites points to an involvement of supracrustal assimilation (Yang et al., 2008).

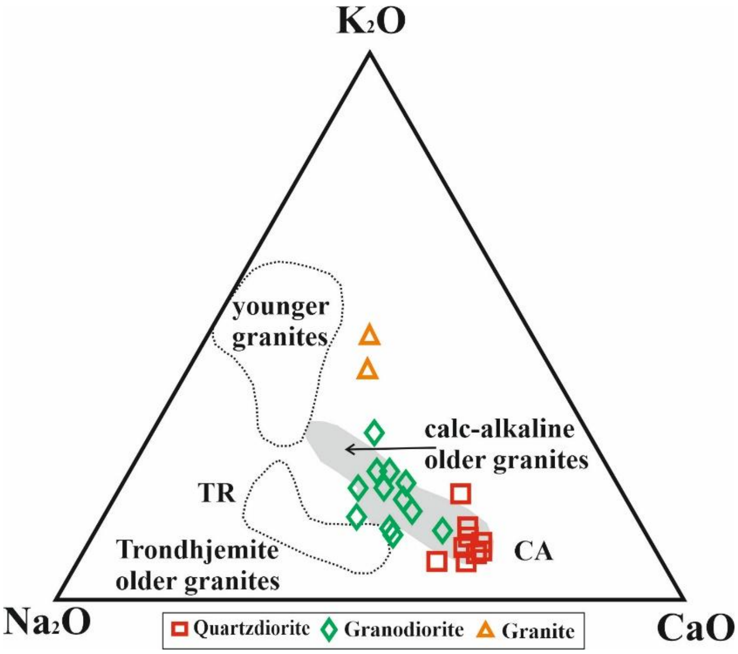

Figure 7.4: Na_2O-K_2O-CaO ternary diagram showing different fields of granites (Hassan and Hashad, 1990). TR (Trondhjemite) and CA (calc-alkaline) fields are from Barker and Arth (1976).

Variations of different major oxides with respect to SiO_2 observed from the Harker variation diagram can be utilized to interpret the melt's evolution, as the crystallization of specific minerals affects the concentration of certain elements, leading to changes in the melt's composition. The positive correlation of Na_2O and K_2O against SiO_2 supports the late fractionation of alkali-rich minerals like K-feldspar, attesting to the moderately evolved nature of most granitoids. The negative correlation between P_2O_5 and SiO_2, but a broadly positive correlation between A/CNK and SiO_2, is akin to common I-type granites. A marked decrease in TiO_2, MgO, CaO, FeO^t, MnO, and P_2O_5 with an increase in SiO_2 indicates that amphibole fractionation played a key role in magma evolution and is also a characteristic indicator of magma mixing and mingling. A distinct negative trend in Ti and V with respect to SiO_2 suggests fractionation of Fe-Ti oxides, amphibole, pyroxenes, and feldspars in an oxidizing environment, and the positive correlation of Rb, Nb, and La against SiO_2 supports progressive fractionation from a mafic melt towards a felsic melt, typical of calc-alkaline magmatic differentiation. The negative correlation between Y and SiO_2 in the granitoids likely reflects the early fractionation of Ca-rich accessory phases such as apatite and titanite, as these minerals preferentially incorporate HFSEs like yttrium (Y) into their crystal structures during early stages of magmatic differentiation. The concurrent negative correlation between P_2O_5 and SiO_2 supports this interpretation.

The calc-alkaline trend exhibited by the quartz diorites and granodiorites in the AFM diagram (Figure 5.2) and transition from calc-alkaline to high-K calc-alkaline series shown in the SiO_2 vs K_2O plot (Figure 5.4) indicate moderate oxidizing conditions and also testify to crystal fractionation playing a dominant role in the generation and evolution of the melt. The granites plotting in close proximity to the shoshonitic series is suggestive of potassium diffusion in a more evolved melt.

Compositional variation from gabbroic diorite to granodiorite and monzonite obtained from the $Na_2O + K_2O$ vs SiO_2 diagram (Figure 5.5) aligns well with the cationic classification that designates the granitoids as gabbroic diorite, monzodiorite, diorite, tonalite, and granodiorite.

Experimental investigations (Patiño Douce, 1997; Skjerlie and Johnston, 1993) have established that melting at shallow crustal levels facilitates dehydration melting of magnesian calc-alkaline granitoids, generating ferroan granitic melts. Consequently, it is inferred that low degrees of partial melting yield silica-enriched, calc-alkalic ferroan granitoids, while higher degrees of melting shift the melt composition toward an alkali-calcic composition, as corroborated in the chemical classification (Figure 5.7) in which all granitoids, except leucogranites, plot in the field of magnesian-rich granites formed under high fugacity conditions. Leucogranites are identified as ferroan-rich granites that crystallized under lower fugacity in a more reduced environment (Albuquerque et al., 2020). This tallies with the inference from the fO_2 plots of biotite and amphibole mineral chemistry.

With the exception of leucogranites, the remaining granitoids predominantly have Mg# values >50 wt% (Figure 7.5a), indicating they originate from mantle-derived melts that interacted with arc crust. Conversely, leucogranites, with low Mg# ranging from 7.09 to 25.71 wt%, relate to remelted arc crust. The molar concentrations of Al_2O_3, CaO, MgO, and FeO^t indicate that quartz diorites and granodiorites resulted from partial melting of a mafic source, whereas granites and leucogranites derive from partial melting of a more alumina-rich crustal source, such as metagreywackes (Figure 7.5b). The high fugacity and metaluminous nature of the quartz diorites and granodiorites, along with the relatively lower fugacity and slight peraluminosity of the granites and leucogranites, further support this inference of a mafic and crustal source for the respective granitoids. The trace elements exhibit depletion in Th, U, Nb, and Ta alongside enrichment in Ba, K, and Sr, showing features characteristic of arc-magmatic settings. Low average concentration of Cr (av. 28.70 ppm) and Ni (av. 6.68 ppm) further suggests derivation from an arc-like mantle source.

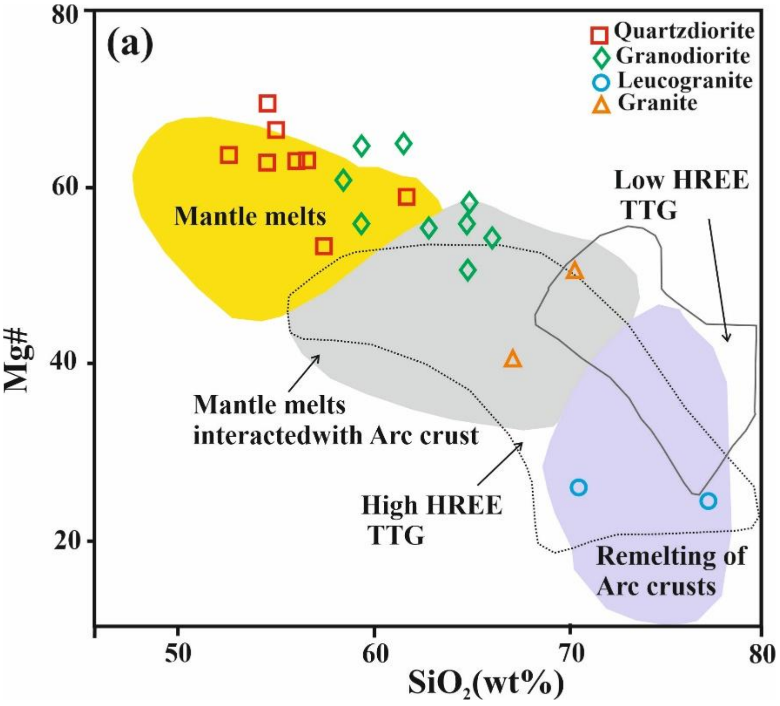

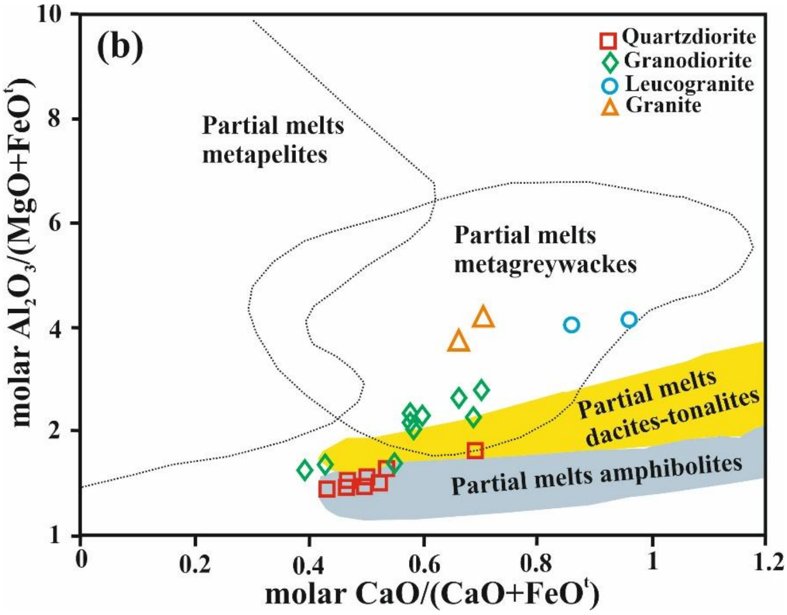

Figure 7.5: Source discrimination diagrams. (a) Mg# versus SiO_2 (after Heilimo et al., 2010) used to discriminate the sources of the Dibang granitoids; (b) molar $Al_2O_3/(MgO+FeO^t)$ vs molar $CaO/(MgO+FeO^t)$.

8.5.2 RARE EARTH ELEMENTS (REE)

The high concentration of Ba+Sr in most of the granitoids (686.04-1735 ppm) along with a positive Ba and Sr anomalies on the primitive-mantle normalized spidergrams (Figure 5.11) suggest an enrichment in the LILEs, likely due to slab-derived fluid during magma genesis in a subduction-related setting. Moreover, the lack of correlation in Ba and Sr with SiO_2 indicates that they were inherited from a hydrous mafic source with no significant fractionation. This is also supported by the negligible or weak Eu anomaly. The leucogranites with lower Ba and Sr (187-570 ppm) indicate a greater involvement of crustal contamination and lower influence from slab-derived fluids.

The moderately enriched LREE [$(La/Sm)_N$=60-4.80; $(La/Lu)_N$=4.30-28.85] and depleted HREE [$(Gd/Yb)_N$=1.29-3.06] in the quartz diorites and granodiorites suggest partial melting of a mantle wedge metasomatized by slab-derived fluids from a subducted oceanic crust. A greater enrichment of LREE [$(La/Sm)_N$=4.26-4.48; $(La/Lu)_N$=17.54-22.41] and similar depleted HREE [$(Gd/Yb)_N$=1.95-2.14] observed in the granites indicates a comparatively higher degree of fractionation, also supported by the weak negative Eu anomaly. The leucogranites, with only slight enrichment in LREE [$(La/Sm)_N$= 0.61-1.19; $(La/Lu)_N$=0.79-2.02] with respect to HREE [$(Gd/Yb)_N$= 1.01-1.21] suggest the least fractionated melt amongst all the granitoids in the present study. Distinct positive Pb anomaly coupled with negative Nb and Ti anomalies in all granitoids is characteristic of continental arc-related igneous rocks formed in a subduction-related environment. In the $(La/Yb)_N$ vs Yb_N (Figure 7.6a) and Sr/Y vs Y (Figure 7.6b) plots, the quartz diorite, granite, and leucogranite mostly have characteristics of arc magmatic rocks, while the granodiorites show a trend of mixing between arc-magmatic and adakitic rocks.

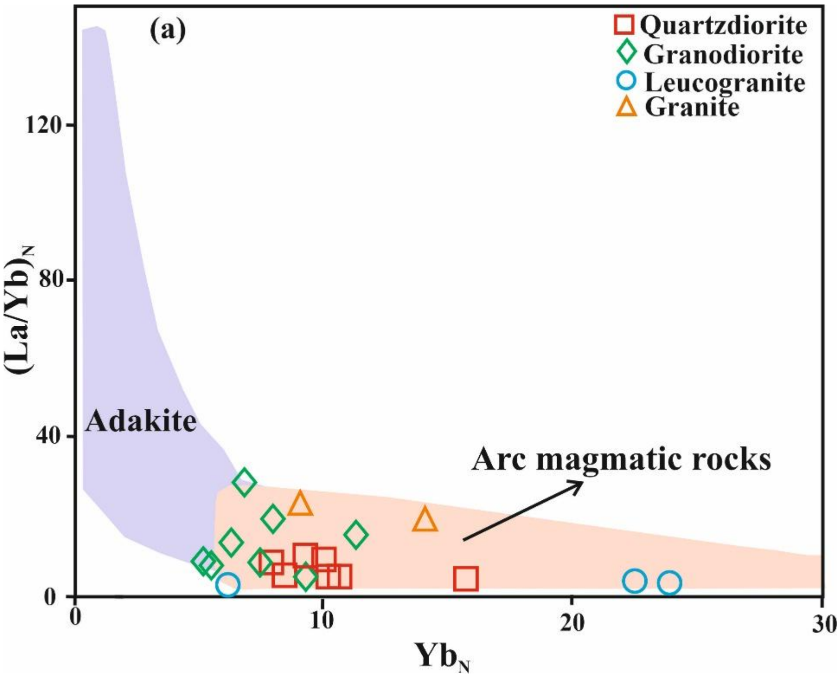

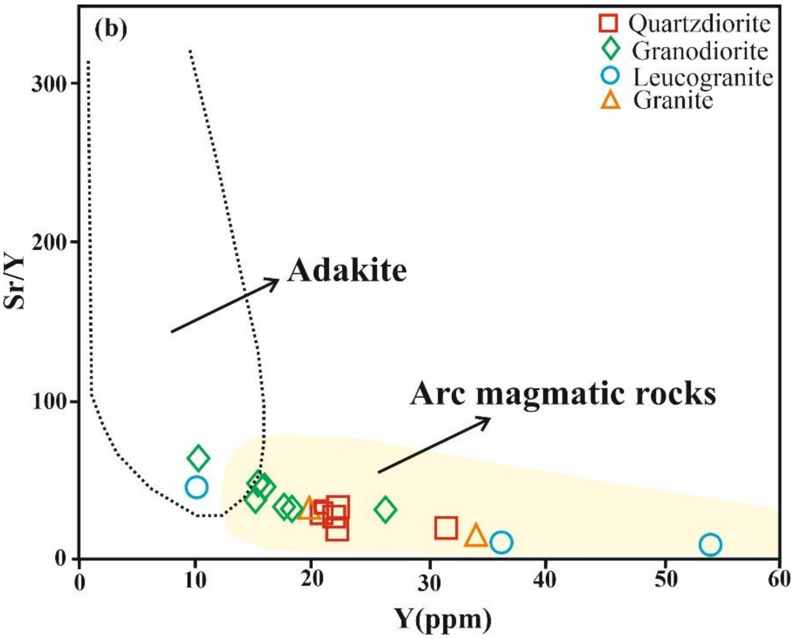

Figure 7.6: Geochemical discrimination diagrams of (a) $(La/Yb)_N$ vs Yb_N; (b) Sr/Y vs Y (Defant and Drummond, 1990).

8.5.3 PETROGENESIS

8.5.3.1 EVIDENCE OF MANTLE-CRUST INTERACTION

Field and textural evidence for magma mixing in the Dibang Valley is well documented. The occurrence of rounded to sub-rounded and lenticular shapes of ME is evidence of enclave magma quenching against the cooler felsic host. Supporting evidence from phase chemistry of biotite is provided from the variation diagram after Zhou (1986), where the biotites from the granitoids (except leucogranite) display a well-defined negative trend, implying derivation from hybridized magmas involving both crustal and mantle sources (Figure 7.2). Leucogranites plot in the 'crust' area, attesting to the involvement of crustal component in its genesis and rendering its peraluminous character.

8.5.3.2 MAGMA SOURCE

Whole-rock geochemistry of representative granitoids from Dibang Valley of the LPC has been used to identify the potential sources and magmatic processes that influenced these plutonic rocks. Fluids released from the subducting oceanic slab via dehydration can trigger partial melting, leading to modifications in the mantle wedge (Peacock et al., 1994; Stern & Kilian, 1996; Hawkesworth et al., 1997; Turner et al., 1997; Class et al., 2000). The enrichment of LILE (B, Sr, Pb) and LREE (La, Ce) and the depletion of HFSE (Nb, Ta, Ti, Zr) suggest their generation in a subduction environment due to partial melting of the upper mantle by slab-derived fluids. This is also supported by the Nb/Th vs. Zr/Nb diagram (Condie, 2015) (Figure 7.7) where all the granitoids plot within the "hydrated mantle" field.

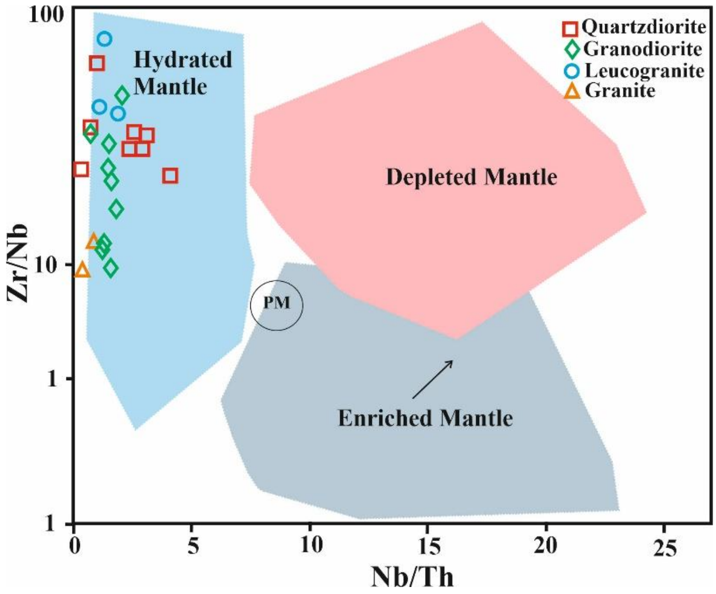

Figure 7.7: Nb/Th vs. Zr/Nb source diagram (Condie, 2015) of Dibang granitoids.

Nb, Zr, and Y are generally unaffected by metasomatism, weathering, or alteration as they are geochemically inactive ($K_D \approx 1$) and can reliably reflect the mantle composition at the source area (Zhang et al., 2020). In the Nb-Zr diagram (Figure 7.8), most granitoids apart from granites and few granodiorites, plot in the depleted mantle field, pointing to a depleted asthenospheric mantle as their source.

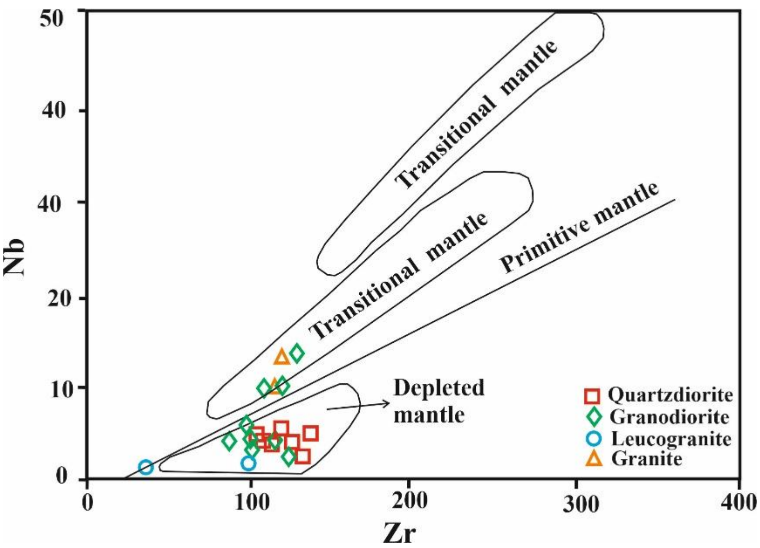

Figure 7.8: Nb vs Zr source variation diagram, where most of the Dibang granitoids plot within the depleted mantle field.

According to Bikramaditya et al. (2020), the granitoids of LPC exhibit a low initial $^{87}Sr/^{86}Sr$ ratio (0.7038-0.7045) and high positive $\varepsilon_{Nd}(t)$ (+2.9 to +5.9), which are characteristic of a juvenile mantle source (Harris et al., 1988; Mo et al., 2005; Chu et al., 2006; Wen et al., 2008; Lee et al., 2012). These isotopic features, in addition to the geochemical characteristics, point to derivation from a metasomatized, depleted mantle source. The granitoids have a low Rb/Sr ratio (0.01-0.44 ppm) comparable to mantle-derived rocks. However, their Nb/La ratio (0.19-0.47 ppm) and Nb/Ce ratio (0.07-0.20 ppm) indicate significant crustal influence. In the La/Yb vs. Nb/La diagram (Figure 7.9a), the granitoids fall within the lithospheric mantle field and close to the mixed mantle source region, suggesting that they were initially derived from partial melting of a mantle source, with a possible contribution from components of asthenospheric mantle (Rudnick and Gao 2003; Ormerod et al., 1988). Additionally, in the $(Hf/Sm)_N$ vs $(Ta/La)_N$ diagram (Figure 7.9b) of La Fl`eche et al. (1998), the granitoids mostly fall within the fluid-related subduction metasomatism.

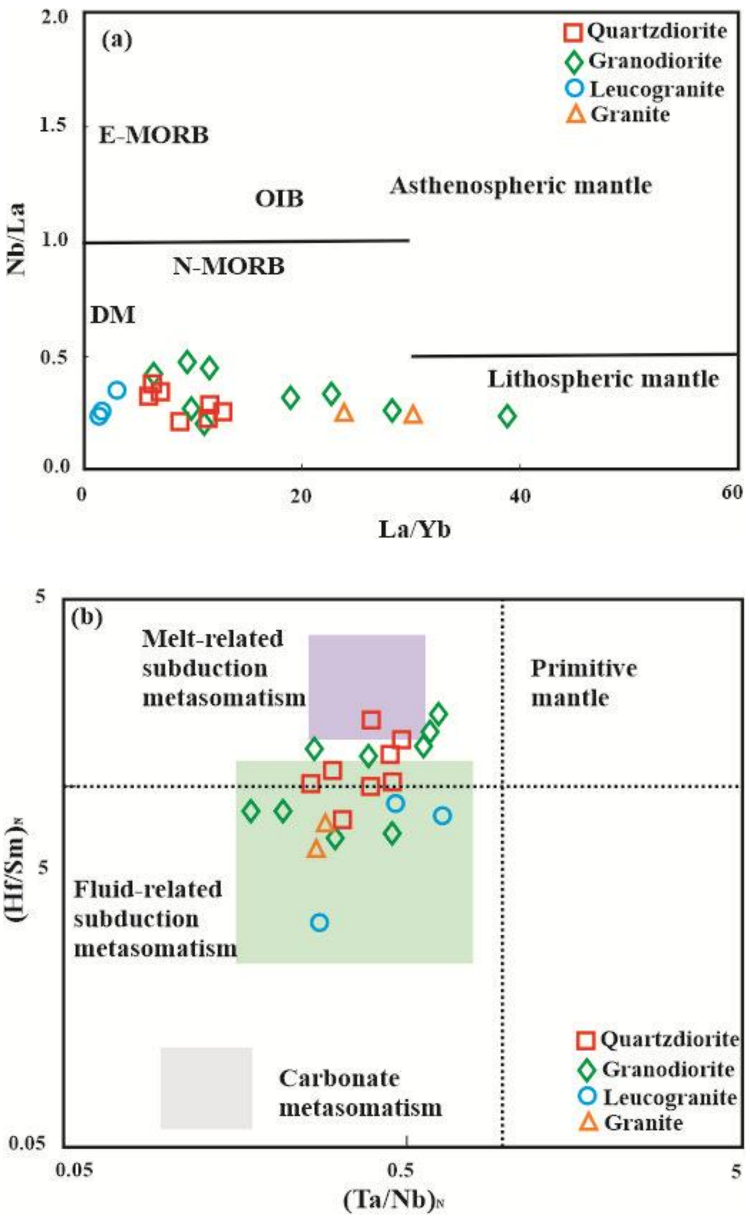

Figure 7.9: (a) Nb/La vs La/Yb diagram to distinguish the lithospheric and asthenospheric mantle (after Abdel-Rahman and Nasar 2004); (b) $(Hf/Sm)_N$ vs $(Nb/La)_N$ diagram (La Fl`eche et al., 1998) showing fluid-related subduction metasomatism of the Dibang granitoids.

From the geochemical discrimination diagrams (after Feng et al., 2015, and Gou et al., 2019) plotted by employing several compatible and incompatible trace element ratios (Figures 7.10a-d), all the granitoids exhibit linear trends in the fluid-related enrichment trend. This strongly implies that metasomatism of the mantle wedge is mainly brought about by the hydrous fluids released from the dehydration of the subducting Neo-Tethyan oceanic lithosphere.

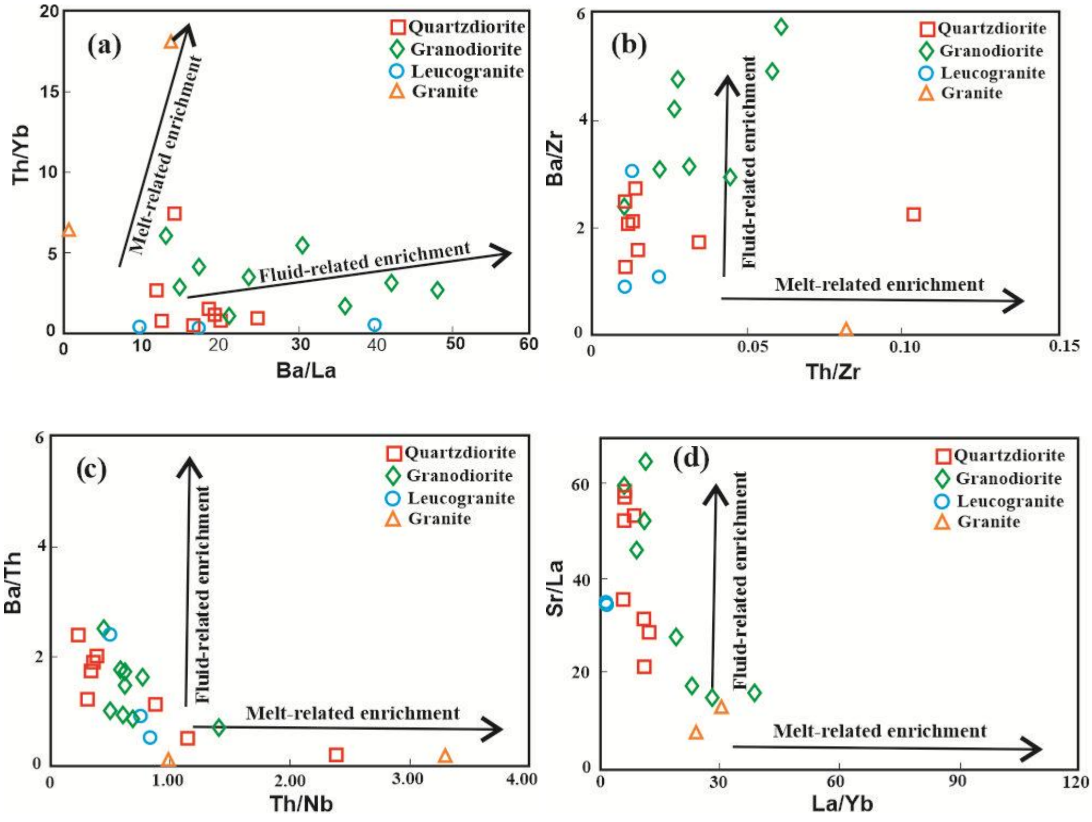

Figure 7.10: Fluid and melt-related enrichment plots (after Feng et al., 2015; Guo et al., 2019). (a) Th/Yb vs. Ba/La; (b) Ba/Zr vs. Th/Zr; (c) Ba/Th vs. Th/Nb; and (d) Sr/La vs. La/Yb for the Dibang granitoids where all granitoids show a fluid-related enrichment trend.

To infer the source composition of the Dibang granitoids, the Sm/Yb vs La/Sm (Figure 7.11a) and Gd/Yb vs La/Yb (Figure 7.11b) have been plotted (after Shaw, 1970; Aldanmaz et al., 2000). These diagrams show that the quartz diorite and granodiorite were derived from 1% to 5% partial melting of a spinel±garnet lherzolite mantle in an arc-related subduction zone.

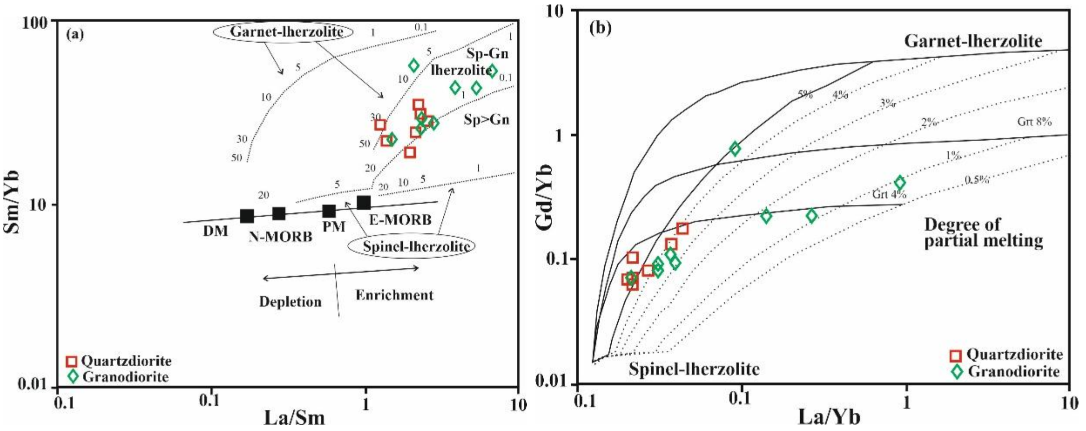

Figure 7.11: (a) Sm/Yb vs. La/Sm diagram (Shaw, 1970); (b) Gd/Yb vs. La/Yb diagram with melting curves of spinel lherzolite, garnet-spinel lherzolite, and garnet lherzolite (after Aldanmaz et al., 2000),

8.5.4 GEOTECTONIC ENVIRONMENT

Based on the multicationic R_1–R_2 classification (De La Roche et al., 1980), the Dibang granitoids reflect emplacement under variable tectonic settings, suggesting that magmatism occurred in multiple episodes ranging from pre-collisional stages to phases approaching the India–Asia continental collision. Supplementing this, from the Rb vs Y+Nb diagram (Pearce, 1996), the granitoids belong to the volcanic arc granites (VAG), indicating an arc-related origin (Figure 5.16b).

From the $(Th/Nb)_N$ vs $(La/Nb)_N$ diagram (Figure 7.12), the granitoids overlap within the continental crust (CC) and subduction-related (SuB) fields. The high Th_N/Nb_N (1.99-20.18 ppm) and La_N/Nb_N (2.20-5.40 ppm) ratios of the granitoids suggest that the magmas were likely generated in a continental arc, where an involvement of both subduction and crustal assimilation/melting was present.

The Th/Yb vs. Ta/Yb discrimination diagram (Figure 7.13) shows that most granitoids (except leucogranite) plot in the active continental margin, which further supports the idea that the melt was generated by partial melting of depleted mantle metasomatized by hydrous fluids released from the subducting slab, typical of subduction-related arc magmatism.

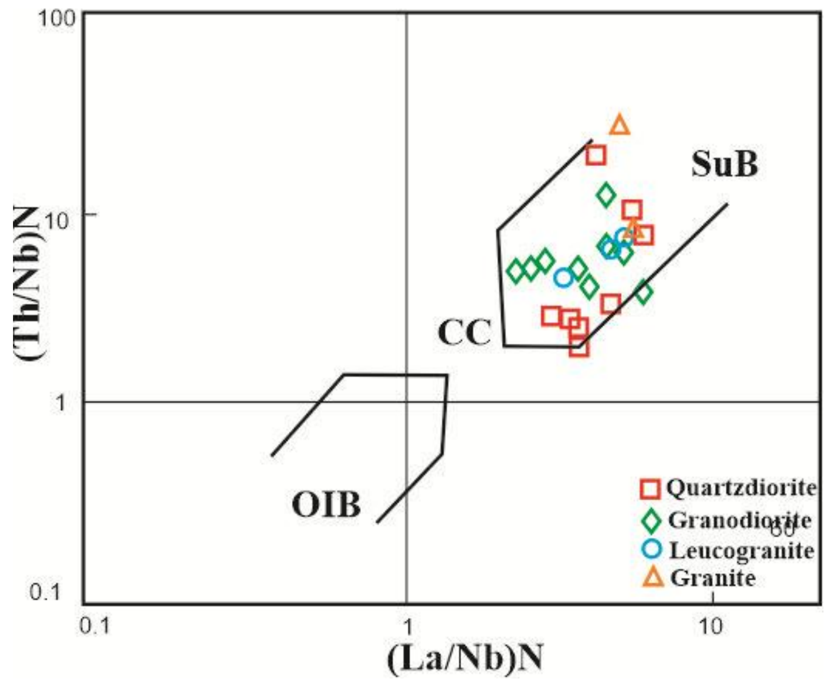

Figure 7.12: $(Th/Nb)_N$ vs $(La/Nb)_N$ diagram. Field CA- Continental Arcs; CC- Continental Crust; IA- Island Arcs; OIB- Ocean Island Basalts; SuB- subduction-related magmatic suites.

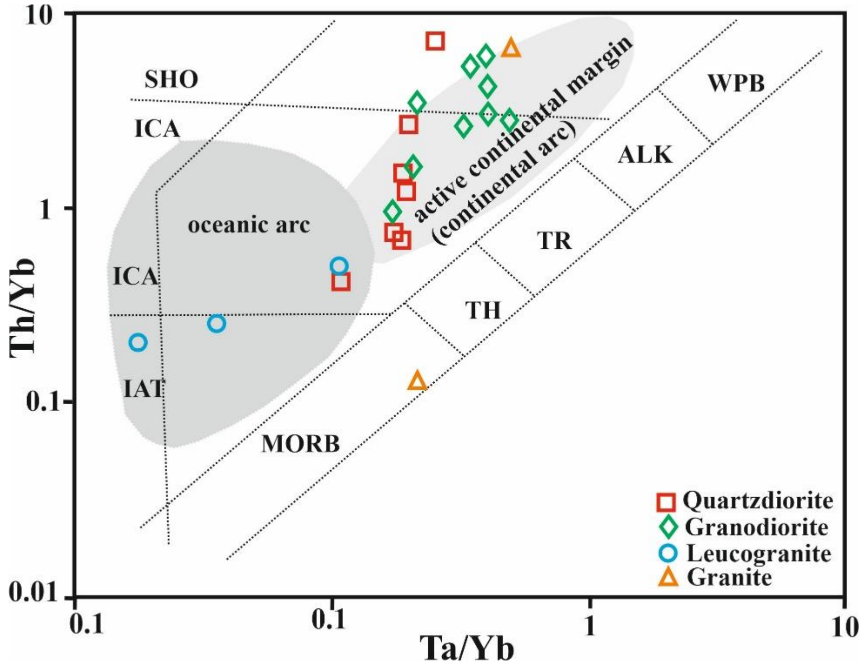

Figure 7.13: Th/Yb vs. Ta/Yb tectonic discrimination diagram (Pearce, 1983) of Dibang granitoids

8.5.6 PHYSICAL CONDITIONS OF CRYSTALLIZATION

The pressure (1.74-4.93 kbar) of the studied granitoids calculated using the Al-in-hornblende barometer (Ridolfi, 2010) suggests their emplacement at shallow (~6km) to mid-crustal (~18km) depths (considering 1kbar=3.7 km of continental crust; Tulloch and Challis, 2000**).** The estimated temperature (≤ 780°C) obtained from the amphibole-plagioclase thermometry (Holland and Blundy, 1994) for the granitoids reflects equilibration at near-solidus conditions, consistent with diffusive re-equilibration during late magmatic stages (Meyase et al., 2023). A summary of estimated intensive crystallization parameters (pressure, temperature, fO_2, ΔNNO, and emplacement depth) using amphibole compositions of granitoids is given in Table 7.

Experimental studies suggest that granitic magma will become solid when the solidification temperature cools to 650–700 °C (e.g., Tuttle and Bowen, 1958; Luth et al., 1964; Piwinskii, 1968). However, lower crystallization temperatures due to repeated cycles of heating and fluxing by water-rich fluids could not be ruled out (Glazner and Johnson, 2013; Challener and Glazner, 2017). The composition of feldspars (K-feldspar and plagioclase) in granite, plotted on the graphical thermometer of Brown and Parsons (1981), gives a range of temperature of about 340 to 450 °C (Figure 7.14), which likely reflects sub-solidus re-equilibration of the feldspars as evidenced by the presence of myrmekite texture. The two feldspars thermometry of granites corroborates well with the previously estimated temperature of about 350 to 405°C (Goswami, 2013a; Pebam and Kamalakannan, 2019). Additionally, the low temperature range of 450-600°C derived from the Ti vs $Mg/(Mg+Fe^t)$ (after Henry et al., 2005) from biotites present in the Dibang granitoids also affirms the sub-solidus re-equilibration of the biotites (Figure 7.15). Thermobarometric estimates of the Dibang granitoids from the Qz-Ab-Or diagram showing experimentally calibrated isobars and isotherms (Johannes and Holtz, 1996), suggest that the granitic melt crystallized under variable pressure (2-10 kbar) and temperatures ranging from 700°C to >760°C (Figure 7.16).

Table 7: Summary of estimated intensive crystallization parameters (pressure, temperature, fO_2, ΔNNO and emplacement depth) using amphibole compositions of granitoids from Dibang Valley.

Rock type	**Quartz diorite**			**Granodiorite**			**Granite**		
	Min	**Max**	**Average**	**Min**	**Max**	**Average**	**Min**	**Max**	**Average**
Aluminium-in-hornblende barometry (kbar)									
Hammarstrom & Zen, 1986	5.80	7.61	6.58	3.85	6.36	4.84	5.73	6.68	6.29
Hollister et.al., 1987	6.13	8.16	7.01	3.96	6.77	5.06	6.05	7.12	6.68
Johnson & Rutherford, 1989	4.71	6.23	5.37	3.08	5.19	3.91	4.65	5.45	5.12
Schmidt, 1992	6.18	7.90	6.92	4.35	6.72	5.28	6.12	7.02	6.65
Anderson & Smith, 1995	6.56	8.24	7.23	2.60	6.29	4.59	5.47	6.64	6.02
Ridolfi et. al., 2010	2.98	4.93	3.74	1.74	3.64	2.35	2.94	3.84	3.46
Ridolfi & Renzulli, 2012	1.49	5.19	2.97	1.43	4.30	2.50	-	-	-
Ridolfi, 2021	1.78	3.95	2.66	1.26	2.64	2.05	-	-	-
Mutch, 2016	4.82	6.39	5.48	3.37	5.34	4.09	4.74	5.54	5.22
Hornblende-plagioclase thermometry (^{o}C)									
Holland & Blundy, 1994	614	702	664	554	780	700	695	718	706
Amphibole only thermometry (^{o}C)									
Ridolfi et. al., 2010	834	924	871	841	904	866	878	905	891
Ridolfi & Renzulli, 2012	711	872	800	767	884	817	-	-	-
Ridolfi, 2021	848	940	880	823	882	856	-	-	-
log fO_2 Ridolfi, 2010	-12.78	-11.08	-12.06	-12.71	-11.36	-12.14	-12.86	-12.45	-12.62
log fO_2 Ridolfi, 2021	-13.65	-10.25	-11.52	-13.42	-10.44	-12.18	-	-	-
ΔNNO Ridolfi, 2010	-0.12	0.66	0.28	-0.45	0.99	0.36	-0.79	-0.49	-0.63
ΔNNO Ridolfi, 2021	-0.81	3.01	0.99	-0.69	3.02	0.87	-	-	-
H2O melt% Ridolfi, 2010	8.17	10.73	9.36	5.18	6.53	5.92	6.08	7.12	6.55

Aluminium-in-hornblende barometry, hornblende-plagioclase and amphibole only thermometry, log fO_2***, and*** ΔNNO were calculated using WinAmptb program (Yavuz & Döner, 2017). ***Selected pressure***: Ridolfi et al.,2010; ***Selected temperature:*** Ridolfi et al.,2010

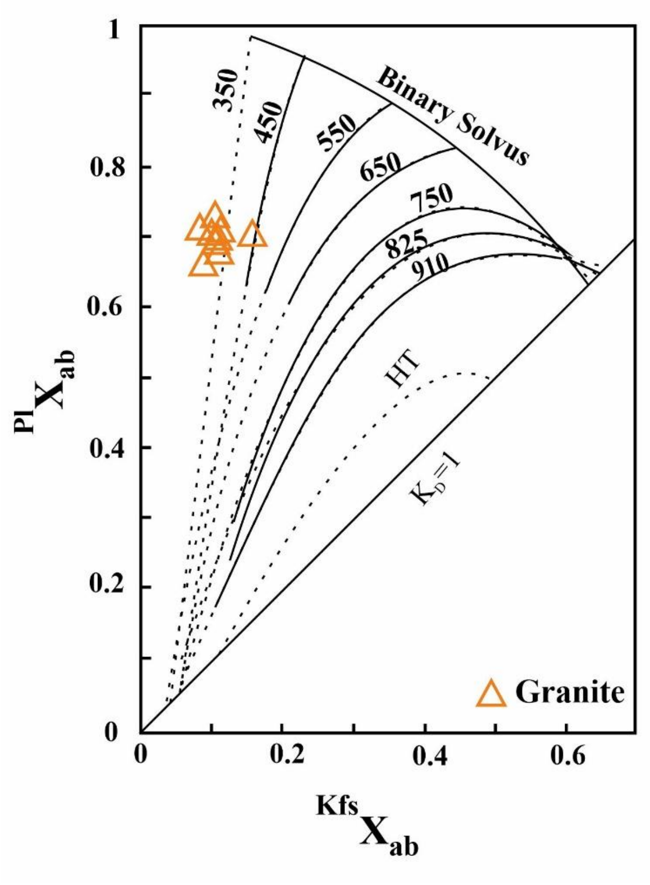

Figure 7.14: Two feldspars thermometry of leucogranites plotted on the graphical thermometer of Brown & Parsons, 1981

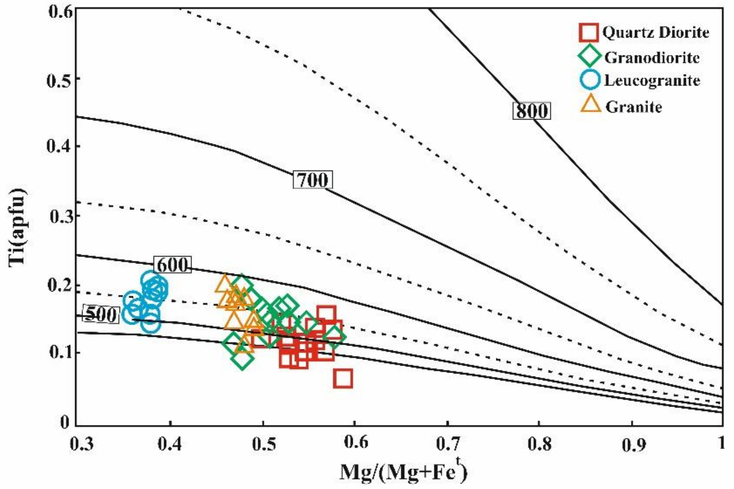

Figure 7.15: Ti vs. Mg/(Mg+Fe^t) plots of biotites of Dibang granitoids (after Henry et al., 2005).

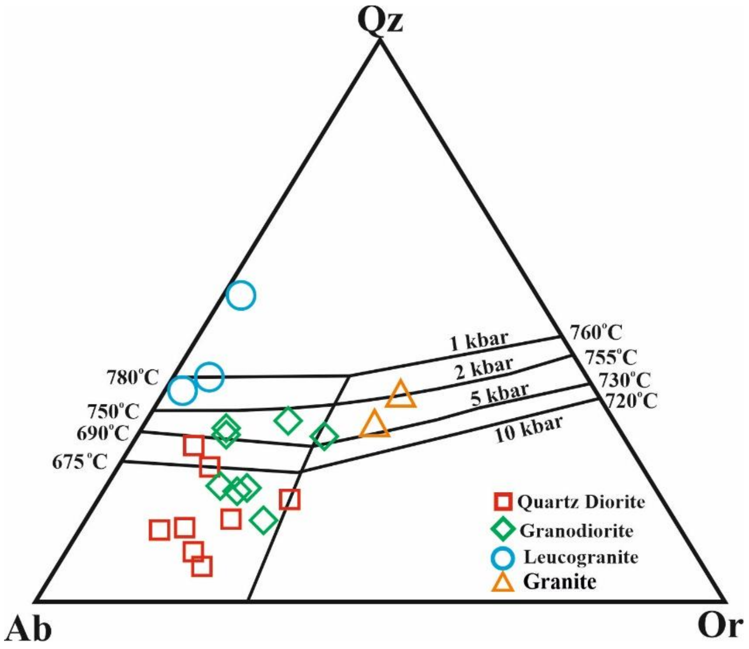

Figure 7.16: Quartz-Albite-Orthoclase diagram showing experimentally calibrated isobars after Johannes and Holtz, 1996

8.5.7 GEOCHRONOLOGICAL FRAMEWORK

The Trans-Himalayan range extends for over 2500 km and comprises three prominent batholithic bodies: the Kohistan/Ladakh batholith in the west, the Gangdese batholith in the central part, and the Lohit batholith in the eastern part of the range. These batholitic bodies were generated as a result of the subduction of Neo-Tethyan oceanic lithosphere beneath the Eurasian plate from mid-Jurassic to the Cretaceous (Honegger et al., 1982; Scharer et al., 1984; Weinberg and Dunlap, 2000; Upadhyay et al., 2008; Zhu et al., 2011; Ji et al., 2009; Zhu et al., 2013).

Magmatism in the Gangdese batholith occurred in three stages (Ji et al., 2009 and references therein). The first stage during the Mesozoic (ca. 205-80 Ma) resulted from the subduction of the Neo-Tethyan slab. It occurred in two parts: the older late Triassic (ca. 205.3 Ma) to Jurassic (ca. 194-151.8 Ma) and a later, widespread magmatism in the Cretaceous (ca. 109-80 Ma). The second stage, during the Palaeocene-Eocene (65-41 Ma), was the most intensive, caused by further subduction, rollback, and slab breakoff. The third stage, post-collisional, in Oligocene-Miocene (26-10 Ma), was due to convective removal (delamination) of thickened lithosphere after the Indian-Asian collision.

The magmatic history of the Ladakh batholith in the western Trans-Himalaya is also marked by three major phases (Bhat and Ahmad, 2021): an early intra-oceanic island arc mafic magmatism phase from 160–80 Ma, the felsic magmatism and formation of the Kohistan–Ladakh batholith between 80–50 Ma, and the intrusion of post-collisional dykes from 35–18 Ma. Several geochronological studies carried out in the Kohistan–Ladakh batholith suggest a minor pulse between ca. 109-105 Ma (Honegger et al., 1982; Ravnikant et al., 2006, 2009; Bouilhol et al., 2011; Kumar et al., 2017; Pundir et al., 2020), a dominant episode from late Cretaceous to Eocene (ca. 73-45 Ma) (Weinberg and Dunlap, 2000; Upadhyay et al., 2008; Ravnikant et al., 2009; St-Onge et al., 2010), and an additional syn- and post-collisional Miocene magmatism of the Himalayan leucogranites from ca. 9-25 Ma (Weinberg et al., 2000; Philips et al., 2004; Ravnikant 2006; Boutonnet et al., 2012; Van Buer et al., 2015). Kumar and Pundir (2021), and references therein, have suggested that magmatism in Ladakh has taken place episodically at around 160-50 Ma and continued approximately till 9 Ma post-collision.

In the eastern part of the Trans-Himalayan range, specifically the Lohit Plutonic Complex, the timing of subduction-related magmatism ranges from about 157 to 50 Ma (Haproff et al., 2019; Bikramaditya et al., 2020; Pebam et al., 2021; Mukherjee et al., 2025). Haproff et al. (2019) identified a Mesoproterozoic basement orthogneiss from Ayeso with an age of 1286 Ma, correlating it with the Bomi-Chayu Complex of Lhasa terrane, while other orthogneisses show ages between 136 and 69 Ma. Additionally, granitoids such as diorite, tonalite, and monzodiorite found between Angolin and Etalin are dated between 93 and 156 Ma. Bikramaditya et al. (2020) reported an age of 145 Ma for gabbroic rocks and approximately 107-90 Ma for diorites in the Dibang section, indicating it to be an early phase of magmatism. U–Pb zircon dating of LPC rocks by Pebam et al. (2021) reveals episodic magmatism in the Arunachal Trans-Himalaya, with crustal magmatism active during the Late Jurassic (~153 Ma), subduction-related magmatism between ~117–50 Ma, and a late phase magmatism with leucogranite emplacement from ~36–30 Ma indicating Oligocene–Miocene crustal recycling. Mukherjee et al. (2025) also gave a similar age of crystallization for the granitoids between ~154-74 Ma and an age of migmatization from ~88-69 Ma.

Zircon U-Pb ages reported from the present study range from the late Cretaceous (ca. 104.8 Ma) to the Eocene (ca. 44.82 Ma), indicating a broad timespan for subduction-related magmatism. The U-Pb age of the quartz diorite sample (MZ-1) from the eastern belt of the LPC in Dibang Valley is approximately 104.8 Ma, which aligns with the early magmatic phase responsible for diorites, granodiorites, and monzogranites from Ladakh and the Gangdese batholiths. Another younger magmatic event, dated approximately between 55.20 and 44.82 Ma, has been identified from granite samples (DZ-1 and DZ-7) from the eastern belt (Alinye and Dambuen) of the pluton.

An integrated isotope and geochronological study of the Trans-Himalayan magmatic arc suggests continuous and coeval magmatism with similar geochemical characteristics from the initiation of subduction during the Jurassic period (Chu et al., 2006; Zhang et al., 2007; Ji et al., 2009) till the impingement/collision of the plates around 57.5-45 Ma (Rowley, 1996; Najman, 2010; Jain, 2014) and another late post-collisional activity from 30-9 Ma. Based on the positive $\varepsilon_{Hf}(T)$ values (Haproff et al., 2019; Bikramaditya et al., 2020; Pebam et al., 2021; Mukherjee et al., 2025) and coeval U-Pb ages, granitoids of LPC are thus considered to be the eastern extension of the Ladakh and Gangdese batholiths (Lin et al., 2013).

8.5.8 GEODYNAMIC EVOLUTION

The geodynamic evolution of the plutonic complex in Dibang Valley, which is a part of the LPC, is generally linked to the subduction of the Neo-Tethyan oceanic slab during the late Jurassic to Paleocene beneath the Eurasian plate, followed by the convergence of the Indian and Asian continents that formed the Himalayan mountain range and uplifted the Tibetan plateau (e.g., Yin and Harrison, 2000; Chung et al., 2005; Searle et al., 2011; Lin et al., 2013; Bikramaditya et al., 2020; Pebam et al., 2021). This tectonic regime led to the development of a continuous Trans-Himalayan magmatic arc, typified by the Gangdese Batholith in southern Tibet and extending eastward to include the LPC.

The LPC records multiple magmatic events from the Late Jurassic to Eocene (Lin et al., 2013; Bikramaditya et al., 2020; Pebam et al., 2019; Mukherjee et al., 2025), consistent with the temporal range of Gangdese magmatism (210-10 Ma) (Chiu et al., 2009; Zhu et al., 2017). According to Bikramaditya et al. (2020), gabbros in the LPC formed from ~5% partial melting of a depleted, slab-fluid–metasomatized mantle wedge in the garnet stability zone around 145 Ma. Continued subduction led to 3–10% remelting of earlier gabbros in the garnet–spinel transition zone, producing diorite and quartz diorite at 100–90 Ma (Bikramaditya et al., 2020). This is consistent with the results of the present study, where the quartz diorite and granodiorites of the Dibang Valley are derived from 5-10% melting of a spinel-garnet lherzolite mantle.

Several studies suggest the Indian lithospheric mantle experienced slab rollback and eventual breakoff with varying subduction angles in the Himalayan-Tibetan collision zones (Ma et al., 2017, and references therein). Subduction-induced dehydration and water-fluxed melting of the mantle wedge generated water-rich mafic magmas, which ascended and underplated the lower crust, causing partial melting and formation of felsic (granite) magmas. The abundant presence of hydrous mineral ‘amphibole’ and the high LILE-LREE geochemical character in the quartz diorites and granodiorites is attributed to partial melting of a metasomatized lithospheric mantle wedge triggered by slab-derived hydrous fluids.

Zircon U-Pb dating indicates ages of approximately 104.8 Ma to 44.82 Ma, which is consistent with the magmatism in the parts of the magmatic arc due to subduction. The quartz diorite and granodiorites are proposed to be generated during the continued subduction between ~107–90 Ma. Several studies (e.g., Chung et al., 2009; Lee et al., 2009, 2012; Zhu et al., 2015) have suggested that a major magmatic flare-up occurred during the Paleocene–Eocene, peaking around 53–50 Ma (Wang et al., 2015), attributed to slab-rollback (~70 Ma) and eventual break-off (~53 Ma). This phenomenon created a significant thermal anomaly. Evidence of this tectono-thermal event is likely expressed by the presence of migmatites in the plutonic complex.

Pebam et al. (2021) reported an early Cretaceous age for the migmatites, indicating active metamorphism during this period. Additionally, this tectonic reconfiguration of the subducting slab also triggered voluminous mantle-derived melts and remelting of earlier calc-alkaline rocks, producing juvenile to mixed source granitoids, as seen in the 55-49 Ma granites from Dibang Valley.

The leucogranites represent the third and youngest phase of magmatism in the LPC during the Oligocene (Pebam et al., 2021). Petrographic, mineralogical, and geochemical data from the leucogranites all suggest a peraluminous, crustally derived melt, suggesting partial melting of metasedimentary rocks possibly driven by residual magmatic heat after slab break-off and/or delamination of thickened continental crust. This phase also coincides with activation of regional NW–SE thrusts, e.g., Lohit Thrust and Walong Thrust (Gururajan & Choudhuri, 2003; Goswami, 2013a), facilitating magma ascent and exhumation.

Based on field, petrographic, mineralogical, and geochemical data in conjunction with the zircon U-Pb radiogenic ages, it is proposed that the Dibang granitoids of Lohit Plutonic Complex result from partial melting of a lithospheric mantle wedge, induced by hydrous fluids from a subducting slab (Figure 7.17). The Cretaceous-Eocene magmatism (this study) probably relates to an initially depleted mantle melt which was rehydrated and enriched by the addition of fluids rich in incompatible elements (e.g. La, Ce, and LILE) from the subducting slab and then emplaced at shallow crustal levels (~ 6-18 km) in two magmatic episodes from Early Cretaceous to Eocene, followed by interactions with the crustal metasedimentary rocks to produce the peraluminous leucogranites.

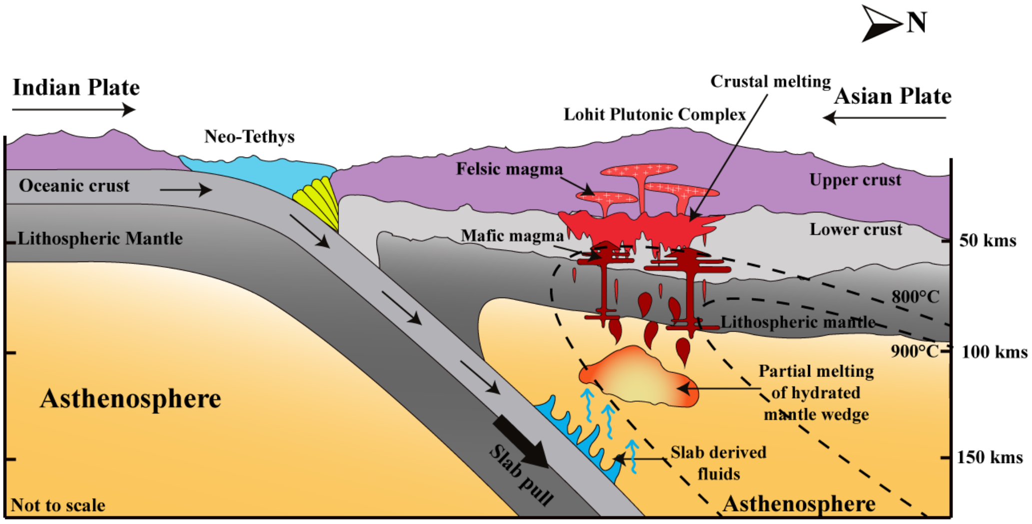

Figure 17.7: Schematic tectonic model for the emplacement of mafic and felsic magmatic rocks in the Lohit Plutonic Complex, showing dehydration of the subducting slab, partial melting of hydrated mantle, and emplacement of gabbro in the lower crust with further crustal melting, and emplacement of felsic magmatic rocks of LPC at shallow crustal level.

REFERENCES

Abdel-Rahman, A. F. M. (1994). Nature of biotites from alkaline, calc-alkaline, and peraluminous magmas. *Journal of Petrology,* 35(2), 525–541. https://doi.org/10.1093/petrology/35.2.525.

Acharyya, S. K. (1980). Geochemistry and geotectonic implications of basic volcanic rocks in the Lower Gondwana sequence (Upper Palaeozoic) of the Sikkim Himalayas. *Geological Magazine, 117*(6), 621–629. https://doi.org/10.1017/S0016756800028995.

Acharyya, S.K. (1987) Cenozoic plate motions creating the Eastern Himalayan and Indo Burmese range around the north east corner of India. In: N.C. Ghosh and S. Varadrajan (Eds.), Amphibolites and Indian plate margin, Patna University, Patna, 143-160.

Acharyya, S. K. (2000). Tectonic setting and nature of the Gondwanic Indian crust. *Geological Survey of India*, 57, 1–8.

Ague, J. J., & Brandon, M. T. (1992). Tilt and northward offset of Cordilleran batholiths resolved using igneous barometry. *Nature, 360*(6400), 146–149. https://doi.org/10.1038/360146a0.

Airo, M.-L. (1999). Aeromagnetic and petrophysical investigations applied to tectonic analysis in the northern Fennoscandian shield. *Report of Investigation*, 145, 51 pp. *Geological Survey of Finland*

Albuquerque, D.C.A.R., (1973). Geochemistry of biotites from granitic rocks, Northern Portugal. *Geochimica et Cosmochimica Acta* 37, 1779–1802. https://doi.org/10.1016/0016-7037(73)90163-4.

Aldanmaz, E., Pearce, J.A., Thirlwall, M.F., & Mitchell, J.G. (2000). Petrogenetic evolution of late Cenozoic post-collision volcanism in western Anatolia, Turkey. *Journal of Volcanology and Geothermal Research*, 102, 67–95, https://doi.org/10.1016/S0377-0273(00)00182-7

Anderson, J. L., & Smith, D. R. (1995). The effects of temperature and fO2 on the Al-in-hornblende barometer. *American Mineralogist,* 80(5–6), 549–559. https://doi.org/10.2138/am-1995-5-614.

Anderson, J.L. (1996). Status of thermobarometry in granitic batholiths. *Transactions of the Royal Society of Edinburgh*, 87(1-2),125–138.

Anderson, J.L., Barth, A.P., Wooden, J.L., & Mazdab, F. (2008). Thermometers and thermobarometers in granitic systems. *Reviews in Mineralogy Geochemistry* 69(1), 121–142.

Arculus, R. J., & Wills, K. J. (1980). Cumulate xenoliths from St. Vincent, Lesser Antilles Island Arc: A petrological study. *Contributions to Mineralogy and Petrology, 73*(2), 161–174. https://doi.org/10.1007/BF00371252.

Aydin, A., Ulusay, R., & Hudson, J. A. (Eds.). (2007). The complete ISRM suggested methods for rock characterization, testing, and monitoring: 1974–2006. *International Society for Rock Mechanics.*

Bachmann, O., & Dungan, M.A. (2002). Temperature-induced aluminium zoning in hornblendes of the Fish Canyon magma, Colorado. *American Minerologist*, 87, 1062-1076.

Barbarin, B. (1990). Granitoids: main petrogenetic classifications in relation to origin and tectonic setting. *Geological Journal,* 25(3-4), 227-238.

Barbarin, B., & Didier, J. (1992). Genesis and evolution of mafic microgranular enclaves through various types of interaction between coexisting felsic and mafic magmas. *Transactions of the Royal Society of Edinburgh: Earth Sciences, 83*(1–2), 145–153. https://doi.org/10.1017/S0263593300007835.

Barbarin, B. (1996). Genesis of the two main types of peraluminous granitoids. *Geology*, 24(4), 295-298.

Barbarin, B. (1999). A review of the relationships between granitoid types, their origins and their geodynamic environments. *Lithos*, 46(3), 605-626.

Barker, F., & Arth, J. G. (1976). Generation of trondhjemitic-tonalitic liquids and Archean bimodal trondhjemite–basalt suites. *Geology, 4*(10), 596–600. https://doi.org/10.1130/0091-7613(1976)4<596:GOTLAA>2.0.CO;2

Barrière, J., & Cotton, J. (1979). Biotite composition as a tool for exploration: An example from the Massif Central, France. *Mineralium Deposita, 14*(1), 1–10. https://doi.org/10.1007/BF00202993 .

Batchelor, R. A., & Bowden, P. (1985). Petrogenetic interpretation of granitoid rock series using multicationic parameters. *Chemical geology*, 48(1-4), 43-55.

Beane, R.E., (1974). Biotite Stability in the Porphyry Copper. *Environmental Economics Geology,* 69,241–256.

Bhat, I. M., & Ahmad, T. (2021). Evolution of the Ladakh Magmatic Arc. *Journal of the Geological Society of India*, *97*(9), 980-984.

Bikramaditya, R.K., Singh A.K., Chung, S.-L., Sharma, R., & Lee, H.-Y. (2019). Zircon U-Pb ages and Lu-Hf isotopes of metagranitoids from the Subansiri region, Eastern Himalaya: implications for crustal evolution along the northern Indian passive margin in the early Paleozoic. *Geological Society, London, Special Publications*, 481(1), 299-318. https://doi.org/10.1144/SP481.7.

Bikramaditya, R.K., Chung, S.-L., Singh A.K., Lee, H.-Y., Lin, T.-H., & Iizuka, Y. (2020). Age and isotope geochemistry of magmatic rocks of the Lohit Plutonic Complex, eastern Himalaya: implications for the evolution of Transhimalayan arc magmatism. *Journal of the Geological Society*, 177(2), 379. https://doi.org/10.1144/jgs2018-214.

Blundy, J. D., & Holland, T. J. B. (1990). Calcic amphibole equilibria and a new amphibole-plagioclase geothermometer. *Contributions to Mineralogy and Petrology*, 104(2), 208–224. https://doi.org/10.1007/ BF00306444.

Bónová, K., Broska, I., & Petrík, I. (2010). Biotite from Čierna hora Mountains granitoids (Western Carpathians, Slovakia) and estimation of water contents in granitoid melts. *Geologica Carpathica*, *61*(1), 3-17.

Bora, S., & Kumar, S. (2015). Geochemistry of biotites and host granitoid plutons from the Proterozoic Mahakoshal Belt, central India tectonic zone: Implication for nature and tectonic setting of magmatism. *International Geology Review*, 57(11–12), 1686–1706. https://doi.org/10. 1080/00206814.2015.1032372.

Bouilhol, P., Connolly, J. A. D., & Burg, J.-P. (2011). Geological evidence and modeling of melt migration by porosity waves in the sub-arc mantle of Kohistan (Pakistan). *Geology, 39*(12), 1091–1094. https://doi.org/10.1130/G32219.1

Boutonnet, E., Leloup, P. H., Arnaud, N., Paquette, J.-L., Davis, W. J., & Hattori, K. (2012). Synkinematic magmatism, heterogeneous deformation, and progressive strain localization in a strike-slip shear zone: The case of the right-lateral Karakorum fault. *Tectonics, 31*, TC4012. https://doi.org/10.1029/2011TC003049

Brown, W.L., & Parsons, I. (1981). Towards a more practical two-feldspar geothermometer. *Contributions to Minerology and Petrology*, 76, 369-377.

Burg, J.–P., Nievergelt, P., Oberli, F., Seward, D., Davy, P., & Maurin, J.–C. (1997). The Namche-Barwa syntaxis: evidence for exhumation related to compressional crustal folding. *Journal of Asian Earth Sciences, 16*(2–3), 239–252. https://doi.org/10.1016/S0743-9547(98)00002-6.

Burg, J. P., & Bouilhol, P. (2018). Timeline of the South–Tibet–Himalayan belt: the geochronological record of subduction, collision, and underthrusting from zircon and monazite U–Pb ages. *Canadian Journal of Earth Sciences, 56*(12), 1318–1332.

Burhanuddin, M., & Nandy, S. (2004). Geology of Roing-Mayudia-Hunli-Ardzu-Angolin area, Dibang valley, Arunachal Pradesh. *GSI unpublished report.*

Burkhard, M. (1991). Temperature and redox path of biotite-bearing intrusives: A method of estimation applied to S- and I-type granites from Australia. *Earth and Planetary Science Letters, 104*(1–4), 89–98. https://doi.org/10.1016/0012-821X(91)90240-I.

Burtman, V. S., & Molnar, P. (1993). Geological and geophysical evidence for deep subduction of continental crust beneath the Pamir. *Geological Society of America Special Paper, 281*, 1–76. https://doi.org/10.1130/SPE281-p1.

Cawthorn, R. G., Arculus, R. J., & Wills, K. J. (1973). Island arc and continent-building magmatism. *Lithos, 6*(2), 85–94. https://doi.org/10.1016/0024-4937(73)90021-2.

Challener, S. C., & Glazner, A. F. (2017). Igneous or metamorphic? Hornblende phenocrysts as greenschist facies reaction cells in the Half Dome Granodiorite, California. *American Mineralogist*, 102(2), 436–444. https://doi.org/10.2138/am-2017-5864.

Chapman, J. B., Scoggin, S. H., Kapp, P., Carrapa, B., Ducea, M. N., Worthington, J., Oimahmadov, I., & Gadoev, M. (2018). Mesozoic to Cenozoic magmatic history of the Pamir. *Earth and Planetary Science Letters, 482*, 181–192. https://doi.org/10.1016/j.epsl.2017.10.041.

Chappell, B.W., & White, A.J.R. (1974). Two contrasting granite types. *Pacific Geology*, 8, 173-174.

Chiu, H. Y., Chung, S. L., Wu, F. Y., et al. (2009). Zircon U–Pb and Hf isotope constraints from eastern Trans-Himalayan batholiths on the pre-collisional magmatic and tectonic evolution in southern Tibet. *Tectonophysics*, doi:10.1016/j.tecto.2009.01.020.

Choudhuri, B. K., Gururajan, N. S., & Singh, R. K. B. (2009). Geology and structural evolution of the eastern Himalayan Syntaxis, Himalayan Geology 30, no. 1, 17–34.

Chu, M.-F., Chung, S.-L., Song, B., Liu, D., O'Reilly, S. Y., Pearson, N. J., Ji, J., & Wen, D.-J. (2006). Zircon U–Pb and Hf isotope constraints on the Mesozoic tectonics and crustal evolution of southern Tibet. *Geology, 34*(9), 745–748. https://doi.org/10.1130/G22725.1

Clark, D. L. (1997). The nature of the chemical bond: An introduction to modern structural chemistry. *Wiley-Interscience*

Class, C., Miller, D.M., Goldstein, S.L. & Langmuir, C.H. (2000). Distinguishing melt and fluid subduction components in Umnak Volcanics, Aleutian Arc. *Geochemistry, Geophysics, Geosystems*, 1, 1–28, https://doi.org/10.1029/1999GC000010

Coggin Brown, J. (1912). A geological reconnaissance through the Dihong Valley, being the geological results of the Abor Expedition (1911–1912). *Records of the Geological Survey of India, 42*(4), 231–264.

Condie, K. (2015). Changing tectonic settings through time: Indiscriminate use of geochemical discriminant diagrams. *Precambrian Research, 266, 587-591.* https://doi.org/10.1016/j.precamres.2015.05.004

Czamanske, G.K., Wones, D.R. (1973). Oxidation during magmatic differentiation, Finnmarka complex, Oslo area, Norway: Part 2, the mafic silicates1. *Journal of Petrology*, 14, 349–380. https://doi.org/10.1093/petrology/14.3.349

Czamanske, G. K., Wones, D. R., & Eichelberger, J. C. (1977). Mineralogy and petrology of the intrusive complex of the Pliny Range, New Hampshire. *American Journal of Sciences*, 277, 1073-1123.

Czamanske, G. K., Ishihara, S., & Atkin, S. A. (1981). Chemistry of rock-forming minerals of the Cretaceous–Paleocene batholith in southwestern Japan and implications for magma genesis. *Journal of Geophysical Research: Solid Earth,* 86(11), 10431–10469. https://doi.org/10.1029/JB086iB11p10431.

Das, A. K., Bakliwal, P. C., and Dhoundial, D. P. (1975). A brief outline of geology of parts of Kameng District, NEFA. *Geological Survey of India, Miscellanous Publication* 24 (1): 115-127.

Davidson, J., Turner, S., Handley, H., Macpherson, C., & Dosseto, A. (2007). Amphibole "sponge" in arc crust?. *Geology*, *35*(9), 787-790.

De Angelis, S.H., Larsen, J., & Coombs, M. (2013). Pre-eruptive magmatic conditions at Augustine volcano, Alaska, 2006: evidence from amphibole geochemistry and textures. *Journal of Petrology*, 54(9), 1939-1961. https://doi.org/10.1093/petrology/egt037.

De la Roche, H. D., Leterrier, J. T., Grandclaude, P., & Marchal, M. (1980). A classification of volcanic and plutonic rocks using R1R2-diagram and major-element analyses—its relationships with current nomenclature. *Chemical geology*, 29(1-4), 183-210.

Debon, F., & Le Fort, P. (1988). A cationic classification of common plutonic rocks and their magmatic associations: principles, method, applications. *Bulletin de Minéralogie*, 111(5), 493-510.

Deer, W.A., Howie, R.A., & Zussman, J. (1963). Rock-forming minerals. Sheet silicates.

Deer, W.A., Howie, R.A., Zussman, J., (1966). An Introduction to the Rock-Forming Minerals, An Introduction to the Rock-Forming Minerals. https://doi.org/10.1180/dhz

Deer, W. A., Howie, R. A., & Zussman, J. (1992). An introduction to the rock-forming minerals 2nd edition, London: *Longman,* https://doi.org/ 10.1180/DHZ.

Dikshitulu, G. R., Pandey, B. K., Krishna, V., & Dhana Raju, R. (1995). Rb-Sr systematics of granitoids of the Central Gneissic Complex, Arunachal Himalaya: Implications on tectonism, stratigraphy and source. *Journal of the Geological Society of India*, 45(1), 51–56.

DiPietro, J. A., & Pogue, K. R. (2004). Tectonostratigraphic subdivisions of the Himalaya: A view from the west. *Tectonics, 23*, Article TC5001. https://doi.org/10.1029/2003TC001554.

Eggler, D. H. (1972). Water-saturated and undersaturated melting relations in a Paricutin andesite and an estimate of water content in the natural magma. *Contributions to Mineralogy and Petrology*, 34(4), 261-271.

El Bouseily, A. M., & El Sokkary, A. A. (1975). The relation between Rb, Ba and Sr in granitic rocks. *Chemical geology*, 16(3), 207-219.

El Sheshtawi, Y. A., Ahmed, A. M., & El Tokhi, M. M. (1993). Origin and geochemistry of Egyptian granitoid rocks in Nuweiba area, eastern Sinai. *Journal* *of African Earth Sciences, 17*(3), 399–413. https://doi.org/10.1016/0899-5362(93)90082-2.

Ellwood, B.B., & Wenner, D.B., (1981). Correlation of magnetic susceptibility with data in late orogenic granites of the southern Appalachian Piedmont. *Earth and Planetary Science Letters,* 54, 200–202.

Emmermann, R., Daieva, L., & Schneider, J. (1975). Petrologic significance of rare earths distribution in granites. *Contributions to Mineralogy and Petrology*, 52(4), 267-283.

Enami, M., Zang, Q., & Yin, Y. (1993). High-pressure eclogites in northern Jiangsu–southern Shandong province, eastern China. *Journal of Metamorphic Geology, 11*(4), 589–603. https://doi.org/10.1111/j.1525-1314.1993.tb00174.x.

Ernst, R. E., & Buchan, K. L. (2001). Large mafic magmatic events through time and links to mantle-plume heads.

Fabriès, J., Conquéré, F., & Arnaud, G. (1984). The mafic silicates in the Saint Quay-Portrieux gabbro-diorite intrusion: crystallization conditions of a calc-alkaline pluton. *Bulletin de minèralogie*, *107*(6), 715-736.

Feng, Z.Q., Jia, J., Liu, Y.J.,Wen, Q.B., Li,W.M., Liu, B.Q., Xing, D.Q., Zhang, L., (2015). Geochronology and geochemistry of the Carboniferous magmatism in the northern Great Xing'an Range, NE China: constraints on the timing of amalgamation of Xing'an and Songnen blocks. Journal of Asian Earth Sciences 113, 411–426.

Förster, H.-J., Tischendorf, G. & Trumbull, R.B. (1997). An evaluation of the Rb v. (Y + Nb) discrimination diagram to infer the tectonic setting of silicic igneous rocks. Lithos, 40, 261–293, https://doi.org/10.1016/S0024-4937(97)00032-7

Foster, M.D., (1960). Interpretation of the composition of trioctahedral micas. *USGS Professional Pap*er, 354, 11–48.

Frost, B. R., & Frost, C. D. (2008). A geochemical classification for feldspathic igneous rocks. *Journal of Petrology*, 49(11), 1955-1969.

Frost, B. R., Barnes, C. G., Collins, W. J., Arculus, R. J., Ellis, D. J., & Frost, C. D. (2001). A geochemical classification for granitic rocks. *Journal of petrology,* 42(11), 2033-2048.

Gansser, A. (1964). Geology of the Himalayas. London & New York: *Interscience Publishers.*

Gansser, A. (1974). Himalaya-Mesozoic–Cenozoic orogenic belts: Data for orogenic studies. *Geological Society of London*. 4, 267–273. https://doi.org/10.1144/gsl.sp.2005.004.01.15**.**

Glazner, A. & Johnson, Breck. (2013). Late crystallization of K-feldspar and the paradox of megacrystic granites. *Contributions to Mineralogy and Petrology*. 166. https://doi.org/10.1007/s00410-013-0914-1.

Gleizes, G., Nédélec, A., Bouchez, J. L., Autran, A., & Rochette, P. (1998). The main Variscan deformation event in the Pyrenees: New data from the Bielsa granite pluton. *Tectonophysics, 285*(1–3), 1–19. https://doi.org/10.1016/S0040-1951(97)00291-3.

Godwin-Austen, H. H. (1875). The geology of part of the Dafla Hills, Assam; lately visited by the force under Brigadier-General Stafford, C. B. *Journal of the Asiatic Society of Bengal, 44*(1), 35–41.

Goswami, T.K. (2011) Collision Induced Deformation of the Trans Himalayan Lohit Batholith, Arunachal Pradesh, India, Memoir of the Geological Society of India, 77, 19-31.

Goswami, T.K. (2013a). Geodynamic significance of leucogranites intrusions in the Lohit batholith near Walong, Eastern Arunachal Pradesh, India. *Current Scie*nce, 104(2): 229–234.

Goswami, T.K. (2013b). Subduction Related Magmatism: Constrains from the REE Pattern in the Lohit Batholith, Arunachal Pradesh, *India. Geosciences*, 3(4): 128-141.

Gou, J., Sun, D.Y., Yang, D.G., Tang, Z.Y., Mao, A.Q., (2019). Late Palaeozoic igneous rocks of the Great Xing'an Range, NE China: the Tayuan example. International Geology Review, 61, 314–340.

Gregorová, D., Hrouda, F., & Kohút, M. (2003). Magnetic susceptibility and geochemistry of Variscan West Carpathian granites: implications for tectonic setting. *Physics and Chemistry of the Earth*, 28, 729-734.

Gururajan, N.S. & Choudhuri, B.K. (2007). Geochemistry and tectonic implications of the Trans-Himalayan Lohit Plutonic Complex, eastern Arunachal Pradesh. Journal of the Geological Society of India, 70, 17–33.

Gururajan, N.S., & Choudhuri, B.K. (2003). Geology and tectonic history of the Lohit Valley, Eastern Arunachal Pradesh, India. Journal of Asian Earth Sciences, 21, 731–741, https://doi.org/10.1016/S1367-9120(02)00040-8.

Hammarstrom, J.M., & Zen, E. (1986). Aluminum in hornblende: An empirical igneous geobarometer. *American Mineralogist*, 71:1297-1313.

Haproff, P. J., Zuza, A. V., & Yin, A. (2018). West-directed thrusting south of the eastern Himalayan syntaxis indicates clockwise crustal flow at the indenter corner during the India-Asia collision. *Tectonophysics*, *722*, 277-285.

Haproff, P.J., Zuza, A.V., Yin, A., Harrison, T.M., Manning, C.E., Dubey, C.S., Ding, L., Wu, C., & Chen, J. (2019). Geologic framework of the northern Indo-Burma Ranges and lateral correlation of Himalayan-Tibetan lithologic units across the eastern Himalayan syntaxis. *Geosphere,* 15(3), 856-881. https://doi.org/10.1130/GES02054.1.

Harris, N. B., Pearce, J. A., & Tindle, A. G. (1986). Geochemical characteristics of collision-zone magmatism. *Geological Society, London, Special Publications*, 19(1), 67-81.

Hart, C.J.R., Goldfarb, R.J., Lewis, L.L., Mair, J.L., 2004. The northern Cordilleran mid-Cretaceous plutonic province: Ilmenite/magnetite-series granitoids and intrusion-related mineralisation. *Resource Geology*, 54, 253–280. https://doi.org/10.1111/j.1751-3928.2004.tb00206.x.

Hassan, M. A., & Hashad, A. H. (1990). Precambrian of Egypt. In R. Said (Ed.), *The Geology of Egypt* (pp. 201–245). A. A. Balkema

Hawkesworth, C. J., McDermott, F., & Dhuime, B. (1997). Elemental U and Th variations in island arc rocks: Implications for U–Th–Pb geochronology. *Chemical Geology, 139*(3–4), 207–221. https://doi.org/10.1016/S0009-2541(97)00036-3.

Hawthorne, F. C., Oberti, R., Harlow, G. E., Maresch, W. V., Martin, R. F., Schumacher, J. C., & Welch, M. D. (2012). Nomenclature of the amphibole supergroup. *American Mineralogist*, *97*(11-12), 2031-2048.

Heilimo, E., Halla, J., & Hölttä, P. (2010). Discrimination and origin of the sanukitoid series: geochemical constraints from the Neoarchean western Karelian Province (Finland). *Lithos*, *115*(1-4), 27-39.

Helz, R. T. (1973). Phase relations of basalts in their melting range at P(H_2O) = 5 kb as a function of oxygen fugacity: Part I, Mafic phases. *Journal of Petrology, 14*(2), 249–302. https://doi.org/10.1093/petrology/14.2.249.

Henry, D.J., Guidotti, C.V., & Thomson, J.A. (2005). The Ti-saturation surface for low-to medium pressure metapelitic biotites: implications for geothermometry and Ti substitution mechanisms. *American Mineralogist*, 90(2-3), 316–328. https://doi.org/10.2138/am.2005.1498.

Holland, T. & Blundy, J., (1994). Non-ideal interactions in calcic amphiboles and their bearing on amphibole-plagioclase thermometry. *Contributions to Mineralogy and Petrology*, 116(4), 433–447. https://doi.org/10.1007/BF00310910.

Hollister, L.S., Grissom, G.C., Peters, E.K., Stowell, H.H., & Sisson, V.B. (1987). Confirmation of the empirical correlation of Al in hornblende with pressure of solidification of calc-alkaline plutons. *American Mineralogist*, 72(3-4), 231–239.

Honegger, K., Dietrich, V., Frank, W., Gansser, A., Thöni, M., & Trommsdorff, V. (1982). Magmatism and metamorphism in the Ladakh Himalayas (the Indus-

Tsangpo suture zone). *Earth and Planetary Science Letters, 60*(2), 253–292. https://doi.org/10.1016/0012-821X(82)90007-3.

Hoskin, P. W. O., & Schaltegger, U. (2003). The composition of zircon and igneous and metamorphic petrogenesis. *Reviews in Mineralogy and Geochemistry*, *53*(1), 27–62. https://doi.org/10.2113/0530027.

Irvine, T. N., & Baragar, W. R. A. F. (1971). A guide to the chemical classification of the common volcanic rocks. *Canadian journal of earth science*s, 8(5), 523-548.

Ishihara, S. (1977). The magnetite-series and ilmenite-series granitic rocks. *Mining Geology*, 27(145), 293–305. https://doi.org/10.11456/ shigenchishitsu1951.27.293.

Ishihara, S., (1979). Lateral variation of magmatic susceptibility of the Japanese granitoids. *Chemical Pharmaceutical Society of Japan Bulletin*, 85, 509–523

Ishihara, S., (2004). The redox state of granitoids relative to tectonic setting and earth history: The magnetite—ilmenite series 30 years later. *Transactions of Royal Society of Edinburgh, Earth Sciences,* 95, 23–33. https://doi.org/10.1017/S0263593300000894.

Jain, A. K. (2014). When did India–Asia collide and make the Himalaya?. *Current Science*, 254-266.

Janoušek, V., Erabn, v., & Gadas, P. (2022). GCDkit.Mineral: a flexible, platform-independent R package for recalculation and plotting of mineral chemistry data. *Cosmochimica Acta*, A67, 186. doi: 10.7185/gold2023.19047.

Ji, W.-Q., Wu, F.-Y., Chung, S.-L., Li, J.-X., & Liu, C.-Z. (2009). Zircon U–Pb geochronology and Hf isotopic constraints on petrogenesis of the Gangdese batholith, southern Tibet. *Chemical Geology, 262*(3–4), 229–245. https://doi.org/10.1016/j.chemgeo.2009.01.020.

Johannes, W., & Holtz, F. (1996). Petrogenesis and experimental petrology of granitic rocks. Minerals and Rocks, 22. *Springer-Verlag*. https://doi.org/10.1007/978-3-642-61049-3.

Johnson, B. R., & Glazner, A. F. (2010). Formation of K-feldspar megacrysts in granodioritic plutons by thermal cycling and late-stage textural coarsening. *Contributions to Mineralogy and Petrology*, 159(5), 599–619. https://doi.org/10.1007/s00410-009-0444-z.

Johnson, M.C., & Rutherford, M.J. (1989). Experimental calibration of the aluminum-in hornblende geo-barometer with application to Long Valley caldera (California) volcanic rocks. *Geology*, 17(9), 837–841. https://doi.org/10.1130/0091-7613(1989)017<0837:ECOTAI>2.3CO;2.

Kopf, M. (1966). Die Untersuchung physikalischer Eigenschaften von granitoiden Gesteinen als neue Methode der Granitforschung. *Geologie (Beiheft)* 55, 1–135.

Kumar, D., et al. (2017). Gold-sulphide mineralization in ultramafic–mafic–granite complex of Jashpur, Bastar Craton, Central India: Evidences from geophysical studies. *Journal of the Geological Society of India, 90*(2), 147–153. https://doi.org/10.1007/s12594-017-0692-x.

Kumar, G. (1997). Geology of Arunachal Pradesh. *Journal of the Geological Society of India,* Bangalore, 217.

Kumar, G., Kumar, S., Mohan, M.R., (2021). Redox series assessment, petrogenetic, and geodynamic appraisal of Neoarchean granites from the Bundelkhand Craton, Central India: Constraints from phase petrology and bulk rock geochemistry. *Geological Journal*, 1–29. https://doi.org/10.1002/gj.4087.

Kumar, G., Shanker, R., Mathur, V., Maithy, P., Bhattacharya, S. K., & Jain, R. (1997). Terminal Proterozoic-Cambrian sequences in India: A review with special reference to Precambrian-Cambrian boundary. *Journal of Palaeosciences, 46*(1–2), 19–31. https://doi.org/10.54991/jop.1997.1314.

Kumar, H. M., Gajaria, S. C., & Radha, K. S. (2004). Growth and development of catla (*Catla catla*) fed with different levels of diet containing *Spirogyra* sp. *Bioresource Technology, 95*(1), 73–76. https://doi.org/10.1016/j.biortech.2004.02.004.

Kumar, M. R., & Singh, A. (2008). Evidence for plate motion related strain in the Indian shield from shear wave splitting measurements. *Journal of Geophysical Research, 113*(B12), B12310. https://doi.org/10.1029/2007JB005128.

Kumar, M., Kumar, A. & Srimal, N. (2000). Tectomagmatic evolution of Dibang valley area, eastern Arunachal Pradesh; *Unpublished Report* (1998–2000).

Kumar, S. (2008). Magnetic susceptibility mapping of Ladakh granitoids, northwest Higher Himalaya: Implication to redox series of felsic magmatism in the subduction environments. *Memoir of Geological Society of India*, *71*, 83–102.

Kumar, S. (2010). Magnetite and ilmenite series granitoids of Ladakh batholith, Northwest Indian Himalaya: implications on redox conditions of subduction zone magmatism. Current Science, 99(9), 1260-1264.

Kumar, S., & Pathak, M. (2010). Mineralogy and geochemistry of biotites from Proterozoic granitoids of western Arunachal Himalaya: Evidence of bimodal granitogeny and tectonic affinity. *Journal of the Geological Society of India, 75*(3), 715–730. https://doi.org/10.1007/s12594-010-0058-0

Kumar, S., & Pieru, T. (2010). Petrography and major elements geochemistry of microgranular enclaves and neoproterozoic granitoids of South Khasi, Meghalaya: Evidence of magma mixing and alkali diffusion. *Journal of the Geological Society of India*, *76*(4), 345-360.

Kumar, S., & Rino, V. (2006). Mineralogy and geochemistry of microgranular enclaves in Palaeoproterozoic Malanjkhand granitoids, central India: Evidence of magma mixing, mingling, and chemical equilibration. Contributions to Mineralogy and Petrology, 152(5), 591–609. https:// doi.org/10.1007/s00410-006-0122-3.

La Flèche, M. R., Jenner, G. A., & Barr, S. M. (1998). Geochemistry of post-Acadian, Carboniferous continental intraplate basalts from the Maritimes Basin, Magdalen Islands, Quebec, Canada. *Chemical Geology, 148*(3–4), 115–138. https://doi.org/10.1016/S0009-2541(98)00002-3.

La Touche, T. H. D. (1885). The geology of Aka Hills, Assam. *Geological Survey of India*, 18(2), 1885.

Lalonde, A. & Bernard, P. (1993). Composition and color of biotite from granites: two useful properties in the characterization of plutonic suites from the Hefburn internal zone of Wopmay Orogen, Northwest Territories. The Canadian Mineralogist, 31, 203–217.

Le Maitre, R.W., Bateman, P., Dudek, A., Keller, J., Le Bas, M.J., Sabine,P. A., Schmid, R., Sorensen, H., Streckeisen, A., Woolley, & A.R., Zanettin, B. (1989). A classification of igneous rocks and glossary of terms. Blackwell, Oxford, 193.

Le Maitre, R.W.B., Streckeisen, A., Zanettin, B., Le Bas, M.J., Bonin, B., Bateman, P., Bellieni, G., Dudek, A., Efremova, S., and Keller, J. (2002). Igneous rocks: a classification and glossary of terms; *Recommendations of the International Union of Geological Sciences*. London, Cambridge University Press, 235.

Leake, B. E. (1971). On aluminous and edenitic hornblendes. *Mineralogical magazine*, *38*(296), 389-407.

Leake, B. E., Woolley, A. R., Arps, C. E. S., Birch, W. D., Gilbert, M. C., Grice, J. D., Youzhi, G. (1997). Nomenclature of amphiboles: Report of the subcommittee on amphiboles of the International Mineralogical Association, Commission on new minerals and mineral names. *Canadian Mineralogist*, 35(1), 219–246.

Leake, B.E., (1978). Nomenclature of Amphiboles. *Mineralogical Magazine*, 42, 533–563.

Lee, H.-Y., Chung, S.-L., Lo, C.-H., Ji, J.-Q., Lee, T.-Y., Qian, Q., & Zhang, Q. (2009). Eocene Neotethyan slab breakoff in southern Tibet inferred from the Linzizong volcanic record. *Tectonophysics, 477*(1–2), 20–35. https://doi.org/10.1016/j.tecto.2009.02.031.

Lee, H.-Y., Chung, S.-L. et al. (2012). Geochemical and Sr–Nd isotopic constraints on the genesis of the Cenozoic Linzizong volcanic successions, southern Tibet.

Journal of Asian Earth Sciences, 53, 96–114, https://doi.org/10.1016/j.jseaes.2011.08.019

Lin, T.-H., Chung, S.-L., Kumar, A., Wu, F.-Y., Chiu, H.-Y. & Lin, I.-J. (2013). Linking a prolonged Neo-Tethyan magmatic arc in South Asia: zircon U–Pb and Hf isotopic constraints from the Lohit Batholith, NE India. *Terra Nova*, 25 (6), 453–458.

Ludwig, K. R. (2009). SQUID 2 (version 2.50): A user's manual. *Berkeley Geochronological Center Special Publication*, 5, 100. arxiv.org+121library.net+12ucl.ac.uk+12

Ludwig, K.R. (2012). User's Manual for Isoplot Version 3.75e4.15: a Geochronological Toolkit for Microsoft Excel. *Berkeley Geochronological Center Special Publication*, 5.

Luth, W.C., Jahns, R.H., & Tuttle, O.F. (1964). The granite system at pressure 4 to 10 kilobars. *Journal of Geophysics Research*, 69(4), 759-773.

Ma, S., Meng, Y., Xu, Z., & Liu, X. (2017). The discovery of late Triassic mylonitic granite and geologic significance in the middle Gangdese batholiths, southern Tibet. *Journal of Geodynamics,* 104, 49-64. https://doi.org/10.1016/j.jog.2016.10.007

Machev, P., Klain, L., &, L. (2004). Mineralogy and chemistry of biotites from the Belogradchik pluton—Some petrological implications for granitoid magmatism in northwest Bulgaria. *Bulgarian Geological Society, Annual Scientific Conference "Geology 2004"*, 48–50.

Maclaren, J. M. (1904). The auriferous occurrences of Assam. Records of the Geological Survey of India, 31(4), 170–232.

Maniar, P. D., & Piccoli, P. M. (1989). Tectonic discrimination of granitoids. *Geological society of America bulletin*, 101(5), 635-643.

Merzbacher, C. I., & Eggler, D. H. (1984). Phase relations of basalts in their melting range at P(H_2O) = 5 kb as a function of oxygen fugacity: Part II, Mafic phases. *Journal of Petrology, 25*(2), 249–302. https://doi.org/10.1093/petrology/25.2.249.

Meyase, D., Rino, V., Kumar, S., & Nagi, R. (2023). Magnetic susceptibility, mineral chemistry, and geothermobarometry of granitoids from Lohit Plutonic Complex, Arunachal Trans-Himalaya, Northeast India: Implications on emplacement and crystallization conditions of oxidized calc-alkaline magmatic arc system. *Island Arc, 32*(1), e12479. https://doi.org/10.1111/iar.12479.

Middlemost, E. A. (1994). Naming materials in the magma/igneous rock system. *Earth-science reviews,* 37(3-4), 215-224.

Misra, D.K. (2009). Lithotectonic sequence and their Regional Correlation along the Lohit and Dibang valleys, Eastern Arunachal Pradesh. Journal Geological Society of India, 73, 213-219.

Misra, D.K. & Singh, T. (2002). Tectonic setting and neotectonic features along the Eastern Syntaxial Bend (Lohit and Dibang), Arunachal Himalaya. In: Charu C. Pant and K. Arun Sharma (Eds.). Aspects of Geology and Environment of the Himalaya, Gyanodaya Prakashan, Nainital, India, 19–40.

Mitchel, A.H.G. (1981). Phanerozoic plate boundaries in the mainland SE Asia, the Himalaya and Tibet. *Journal Geological Society of London*, 152, 689-701.

Mo, X.X., Dong, G.C., Zhao, Z.D., Guo, T.Y., Wang, L.L. & Chen, T. (2005). Timing of magma mixing in Gangdese magmatic belt during the India–Asia collision: Zircon SHIRMP U–Pb dating. *Acta Geologica Sinica*, 79, 66–76, https://doi.org/10.1111/j.1755-6724.2005.tb00868.

Mukherjee, K., Pundir, S., Adlakha, V., Singhal, S., Kumar, P., & Banerjee, S. (2025). Synchronous Cretaceous magmatism and migmatization in the Lohit and Dibang Valley, Easternmost Himalaya. *Journal of the Geological Society*, jgs2024-217.

Mutch, E. J. F., Blundy, J. D., Tattitch, B. C., Cooper, F. J., & Brooker, R. A. (2016). An experimental study of amphibole stability in low-pressure granitic magmas and a revised Al-in-hornblende geobarometer. *Contributions to Mineralogy and Petrology*, 171(10), 1–27. https://doi.org/10. 1007/s00410-016-1298-9.

Nachit, H., Ibhi, A., Abia, El.H. & Ohoud, M. B. (2005). Discrimination between primary magmatic biotites, reequilibrated biotites and neoformed biotites. *Comptes Rendus Geoscience,* 337(16), 1415–1420. https://doi.org/10.1016/j.crte.2005.09.002.

Najman, Y., Appel, E., Boudagher-Fadel, M., Bown, P., Carter, A., Garzanti, E., Godin, L., Han, J., Liebke, U., Oliver, G., Parrish, R. & Vezzoli, G. (2010). Timing of India-Asia collision: Geological, biostratigraphic, and palaeomagnetic constraints. *Journal of Geophysical Research: Solid Earth*, 115(B12).

Nandy, D. R. (1976). The Assam syntaxis of the Himalayas—A re-evaluation. *GSI Miscellaneous Publication*, 24(2), 364–367.

Nandy, D. R. (1981). Tectonic patterns in northeastern India—a discussion. *Indian Journal of Earth Sciences, 8*(1), 82–86.

Nandy, D. R. (2001). Geodynamics of Northeastern India and the Adjoining Region. Kolkata: *ACB Publications*.

Nandy S, Konwar P, Borah P., and Sarma K. P. (2005). A renewed look on the geology of Dibang Valley District, Mishmi Block of Arunachal Himalaya. *Journal of Geosciences*, 9 63-74.

Naney, M. T. (1983). Phase equilibria of rock-forming ferromagnesian silicates in granitic systems. *American Journal of Science, 283*(10), 993–1033. https://doi.org/10.2475/ajs.283.10.993.

Ningthoujam, P.S., Dubey, C.S., Lolee, L.K., Shukla, D.P., Naorem S.S. & Singh., S.K. (2015). Tectonic studies and crustal shortening across Easternmost Arunachal Himalaya. *Journal of Asian Earth Sciences*, 111, 339– 349.

O' Connor, J.T. (1965). A classification for quartz-rich igneous rocks based on feldspar ratios: *U. S. Geological Survey Professional Paper* 525-B, B79-B84.

Ormerod, D. S., Hawkesworth, C. J., Rogers, N. W., Leeman, W. P., & Menzies, M. A. (1988). Tectonic and magmatic transitions in the Western Great Basin, USA. Nature, 333(6171), 349-353.

Paces, J. B., & Miller, J. D. (1993). Precise U-Pb ages of Duluth Complex and related mafic intrusions, northeastern Minnesota: Geochronological insights to physical, petrogenetic, paleomagnetic, and tectonomagmatic processes associated with the 1.1 Ga Midcontinent Rift System. *Journal of Geophysical Research: Solid Earth*, 98(B8), 13997-14013. https://doi.org/10.1029/93JB01159.

Pandey, A., Rao, N. C., Chakrabarti, R., Pandit, D., Pankaj, P., Kumar, A., & Sahoo, S. (2017). Petrogenesis of a Mesoproterozoic shoshonitic lamprophyre dyke from the Wajrakarur kimberlite field, eastern Dharwar craton, southern India: Geochemical and Sr-Nd isotopic evidence for a modified sub-continental lithospheric mantle source. *Lithos*, *292*, 218-233.

Patiño Douce, A. E. (1997). Generation of metaluminous A-type granites by low-pressure melting of calc-alkaline granitoids. *Geology*, 25(8), 743–746. https://doi.org/10.1130/0091-7613(1997)0252.3.CO;2.

Peacock, S., McCann, C., Sothcott, J., & Astin, T. R. (1994). Experimental measurements of seismic attenuation in microfracture sedimentary rock. *Geophysics, 59*(9), 1386–1398. https://doi.org/10.1190/1.1443693.

Pearce, J. A., Harris, N. B., & Tindle, A. G. (1984). Trace element discrimination diagrams for the tectonic interpretation of granitic rocks. *Journal of petrology*, 25(4), 956-983.

Pebam, J., & Kamalakannan, D. (2019). Petrogenesis and emplacement of magmatic rocks of Lohit Plutonic Complex, Arunachal Trans-Himalaya, Northeast India. Indian Journal of Geosciences, 73(3), 213- 230.

Pebam, J., Duraisamy, K., Krishna, K. V. S. S., Sengupta, S., Ghosh, J. G., Kumar, R., Basak, K., & Guha, D. (2021). Zircon U–Pb ages of Lohit Plutonic Complex, NE India: Constraints on episodic magmatism of eastern Trans-Himalaya. *Geological Journal, 57*(2), 503–513. https://doi.org/10.1002/gj.4353.

Peccerillo, A., & Taylor, S. R. (1976). Geochemistry of Eocene calc-alkaline volcanic rocks from the Kastamonu area, northern Turkey. *Contributions to mineralogy and petrology*, 58(1), 63-81.

Phillips, M. W., Popp, R. K., & Clowe, C. A. (1988). Structural adjustments accompanying oxidation-dehydrogenation in amphiboles. *American Mineralogist*, 73(5-6), 500-506.

Phillips, R.J., Parrish, R.R. & Searle, M.P. (2004). Age constraints on ductile deformation and long-term slip rates along the Karakoram fault zone, Ladakh.Earth and Planetary Science Letters, 226, 305–319

Pitcher, W. S. (1983). Granite type and tectonic environment. *In Symposium on mountain building* (pp. 19-40).

Piwinskii, A. J. (1968). Experimental studies of igneous rock series: A zoned pluton in the Wallowa Batholith, Oregon. *Journal of Geology*, 76(6), 548–570. https://doi.org/10.1086/627064.

Pundir, S., Adlakha, V., Devrani, R., & Kumar, S. (2021). Tectonic control over shallow crustal exhumation across the India–Asia convergent margin. *Tectonics, 40*(10), e2021TC006722. https://doi.org/10.1029/2021TC006722.

Pundir, S., Adlakha, V., Kumar, S., & Singhal, S. (2020). Petrology, geochemistry and geochronology of granites and granite gneisses in the SE Karakoram, India: Record of subduction-related and pre- to syn-kinematic magmatism in the Karakoram Fault Zone. *Mineralogy and Petrology, 114*(5), 413–434. https://doi.org/10.1007/s00710-020-00706-y.

Rai, S. M. (1980). Geology of the Lesser and Higher Himalayan sequences along the Bhotekoshi River section between Syabru Besi and Rasuwa Gadhi, Nepal–China border area, central Nepal Himalaya. *Himalayan Geology, 10*(1), 1–24. https://www.researchgate.net/publication/322917141.

Ravikant, V. (2006). Sm–Nd isotopic evidence for Late Mesoproterozoic metamorphic relics in the East African Orogen from the Schirmacher Oasis, East

Antarctica. *The Journal of Geology, 114*(5), 615–625. https://doi.org/10.1086/506163.

Ravikant, V. (2009). Tectono-metamorphic events recorded in high-grade rocks from Filchnerfjella: Further evidence for Pan-African reworking of the Grenville-aged crust in central Dronning Maud Land, East Antarctica. *Indian Journal of Geosciences, 63*(2), 141–152.

Richards, A., Argles, T., Harris, N., Parrish, R., Ahmad, T., Darbyshire, F., & Draganits, E. (2005). Himalayan architecture constrained by isotopic tracers from clastic sediments. Earth and Planetary Science Letters, 236, 773–796.

Ridolfi, F., Zanetti, A., Renzulli, A., Perugini, D., Holtz, F., & Oberti, R. (2018). AMFORM, a new mass-based model for the calculation of the unit formula of amphiboles from electron microprobe analyses. American Mineralogist, 103, 1112–1125.

Ridolfi, F. (2021). Amp-TB2: an updated model for calcic amphibole thermobarometry. *Minerals*, *11*(3), 324.

Ridolfi, F., Renzulli, A., & Puerini, M. (2010). Stability and chemical equilibrium of amphibole in calc-alkaline magmas: an overview, new thermobarometric formulations and application to subduction-related volcanoes. *Contributions to Mineralogy and Petrology,* 160, 45–66.

Ridolfi, F., & Renzulli, A. (2012). Calcic amphiboles in calc-alkaline and alkaline magmas: Thermobarometric and chemometric empirical equations valid up to 1,130 ºC and 2.2 GPa. *Contributions to Mineralogy and Petrology*, 163(5), 877–895. https://doi.org/10.1007/s00410-011- 0704-6.

Rieder, M., Cavazzini, G., D'Yakonov, Y. S., Frank-Kamenetskii, V. A., Gottardt, G., Guggenheim, S., Koval, P. V., Muller, G., Neiva, A. M. R., Radoslovich, E. W., Robert, J. L., Sassi, F. P., Takeda, H., Weiss, Z., & Wones, D. R. (1998). Nomenclature of the micas. *The Canadian Mineralogist, 36*(3), 905–912. https://doi.org/10.1346/CCMN.1998.0460513.

Rowley, D. B. (1996). Age of initiation of collision between India and Asia: A review of stratigraphic data. *Earth and Planetary Science Letters*, 145(1-4), 1-13.

Rudnick, R. L., & Gao, S. (2003). Composition of the continental crust. In R. L. Rudnick (Ed.), *Treatise on geochemistry* (Vol. 3, pp. 1–64). Elsevier.

Sant'Ovaia, H., Martins. H., & Noronha, F. (2013). Oxidized and reduced Portuguese Variscan granites associated with W and Sn hydrothermal lode deposits: magnetic susceptibility results. *Comunicações Geológicas*, 100, 1, 33-39.

Sarma, K. P., Nandy, S., Devi, N. R., & Konwar, P. (2009). Is Mishmi Block a Tectonic Roof? Some Observations. In: Magmatism, Tectonism and Mineralization, edited by Kumar S (*Macmilan Publishers India Ltd., New Delhi, India),* 167-178.

Sarma, K. P., Nandy, S., & Mazumdar, N. (2012). Structural studies of the Mishmi block in parts of Dibang Valley of Arunachal Himalaya, Northeast India. *International Journal of Geology, Earth and Environmental Sciences*, 2(3), 43-56.

Sarma, K. P., Sharma, R., & Mazumdar, N. (2017). Geological framework of Western Arunachal Himalaya and Eastern Arunachal Himalaya – Are they identical? Some observations. American International *Journal of Research in Science, Technology, Engineering and Mathematics*, 19, 51–58.

Satyanarayanan, M., Balaram, V., Sawant, S. S., Subramanyam, K. S. V., Krishna, G. V., Dasaram, B., & Manikyamba, C. (2018). Rapid determination of REEs, PGEs, and other trace elements in geological and environmental materials by high resolution inductively coupled plasma mass spectrometry. *Atomic Spectroscopy,* 39(1), 1–15. https://doi.org/10.46770/as.2018.01.001.

Saunders, A. D., Norry, M. J., & Tarney, J. (1991). Fluid influence on the trace element compositions of subduction zone magmas. Philosophical Transactions of the Royal Society of London. Series A: *Physical and Engineering Sciences*, 335(1638), 377-392.

Schärer, U. R. H. Xu, & C. J. Allègre (1984). U–Pb geochronology of Gangdese (Transhimalaya) plutonism in the Zhasa–Xigaze region, Tibet. *Earth and Planetary Science Letters, 69*, 311–320.

Schmidt, M. W. (1992). Amphibole composition in tonalite as a function of pressure: An experimental calibration of the Al-in-hornblende barometer. *Contributions to Mineralogy and Petrology*, 110(2–3), 304–310. https://doi.org/10.1007/BF00310745.

Schmidt, M. W., & Poli, S. (2004). Magmatic epidote. *Reviews in Mineralogy and Geochemistry, 56*(1), 399–430. https://doi.org/10.2138/gsrmg.56.1.399

Shand, S. J. (1927). On the relations between silica, alumina, and the bases in eruptive rocks, considered as a means of classification. *Geological Magazine*, 64(10), 446-449.

Sharma, K. K., & Kumar, S. (1978). Contributions to the geology of Ladakh. *Himalayan Geology, 8*(2), 252–287.

Shaw, D. M. (1970). Trace element fractionation during anatexis. *Geochimica et cosmochimica acta*, 34(2), 237-243.

Singh, B., Kumar, S., (2005). Petrogenetic appraisal of early Palaeozoic granitoids of Kinnaur District, Higher Himachal Himalaya, India. *Gondwana Research*, 8, 67–76. https://doi.org/10.1016/S1342-937X(05)70263-X.

Singh, B., Kumar, S., Ban, M., Nakashima, K., (2016). Mineralogy and geochemistry of granitoids from Kinnaur region, Himachal Higher Himalaya, India: Implication on the nature of felsic magmatism in the collision tectonics. *Journal of Earth Sciences*. 125, 1329–1352. https://doi.org/10.1007/s12040-016-0748-0.

Singh, S. & Chowdhury, P.K. (1990). An outline of the Geological framework of the Arunachal Himalaya, *Journal of Himalayan Geology*, 1(2), 189-197.

Singh, S., & Malhotra, G. (1983). Tectonic set-up of Yang Sang Chu Valley, West Siang, Arunachal Pradesh. In P. S. Saklani (Ed.), *Himalayan Shears* (pp. 107–113). Hindustan Books.

Skjerlie, K. P., & Johnston, A. D. (1993). Fluid-absent melting behavior of an F-rich tonalitic gneiss at mid-crustal pressures: implications for the generation of anorogenic granites. *Journal of Petrology*, 34(4), 785-815.

Spear, F. S. (1981). Phase composition as a measure of reaction progress: An experimental study of a mid-ocean ridge tholeiite. *American Mineralogist, 69*(5–6), 677–687.

Speer, J.A. (1987). Evolution of magmatic AFM mineral assemblages in granitoid rocks: The hornblende+melt=biotite reaction in the Liberty Hill pluton, South Carolina; *American Mineralogist*, 72, 9–10.

Stacey, J.S., & Kramers, J.D. (1975). Approximation of terrestrial lead isotope evolution by a Two-Stage Model. *Earth and Planetary Science Letters*, 26, 207-221. https://doi.org/10.1016/0012-821X(75)90088-6.

Stein, E., & Dietl, C., 2001. Hornblende thermobarometry of granitoids from the central Odenwald (Germany) and their implications for the geotectonic development of the Odenwald. *Mineralogy and Petrology*, 72, 185–207.

Stern, C. R., & Kilian, R. (1996). Role of the subducted slab, mantle wedge, and continental crust in the generation of adakites from the Andean Austral Volcanic Zone. *Contributions to Mineralogy and Petrology, 123*(3), 263–281. https://doi.org/10.1007/s004100050155.

St-Onge, M. R., Corrigan, D., & Hanmer, S. (2009). Tectonothermal evolution of the middle crust in the Trans-Hudson Orogen, Baffin Island, Canada: Evidence from petrology and monazite geochronology of sillimanite-bearing migmatites. *Lithos*, 112(1–2), 143–162. https://doi.org/10.1016/j.lithos.2009.02.008.

Streckeisen, A. L. (1974). Classification and nomenclature of plutonic rocks: Recommendations of the IUGS Subcommission on the Systematics of Igneous Rocks. *Geologische Rundschau, 63*(2), 773–785. https://doi.org/10.1007/BF01820841.

Stussi, J.M., & Cuney, M. (1996). Nature of Biotites from alkaline, calcalkaline and peraluminous magmas by Abdel-Fattah M. Abdel-Rahman: A Comment. *Journal of Petrology,* 37(5), 1025-1029.

Sun, S. S., & McDonough, W. F. (1989). Chemical and isotopic systematics of oceanic basalts: implications for mantle composition and processes. *Geological Society, London, Special Publications*, 42(1), 313-345.

Takagi, T. (2004). Origin of magnetite-and ilmenite-series granitic rocks in the Japan Arc. *American Journal of Science*, 304(2), 169–202. https://doi.org/10.2475/ajs.304.2.169.

Tan, W., Liu, P., He, H., Wang, C. Y., & Liang, X. (2016). Mineralogy and origin of exsolution in Ti-rich magnetite from different magmatic Fe-Ti oxide-bearing intrusions. The Canadian Mineralogist, 54(3), 539-553.Thakur, V. C., & Jain, A. K. (1974). Tectonics of the region of Eastern Himalayan syntaxis. *Current Science*, 43(24), 783-785.

Thakur, V.C. & Jain, A.K. (1975) Some observation on deformation, metamorphism and tectonic significance of rocks of some parts of Mishmi hills, Lohit District (NEFA) Arunachal Pradesh. *Himalayan Geology*, 5, 339-364.

Thomson, J., & Oldfield, F. (1986). *Environmental magnetism.* Allen & Unwin.

Tulloch, A.J., & Challis, G.A. (2000). Emplacement depths of Paleozoic-Mesozoic plutons from western New Zealand estimated by hornblende-AI geobarometry. New Zealand *Journal of Geology and Geophysics*, 43(4), 555-567. https://doi.org/10.1080/00288306.2000.9514908.

Turnbull, R., Weaver, S., Tulloch, A., Cole, J., Handler, M., & Ireland, T. (2010). Field and geochemical constraints on Mafic–Felsic interactions, and processes in high-level arc magma chambers: an example from the Halfmoon Pluton, New Zealand. *Journal of Petrology*. https://doi.org/10.1093/petrology/egq026.

Turner, S. P., Hawkesworth, C. J., & Menzies, M. A. (2013). Geochemical constraints on the origin and evolution of the Azores mantle plume. *Geology, 41*(4), 491–494. https://doi.org/10.1130/G34886.1

Tuttle, O.F., & Bowen, N.L. (1958). Origin of granite in the light of experimental studies in the System $NaAlSi_3O_8$-$KAlSi_3O_8$-SiO_2-H_2O. *Geological Society of America Memoir*, 74, 153 https://doi.org/10.1130/MEM74-p1.

Upadhyay, R., Frisch, W., & Siebel, W. (2008). Tectonic implications of new U–Pb zircon ages of the Ladakh batholith, Indus suture zone, northwest Himalaya, India. Terra Nova, 20(4), 309-317.

Van Buer, N. J., Jagoutz, O., Upadhyay, R., & Guillong, M. (2015). Mid-crustal detachment beneath western Tibet exhumed where conjugate Karakoram and Longmu–Gozha Co faults intersect. *Earth and Planetary Science Letters*, 413, 144-157.

Verma, S. P. (1999). Geochemistry of evolved magmas and their relationship to subduction-unrelated mafic volcanism at the volcanic front of the central Mexican Volcanic Belt. *Journal of Volcanology and Geothermal Research*, 93, 151–171.

Verosub, K. L., & Roberts, A. P. (1995). Environmental magnetism: Past, present, and future. *Journal of Geophysical Research, 100*(B12), 21755–21776. https://doi.org/10.1029/95JB01453.

Villaseca, C., Barbero, L., & Rogers, G. (1998). Crustal origin of Hercynian peraluminous granitic batholiths of Central Spain: petrological, geochemical and isotopic (Sr, Nd) constraints. *Lithos*, 43(2), 55-79.

Wang, R., Richards, J. P., Zeng-qian, H., An, F., & Creaser, R. A. (2015). Zircon U-Pb age and Sr-Nd-Hf-O isotope geochemistry of the Paleocene–Eocene igneous rocks in western Gangdese: Evidence for the timing of Neo-Tethyan slab breakoff. *Lithos*, 224, 179–194.

Weinberg, R. F., & Dunlap, W. J. (2000). Growth and deformation of the Ladakh Batholith, Northwest Himalayas: Implications for timing of continental collision and origin of calc-alkaline batholiths. *Journal of Geology, 108*(3), 303–320. https://doi.org/10.1086/314405.

Wen, D.-R., Liu, D. et al. 2008b. Zircon SHRIMP U–Pb ages of the Gangdese Batholith and implications for Neotethyan subduction in southern Tibet. *Chemical Geology*, 252, 191–201. https://doi.org/10.1016/j.chemgeo.2008.03.003.

Whalen, J. B., Currie, K. L., & Chappell, B. W. (1987). A-type granites: geochemical characteristics, discrimination and petrogenesis. *Contributions to mineralogy and petrology*, 95(4), 407-419.

White, A. J., & Chappell, B. W. (1977). Ultrametamorphism and granitoid genesis. *Tectonophysics*, 43(1-2), 7-22.

Williams, I. S. (1998). U-Th-Pb Geochronology by Ion Microprobe. In: McKibben, M. A., Shanks III, W. C., Ridley, W. I. (Eds.), Applications of microanalytical techniques to understanding mineralizing processes. *Reviews in Economic Geology*, 7, 1-35.

Wones, D. R. (1989). Significance of the assemblage titanite + magnetite + quartz in granitic rocks. The American Mineralogist, 74(7–8), 744–749.

Wones, D. R., & Eguster, H. P. (1965). Stability of biotite: Experiment, application, theory, and application. *The American Mineralogist*, 50, 1228–1272.

Wones, D.R. (1981). Mafic minerals as indicators of intensive variables in granitic magmas. *Mining and Geology*, 31, 19–122.

Yang, L., Miller, C. F., & Wu, F. Y. (2022). Estimating crystallization pressure of peraluminous melts: an experimentally based empirical approach. *Contributions to Mineralogy and Petrology*, 177(8), 78.

Yavuz, F., & Döner, Z. (2017). WinAmptb: A windows program for calcic amphibole thermobarometry. *Periodico Di Mineralogia,* 86(2), 135–167. https://doi.org/10.2451/2017PM710.

Yavuz, F., & Öztaş T., (1997). BIOTERM - A program for 163 P M WinAmptb: A Windows program for calcic amphibole thermobarometry evaluating and plotting microprobe analyses of biotite from barren and mineralized magmatic suites. Computers & Geosciences 23, 897-207.

Zartman, R. E., & Doe, B. R. (1981). Plumbotectonics—the model. *Tectonophysics,* 75(1-2), 135-162.

Zen, E.-an., & Hammarstrom, J. M. (1984). Magmatic epidote and its petrologic significance. *Geology, 12*(9), 515–518. https://doi.org/10.1130/0091-7613(1984)12<515:MEAIPS>2.0.CO;2.

Zhang, P., Molnar, P., & Xu, X. (2007). Late Quaternary and present-day rates of slip along the Altyn Tagh Fault, northern margin of the Tibetan Plateau. *Tectonics, 26*. https://doi.org/10.1029/2006TC002014.

Zhou, Z. X. (1986). The origin of intrusive mass in Fengshandong, Hubei province. *Acta Petrologica Sinica,* 2(2), 59–70.

Zhu, D. C., Zhao, Z. D., Niu, Y., Dilek, Y., & Mo, X. X. (2011). Lhasa terrane in southern Tibet came from Australia. Geology, 39(8), 727-730.

Zhu, D. C., Zhao, Z. D., Niu, Y., Dilek, Y., Hou, Z. Q., & Mo, X. X. (2013). The origin and pre-Cenozoic evolution of the Tibetan Plateau. Gondwana Research, 23(4), 1429-1454.

DEPARTMENT OF GEOLOGY

FACULTY OF EARTH SCIENCES

MOHANLAL SUKHADIA UNIVERSITY, UDAIPUR

Certificate of Participation

This is to certify that

Mr./Ms./Dr. Diezeneino Meyase

From Nagaland University

Presented a paper / participated in GEOYOUTH-2020

(10th All India Students Symposium on Geology) from 05th – 06th February, 2020

and awarded Best paper *presentation prize.*

Prof. S. R. Jakhar
Chairman, GEOYOUTH-2020 &
Head Department of Geology

Dr. Harish Kapasya
Convener
GEOYOUTH-2020

Azadi Ka Amrit Mahotsav

6th NATIONAL GEO-RESEARCH SCHOLARS' MEET
on
GEOSCIENCES IN LADAKH HIMALAYA

Organized by: University of Ladakh, Leh
in Association with: Wadia Institute of Himalayan Geology, Dehradun

This Certificate is Awarded to

Prof./ Dr./ Mr./ Ms. Diezeneino Meyase

of Nagaland University for

Invited Talk/ Oral-Poster Presentation held at University of Ladakh, Leh Campus, Leh during June 7-10, 2022.

Prof. Kalachand Sain
Director
WIHG, Dehradun

Dr. Jayangonda Perumal
Convener
WIHG, Dehradun

Dr. Riyaz M.K. Khan
Convener
University of Ladakh

Prof. S.K. Mehta
Vice Chancellor
University of Ladakh

Certificate of Participation

THIS CERTIFICATE IS PRESENTED TO

DIEZENEINO MEYASE

for active participation in **the 37th International Geological Congress 2024 (IGC 2024)** held during 25-31 August 2024 at BEXCO, Busan, Korea.

Jin Yong Lee

Daekyo CHEONG
Chairman of
the Organizing Committee of IGC 2024

IUGS

Jin-Yong LEE
Chair of the Scientific Program Committee